A NOVEL STABILITY CONTROL SYSTEM FOR TWO-WHEELED ROBOTIC WHEELCHAIRS

A THESIS SUBMITTED TO AUCKLAND UNIVERSITY OF TECHNOLOGY
IN FULFILMENT OF THE REQUIREMENTS FOR THE DEGREE OF
DOCTOR OF PHILOSOPHY

Supervisor
A.Prof. Loulin Huang
Prof. Ahmed M.Aljumaily
A.Prof. Behrooz Lotfi

June 2021

By
Mostafa Nikpour
School of Engineering, Computer and Mathematical Sciences

Abstract

Most conventional robotic wheelchairs contain four wheels (two active driving wheels and two passive casters) which makes them statically stable. In comparison, a two-wheeled robotic wheelchair (TWRW) offers much better maneuverability, while without the support of casters, it is inherently unstable and requires a stability control. Majority of stability controllers rely on the driving torques of the wheels which are high in magnitude and results in the increase of energy consumption. Various disturbances in the system also affect the performance of the controller.

In this research, these issues will be resolved through a novel control approach where the stability is kept by the motion of a pendulum-like movable mechanism added to the TWRW. The control schemes including PID control, Computed torque control (CTC), Sliding mode control (SMC), and Second-order sliding mode control (SOSMC) are developed for stability control. The model-based controllers (CTC, SMC, and SOSMC) are developed from the dynamic model established through the Euler-Lagrangian method in which the disturbances caused by model uncertainties and rider's motion are considered. Simulation results show the stability is achieved through the proposed system with much less torque, power, and energy consumption than the conventional control system.

Stability control becomes more challenging when a TWRW is also required to move in a desired direction. To rely on the wheels' motions to achieve both stability and direction control tend to impose a large burden on the wheels' driving motors

or other types of actuators in terms of their driving torque and energy consumption. To solve these problems, the added movable mechanism is used to assist the wheels to produce control actions. The simulation results validate the effectiveness of the proposed system, where the TWRW can achieve stability and direction control in a similar pattern to the conventional system. However, the input torque, input power, and energy consumption of motors in the proposed system are much smaller than those required in the conventional approach.

To verify the simulation results, the experimental results are provided, where a scaled-down TWRW is designed and modelled to evaluate the stability control systems. The experimental results confirm the results obtained from the simulation.

Contents

List of Tables

List of Figures

Attestation of Authorship

I hereby declare that this submission is my own work and that, to the best of my knowledge and belief, it contains no material previously published or written by another person nor material which to a substantial extent has been accepted for the qualification of any other degree or diploma of a university or other institution of higher learning.

Signature of candidate

Publications

Journal Papers:

Nikpour, M., Huang, L., Al-Jumaily, A.M.: Stability and Direction Control of a Two-Wheeled Robotic Wheelchair Through a Movable Mechanism, *IEEE Access*, vol. 8, pp. 45221-45230 (2020)

Nikpour, M., Huang, L., Al-Jumaily, A.M.: An Approach on Velocity and Stability Control of a Two-Wheeled Robotic Wheelchair, *Applied Sciences*, vol. 10, no. 18 pp. 6446 (2020)

Conference Papers:

Nikpour, M., Huang, L., Al-Jumaily, A.M., Lotfi, B.: Stability control of mobile inverted pendulum through an added movable mechanism, *25th International Conference of Mechatronics and Machine Vision in Practice (M2VIP)*, pp. 1-6 (2018)

Nomenclature

Notation	**Definition**
$\boldsymbol{X^W}$ – $\boldsymbol{Y^W}$ – $\boldsymbol{Z^W}$	World coordinate frame attached to the ground
$\boldsymbol{X^L}$ – $\boldsymbol{Y^L}$ – $\boldsymbol{Z^L}$	TWRW coordinate frame attached to the middle of wheels axle
$\boldsymbol{x^r}$ – $\boldsymbol{y^r}$ – $\boldsymbol{z^r}$	The right wheel's local frame
$\boldsymbol{x^l}$ – $\boldsymbol{y^l}$ – $\boldsymbol{z^l}$	The left wheel's local frame
$\boldsymbol{x^b}$ – $\boldsymbol{y^b}$ – $\boldsymbol{z^b}$	The body's local frame
$\boldsymbol{x^p}$ – $\boldsymbol{y^p}$ – $\boldsymbol{z^p}$	The movable mechanism's local frame
O	Middle of wheel axle
P	The point movable mechanism is added to the TWRW
θ_r, θ_l	Rotation angle of the right and left wheel measured from $\boldsymbol{Y^L}$ axis
θ_b	Rotation angle of the body (pitch angle) measured from $\boldsymbol{Y^L}$ axis
θ_p	Rotation angle of the movable mechanism measured from link OP
θ_y	Yaw angle of the TWRW measured from $\boldsymbol{X^W}$ axis
m_w, m_b, m_p	Mass of each wheel, body and movable mechanism, respectively
J_{w_x}, J_{w_y}, J_{w_z}	Moment of inertia of each wheel defined at their local frame
J_{b_x}, J_{b_y}, J_{b_z}	Moment of inertia of body defined at its local frame
J_{p_x}, J_{p_y}, J_{p_z}	Moment of inertia of movable mechanism defined at its local frame
r	Radius of each wheel
d	Length of wheels axle
l	Distance between the body's CoG and point O
l'	Length of the movable mechanism' rod
b	Distance between point O and P
x_b	Change of the body's COG position along the seat
τ_r, τ_l, τ_p	Input torque of the right and left wheel and the movable mechanism, respectively
τ_w	Total torque of the right and left wheel
P_r, P_l, P_p	Input power of the right wheel, left wheel, and the movable mechanism motors, respectively
E_r, E_l, E_p	Energy consumption of the right wheel, left wheel, and the movable mechanism motors, respectively

List of Abbreviations

TWRW	Two-Wheeled Robotic Wheelchair
PID	Proportional-Integral-Derivative
CTC	Computed Torque Control
SMC	Sliding Mode Control
SOSMC	Second-Order Sliding Mode Control
HSMC	Hierarchical Sliding Mode Control
TWIP	Two-Wheeled Inverted Pendulum
UW-Car	Uni-Directional Wheel Car
EOM	Equation of Motion
ANN	Artificial Neural Network
LQR	Linear Quadratic Regulator
SDRE	State-Dependent Riccati Equation
HJBI	Hamilton–Jacobi–Bellman–Isaacs
COG	Centre of Gravity
DC	Direct Current
BLDC	Brushless Direct Current
IMU	Inertial Measurement Unit
GNSS	Global Navigation Satellite Systems
PC	Personal Computer
USB	Universal Serial Bus
I^2C	Inter-Integrated Circuit
WiFi	Wireless Fidelity
PWM	Pulse Width Modulation
UART	Universal Asynchronous Receiver/Transmitter

Acknowledgements

First and foremost, I would like to express my deepest gratitude to my supervisor, A. Prof Loulin Huang, for his support, and guidance. The success of this research would have not been possible without his great support. Also, I would like to acknowledge Prof. Ahmed Aljumaily for his support throughout this research.

I would like to thank Dr. Behrooz Lotfi for his guidance. His encouragement was the greatest motivation for me to do this research. I would like to extend my honest gratitude to Simon Hartley for his help with providing the experimental setup. Also, I would like to thank Anushka Siriwardane who joined us as an Intern to assist in building the wheelchair.

I would like to thank the Auckland University of Technology for providing this opportunity for me to do my Ph.D. study. Also, I would like to acknowledge the Institute of Biomedical Technologies (IBTec) for their financial support of this research. It has been my pleasure to work at IBTec.

Lastly, I would like to thank my family for their support and encouragement I have always received throughout my life.

Chapter 1

Introduction

1.1 Two-wheeled robotic wheelchair (TWRW)

The life of elderly people, paralysed people, etc., relies on wheelchairs which can provide mobility for them [1]. Robotic wheelchairs have become popular as they are easy to use and the rider doesn't need to consume their own energy to make it move [2]. Most existing robotic wheelchairs are four-wheeled (two driving wheels and two casters) which are statically stable, but they have a poor dexterity for they cannot make spot turn and cannot move easily on uneven surfaces or manoeuvrer in narrow spaces [3].

To resolve these problems, a two-wheeled robotic wheelchair (TWRW) is proposed. It has better maneuverability than conventional robotic wheelchairs, as it can turn on the spot and has small footprints [4]. In addition to having the ability to pass from narrow places, they can climb small steps [5]. Contrary to conventional robotic wheelchairs which have two casters, the TWRW has no caster and is equipped with only two driving wheels [6]. Without the support of casters, it becomes an inherently unstable system and an active controller should be developed to keep it stable [7]. TWRW is similar to the Segway, in which its mobility and stability are provided by driving wheels [8]. When using the Segway the rider stands upright, while he would sit on the TWRW's seat which makes him feel more comfortable [9].

1.2 TWRW stability control

The design and development of a proper stability control system are crucial for TWRW. The stability of TWRW is measured by the position of rider with respect to the upright position [10]. This position is denoted by pitch angle which is explained in details in Chapter. 2. Most conventional stability control systems rely on the torques applied to the driving wheels [11, 12]. In this control system, the wheels are responsible for mobility and stability at the same time. When TWRW moves on uneven surfaces or with high acceleration, it is likely torque and power required from the motors become huge and exceed the motor's capacity [13]. To resolve this problem, motors with high power capacity are used. These motors are costly, bulky, and their energy consumption is huge, which reduces the battery's life. Some control systems like using a movable seat or a movable mass under the seat are also used [14, 15]. They have some constraints like limited space for their linear motion.

In addition to the motors' capacity and energy consumption, the robustness of the stability control system is an important component. The control system should be able to overcome the disturbances applied to the system [16]. These disturbances include uneven surfaces, sensor noise, rider's motion, system uncertainties, etc. The robustness of the control system is dependent on the control scheme developed for the system [17]. Several control schemes can be used, like model-free controllers (e.g. PID control, fuzzy control, etc.) or model-based controllers (e.g. Computed torque control, Sliding mode control, etc.). The model-based controllers which require the dynamic model of the system are more robust than model-free controllers [18]. The second-order sliding mode control is one of the most common robust controller used for real-time systems, as it doesn't require high complex computations [19].

Real time states of the TWRW such as its pitch angle and the rate of its change are needed for the implementation of the stability controller [20]. These variables can be measured through encoders, tilt sensor, gyroscope, accelerometer etc. whose output signals tend to contain noises [21].

1.3 Research methodology

In this research, a novel stability control system is proposed and various control schemes are examined for the TWRW. The proposed system is developed around a pendulum-like movable mechanism added to the TWRW. The mechanism is added under the seat to assist the system's stability. Through the motion control of this mechanism, the centre of gravity of the system including the rider can be varied as needed to keep the stability of the system. In this approach, instead of applying the torque to the wheels, it should be applied to the movable mechanism to keep the system stable. Thus, this control system is not reliant upon the wheel motors for stabilising the system; this allows the wheel movement to be controlled by the full capabilities of the wheel motors.

To analyze the performance of the proposed system, the stability control through the conventional system is developed. In the conventional system, the stability of system which is shown by pitch angle is supplied by driving wheels. Therefore, in both control systems the controller aim is stability (pitch angle). However, the controller input for the conventional and proposed systems are the input torque of the driving wheels (right and left wheels), and input torque of the added movable mechanism, respectively. These two control systems can be summarized as follows:

TWRW Stability Control:

Conventional System

- **Controller input**
  - Input torque of right wheel
  - Input torque of left wheel
- **Controller aim**
  - Stability (Pitch angle)

Proposed System

- **Controller input**
  - Input torque of added movable mechanism
- **Controller aim**
  - Stability (Pitch angle)

In addition to stability, direction control is also important. In this control system, the TWRW should follow its desired direction, while remaining stable. The direction of system is measured by yaw angle which is explained with more details in Chapter. 3. In the conventional approach, the driving wheels are responsible for stability and direction control simultaneously. This control system requires significant input torque and power and its energy consumption is large. In the control system proposed in this thesis, the added mechanism is used to aid the wheels for both stability and direction control. Therefore, the control inputs are input torques of the right wheel, left wheel, and added movable mechanism.

The TWRW stability and direction control for the conventional and proposed systems are developed. In the conventional approach, the controller aims are stability (pitch angle) and direction (yaw angle), and the controller input are the input torques of the right and left wheels. For proposed system, the controller aims are same as the conventional one, while it has three control input including the input torque of the right and left wheels, and the movable mechanism. Both control systems can be summarized as follows:

TWRW Stability and Direction Control:

Conventional System

- **Controller input**
  - Input torque of right wheel
  - Input torque of left wheel
- **Controller aim**
  - Stability (Pitch angle)
  - Direction (Yaw angle)

Proposed System

- **Controller input**
  - Input torque of right wheel
  - Input torque of left wheel
  - Input torque of added movable mechanism
- **Controller aim**
  - Stability (Pitch angle)
  - Direction (Yaw angle)

To develop the controller for TWRW, some control schemes including Proportional-Integral–Derivative (PID) control, Computed torque control (CTC), Sliding mode control (SMC), and Second-order sliding mode control (SOSMC) are used. The PID control which is a model-free controller doesn't need the dynamic model of the system. However, to utilize the CTC, SMC, and SOSMC, the dynamic model of the system is needed. The Euler-Lagrangian method is used to establish the dynamic model where the disturbances including rider's motion and the model uncertainties are considered.

In the control schemes used for the TWRW stability, the controller's feedback is the state of wheelchair (e.g., pitch angle and pitch velocity). The sensors used for the state feedback like tilt sensor (which can measure rotation angle directly) and IMU (inertia measurement unit which include gyro sensor and accelerometer) suffer from low accuracy due to the measurement noise. Considering the special features of sensor signals, a Kalman Filter which is one of the best real-time filtering method is used to filter noises.

To compare the performance of the conventional and proposed systems, the TWRW is simulated under various controllers. The simulation results for stability control prove that under the conventional and proposed systems, the TWRW can keep its stability in a similar pattern, while the required input torque, input power, and energy consumption in the proposed system is much smaller than those in the conventional one. This is also the case for both stability and direction control. Besides, the input power and energy consumption of the added mechanism are very small and can be almost neglected. To verify the simulation results, the experimental setup is designed and implemented. A scaled-down TWRW is modelled and the stability control systems are tested under some cases. Due to the time constraints, the experimental results are only provided for stability control and the direction control is not implemented. The experimental results obtained for stability control confirm the simulation results.

1.4 Thesis structure

The rest of the thesis is organized as follows:

In Chapter 2, the background and literature of wheelchairs including manual and robotic wheelchairs are reviewed. They are compared to each other and their advantages and disadvantages are explained. Furthermore, the new type of robotic wheelchair (TWRW) is discussed and its superiority over the conventional robotic wheelchairs is investigated. Additionally, the main shortcoming of TWRW (stability) is explained and the current stability control systems are discussed. The dynamic modeling is derived in Chapter 3. Also, the common disturbances applied to the system including rider's motion and model uncertainties are modeled. From dynamic modeling, the nonlinear equation of motion (EOM) is established.

The stability control is developed in Chapter 4. In this chapter, various control schemes including PID, CTC, SMC, and SOSMC are used to develop stability control. The simulation results are provided to compare the performance of the conventional and proposed approaches through the control schemes mentioned above. In Chapter 5, the stability and direction control are developed through conventional and proposed approaches. The CTC, SMC, and SOSMC are utilized to develop the controllers. To verify the simulation results, the experimental setup is provided and explained in detail in Chapter 6. This chapter further discusses the experimental results of stability control through the conventional and proposed methods. Conclusion and future works are provided in Chapter 7. The dynamic modelling details of the conventional and proposed systems are provided in Appendix A and Appendix B, respectively. Appendix C provides the detail of experimental setup explained in Chapter. 6.

Chapter 2

Literature Review

2.1 Robotic wheelchairs

In the recent decade, the ageing population in the world increased drastically. For instance, 25 percent of population in Japan are above 65 years old [7]. Additionally, there are a number of people in the world suffering from motor impairment [22, 23]. Wheelchairs have become an essential transportation device that are often utilized by these groups of people. They can provide sufficient mobility which is crucial for handicapped people's life [24–27]. Wheelchairs can be categorized into two parts: manual and robotic.

A manual wheelchair, seen in Figure. 2.1 [28], is driven manually by the rider or caregiver. Statistics show that about 90% of all wheelchairs are manual wheelchairs [29, 30]. They are the most common type of wheelchair used by people, as they are inexpensive, light, and easy to use [31]. However, repetitive use of manual wheelchairs causes pain on the upper body of the rider, especially their shoulders and wrists [32–34].

Figure 2.1: Manual wheelchair [28].

Robotic wheelchairs can decrease some problems experienced by manual wheelchair users. A robotic wheelchair is driven by actuators (usually electrical motors), and the rider doesn't need to consume his own energy to make it move and can achieve autonomy in response to different motion requirements [35–37].

2.1.1 Conventional robotic wheelchairs

Most conventional robotic wheelchairs are four-wheeled (two driving wheels and two casters). In this wheelchair, the required power for wheelchair motion is supplied by the motors on both wheels [38]. Each wheel has a separate motor which enables the rider to pass his desired trajectory. The rider can control the wheelchair through a joystick [39]. The front casters are used to assist the system's stability. Even though the casters decrease wheelchair's mobility as it leads to increasing the turning radius [40–43].

Additionally, there are some limitations for the users of this type of robotic wheelchairs. For example, they can't pass from narrow places, uneven surfaces, steps, etc [44]. Figure. 2.2 shows a conventional robotic wheelchair [45].

Figure 2.2: Conventional robotic wheelchair [45].

2.1.2 Two-wheeled robotic wheelchair

A new type of casters-free TWRW can achieve good stability and mobility at the same time. It can turn on the spot and climb small steps [46, 47]. It is a compact-sized wheelchair that enables it to pass narrow spaces [48, 49]. Nevertheless, removing the wheelchair's casters can make it unstable as shown by the variation of its pitch angle when it moves. A controller is needed to prevent it from overturning when the pitch angle reaches a limit [50–53].

A TWRW can be modelled as a two-wheeled inverted pendulum (TWIP). The rider who sits on the wheelchair can be considered as a part of the pendulum of the TWIP [54, 55]. With the assumption that there is no slip between wheels and the ground, the TWRW has three degrees of freedom (angle of the left and right wheel, and pitch angle) [56–58] which are depicted in Figure. 2.3.

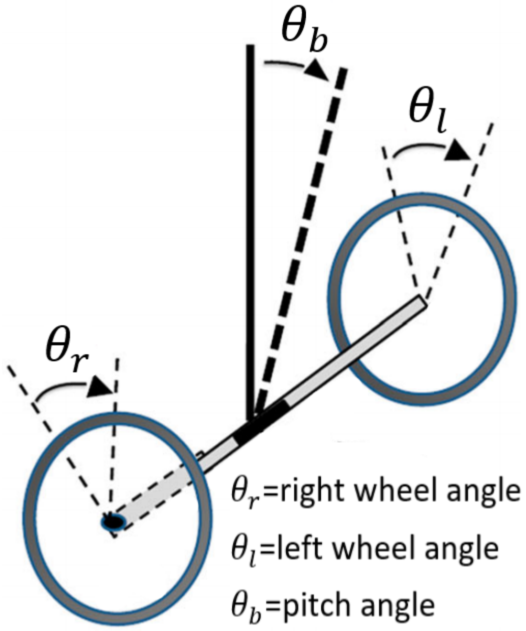

Figure 2.3: Description of rotation angles for a two-wheeled inverted pendulum.

There are two inputs in the TWRW: the torques applied on the right and left wheels. As the number of inputs is less than the degrees of freedom, it is considered as an underactuated system [59–61]. In an underactuated system, not all degrees of freedom can be controlled directly. The TWRW relies on the relative angular velocity between two wheels to produce different motion patterns such as turning or going straight. This is normally called differential driven mechanism [62, 63].

In 1990, the iBOT, a powered wheelchair, was introduced (see Figure. 2.4 [64]). The iBOT has four wheels and is able to change its configuration. Two wheels of this vehicle can be lifted to increase the height of the seat of the rider. As seen in this configuration, the wheelchair stands only on two wheels, the mechanism becomes a TWRW. Besides, iBOT can move on uneven surfaces including sand and gravel. A patented iBalanceTM technology, a synthesis of computers and gyroscope, is used to keep the wheelchair stable [65–68].

Figure 2.4: The iBOT wheelchair [64].

Nakamura and Murakami designed a new robotic wheelchair from a conventional wheelchair where two casters were removed (see Figure. 2.5 [69]). This robotic wheelchair can pass the trajectory commanded by the joystick and keep its stability simultaneously. This TWRW is resistant to road disturbances. Also, it can climb small steps and move on steep slopes while keeping its stability [70–73].

Baloh and Parent built a two-wheeled transportation vehicle called B2 as a more environment friendly alternative to a taxi (see Figure. 2.6 [74]). B2 can keep the stability of the rider when there are disturbances from the road. It can turn on the spot as TWRWs do and is suitable for use on narrow roads [75–77].

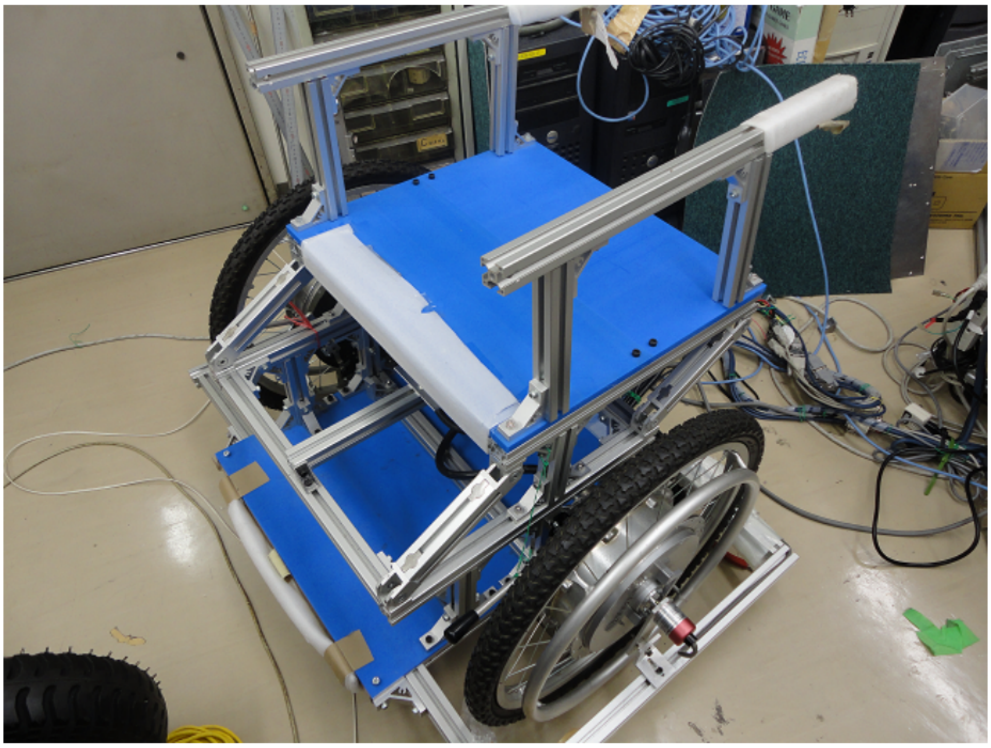

Figure 2.5: TWRW proposed by Nakamura and Murakami [69].

Figure 2.6: The two-wheeled vehicle B2 [74].

Huang et al. proposed a TWRW called Uni-Directional Wheel (UW-Car). UW-Car is equipped with a movable seat driven by a motor to keep the rider upright and the system stable. It has high mobility and has a good performance in steering and braking. It is also robust to parameter uncertainties and noise disturbances [78, 79]. Figure. 2.7 depicts the UW-Car wheelchair [80].

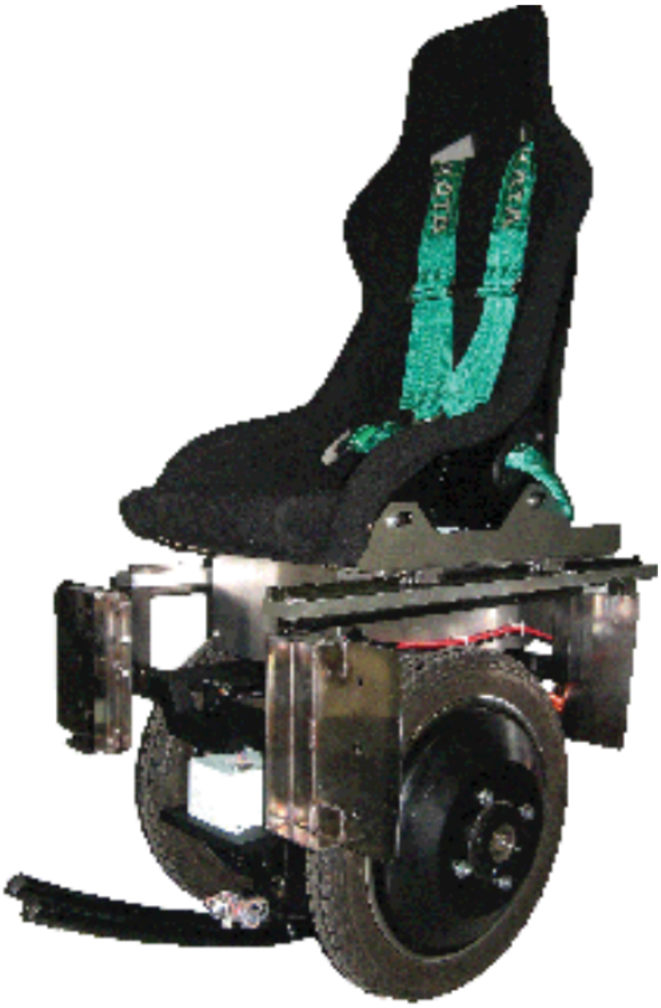

Figure 2.7: The UW-Car [80].

General Motors in collaboration with Segway designed a two-wheeled vehicle called PUMA (see Figure. 2.8 [81]). The stability control of this vehicle is similar to UW-Car which relies on a movable seat. Also, the two wheels activated with two DC motors are used to drive the PUMA and assist its stability control [82–84].

Figure 2.8: Transportation vehicle PUMA [81].

Sago et al. designed a TWRW which has two large wheels. Large wheels are selected as they increases the stability control performance of the system on uneven surfaces and enable the wheelchair to climb small gaps and steps [15]. The centre of gravity of this mechanism is lower than the wheel axis to reduce the possibility of wheelchair overturning [85]. Figure. 2.9 shows a prototype of the mentioned wheelchair [86].

Ahmed et al. theoretically proposed a reconfigurable wheelchair which has two wheels and two front casters [87–93]. It has four wheels and is statically stable. However, it is able to transform into a TWRW and lift the chair to a higher position to make the rider pick and place items and have the eye to eye contact with other people which makes them feel more comfortable. Figure. 2.10 shows the mentioned wheelchair in two-wheeled and four-wheeled configurations [94].

Figure 2.9: The TWRW with large wheels [86].

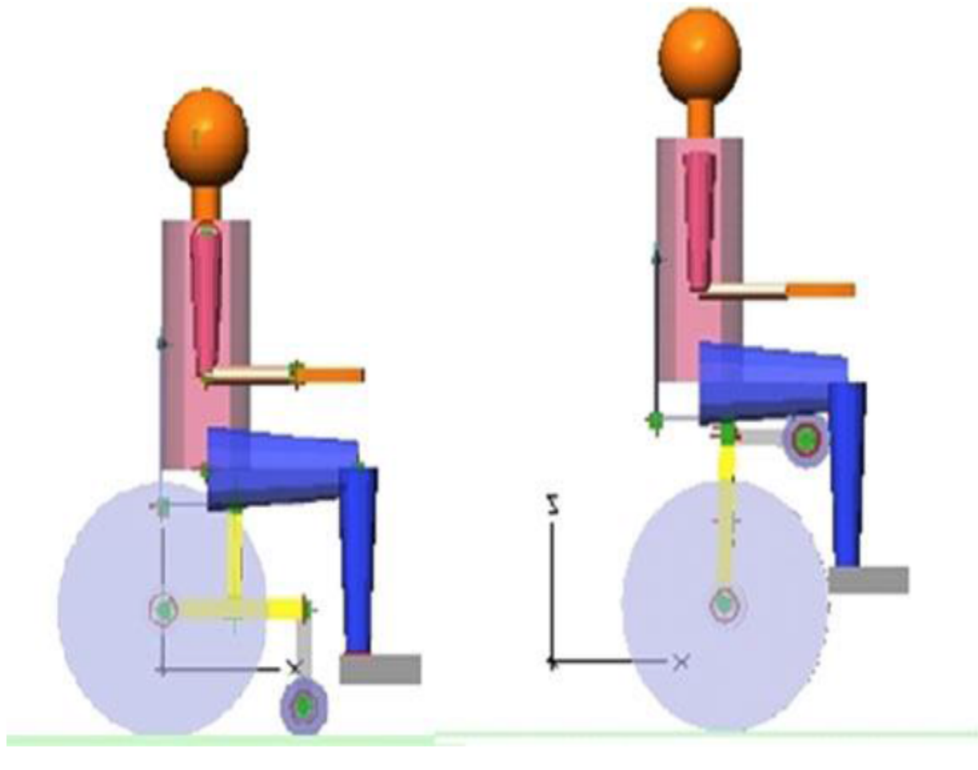

Figure 2.10: The structure of the reconfigurable wheelchair [94].

2.2 TWRW stability control

To keep the stability of a TWRW, a controller should be developed to make its pitch angle near the value (e.g. zero relative to the upright direction perpendicular to the road surface) corresponding to the equilibrium position of the wheelchair. In the equilibrium position, the wheelchair can move while it doesn't overturn [95–99]. However, in practice, the pitch angle cannot be set to zero exactly when it deviates from its equilibrium position (0) during the motion of system [100–102]. Therefore, an acceptable domain of the angle should be defined.

The stability of a TWRW is affected by many factors such as uncertainties of system parameters, noise in sensors, external disturbances felt by the left and right wheels, etc [103–106]. The external disturbances are caused by uneven surfaces, obstacles, steps, etc. Another disturbance to consider is the motion of the passenger on the seat which affect the centre of gravity of the whole system [107–109]. Other factors contributing disturbances include ground friction, external loads, internal friction force, etc [110–112].

2.2.1 Mechanisms for stabilisation

To keep the TWRW stable, a control system should be developed to maintain the pitch angle near zero. According to the mechanism chosen for stability control, the control system is developed. Therefore, selecting the proper mechanism is crucial [113–115]. There are some mechanisms proposed to compensate the deviation of pitch angle, including driving wheels, movable seat, and movable mass under the seat.

2.2.1.1 Driving wheels (conventional system)

A TWRW can be stabilized in a way similar to that adopted by a person to stabilize himself. For example, when the system bends forward, it starts to move forward and when it bends backward, it moves backward [116, 117]. Most conventional control systems used to stabilize the TWRW are applying torque to the driving wheels to compensate the deviation of pitch angle [74–76, 84, 118–123]. Therefore, driving wheels provide mobility and stability simultaneously. This procedure requires large input torque and power and causes huge energy consumption. Another issue is that the required input torque might exceed the driving wheels' payload which leads to control system failure [124–126].

2.2.1.2 Movable seat

To keep the stability of TWRW, a movable seat can be used to keep the rider in an upright position. This adjustable seat can move forward and backward according to the pitch angle of the wheelchair [14, 127, 128]. Similar to the driving wheels mechanism, this control system requires large input linear force to move the seat and rider. Though a movable seat can be used to stabilize the TWRW, it makes the rider feel uncomfortable and even unsafe. Furthermore, due to space limitations for the motion of the seat, this method is not effective to compensate large disturbances. Figure. 2.11 demonstrates the structure of the mechanism [80].

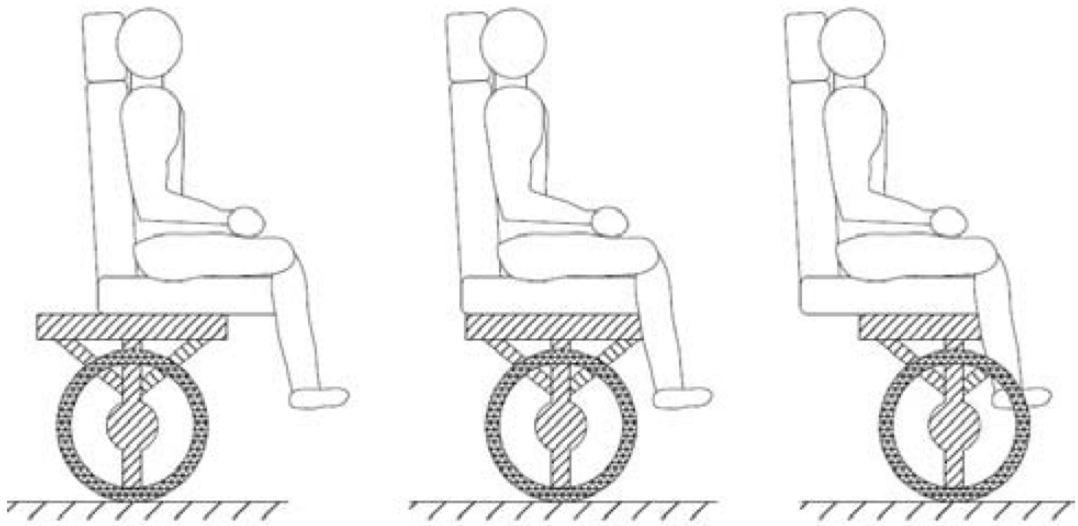

Figure 2.11: The movable seat of TWRW in different positions [80].

2.2.1.3 Movable mass under seat

To reduce the TWRW swinging (pitch angle), a movable mass can be added under the seat[50]. The mass moves along an axis to compensate the centre of gravity change of the whole system to keep it stable [15, 85, 86]. Similar to the movable seat, it is not able to compensate the large deviation of pitch angle from its equilibrium position due to the limited space for the motion of the mass. Figure. 2.12 shows the movable mass installed under the seat of the wheelchair [15].

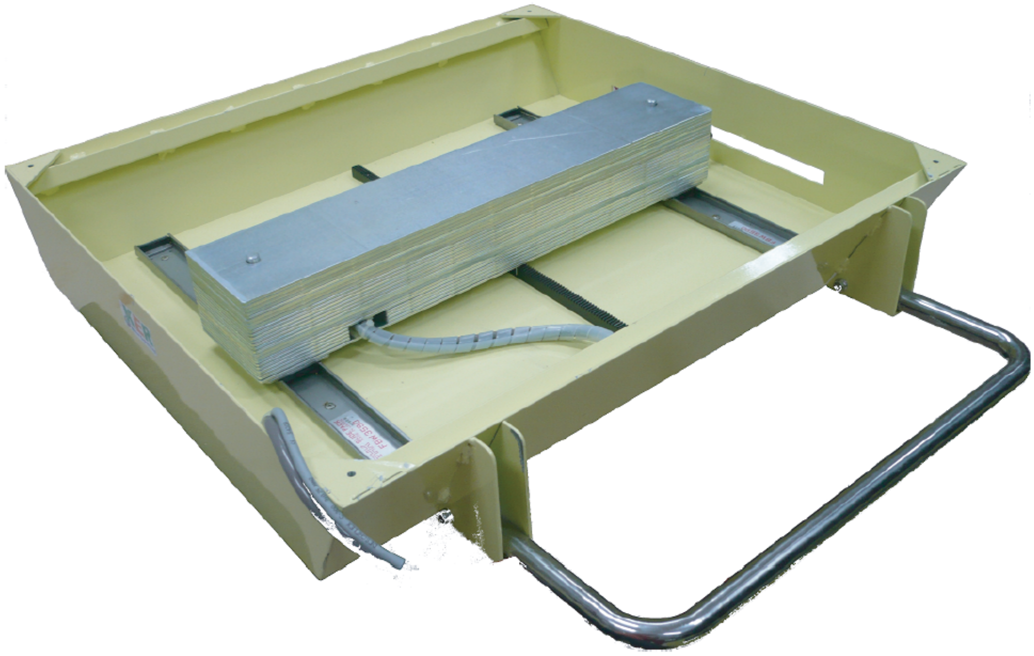

Figure 2.12: The movable mass mounted under TWRW's seat [15].

2.2.2 Dynamic modelling and control schemes

To develop a robust and optimized control system, the accurate dynamic modelling of TWRW should be derived [129–131]. There are three methods to establish dynamic modelling: Newton method, Euler-Lagrangian method, and Kane method [132]. In Newton method, the Newton's laws of mechanics are applied in each part of the system (so-called free-body) and internal forces between the parts are explicitly considered for the development of the equation of motion (EOM) [133–135]. In this method, the direction of internal and external forces and torques should be accurately considered.

In the Euler-Lagrangian method, the kinetic and potential energy of the whole system are calculated first and then the Euler-Lagrangian formulation is used to derive the EOM of the system [136–139]. In this method, the internal forces between the TWRW's part are not considered which makes it easier than the Newton method. The Kane method is similar to the Newton method except that generalised inertia and active forces are considered instead of internal forces [140–142].

To obtain the required input of the TWRW stability control, there are a number of control schemes that can be used. The control system features such as accuracy, and robustness are completely dependent on the control scheme chosen for the system [143–146]. Furthermore, by selecting a proper control scheme, the control input including input torque, input power, and energy consumption can be optimized [147, 148]. The control schemes can be divided into two parts: Model-free and Model-based controllers.

2.2.2.1 Model-free control schemes

The dynamic model of TWRW is highly nonlinear and it is complex to derive it accurately. To resolve this problem, the model-free controllers which are developed without dynamic model details are used [149–151]. The PID controller used in most real-time control systems is one of the model-free controllers. In this controller, the error value which is the difference between the controller aim (e.g. pitch angle) and its desired value is continuously calculated. According to the error values and the proportional, integral, and derivative control gains, the control input is obtained [152, 153].

Intelligent controllers based on fuzzy logic and artificial neural network (ANN) are also considered model-free controllers [154, 155]. Fuzzy logic is a mathematical system which assess analog input values as a logical variable and considers the values between 0 and 1 [156–159]. ANN is based on the function of the human brain. ANNs are considered nonlinear statistical data modelling tools, where the complex relationships between inputs and outputs are modelled or patterns are found [160–162].

2.2.2.2 Model-based control schemes

To achieve a robust and optimal control system, the model-based controllers developed from the dynamic model of the system should be used. The dynamic model of TWRW is highly nonlinear for which linear controllers cannot be applied or justified directly. Therefore, in order to use some well-established linear controllers like linear quadratic regulator (LQR) based on full state feedback, the system's dynamic model is usually linearized first [163, 164]. The dynamic model of the system is described through a set of linear differential equations. If nonlinear parameters of the system, especially nonlinear coupling terms are not considered in the dynamic modelling, the stability controller developed from the model cannot perform well [165–167].

Nonlinear controllers are also used for the stability control. Nonlinear State-Dependent Riccati Equation (SDRE) controller is an example of the nonlinear control schemes. This controller can be considered as the nonlinear version of LQR controller. It is developed from the nonlinear dynamic model of the system as opposed to LQR controller which needs linearization of the dynamic model. It can perform multiple functions such as observer designs, nonlinear regulation, and parameter estimations. This feature also makes it robust against disturbances. The main drawback of this controller is that it can only perform well when the system is operating around its stable position [168, 169].

The CTC control which uses the nonlinear feedback of system can be utilized for stability control of the TWRW [170]. In this control method, the control inputs (torques) are derived from nonlinear state feedback and closed-loop tracking errors through the dynamic model. However, it requires an accurate dynamic model of the system and is not robust against internal and external disturbances [171, 172]. For the cases where the system dynamics cannot be accurately modelled, or there are external disturbances, nonlinear H_∞, which is robust against disturbances can be used [173, 174]. Nonlinear H_∞ control is developed based on the Hamilton–Jacobi–Bellman–Isaacs (HJBI) equation which is hard to solve in real-time though [175–177].

In comparison, SMC control is more robust against disturbances and is more computationally efficient [178–180]. In this controller, the closed-loop tracking errors are forced to be near a predefined surface, called sliding surface, in the state space of the system. For an underactuated system where the number of inputs is less than the number of controlled outputs, hierarchical sliding mode control (HSMC) can be applied [181]. In HSMC, the system is divided into several subsystems for each of which, a so-called *layer sliding surface* is designed. The main drawback of SMC control is the chattering phenomenon which leads to high vibration in the system. This problem can be solved by replacing a smooth sigmoid function with a non-smooth sign function found in a SMC controller [182, 183]. Another effective solution is higher-order SMC controllers like the SOSMC controller [184–186]. In this controller, a discontinuous integrator is added to the control input to eliminates the chattering phenomenon.

2.2.3 State estimation of the TWRW

In order to develop a controller to stabilize the TWRW when it deviates from its equilibrium position, the states of the system are required. For example, we need to know the pitch angle and its velocity, the angular displacements and velocities of the left and right wheels, and also the roll and yaw angles of the system if we want to consider them in the controller. These feedbacks can be achieved through sensors like encoder, tilt sensor, gyroscope, accelerometer, etc. mounted on the TWRW [187]. The performance of these sensors is affected by many factors such as bias, scale factor, misalignment, temperature variation, and noise errors, causing errors in sensor readings.

The system errors whose sources can be identified are compensated through calibration methods. The noise errors known as measurement noise are random and its effect can't be removed using calibration procedures. They can be reduced or eliminated through filtering techniques [188–191]. Filtering techniques like Kalman and Particle filters can reduce the noise effect on sensor outputs and make them close to real measurement values.

2.2.3.1 Sensors for state estimation

The position and orientation of TWRW can be measured by the sensors called encoder which measures the angular displacement of the wheels. Though, through the system's kinematic model, it can be used to indirectly measure the yaw angle of the wheelchair under some assumptions, it cannot be utilized to measure the intended angle of system like pitch angle [187]. The tilt sensor can determine the pitch angle of system directly, although it suffers from the measurement noise and low-frequency response [192]. Figure. 2.13 represents the angles measured by tilt sensor and encoder [124]. The measurement noise on tilt sensor can be seen. The accelerometer which is able to measure the vector of gravity can be used instead of a tilt sensor or an encoder [193,194].

The pitch angle can be obtained from a gyroscope which measures the rate of change of angle [193–195]. Compared to the tilt sensor, the gyroscope has a faster response and its noise error is less. Furthermore, it is less sensitive to external disturbances than tilt sensor [195]. Figure. 2.14 shows the performance of the tilt sensor and gyroscope when the rider starts moving quickly on a Segway similar to a TWRW [196]. As it can be seen, chattering occurs on measured angle from tilt sensor when the rider moves quickly.

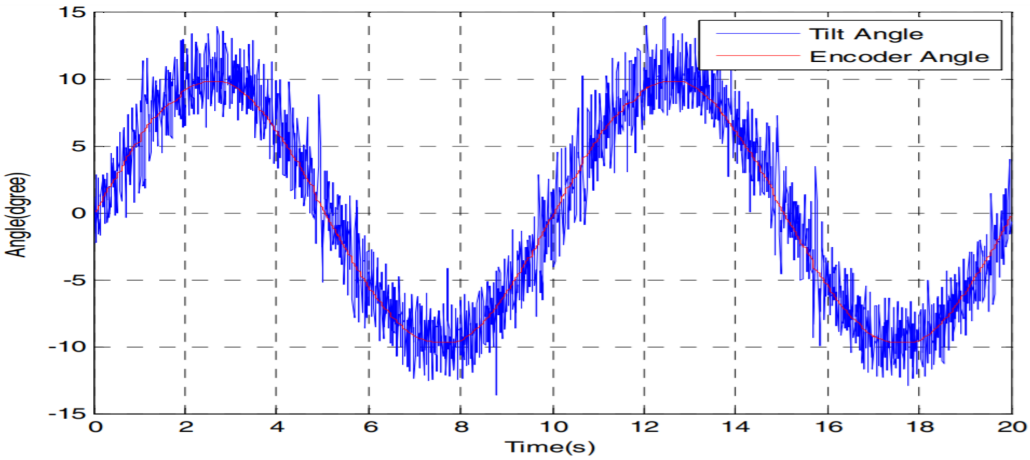

Figure 2.13: The comparison of measured angle by tilt sensor and encoder [124].

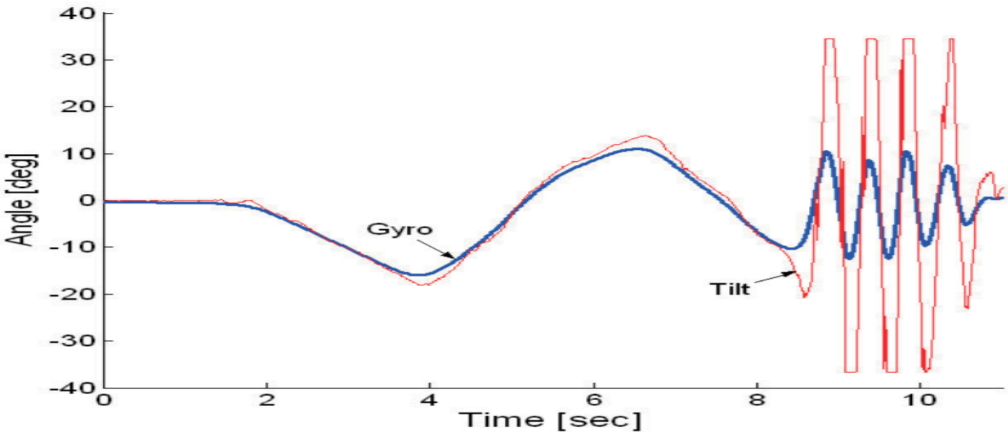

Figure 2.14: The comparison of the tilt and gyro sensor when the rider moves forward and backward quickly in the interval time 8 to 11 sec on the Segway [196].

As the measured data of gyroscope are integrated to obtain the corresponding angle, as the time goes on the drift error will increase and dramatically deteriorate the accuracy of angle measurement. The drift phenomenon effect is so significant even when the noise measurement is small. Therefore, the measured angle derived by gyroscope would be unreliable for a long time [197, 198]. Figure. 2.15 depicts the pitch angle of rider derived by tilt and gyro sensor on a Segway when he doesn't move [196]. It is obvious by the time goes on the output of the gyro becomes unreliable as it deviates from the real value of pitch angle.

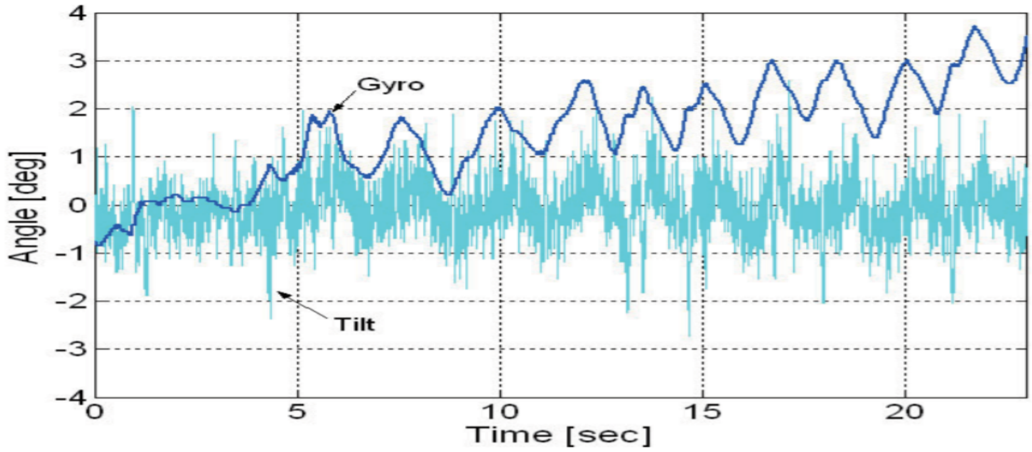

Figure 2.15: The comparison of the tilt and gyro sensor when the rider doesn't move on the Segway [196].

To improve the accuracy of state estimation, the gyroscope and tilt sensors can be combined [124]. Figure. 2.16 demonstrates the fusion of a gyroscope and inclinometer (tilt sensor) to obtain the pitch angle of an inverted pendulum [199]. Through interpolation, data measured by sensors which have different frequencies can be fused [200].

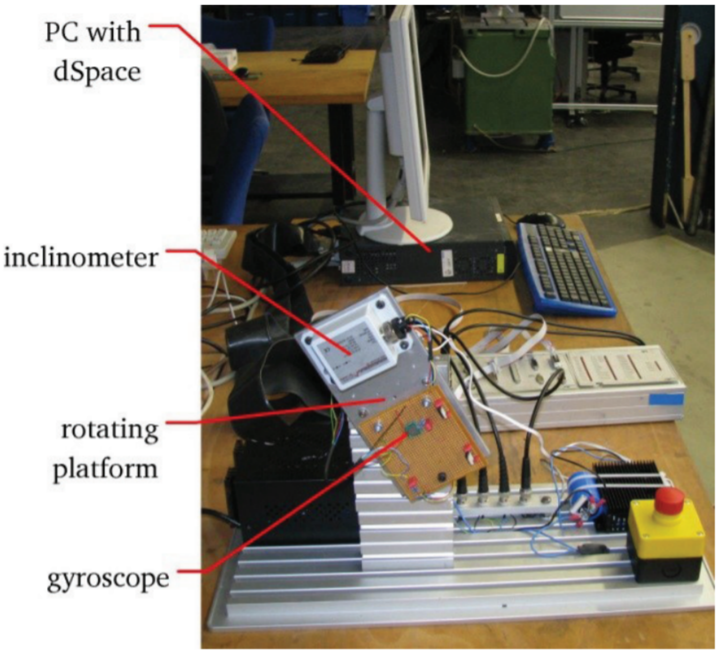

Figure 2.16: Test setup of measuring pitch angle of a mobile inverted pendulum using inclinometer (tilt sensor) and gyro sensor [199].

2.2.3.2 Conventional approaches for state estimation

Kalman filter, an optimal filter, is usually used to filter out noise in the output data collected by sensors like accelerometer, gyroscope, and tilt sensor [201]. However, when the noise on sensor output is non-Gaussian and the system's state-space model is nonlinear, the particle filter is a better option. This filter consists of a set of algorithms used to estimate the state of system when non-regular perturbations are present in sensors [202]. The Particle filter is an effective filtering algorithm to estimate orientation through the sensor outputs. In addition, when the initial states are not known, the estimation achieved by this filter converges into a true value.

In order to better determine of the TWRW's position and orientation, the data collected by the accelerometer, gyroscope, and position sensor can be synthesised and modified through the Kalman and Particle filters. Figure. 2.17 shows the outline of the mentioned method [203]. Besides, the low pass filter is a good filtering method to eliminate low-frequency noises, but it causes a time delay and decreases the real-time performance of the system [204].

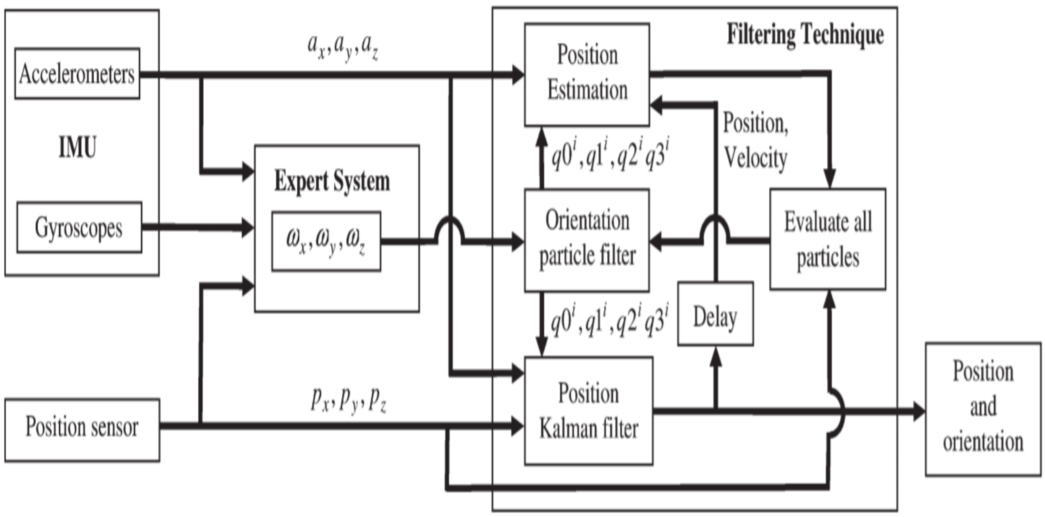

Figure 2.17: The block diagram of the Kalman and Particle filters fusion method for state estimation [203].

2.3 Summary

In this chapter, a literature review was conducted on manual and robotic wheelchairs. Their merits and weaknesses points were explained and compared to each other. A new type of robotic wheelchair (TWRW) was introduced and its superiorities over the conventional robotic wheelchairs (four-wheeled) were explained. Some existing TWRW examples were introduced and their features and applications were presented. The importance to actively stabilize a TWRW was discussed and the mechanisms used to keep the system stable were explained. The methods used to establish the dynamic modelling were presented and some control schemes including model-free and model-based controllers used to develop the stability controllers were explained. The sensors used to measure the system's states (e.g. pitch angle and its velocity) were introduced and their features were discussed. The filtering methods utilized to increase the accuracy of sensor measurements were explained.

In the next chapter, the dynamic modelling of TWRW for the conventional and proposed systems are provided where the defect of disturbance including the rider's motion and the model uncertainties are considered.

Chapter 3

Dynamic Modelling

3.1 Introduction

To develop a controller for the TWRW, its dynamic model is derived and presented in this chapter. A TWRW consists of two wheels and a seat for the rider which can rotate freely around the wheels' axle. The seat and the rider are combined to form a body. In the proposed system, a pendulum-like movable mechanism is placed under the seat to assist the wheels for stability and direction control. This mechanism consists of a rod and a mass placed at one end of the rod. The mass of the rod is small and is neglected.

Figure. 3.1 shows a prototype of a TWRW designed in Solidwork. Figure. 3.2a and 3.2b show the schematic view of the TWRW and the proposed mechanism from the side and top views, respectively. The mass of each wheel, body, and movable mechanism are denoted by m_{w}, m_b, and m_p, respectively. The radius of each wheel and the length of the wheels' axle are denoted by r and d, respectively. The middle of the wheels' axle is shown by O, and P is the point that movable mechanism is added to the system. l is the distance between the body's centre of gravity (COG) and point O, and the length of the movable mechanism's rod is denoted by l'. The distance between point O and P is denoted by b.

Figure 3.1: TWRW Prototype.

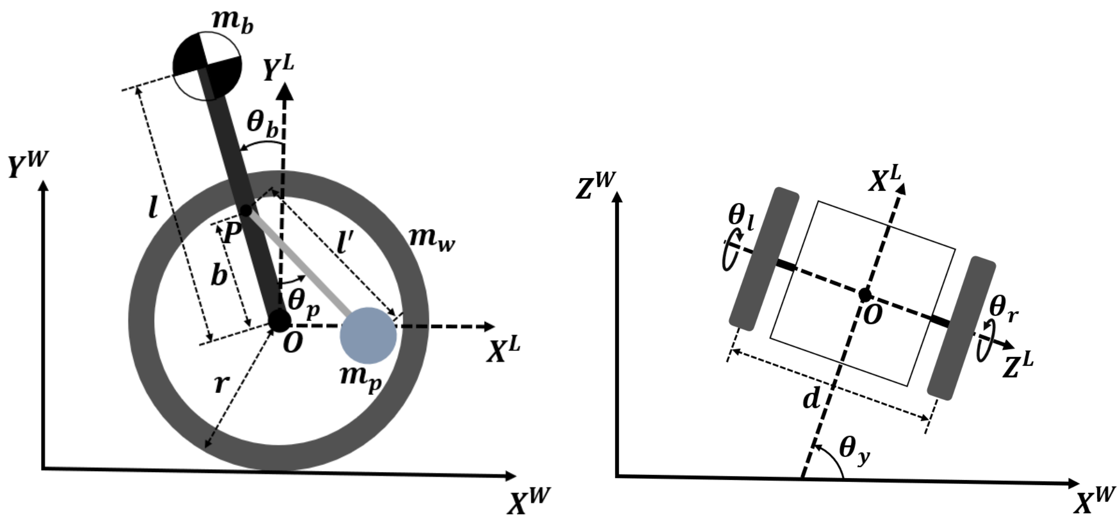

(a): Side view (b): Top view

Figure 3.2: Schematic view of the TWRW and the proposed mechanism

To define parameters, two coordinate systems are defined. $\mathbf{X^W} - \mathbf{Y^W} - \mathbf{Z^W}$ is the world coordinate frame which is fixed to the ground. $\mathbf{X^L} - \mathbf{Y^L} - \mathbf{Z^L}$ is the coordinate frame attached to the middle of the wheels' axle. The rotation angles of the right and left wheels measured from the $\mathbf{Y^L}$ axis are denoted by θ_r and θ_l, respectively. The rotation angle of the body (pitch angle) is measured from the $\mathbf{Y^L}$ axis and shown by θ_b. θ_p denotes the rotation angle of the movable mechanism measured from link OP. The yaw angle is measured from the $\mathbf{X^W}$ axis and denoted by θ_y.

To present the moment of inertia of TWRW's components, their local frames are defined at the COG of each component and shown by the red lines in Figure. 3.3. The moment of inertia of each wheel is denoted by J_{w_x}, J_{w_y}, and J_{w_z}. Also, the moment of inertia of the body is denoted by J_{b_x}, J_{b_y}, and J_{b_z}. J_{p_x}, J_{p_y}, and J_{p_z} denote the moment of inertia of the movable mechanism. τ_r, τ_l, and τ_p denote the input torque of the right wheel, left wheel, and movable mechanism, respectively. Their input powers are denoted by P_r, P_l, and P_p, respectively. E_r, E_l, and E_p are used to denote their energy consumption, respectively.

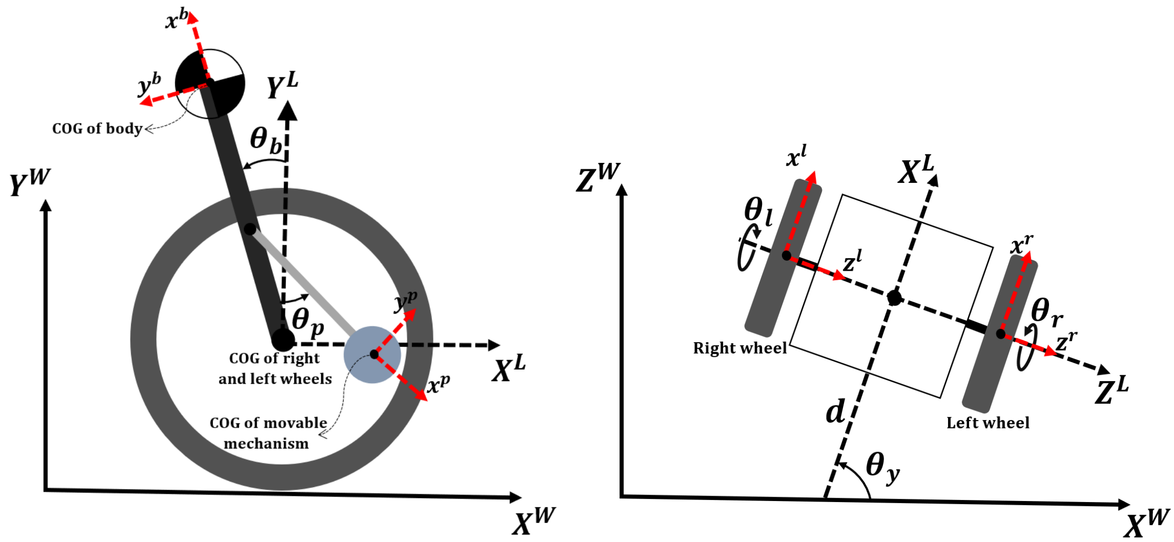

(a): Body and movable mechanism (b): Right and left wheels

Figure 3.3: The local frames of the TWRW

3.2 Dynamic model of the conventional system

To derive the dynamic modelling, the Euler-Lagrange formulation is used [205],

$$\frac{d}{dt}\left(\frac{\partial L}{\partial \dot{q}_i}\right) - \frac{\partial L}{\partial q_i} = Q_i \tag{3.1}$$

where $L = T - U$ is known as Lagrangian and T and U are the kinetic and potential energy of the whole system, respectively. The system's generalized coordinates and their corresponding inputs are shown by q_i and Q_i, respectively. The friction forces between joints are not considered, and it is assumed that the wheels don't slip on the ground.

3.2.1 Kinetic and potential energy

In the conventional system, the wheels' torque are the control input. Therefore, the overall kinetic and potential energy of the system can be obtained through

$$T = T_r + T_l + T_b, \qquad U = U_r + U_l + U_b.$$

T_r and T_l are the kinetic energy of the right and left wheel, respectively. T_b is the kinetic energy of the body (including rider and seat frame). Similarly, U_r, U_l, and U_b are their potential energies.

The kinetic energy of the right wheel can be obtained as [206]

$$T_r = \frac{1}{2}m_{\mathrm{w}}(v_x^2+v_y^2+v_z^2)+\frac{1}{2}(J_{\mathrm{w}_x}\omega_x^2+J_{\mathrm{w}_y}\omega_y^2+J_{\mathrm{w}_z}\omega_z^2)-(J_{\mathrm{w}_{xy}}\omega_x\omega_y+J_{\mathrm{w}_{xz}}\omega_x\omega_z+J_{\mathrm{w}_{yz}}\omega_y\omega_z) \tag{3.2}$$

where v_x, v_y, and v_z are the linear velocities of the right wheel at its CoG defined in the right wheel's local frame. Similarly, ω_x, ω_y, and ω_z are its angular velocities. $J_{\mathrm{w}_{xy}}$, $J_{\mathrm{w}_{xz}}$, and $J_{\mathrm{w}_{yz}}$ are the products of inertia of each wheel. As the values of the products of inertia are so small, they can be neglected. Therefore, Eq. (3.2) can be rewritten as

$$T_r = \frac{1}{2} m_{\mathrm{w}} (v_x^2 + v_y^2 + v_z^2) + \frac{1}{2} (J_{\mathrm{w}_x} \omega_x^2 + J_{\mathrm{w}_y} \omega_y^2 + J_{\mathrm{w}_z} \omega_z^2) \tag{3.3}$$

For the right wheel we have

$$v_x = r\dot{\theta}_r, \quad v_y = 0, \quad v_z = 0, \quad \omega_x = 0, \quad \omega_y = \dot{\theta}_y, \quad \omega_z = \dot{\theta}_r.$$

Then.

$$T_r = \frac{1}{2} m_{\mathrm{w}} r^2 \dot{\theta}_r^2 + \frac{1}{2} J_{\mathrm{w}_y} \dot{\theta}_y^2 + \frac{1}{2} J_{\mathrm{w}_z} \dot{\theta}_r^2$$

Similarly, for the left wheel we have

$$v_x = r\dot{\theta}_l, \quad v_y = 0, \quad v_z = 0, \quad \omega_x = 0, \quad \omega_y = \dot{\theta}_y, \quad \omega_z = \dot{\theta}_l.$$

Then.

$$T_l = \frac{1}{2} m_{\mathrm{w}} r^2 \dot{\theta}_l^2 + \frac{1}{2} J_{\mathrm{w}_y} \dot{\theta}_y^2 + \frac{1}{2} J_{\mathrm{w}_z} \dot{\theta}_l^2$$

$\dot{\theta}_y$ which is the yaw angular velocity can be obtained as [207]

$$\dot{\theta}_y = \frac{r}{d} (\dot{\theta}_r - \dot{\theta}_l) \tag{3.4}$$

For the body we have

$$v_x = V \sin\theta_b, \; v_y = V \cos\theta_b + l\dot{\theta}_b, \; v_z = l\dot{\theta}_y \sin\theta_b, \; \omega_x = \dot{\theta}_y \cos\theta_b, \; \omega_y = \dot{\theta}_y \sin\theta_b, \; \omega_z = \dot{\theta}_b.$$

where V is the linear velocity of centre of wheels' axle which is [207]

$$V = \frac{r}{2} (\dot{\theta}_r + \dot{\theta}_l) \tag{3.5}$$

The kinetic energy of the body can be obtained as

$$T_b = \frac{1}{2}m_b(V^2 + l^2\dot{\theta}_b^2 + l^2\dot{\theta}_y^2\sin^2\theta_b + 2Vl\dot{\theta}_b\cos\theta_b) + \frac{1}{2}(J_{b_x}\dot{\theta}_y^2\sin^2\theta_b + J_{b_y}\dot{\theta}_y^2\cos^2\theta_b + J_{b_z}\dot{\theta}_b^2)$$

The potential energy of the right and left wheel, and the body can be shown as

$$U_r = U_l = 0, \qquad U_b = m_b g l\cos\theta_b.$$

3.2.2 Dynamic model equations

From Eq. (3.1), the dynamic model's equations can be derived and found in Appendix A. They can be presented in a matrix form as [208]

$$\mathbf{M_c}\ddot{\mathbf{q}}_\mathbf{c} + \mathbf{C_c}\dot{\mathbf{q}}_\mathbf{c} + \mathbf{G_c} = \mathbf{B_c}\boldsymbol{\tau}_\mathbf{c} \tag{3.6}$$

where $\mathbf{q_c}$ is the generalized coordinates vector that can be shown as

$$\mathbf{q_c} = \begin{bmatrix} \theta_r & \theta_l & \theta_b \end{bmatrix}^T$$

$\mathbf{M_c}$ is the symmetric matrix called the inertia matrix.

$$\mathbf{M_c} = \begin{bmatrix} M_{c_{11}} & M_{c_{12}} & M_{c_{13}} \\ M_{c_{21}} & M_{c_{22}} & M_{c_{23}} \\ M_{c_{31}} & M_{c_{32}} & M_{c_{33}} \end{bmatrix}$$

$\mathbf{M_c}$ elements can be found in Appendix A. $\mathbf{C_c}$ is the Centrifugal and Coriolis forces matrix. The Coriolis forces matrix is normally represented in a way to make the

$\dot{\mathbf{M}}_\mathbf{c} - 2\mathbf{C}_\mathbf{c}$ matrix skew-symmetric. The $\dot{\mathbf{M}}_\mathbf{c} - 2\mathbf{C}_\mathbf{c}$ matrix is skew-symmetric if [209]

$$\dot{\mathbf{M}}_\mathbf{c} - 2\mathbf{C}_\mathbf{c} = -(\dot{\mathbf{M}}_\mathbf{c} - 2\mathbf{C}_\mathbf{c})^T \tag{3.7}$$

The Coriolis forces matrix can satisfy Eq. (3.7) if its elements are obtained through Christoffel symbols as [210]

$$\mathbf{C}_\mathbf{c} = \{C_{c_{ij}}\} = \{\sum_{k=1}^{n} C_{c_{ijk}} \dot{q}_{c_k}\} \tag{3.8}$$

where

$$C_{c_{ijk}} = \frac{1}{2}(\frac{\partial M_{c_{ij}}}{\partial q_{c_k}} + \frac{\partial M_{c_{ik}}}{\partial q_{c_j}} - \frac{\partial M_{c_{jk}}}{\partial q_{c_i}}) \tag{3.9}$$

Considering Eqs. (3.7)-(3.9), we have

$$\begin{aligned}(\dot{\mathbf{M}}_\mathbf{c} - 2\mathbf{C}_\mathbf{c})_{ij} &= \sum_{k=1}^{n}(\frac{\partial M_{c_{ij}}}{\partial q_{c_k}}\dot{q}_{c_k} - \frac{\partial M_{c_{ij}}}{\partial q_{c_k}}\dot{q}_{c_k} - \frac{\partial M_{c_{ik}}}{\partial q_{c_j}}\dot{q}_{c_k} + \frac{\partial M_{c_{jk}}}{\partial q_{c_i}}\dot{q}_{c_k}) \\ &= \sum_{k=1}^{n}(\frac{\partial M_{c_{jk}}}{\partial q_{c_i}}\dot{q}_{c_k} - \frac{\partial M_{c_{ik}}}{\partial q_{c_j}}\dot{q}_{c_k}).\end{aligned} \tag{3.10}$$

It can be seen From Eq. (3.10) that $(\dot{\mathbf{M}}_\mathbf{c} - 2\mathbf{C}_\mathbf{c})_{ij} = -(\dot{\mathbf{M}}_\mathbf{c} - 2\mathbf{C}_\mathbf{c})_{ji}$. Therefore, it is concluded that $\dot{\mathbf{M}}_\mathbf{c} - 2\mathbf{C}_\mathbf{c} = -(\dot{\mathbf{M}}_\mathbf{c} - 2\mathbf{C}_\mathbf{c})^T$.

Considering Christoffel symbols, The Coriolis forces matrix can be shown as

$$\mathbf{C}_\mathbf{c} = \begin{bmatrix} C_{c_{11}} & C_{c_{12}} & C_{c_{13}} \\ C_{c_{21}} & C_{c_{22}} & C_{c_{23}} \\ C_{c_{31}} & C_{c_{32}} & 0 \end{bmatrix},$$

$\mathbf{C}_\mathbf{c}$ elements can be found in Appendix A. $\mathbf{G}_\mathbf{c}$ is the gravity matrix.

$$\mathbf{G}_\mathbf{c} = \begin{bmatrix} 0 & 0 & -m_b g l \sin\theta_b \end{bmatrix}^T$$

$\mathbf{B_c}$ is the control coefficient matrix.

$$\mathbf{B_c} = \begin{bmatrix} 1 & 0 & 0 \\ 0 & 1 & 0 \end{bmatrix}^T$$

and $\boldsymbol{\tau}_\mathbf{c}$ is the control input vector.

$$\boldsymbol{\tau}_\mathbf{c} = \begin{bmatrix} \tau_r & \tau_l \end{bmatrix}^T$$

The input power of the right and left wheel motors can be obtained as [211]

$$P_r = \tau_r \dot{\theta}_r, \qquad P_l = \tau_l \dot{\theta}_l.$$

Also, their overall energy consumption can be obtained as [211]

$$E_r = \int P_r dt, \qquad E_l = \int P_l dt.$$

3.2.3 Dynamic model with disturbances

Considering disturbances like model uncertainties due to the varying mass of the rider and the variations of the body's CoG from the motions of the rider, the dynamic model of the system should be reformulated as

$$\hat{\mathbf{M}}_\mathbf{c}\ddot{\mathbf{q}}_\mathbf{c} + \hat{\mathbf{C}}_\mathbf{c}\dot{\mathbf{q}}_\mathbf{c} + \hat{\mathbf{G}}_\mathbf{c} + \mathbf{D_c} + \mathbf{R_c} = \mathbf{B_c}\boldsymbol{\tau}_\mathbf{c} \tag{3.11}$$

where $\mathbf{D_c}$ and $\mathbf{R_c}$ denote the disturbances caused by model uncertainties and change of the body's CoG position, respectively. $\hat{\mathbf{M}}_\mathbf{c}$, $\hat{\mathbf{C}}_\mathbf{c}$, and $\hat{\mathbf{G}}_\mathbf{c}$ are the nominal inertia, centrifugal, and gravity matrices, respectively. They are shown as

$$\hat{\mathbf{M}}_\mathbf{c} = \mathbf{M_c} - \mathbf{\Delta M_c}, \qquad \hat{\mathbf{C}}_\mathbf{c} = \mathbf{C_c} - \mathbf{\Delta C_c}, \qquad \hat{\mathbf{G}}_\mathbf{c} = \mathbf{G_c} - \mathbf{\Delta G_c}.$$

The disturbance caused by the uncertain mass of the body can be shown as

$$\mathbf{D_c} = \mathbf{\Delta M_c}\ddot{\mathbf{q}}_\mathbf{c} + \mathbf{\Delta C_c}\dot{\mathbf{q}}_\mathbf{c} + \mathbf{\Delta G_c}$$

where

$$\mathbf{\Delta M_c} = \begin{bmatrix} \Delta M_{11} & \Delta M_{12} & \Delta M_{13} \\ \Delta M_{21} & \Delta M_{22} & \Delta M_{23} \\ \Delta M_{31} & \Delta M_{32} & \Delta M_{33} \end{bmatrix}$$

$$\mathbf{\Delta C_c} = \begin{bmatrix} \Delta C_{11} & \Delta C_{12} & \Delta C_{13} \\ \Delta C_{21} & \Delta C_{22} & \Delta C_{23} \\ \Delta C_{31} & \Delta C_{32} & 0 \end{bmatrix}, \qquad \mathbf{\Delta G_c} = \begin{bmatrix} 0 & 0 & -\Delta m_b g l \sin\theta_b \end{bmatrix}^T.$$

$\mathbf{\Delta M_c}$ is a symmetric matrix. $\mathbf{\Delta M_c}$ and $\mathbf{\Delta C_c}$ components are shown in Appendix A. $\Delta m_b = m_b - \hat{m}_b$, where m_b and $\hat{m}_b$ are the real and nominal values of the body's mass, respectively.

The body's CoG varies when the rider moves on the seat. Assume its position along the forward direction is defined by x_b as shown in Fig. 3.4, the kinetic and potential energy of the body are reformulated as

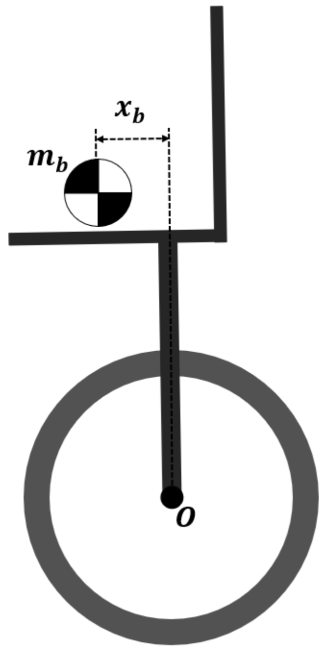

Figure 3.4: Change of body's CoG position

$$T_b = \frac{1}{2}m_b[V^2 + l^2\dot{\theta}_b^2 + l^2\dot{\theta}_y^2\sin^2\theta_b + 2Vl\dot{\theta}_b\cos\theta_b + x_b^2\dot{\theta}_b^2 + x_b^2\dot{\theta}_y^2\cos^2\theta_b + lx_b\dot{\theta}_y^2\sin2\theta_b$$
$$- 2x_bV\dot{\theta}_b\sin\theta_b] + \frac{1}{2}(J_{b_x}\dot{\theta}_y^2\sin^2\theta_b + J_{b_y}\dot{\theta}_y^2\cos^2\theta_b + J_{b_z}\dot{\theta}_b^2\cos^2\theta_b),$$

$$U_b = m_bg(l\cos\theta_b + h\sin\theta_b).$$

The effect of change of body's CoG position can be shown as

$$\mathbf{R_c} = \begin{bmatrix} R_1 & R_2 & R_3 \end{bmatrix}^T$$

The $\mathbf{R_c}$ elements are shown in Appendix A. From Eq. (3.11), we have

$$\ddot{\mathbf{q}}_\mathbf{c} = \hat{\mathbf{M}}_\mathbf{c}^{-1}(-\hat{\mathbf{C}}_\mathbf{c}\dot{\mathbf{q}}_\mathbf{c} - \hat{\mathbf{G}}_\mathbf{c} - \mathbf{D_c} - \mathbf{R_c} + \mathbf{B_c}\boldsymbol{\tau}_\mathbf{c}) \tag{3.12}$$

Therefore, the nonlinear equations of motion (EOM) can be shown as

$$\ddot{\theta}_r = A_{c_1} + B_{c_1} + \hat{M}_{c11}^{-1}\tau_r + \hat{M}_{c12}^{-1}\tau_l \tag{3.13}$$

$$\ddot{\theta}_l = A_{c_2} + B_{c_2} + \hat{M}_{c21}^{-1}\tau_r + \hat{M}_{c22}^{-1}\tau_l \tag{3.14}$$

$$\ddot{\theta}_b = A_{c_3} + B_{c_3} + \hat{M}_{c31}^{-1}\tau_r + \hat{M}_{c32}^{-1}\tau_l \tag{3.15}$$

The definition of A_{c_1}, A_{c_2}, A_{c_3}, B_{c_1}, B_{c_2}, and B_{c_3} can be found in Appendix A.

Differentiating Eq. (3.4) with respect to time leads to

$$\ddot{\theta}_y = \frac{r}{d}(\ddot{\theta}_r - \ddot{\theta}_l) \tag{3.16}$$

Then.

$$\ddot{\theta}_y = \frac{r}{d}[A_{c_1} + B_{c_1} - A_{c_2} - B_{c_2} + (\hat{M}_{c11}^{-1} - \hat{M}_{c21}^{-1})\tau_r + (\hat{M}_{c12}^{-1} - \hat{M}_{c22}^{-1})\tau_l] \tag{3.17}$$

3.3 Dynamic model of the proposed system

In the proposed system, a pendulum-like movable mechanism is added to the TWRW. Similar to the conventional system, the Euler-Lagrange formulation is used to derive its dynamic model.

3.3.1 Kinetic and potential energy

The overall kinetic and potential energy are obtained as

$$T = T_r + T_l + T_b + T_p, \qquad U = U_r + U_l + U_b + U_p.$$

where T_p and U_p are the kinetic and potential energy of the movable mechanism, respectively.

For the movable mechanism, we have

$$
\begin{aligned}
&v_x = -V\sin(\theta_b+\theta_p) - b\dot{\theta}_b\sin\theta_p,\;\; v_y = -V\cos(\theta_b+\theta_p) - b\dot{\theta}_b\cos\theta_p + l'(\dot{\theta}_b+\dot{\theta}_p),\\
&v_z = b\dot{\theta}_y\sin\theta_b - l'\dot{\theta}_y\sin(\theta_b+\theta_p),\;\; \omega_x = -\dot{\theta}_y\cos(\theta_b+\theta_p),\;\; \omega_y = \dot{\theta}_y\sin(\theta_b+\theta_p),\\
&\omega_z = \dot{\theta}_b+\dot{\theta}_p.
\end{aligned}
$$

T_p and U_p can be presented as

$$
\begin{aligned}
&T_p = \frac{1}{2}m_p[V^2 + b^2\dot{\theta}_b^2 + 2bV\dot{\theta}_b\cos\theta_b + l'^2(\dot{\theta}_b+\dot{\theta}_p)^2 - 2l'V(\dot{\theta}_b+\dot{\theta}_p)\cos(\theta_b+\theta_p)\\
&-2bl'\dot{\theta}_b(\dot{\theta}_b+\dot{\theta}_p)\cos\theta_p + b^2\dot{\theta}_y^{\,2}\sin^2\theta_b + l'^2\dot{\theta}_y^{\,2}\sin^2(\theta_b+\theta_p) - 2bl'\dot{\theta}_y^{\,2}\sin\theta_b\sin(\theta_b+\theta_p)]\\
&+\frac{1}{2}[J_{p_x}\dot{\theta}_y^2\sin^2(\theta_b+\theta_p) + J_{p_y}\dot{\theta}_y^2\cos^2(\theta_b+\theta_p) + J_{p_z}(\dot{\theta}_b+\dot{\theta}_p)^2],
\end{aligned}
$$

$$U_p = m_p g(b\cos\theta_b - l'\cos(\theta_p+\theta_b)).$$

3.3.2 Dynamic model equations

From Eq. (3.1), the dynamic modelling equations are derived and presented in Appendix B. The dynamic modelling can be shown as

$$\mathbf{M_p}\ddot{\mathbf{q}}_\mathbf{p} + \mathbf{C_p}\dot{\mathbf{q}}_\mathbf{p} + \mathbf{G_p} = \mathbf{B_p}\boldsymbol{\tau}_\mathbf{p} \tag{3.18}$$

where

$$\mathbf{q_p} = \begin{bmatrix} \theta_r & \theta_l & \theta_b & \theta_p \end{bmatrix}^T, \qquad \mathbf{M_p} = \begin{bmatrix} M_{p_{11}} & M_{p_{12}} & M_{p_{13}} & M_{p_{14}} \\ M_{p_{21}} & M_{p_{22}} & M_{p_{23}} & M_{p_{24}} \\ M_{p_{31}} & M_{p_{32}} & M_{p_{33}} & M_{p_{34}} \\ M_{p_{41}} & M_{p_{42}} & M_{p_{43}} & M_{p_{44}} \end{bmatrix},$$

$$\mathbf{C_p} = \begin{bmatrix} C_{p_{11}} & C_{p_{12}} & C_{p_{13}} & C_{p_{14}} \\ C_{p_{21}} & C_{p_{22}} & C_{p_{23}} & C_{p_{24}} \\ C_{p_{31}} & C_{p_{32}} & C_{p_{33}} & C_{p_{34}} \\ C_{p_{41}} & C_{p_{42}} & C_{p_{43}} & 0 \end{bmatrix},$$

$$\mathbf{G_p} = \begin{bmatrix} 0 \\ 0 \\ -(m_b l + m_p b) g \sin\theta_b + m_p g l' \sin(\theta_b + \theta_p) \\ m_p g l' \sin(\theta_b + \theta_p) \end{bmatrix},$$

$$\mathbf{B_p} = \begin{bmatrix} 1 & 0 & 0 & 0 \\ 0 & 1 & 0 & 0 \\ 0 & 0 & 0 & 1 \end{bmatrix}^T, \qquad \boldsymbol{\tau}_\mathbf{p} = \begin{bmatrix} \tau_r & \tau_l & \tau_p \end{bmatrix}^T.$$

$\mathbf{M_p}$ and $\mathbf{C_p}$ elements can be found in Appendix B. $\mathbf{C_p}$ elements are derived through the Christoffel symbols. The input power and energy consumption of the movable mechanism are obtained as

$$P_p = \tau_p \dot{\theta}_p, \qquad E_p = \int P_p dt.$$

3.3.3 Dynamic model with disturbances

Considering model uncertainties and change of the body's CoG position, the dynamic model is rewritten as

$$\hat{\mathbf{M}}_{\mathbf{p}}\ddot{\mathbf{q}}_{\mathbf{p}} + \hat{\mathbf{C}}_{\mathbf{p}}\dot{\mathbf{q}}_{\mathbf{p}} + \hat{\mathbf{G}}_{\mathbf{p}} + \mathbf{D}_{\mathbf{p}} + \mathbf{R}_{\mathbf{p}} = \mathbf{B}_{\mathbf{p}}\boldsymbol{\tau}_{\mathbf{p}} \tag{3.19}$$

where

$$\mathbf{D}_{\mathbf{p}} = \boldsymbol{\Delta}\mathbf{M}_{\mathbf{p}}\ddot{\mathbf{q}}_{\mathbf{p}} + \boldsymbol{\Delta}\mathbf{C}_{\mathbf{p}}\dot{\mathbf{q}}_{\mathbf{p}} + \boldsymbol{\Delta}\mathbf{G}_{\mathbf{p}}$$

$$\boldsymbol{\Delta}\mathbf{M}_{\mathbf{p}} = \begin{bmatrix} \Delta M_{11} & \Delta M_{12} & \Delta M_{13} & 0 \\ \Delta M_{21} & \Delta M_{22} & \Delta M_{23} & 0 \\ \Delta M_{31} & \Delta M_{32} & \Delta M_{33} & 0 \\ 0 & 0 & 0 & 0 \end{bmatrix},$$

$$\boldsymbol{\Delta}\mathbf{C}_{\mathbf{p}} = \begin{bmatrix} \Delta C_{11} & \Delta C_{12} & \Delta C_{13} & 0 \\ \Delta C_{21} & \Delta C_{22} & \Delta C_{23} & 0 \\ \Delta C_{31} & \Delta C_{32} & 0 & 0 \\ 0 & 0 & 0 & 0 \end{bmatrix},$$

$$\boldsymbol{\Delta}\mathbf{G}_{\mathbf{p}} = \begin{bmatrix} 0 & 0 & -\Delta m_b g l \sin\theta_b & 0 \end{bmatrix}^T, \qquad \mathbf{R}_{\mathbf{p}} = \begin{bmatrix} R_1 & R_2 & R_3 & 0 \end{bmatrix}^T.$$

$\boldsymbol{\Delta}\mathbf{M}_{\mathbf{p}}$, $\boldsymbol{\Delta}\mathbf{C}_{\mathbf{p}}$, and $\mathbf{R}_{\mathbf{p}}$ elements are similar to those derived in the conventional system and can be found in Appendix A. From Eq. (3.19), we have

$$\ddot{\mathbf{q}}_{\mathbf{p}} = \hat{\mathbf{M}}_{\mathbf{p}}^{-1}(-\hat{\mathbf{C}}_{\mathbf{p}}\dot{\mathbf{q}}_{\mathbf{p}} - \hat{\mathbf{G}}_{\mathbf{p}} - \mathbf{D}_{\mathbf{p}} - \mathbf{R}_{\mathbf{p}} + \mathbf{B}_{\mathbf{p}}\boldsymbol{\tau}_{\mathbf{p}}) \tag{3.20}$$

Therefore, the nonlinear EOM are represented as

$$\ddot{\theta}_r = A_{p_1} + B_{p_1} + \hat{M}_{p_{11}}^{-1}\tau_r + \hat{M}_{p_{12}}^{-1}\tau_l + \hat{M}_{p_{14}}^{-1}\tau_p \tag{3.21}$$

$$\ddot{\theta}_l = A_{p_2} + B_{p_2} + \hat{M}^{-1}_{p21}\tau_r + \hat{M}^{-1}_{p22}\tau_l + \hat{M}^{-1}_{p24}\tau_p \tag{3.22}$$

$$\ddot{\theta}_b = A_{p_3} + B_{p_3} + \hat{M}^{-1}_{p31}\tau_r + \hat{M}^{-1}_{p32}\tau_l + \hat{M}^{-1}_{p34}\tau_p \tag{3.23}$$

$$\ddot{\theta}_p = A_{p_4} + B_{p_4} + \hat{M}^{-1}_{p41}\tau_r + \hat{M}^{-1}_{p42}\tau_l + \hat{M}^{-1}_{p44}\tau_p \tag{3.24}$$

The definition of A_{p_1}, A_{p_2}, A_{p_3}, A_{p_4}, B_{p_1}, B_{p_2}, B_{p_3}, and B_{p_4} can be found in Appendix B. Also, from Eq. (3.16) we have

$$\ddot{\theta}_y = \frac{r}{d}[A_{p_1} + B_{p_1} - A_{p_2} - B_{p_2} + (\hat{M}^{-1}_{p11} - \hat{M}^{-1}_{p21})\tau_r + (\hat{M}^{-1}_{p12} - \hat{M}^{-1}_{p22})\tau_l + (\hat{M}^{-1}_{p14} - \hat{M}^{-1}_{p24})\tau_p] \tag{3.25}$$

3.4 Summary

In this chapter, through the Euler- Lagrangian method the dynamic model of TWRW for the conventional and proposed system was established. To obtain the dynamic modelling equations, the kinetic and potential energy of the whole system were calculated. These equations were presented in a matrix form to depict the inertia, the centrifugal and coriolis forces, and the gravity matrices. To achieve more accurate modelling, the effect of disturbances including the model uncertainties and the rider's motion were derived. From the dynamic modelling equations and the disturbances modelling, the nonlinear EOM was obtained.

In the next chapter, the stability control of TWRW for the conventional and the proposed approaches are developed. PID, CTC, SMC, and SOSMC control schemes are used to develop the stability control. The simulation results are provided to show the effectiveness of the proposed system.

Chapter 4

Stability Control

4.1 Introduction

The TWRW is statically unstable and an active controller is needed to keep it stable. In this chapter, the stability control of the TWRW for conventional and proposed methods are developed. As explained in Chapter. 1, In both control systems, the controller aim is stability where the pitch angle should be kept near zero. The controller input of the conventional system are the input torque of the right and left wheels, while in the proposed system it is the input torque of the movable mechanism.

The controllers aim and input of both control system are categorized below:

Conventional System

- **Controller input**
  - Input torque of right wheel
  - Input torque of left wheel
- **Controller aim**
  - Stability (Pitch angle)

$$\textbf{Proposed System} \begin{cases} \bullet\textbf{Controller input} \begin{cases} \text{Input torque of added movable mechanism} \end{cases} \\ \\ \bullet\textbf{Controller aim} \begin{cases} \text{Stability (Pitch angle)} \end{cases} \end{cases}$$

To develop the stability controller, four control schemes including Proportional-Integral-Derivative (PID), Computed Torque Control (CTC), Sliding Mode Control (SMC), and Second-Order Sliding Mode Control (SOSMC) are utilized to keep the wheelchair stable. The stability control through the control schemes mentioned above is developed for both conventional and proposed approaches.

4.2 PID control

4.2.1 Stability control of the conventional system

The model-free PID control is the most common controller used for real-time systems, as it is easy to develop and doesn't require complex computation. However, this control scheme is not robust against disturbances and has small working range. To calculate the control input of PID, the dynamic model of system is not required, and it is obtained from the feedback of controller aim (pitch angle and its velocity) and the controller gains. The PID control input is defined as [212]

$$u = K_d\dot{e} + K_p e + K_i \int e dt \tag{4.1}$$

where u is the control input of the system. K_d, K_p, and K_i are the derivative, proportional, and integral gains, respectively. e is the tracking error.

In the conventional system, the control input is the right and left wheels' torques.

The total input torque can be shown as

$$\tau_{\mathrm{w}} = \tau_r + \tau_l \tag{4.2}$$

To prevent an undesired change of the TWRW direction, the same input torque is applied to the right and left wheels, which means $\tau_r = \tau_l$. Therefore,

$$\tau_r = \tau_l = \frac{1}{2}\tau_{\mathrm{w}} \tag{4.3}$$

The parameter aimed to be controlled is the pitch angle which is depicted by θ_b. This angle should remain zero to keep the rider in the upright position (see Figure. 3.2a). Therefore, the tracking error can be defined as

$$e = \theta_b - \theta_{b_d}$$

where θ_{b_d} is the desired value of pitch angle. To obtain the total torque of the right and left wheels, Eq. (4.1) is rewritten as

$$\tau_{\mathrm{w}} = K_d(\dot{\theta}_b - \dot{\theta}_{b_d}) + K_p(\theta_b - \theta_{b_d}) + K_i \int (\theta_b - \theta_{b_d})dt \tag{4.4}$$

Since the controller aim is to converge pitch angle to zero, therefore.

$$\theta_{b_d} = 0, \qquad \dot{\theta}_{b_d} = 0.$$

Eq. (4.4) is rewritten as

$$\tau_{\mathrm{w}} = K_d\dot{\theta}_b + K_p\theta_b + K_i \int \theta_b dt \tag{4.5}$$

4.2.2 Stability control of the proposed system

In stability control through the proposed system, the controller input is the added mechanism's torque (τ_p), and the input torques of the right and left wheels are not considered. It means:

$$\tau_r = \tau_l = 0 \tag{4.6}$$

To calculate τ_p, Eq. (4.5) is reformulated as

$$\tau_p = K_d\dot{\theta}_b + K_p\theta_b + K_i\int\theta_b dt \tag{4.7}$$

4.2.3 Simulation results

To demonstrate the superiority of the proposed system over the conventional approach, the physical dimensions of the TWRW chosen for simulations are listed in Table. 4.1. These parameters are used for the simulation of all control schemes used in this chapter. The physical dimensions of the wheels used for the experimental tests (Chapter. 6) are set for the simulation. The rider's parameters are chosen from the physical details of a human whose mass and height are $80\,kg$, and $180\,cm$, respectively. To obtain the best performance of the stability control, the reasonable values for added movable mechanism's parameters which consider the physical constraint of the TWRW are selected. The performance of the control systems for stability control are to be simulated in three cases.

Case 1:

For Case 1, it is assumed that there is no disturbance applied to the TWRW. The initial values for pitch angle, the rotation angle of the right and left wheels, and the rotation angle of the movable mechanism angle are respectively set as

$$\theta_{b_0} = 2\,deg \quad \dot{\theta}_{b_0} = 0 \quad \theta_{r_0} = 0 \quad \dot{\theta}_{r_0} = 0 \quad \theta_{l_0} = 0 \quad \dot{\theta}_{l_0} = 0 \quad \theta_{p_0} = 0 \quad \dot{\theta}_{p_0} = 0$$

Table 4.1: Physical parameters of the TWRW for simulation

Property	**Value**	**Unit**
m_{w}	10	kg
m_b	80	kg
m_p	30	kg
J_{w_x}, J_{w_y}, J_{w_z}	0.32, 0.32, 0.64	kg.m^2
J_{b_x}, J_{b_y}, J_{b_z}	10.03, 12.40, 13.39	kg.m^2
J_{p_x}, J_{p_y}, J_{p_z}	0.26, 0.39, 0.35	kg.m^2
r	0.37	m
d	0.5	m
b	0.25	m
l	0.6	m
l'	0.42	m

As there is no kinematic equation relating the wheel's angle, the movable mechanism's angle, and their velocities to the pitch angle, their initial conditions cannot affect the TWRW's stability (pitch angle). Additionally, setting the non-zero initial value for a real TWRW's pitch angular velocity is difficult. Therefore, the only parameter whose initial condition is chosen as a non-zero value is the pitch angle.

The PID controller gains chosen for both control systems are selected as

$$K_p = 700 \qquad K_d = 100 \qquad K_i = 2$$

Case 2:

For Case 2, the TWRW is simulated under the disturbances produced by the motion of the body's CoG and the uncertainty of the body's mass. The motion of the body's CoG, which diverges the pitch angle from zero, directly affects the stability of the TWRW. However, the uncertainty of the body's mass, which causes the initial miscomputation of the control input, does not directly affect the TWRW stability.

In this case, the body's CoG motion is constrained as

$$x_b = \begin{cases} 2\,cm & 5\,s \le t < 15\,s \\ 0 & \text{elsewhere} \end{cases}$$

The uncertainty of the body's mass is set as

$$\Delta m_b = 20kg$$

The initial conditions below are considered.

$$\theta_{b_0} = 0 \quad \dot{\theta}_{b_0} = 0 \quad \theta_{r_0} = 0 \quad \dot{\theta}_{r_0} = 0 \quad \theta_{l_0} = 0 \quad \dot{\theta}_{l_0} = 0 \quad \theta_{p_0} = 0 \quad \dot{\theta}_{p_0} = 0$$

The controller gains below are chosen:

$$K_p = 1500 \qquad K_d = 200 \qquad K_i = 5$$

Case 3:

For Case 3, the motion of the body's CoG and the uncertainty of the body's mass are assumed as

$$x_b = \begin{cases} 2\,|\ \sin\frac{\pi}{2}(t-5)\ |\ cm & 5\,s \le t < 15\,s \\ 0 & \text{elsewhere} \end{cases} \qquad \Delta m_b = 20kg$$

The same initial condition and controller gains chosen in Case 2 are set for Case 3. The body' CoG motion in Case 1-3 are depicted in Figure. 4.1.

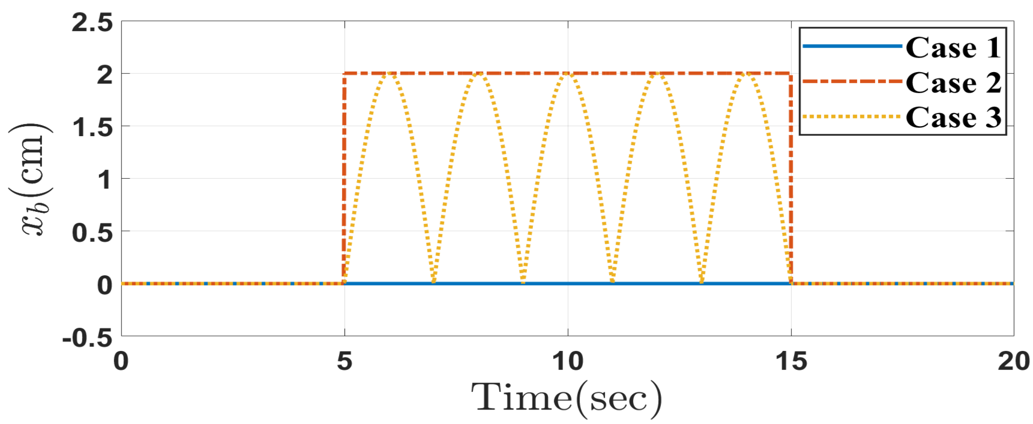

Figure 4.1: The motion of the body's CoG in Case1-3 for stability control evaluation.

To obtain the reasonable results from simulation, the control input torque should not exceed the capacity of the real motors (up to $50\,N.m$). Therefore, all parameters, including physical details of the TWRW, initial conditions, and the control gains are chosen in a way to produce the reasonable control input.

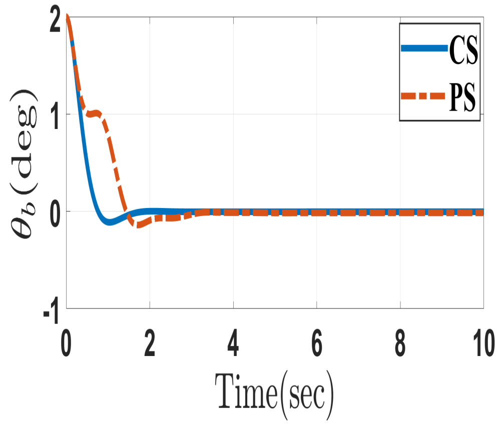

(a): Pitch angle

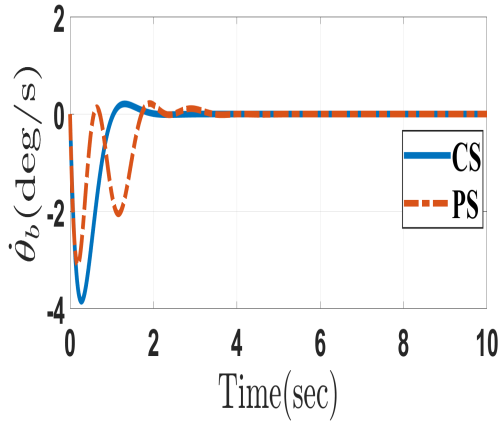

(b): Pitch angular velocity

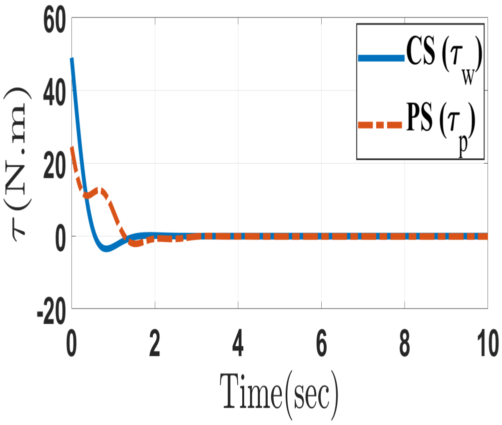

(c): Input torque

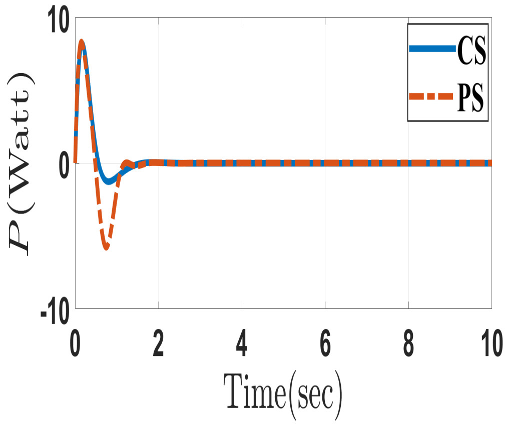

(d): Input power

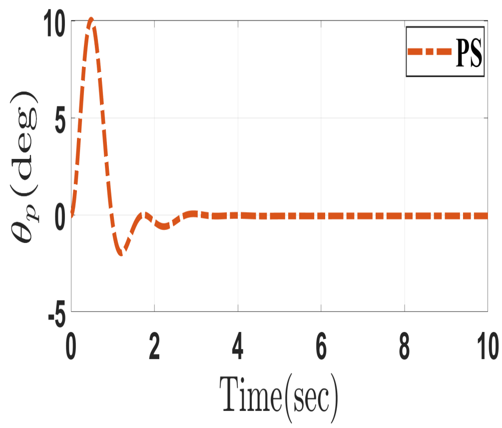

(e): Movable mechanism angle

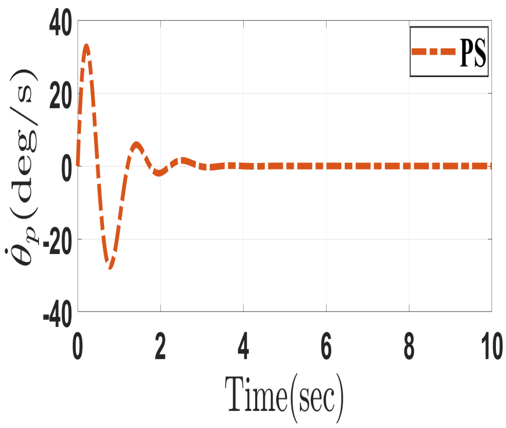

(f): Movable mechanism angular velocity

Figure 4.2: The TWRW stability control response for the conventional system (CS) and proposed system (PS) through PID control in Case 1.

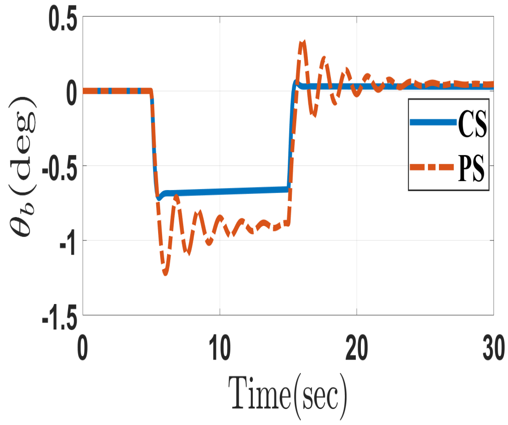

(a): Pitch angle

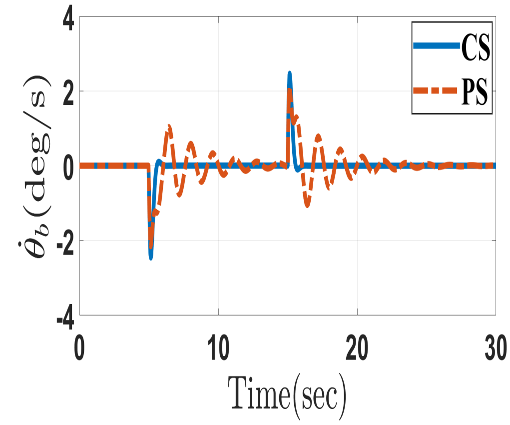

(b): Pitch angular velocity

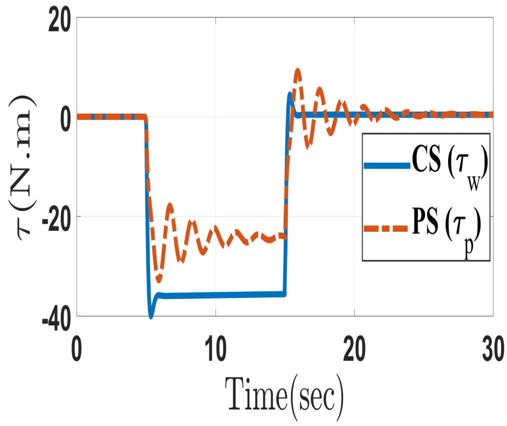

(c): Input torque

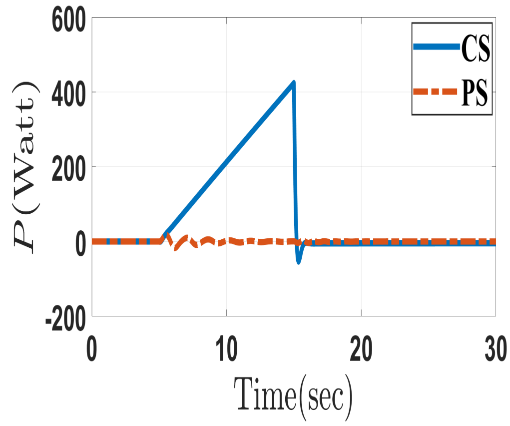

(d): Input power

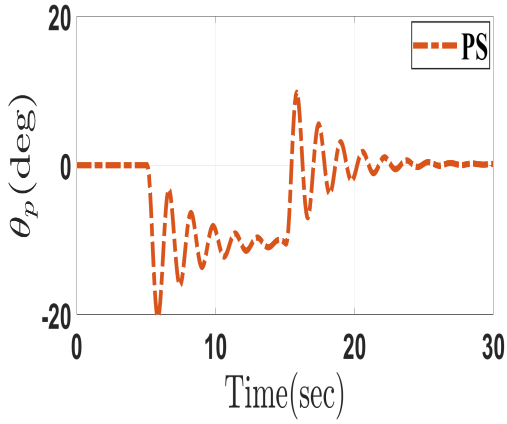

(e): Movable mechanism angle

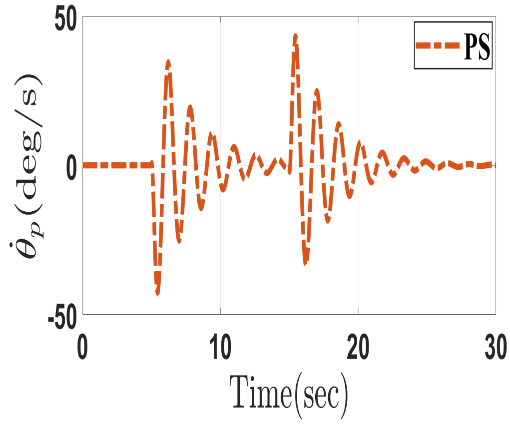

(f): Movable mechanism angular velocity

Figure 4.3: The TWRW stability control response for the conventional system (CS) and proposed system (PS) through PID control in Case 2.

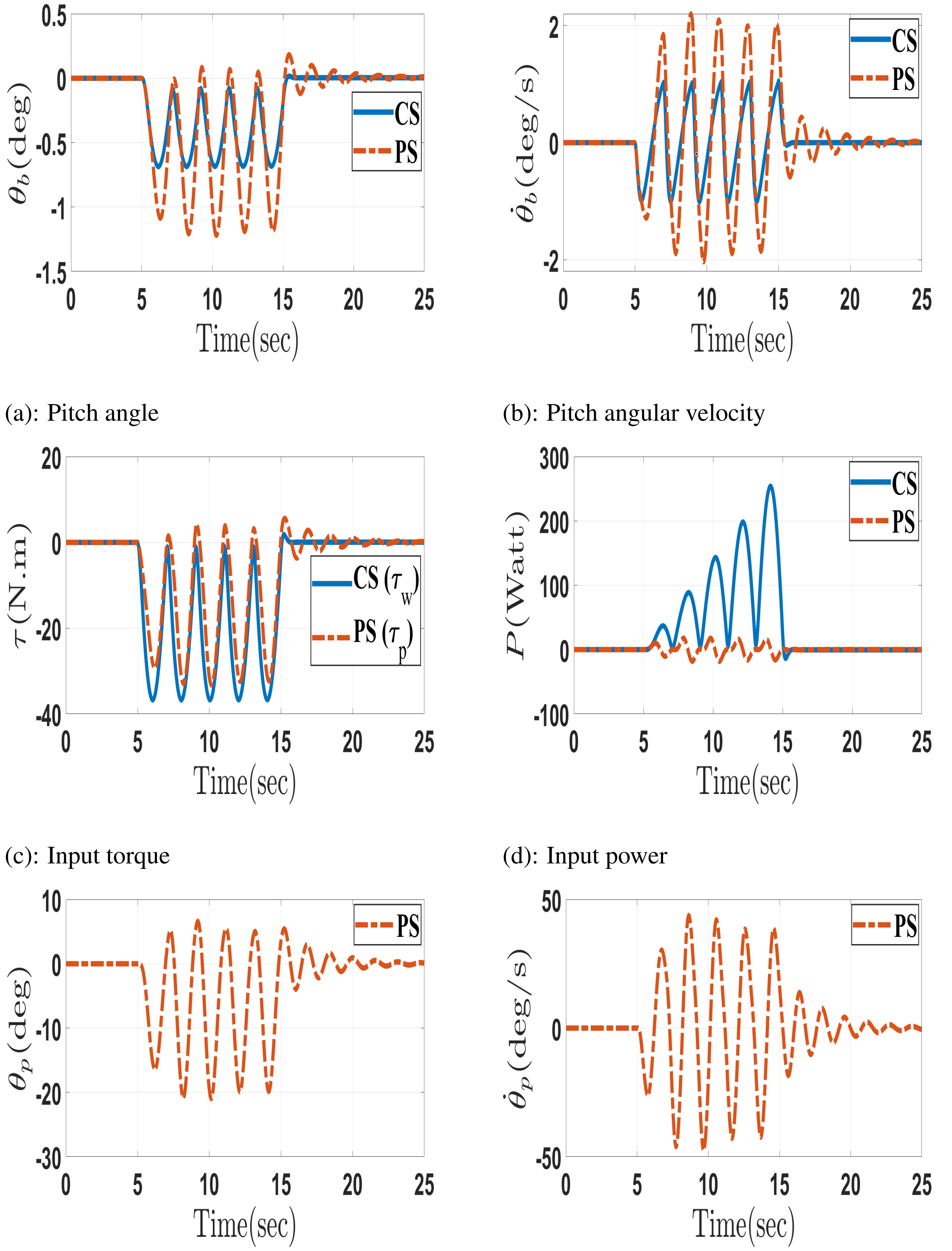

(a): Pitch angle

(b): Pitch angular velocity

(c): Input torque

(d): Input power

(e): Movable mechanism angle

(f): Movable mechanism angular velocity

Figure 4.4: The TWRW stability control response for the conventional system (CS) and proposed system (PS) through PID control in Case 3.

Simulation results of stability control for the conventional and the proposed systems through PID control in Case 1 are depicted in Figure. 4.2. It can be seen that under both controllers, the pitch angle and its velocity converge to zero in a similar pattern, where pitch angle, and its velocity reach and remain at zero after almost $2\,sec$ (see Figures. 4.2a and 4.2b). Whereas, in the proposed system, the required torque is lower than the conventional one (see Figure. 4.2c). It can be seen that the maximum input torque in the conventional and proposed approaches are $50\,N.m$, and $24\,N.m$, respectively. However, the input power in the proposed system is a bit larger than the conventional method, where the maximum input power in the conventional and proposed approaches are $8\,Watt$, and $8.3\,Watt$, respectively. (see Figure. 4.2d).

Figures. 4.2e and 4.2f depict the angular motion of the movable mechanism and its velocity, respectively. It can be seen that the range of angular displacement of the movable mechanism, where its maximum value is $10\,deg$ is very small. This shows that it can be made compact and be operated in a small space to achieve the control objectives without causing large disturbances to the system including the rider.

Figures. 4.3 and 4.4 show the response of the stability control in Case 2 and Case 3, respectively. As shown in Figures. 4.3a 4.3b, 4.4a, and 4.4b the range of pitch angle and pitch velocity in the proposed approach is a bit larger than the conventional system. Whereas, the input torque and power of the proposed method is lower than the conventional one (see Figures. 4.3c and 4.4c). Furthermore, the input power in the proposed system is much lower than the conventional approach (see Figures. 4.3d and 4.4d). Similar to Case 1, the range of angular displacement of movable mechanism in Case 2 and Case 3 are small (see Figures. 4.3e and 4.4e).

The energy consumption of motors in Case 1 to Case 3 through PID control are shown in Table. 4.2. The Energy consumption of the proposed system in Case 1 is a bit larger than the conventional approach. While, it is much lower than the conventional method in Case 2 and Case 3. It can be seen that in Case 1, where no disturbance is applied to the TWRW and a non-zero initial condition is set for pitch angle, the response of the proposed system like pitch angle, input torque, input power, etc., are similar to those obtained in the conventional one. However, in Case 2 and Case 3, where the system is under disturbances, the input torque, input power, and energy consumption of the proposed system are much lower than those required in the conventional system. Besides, the pitch angle and its velocity converge to zero in a similar pattern under both control approaches and there are small differences between them. It can be concluded that the performance of the proposed system is much better than the conventional method when the TWRW is under disturbances.

Table 4.2: Energy consumption of the conventional and the proposed systems through PID control for the TWRW stability control.

Case	1	2	3
Conventional system (E_r + E_l)	3.42 J	2238.30 J	878.99 J
Proposed system (E_p)	4.70 J	41.71 J	74.34 J

4.3 CTC control

4.3.1 Stability control of the conventional system

TThe model-based CTC control uses the dynamic model of system, the feedback of controller aim, and the controller gains to obtain the controller input. This control scheme has a larger working range than PID, while it is not robust against disturbances like model uncertainties and rider's motion which are applied to the TWRW. The overall control function of CTC control can be expressed as [208]

$$\ddot{e} + K_d\dot{e} + K_p e + K_i \int e dt = 0 \tag{4.8}$$

Similar to PID control, the tracking error is defined as

$$e = \theta_b - \theta_{b_d}$$

Eq. (4.8) can be rewritten as below.

$$\ddot{\theta}_b - \ddot{\theta}_{b_d} + K_d(\dot{\theta}_b - \dot{\theta}_{b_d}) + K_p(\theta_b - \theta_{b_d}) + K_i \int (\theta_b - \theta_{b_d}) dt = 0 \tag{4.9}$$

Since the aim of controller is to converge pitch angle to zero, therefore.

$$\theta_{b_d} = 0, \qquad \dot{\theta}_{b_d} = 0, \qquad \ddot{\theta}_{b_d} = 0.$$

which leads to

$$\ddot{\theta}_b = -K_d\dot{\theta}_b - K_p\theta_b - K_i \int \theta_b dt \tag{4.10}$$

$\ddot{\theta}_b$ can be obtained from the dynamic modelling derived in Chapter. 3. Comparing Eqs. (3.15) and (4.10), we have

$$A_{c_3} + B_{c_3} + \hat{M}_{c_{31}}^{-1}\tau_r + \hat{M}_{c_{32}}^{-1}\tau_l = -K_d\dot{\theta}_b - K_p\theta_b - K_i \int \theta_b dt \tag{4.11}$$

B_{c_3} contains the disturbance elements. To calculate the control input through the CTC control, the disturbances elements are not considered and removed. Therefore, Eq. (4.11) is rewritten as:

$$\hat{M}_{c_{31}}^{-1}\tau_r + \hat{M}_{c_{32}}^{-1}\tau_l = -A_{c_3} - K_d\dot{\theta}_b - K_p\theta_b - K_i \int \theta_b dt \tag{4.12}$$

From Eqs. (4.3) and (4.12), we have

$$\tau_{\mathrm{w}} = \frac{2(-A_{c_3} - K_d\dot{\theta}_b - K_p\theta_b - K_i\int\theta_b dt)}{\hat{M}_{c31}^{-1} + \hat{M}_{c32}^{-1}} \tag{4.13}$$

4.3.2 Stability control of the proposed system

Similar to the conventional system, comparing Eqs. (3.23) and (4.10) leads to

$$A_{p_3} + B_{p_3} + \hat{M}_{p31}^{-1}\tau_r + \hat{M}_{p32}^{-1}\tau_l + \hat{M}_{p34}^{-1}\tau_p = -K_d\dot{\theta}_b - K_p\theta_b - K_i\int\theta_b dt \tag{4.14}$$

B_{p_3} contains the disturbance elements and is removed from the control input.

From Eqs. (4.6) and (4.14), we have

$$\tau_p = \frac{-A_{p_3} - K_d\dot{\theta}_b - K_p\theta_b - K_i\int\theta_b dt}{\hat{M}_{p34}^{-1}} \tag{4.15}$$

4.3.3 Simulation results

To simulate the stability control through CTC control, the three cases which are similar to those used for PID control are considered. In Case 1 to Case 3, the controller gains below are set

Case 1:

For Case 1, the controller gains are chosen as

$$K_p = 9 \qquad K_d = 6 \qquad K_i = 0.05$$

Case 2 and 3:

For Case 2 and 3, the controller gains below are selected.

$$K_p = 35 \qquad K_d = 23 \qquad K_i = 0.05$$

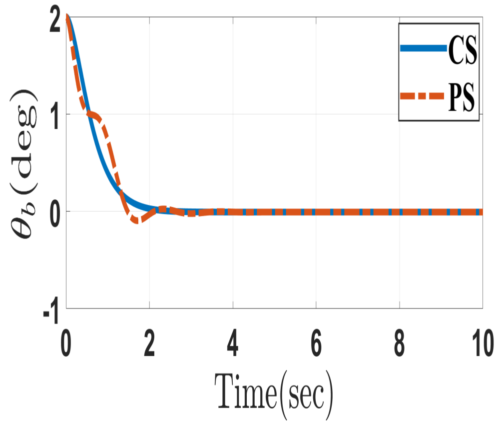

(a): Pitch angle

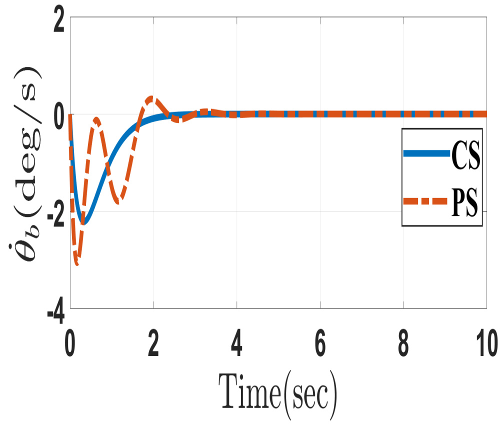

(b): Pitch angular velocity

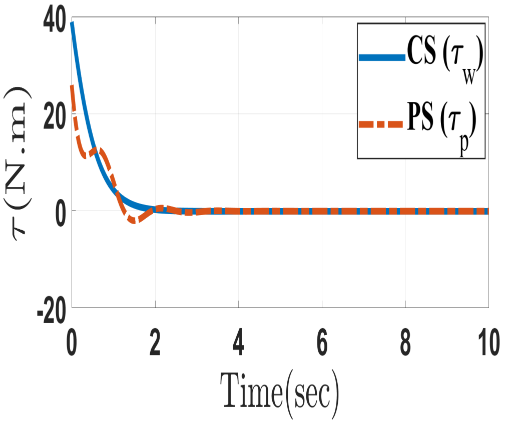

(c): Input torque

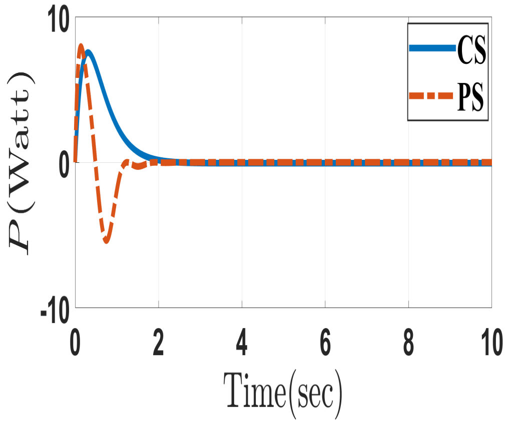

(d): Input power

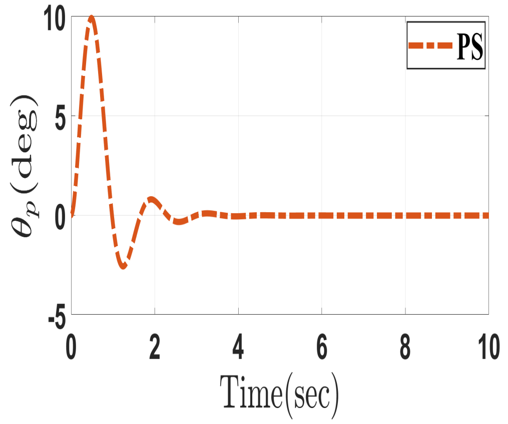

(e): Movable mechanism angle

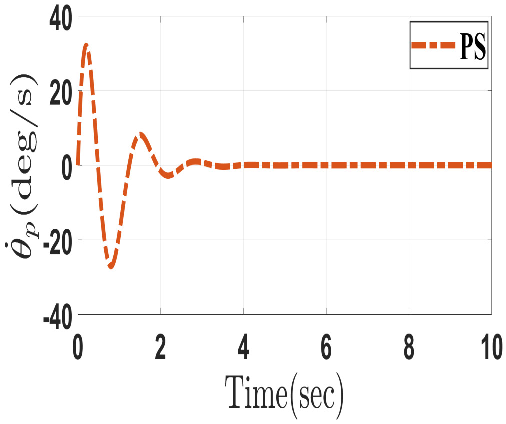

(f): Movable mechanism angular velocity

Figure 4.5: The TWRW stability control response for the conventional system (CS) and proposed system (PS) through CTC control in Case 1.

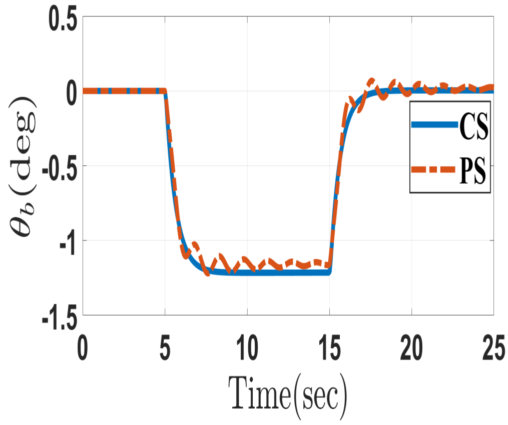

(a): Pitch angle

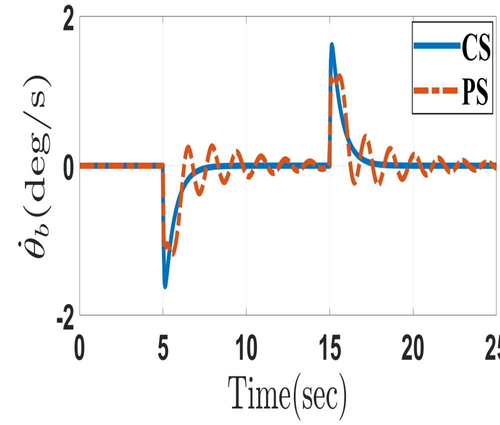

(b): Pitch angular velocity

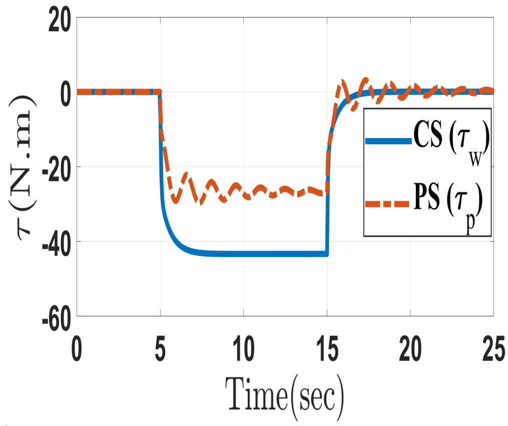

(c): Input torque

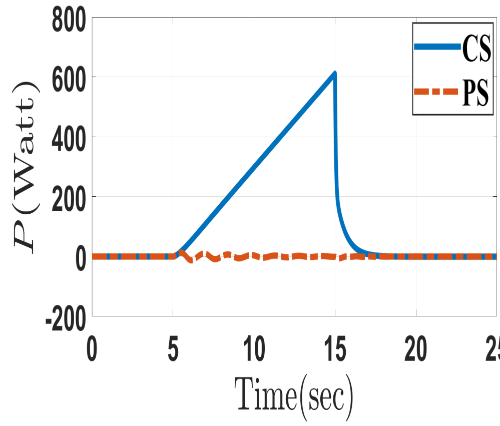

(d): Input power

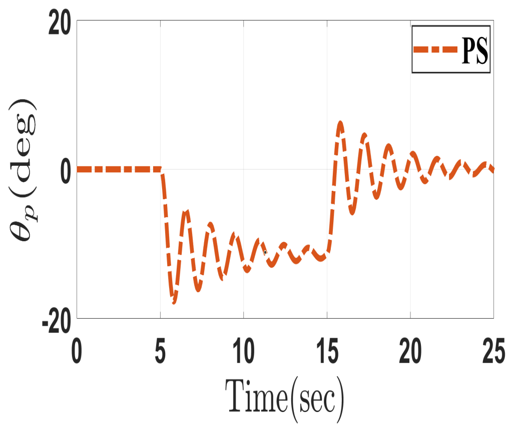

(e): Movable mechanism angle

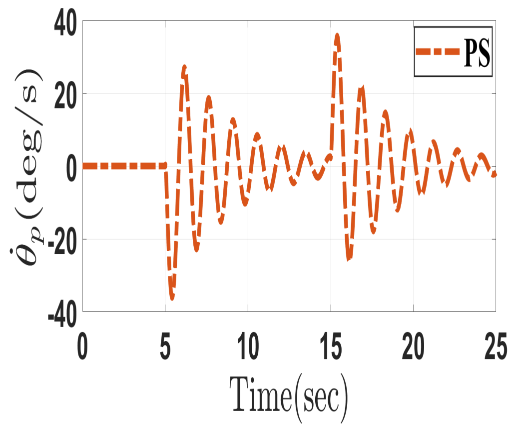

(f): Movable mechanism angular velocity

Figure 4.6: The TWRW stability control response for the conventional system (CS) and proposed system (PS) through CTC control in Case 2.

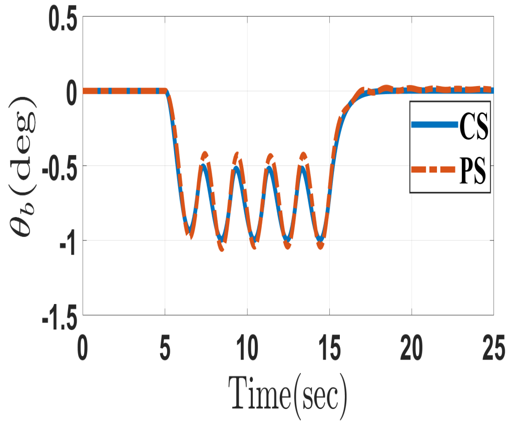

(a): Pitch angle

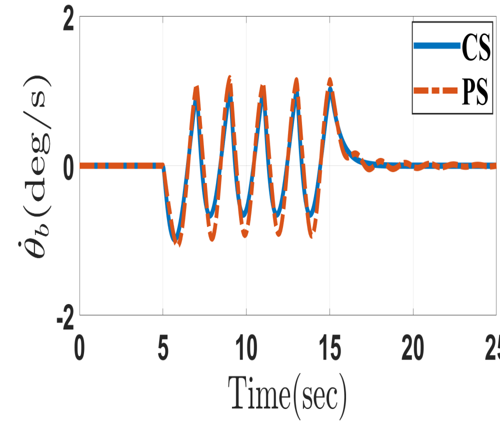

(b): Pitch angular velocity

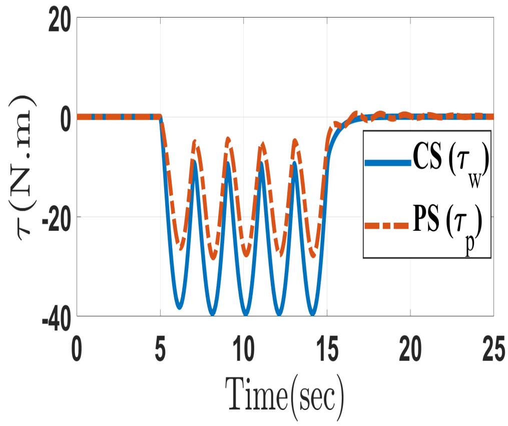

(c): Input torque

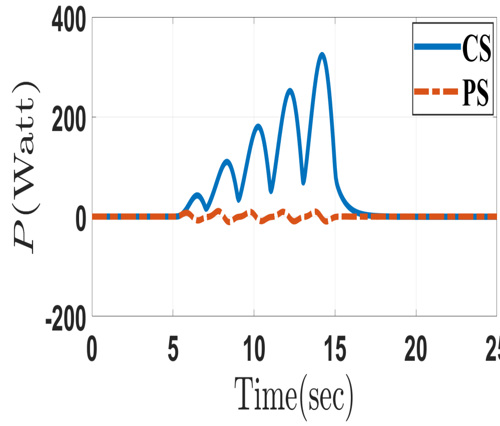

(d): Input power

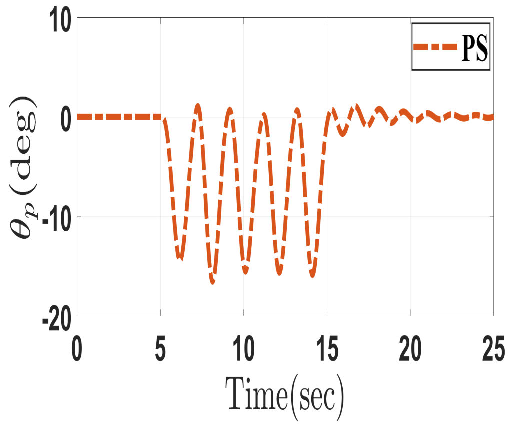

(e): Movable mechanism angle

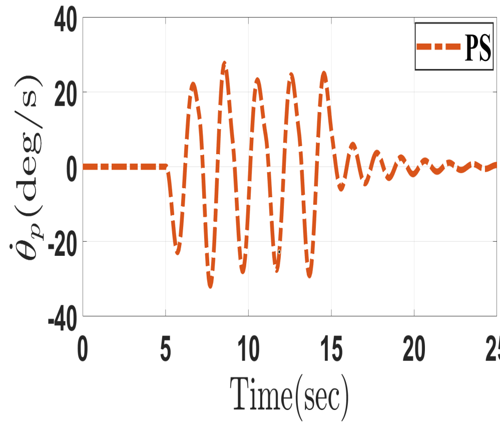

(f): Movable mechanism angular velocity

Figure 4.7: The TWRW stability control response for the conventional system (CS) and proposed system (PS) through CTC control in Case 3.

Figure. 4.5 depicts the simulation results of the TWRW stability control for the conventional and proposed systems through CTC control in Case 1. Similar to the results obtained for PID control, the pitch angle and its velocity converge to zero in a similar pattern, where it takes $2\,sec$ that they stabilize under both systems (see Figures. 4.5a and 4.5b). While the input torque in the proposed method is lower than the conventional one, the input power is similar for both control systems (see Figures. 4.5c and 4.5d). The maximum input torque in the conventional and proposed approaches are $40\,N.m$, and $24\,N.m$, respectively. Whereas, the maximum input torque for both approaches is almost the same ($8\,Watt$). In addition, the range of angular displacement of the movable mechanism, where its maximum value is similar to that obtained for PID control is small. (see Figures. 4.5e and 4.5f).

The simulation results of stability control through CTC control in Case 2 and Case 3 are shown in Figures. 4.6 and 4.7, respectively. Figures. 4.6a and 4.7a depict the motion of pitch angle in Case 2 and Case 3, respectively. Also, the pitch angular velocity response in Case 2 and Case 3 are shown in Figures. 4.6b and 4.7b, respectively. It can be seen that pitch angle and its velocity follow a similar pattern under both control methods. As shown in Figures. 4.6c and 4.7c, the input torque in the proposed approach is lower than in the conventional one. Furthermore, the input power in the proposed system is much lower than those obtained in the conventional method (see Figures. 4.6d and 4.7d). The energy consumption of motors in Case 1 to Case 3 through CTC control are shown in Table. 4.3. It can be seen that the energy consumption for the proposed approach is much smaller than the conventional system, especially in Case 2 and Case 3.

Table 4.3: Energy consumption of the conventional and the proposed system through CTC control for TWRW stability control.

Case	1	2	3
Conventional system ($E_r + E_l$)	6.60 J	3140.40 J	1270.90 J
Proposed system (E_p)	4.57 J	40.04 J	49.87 J

4.4 SMC control

4.4.1 Stability control of the conventional system

To resolve the problem of non-robustness of PID and CTC, SMC control which is robust against disturbances are developed for stability control. In this control scheme, the tracking errors are forced to slide along a surface called sliding surface.

To use the SMC, a state vector is chosen as

$$\mathbf{x} = \begin{bmatrix} x_1 & x_2 \end{bmatrix}^T$$

As the controller aim is pitch angle, x_1 and x_2 are selected as

$$x_1 = \theta_b, \qquad x_2 = \dot{\theta}_b.$$

Therefore,

$$\dot{x}_1 = x_2, \qquad \dot{x}_2 = \ddot{\theta}_b \tag{4.16}$$

Comparing Eqs. (3.15) and (4.16), there is

$$\dot{x}_1 = x_2, \qquad \dot{x}_2 = A_{c_3} + B_{c_3} + \hat{M}_{c31}^{-1}\tau_r + \hat{M}_{c32}^{-1}\tau_l \tag{4.17}$$

The tracking errors are defined as

$$e_1 = \theta_b - \theta_{b_d}, \qquad e_2 = \dot{\theta}_b - \dot{\theta}_{b_d}.$$

Based on the SMC structure, the system dynamic model can be simplified as [213]

$$\dot{e}_1 = e_2, \qquad \dot{e}_2 = u + f. \tag{4.18}$$

where u is the so-called *equivalent control input* and f is the disturbance. The magnitude of f is bounded as

$$\mid f \mid \leq L > 0$$

From Eqs. (4.17) and (4.18), we have

$$u = A_{c_3} + \hat{M}_{c31}^{-1}\tau_r + \hat{M}_{c32}^{-1}\tau_l - \ddot{\theta}_{b_d}, \qquad f = B_{c_3}. \tag{4.19}$$

The controller aim is to make the pitch angle remains at zero. Then,

$$\theta_{b_d} = 0, \qquad \dot{\theta}_{b_d} = 0, \qquad \ddot{\theta}_{b_d} = 0.$$

The sliding surface is defined as

$$\sigma = e_2 + ce_1 \tag{4.20}$$

c is the positive design parameter. The equivalent control input is assumed as

$$u = -ce_2 - \rho\,\mathrm{sign}(\sigma) \tag{4.21}$$

where ρ is the control gain and

$$\mathrm{sign}(\sigma) = \begin{cases} 1 & \text{if } \sigma > 0 \\ 0 & \text{if } \sigma = 0 \\ -1 & \text{if } \sigma < 0 \end{cases}$$

Define The Lyapanov function as

$$V = \frac{1}{2}\sigma^2 \tag{4.22}$$

The below conditions should be satisfied to provide stability of the SMC controller.

$$\text{(a)}\ \dot{V} < 0 \quad \text{for } \sigma \neq 0, \qquad \text{(b)}\ \lim_{\sigma \to \infty} V = \infty$$

Obviously, condition (b) is satisfied by Eq. (4.22). To achieve finite-time stability, condition (a) can change to [213]

$$\dot{V} \leq -\alpha V^{1/2} = -\frac{\alpha}{\sqrt{2}} \mid \sigma \mid$$

where $\alpha > 0$. By differentiating V, we have

$$\dot{V} = \sigma\dot{\sigma}$$

$\dot{\sigma}$ can be computed as

$$\dot{\sigma} = \dot{e}_2 + c\dot{e}_1 = u + f + ce_2 = -\rho\,\mathrm{sign}(\sigma) + f$$

Therefore,

$$\dot{V} = \sigma f - \sigma\rho\,\mathrm{sign}(\sigma) \leq - \mid \sigma \mid (\rho - L)$$

To satisfy condition (a), we have

$$\rho = L + \frac{\alpha}{\sqrt{2}}$$

Therefore, by selecting $u = -ce_2 - \rho\,\mathrm{sign}(\sigma)$ and $\rho = L + \dfrac{\alpha}{\sqrt{2}}$, the controller stability is guaranteed.

Using Eqs. (4.3), (4.19), and (4.21), the total torque of the wheels can be obtained as

$$\tau_{\mathrm{w}} = \frac{2(-A_{c_3} - c\dot{\theta}_b - \rho\,\mathrm{sign}(\sigma))}{\hat{M}_{c31}^{-1} + \hat{M}_{c32}^{-1}} \tag{4.23}$$

As the non-smooth function ($\mathrm{sign}(\sigma)$) is used in the equivalent control input, the SMC developed here suffers from the problem of chattering. To resolve this problem, the non-smooth function $\mathrm{sign}(\sigma)$ can be replaced with the equivalent smooth function as [213]

$$\mathrm{sign}(\sigma) \approx \frac{\sigma}{\mid \sigma \mid + \varepsilon} \tag{4.24}$$

where ε is a small positive scalar. Also, we have

$$\lim_{\varepsilon \to 0} \frac{\sigma}{\mid \sigma \mid + \varepsilon} = \mathrm{sign}(\sigma)$$

Therefore, Eq. (4.23) can be rewritten as

$$\tau_{\mathrm{w}} = \frac{2(-A_{c_3} - c\dot{\theta}_b - \rho\frac{\sigma}{\mid \sigma \mid + \varepsilon})}{\hat{M}_{c31}^{-1} + \hat{M}_{c32}^{-1}} \tag{4.25}$$

4.4.2 Stability control of the proposed system

Similar to the conventional system, from Eqs. (3.23) and (4.16), we have

$$\dot{x}_1 = x_2, \qquad \dot{x}_2 = A_{p_3} + B_{p_3} + \hat{M}_{p31}^{-1}\tau_r + \hat{M}_{p32}^{-1}\tau_l + \hat{M}_{p34}^{-1}\tau_p \tag{4.26}$$

Comparing Eqs. (4.18) and (4.26), it follows that

$$u = A_{p_3} + \hat{M}_{p31}^{-1}\tau_r + \hat{M}_{p32}^{-1}\tau_l + \hat{M}_{p34}^{-1}\tau_p - \ddot{\theta}_{b_d}, \qquad f = B_{p_3}. \tag{4.27}$$

Considering Eqs. (4.6), (4.21), (4.24), and (4.27), the input torque of the movable mechanism is obtained as

$$\tau_p = \frac{-A_{p_3} - c\dot{\theta}_b - \rho\dfrac{\sigma}{\mid \sigma \mid + \varepsilon}}{\hat{M}_{p34}^{-1}} \tag{4.28}$$

4.4.3 Simulation results

Three cases which are similar to those used for PID control are assumed for simulation of stability control through SMC control. For Case 1 to Case 3, the controller gains are chosen as

Case 1:

For Case 1, the controller gains below are set for both control systems.

$$c = 2 \qquad \rho = 5 \qquad \epsilon = 0.05$$

Case 2 and 3:

For Case 2 and 3, the controller gains are chosen as

$$c = 5 \qquad \rho = 200 \qquad \epsilon = 0.05$$

Figures. 4.8-4.10 show the simulation results of TWRW stability control through SMC control in Case 1 to Case 3, respectively. The performance analysis of the conventional and the proposed systems for all three cases are similar to those explained in CTC simulation results (section 4.3.3). However, the input power of SMC in Case 2, and Case 3 are smaller than those obtained in CTC. For example, the maximum input power of the conventional method for SMC in Case 2, and Case 3 are $500\,Watt$, and $290\,Watt$, respectively. While, these values for CTC are $600\,Watt$, and $350\,Watt$, respectively. Table. 4.4 shows the energy consumptions in Case 1 to Case 3 through SMC control for both control approaches.

Table 4.4: Energy consumption of the conventional and the proposed systems through SMC control for TWRW stability control.

Case	1	2	3
Conventional system ($E_r + E_l$)	6.99 J	2453.20 J	992.64 J
Proposed system (E_p)	4.57 J	38.74 J	55.44 J

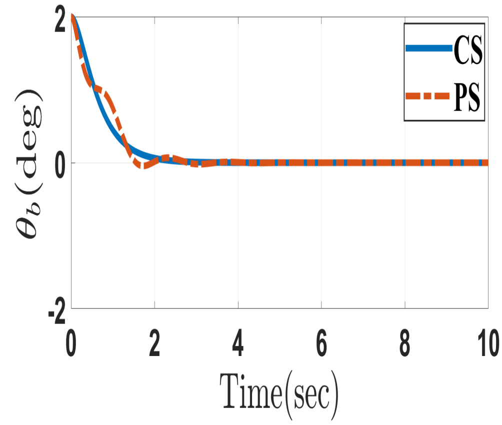

(a): Pitch angle

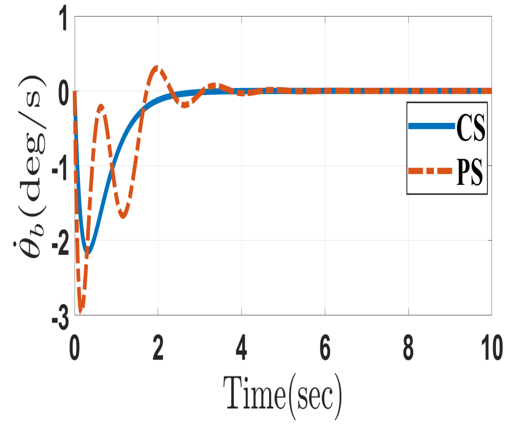

(b): Pitch angular velocity

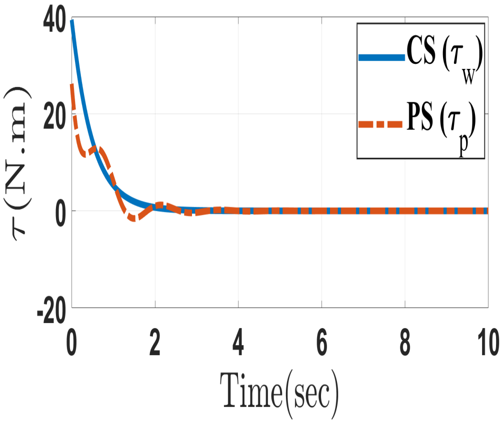

(c): Input torque

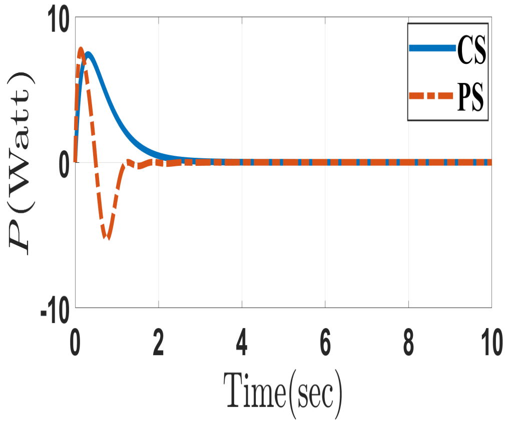

(d): Input power

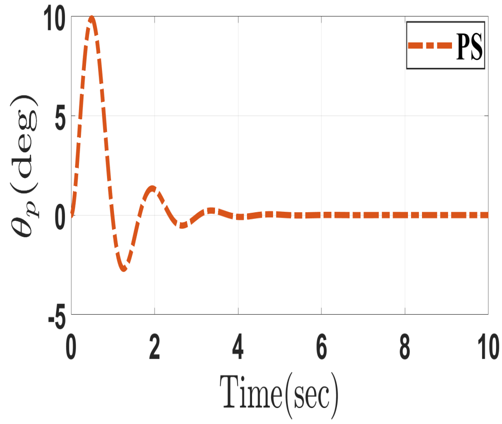

(e): Movable mechanism angle

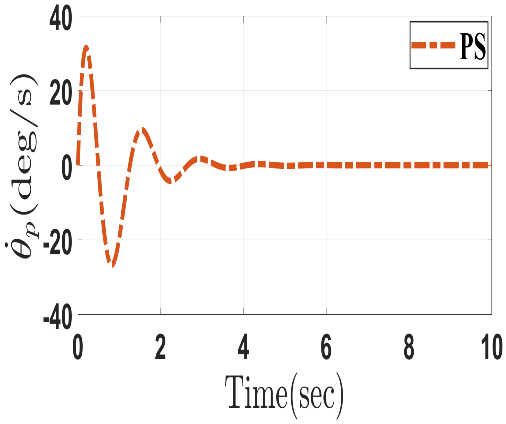

(f): Movable mechanism angular velocity

Figure 4.8: The TWRW stability control response for the conventional system (CS) and proposed system (PS) through SMC control in Case 1.

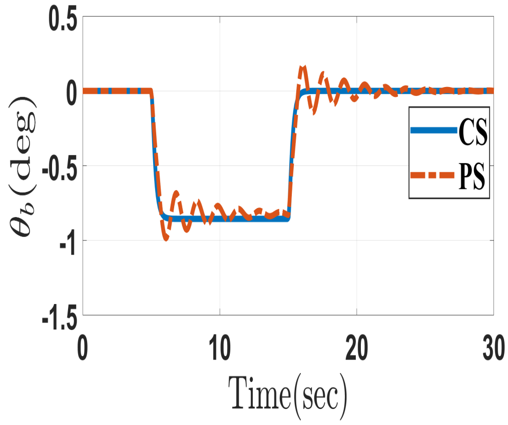

(a): Pitch angle

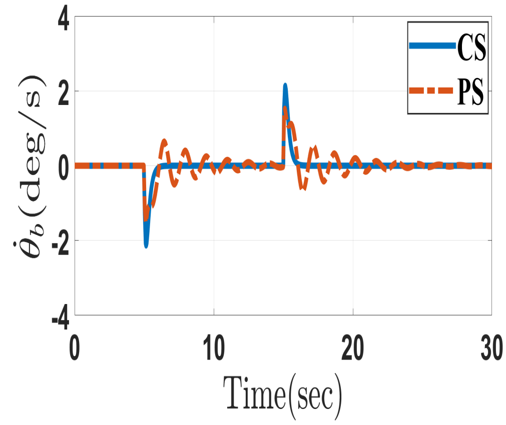

(b): Pitch angular velocity

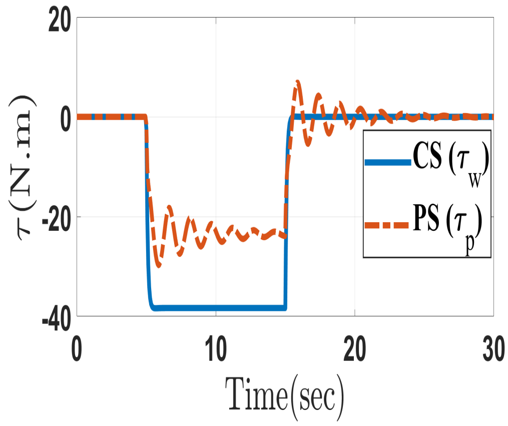

(c): Input torque

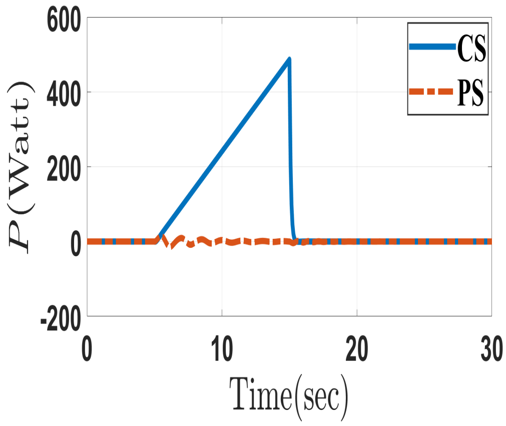

(d): Input power

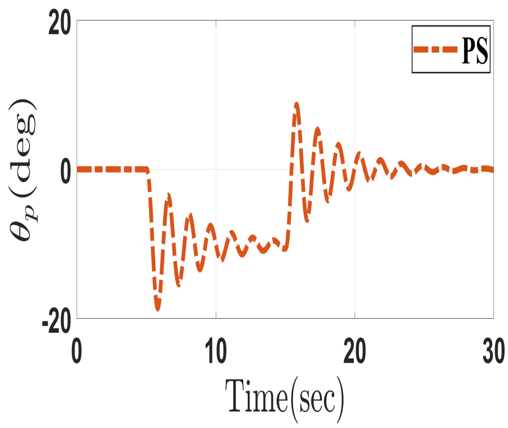

(e): Movable mechanism angle

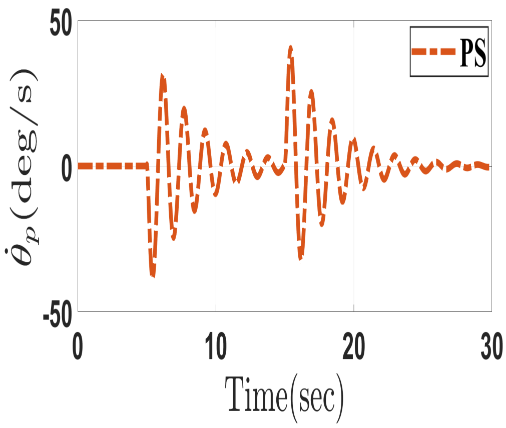

(f): Movable mechanism angular velocity

Figure 4.9: The TWRW stability control response for the conventional system (CS) and proposed system (PS) through SMC control in Case 2.

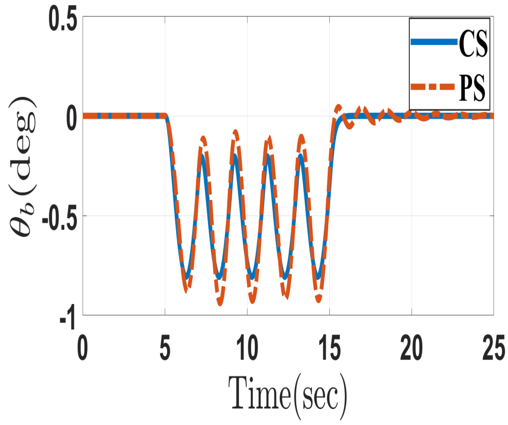

(a): Pitch angle

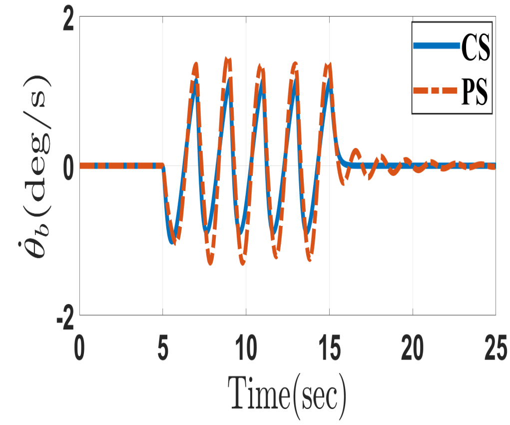

(b): Pitch angular velocity

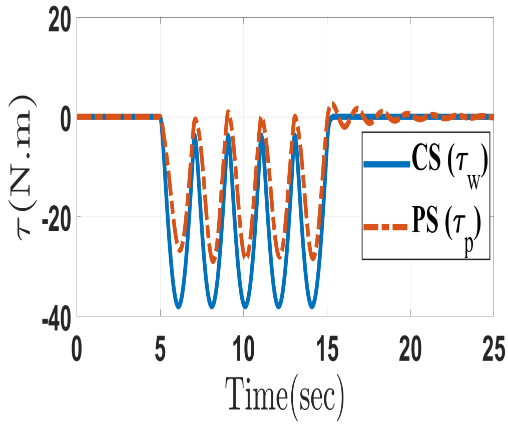

(c): Input torque

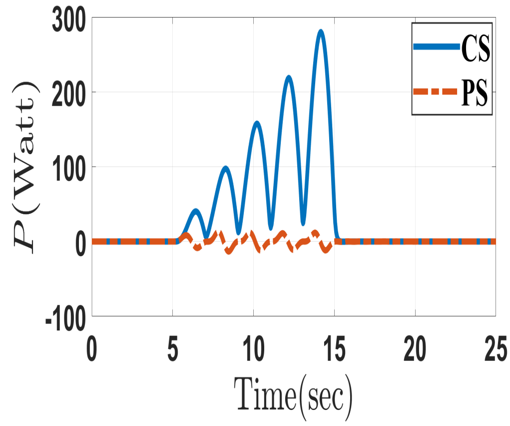

(d): Input power

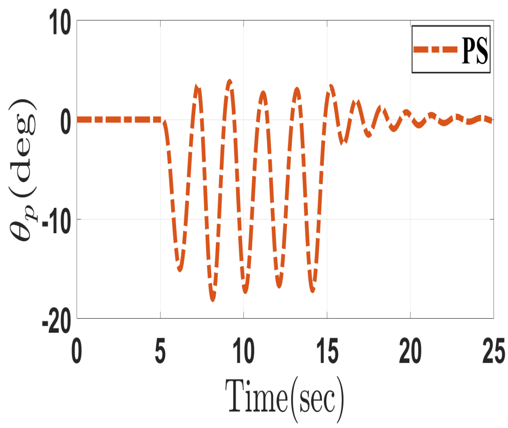

(e): Movable mechanism angle

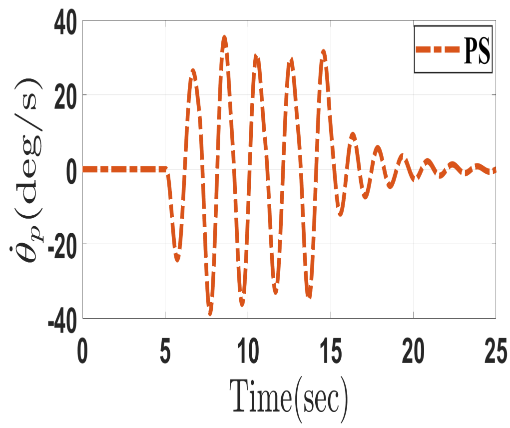

(f): Movable mechanism angular velocity

Figure 4.10: The TWRW stability control response for the conventional system (CS) and proposed system (PS) through SMC control in Case 3.

4.5 SOSMC control

4.5.1 Stability control of the conventional system

To resolve the chattering problem, the higher-order SMC like SOSMC control are recommended to be used, which are more robust against disturbances. To control the pitch angle through the SOSMC, the sliding surface is defined as

$$\sigma = e_2 + ce_1 \tag{4.29}$$

c is the positive design parameters. e_1 and e_2 are the tracking errors of pitch angle and pitch angular velocity, respectively. e_1 and e_2 are defined as

$$e_1 = \theta_b - \theta_{b_d}, \qquad e_2 = \dot{\theta}_b - \dot{\theta}_{b_d}.$$

According to the controller aim, θ_{b_d} and $\dot{\theta}_{b_d}$ are set as

$$\theta_{b_d} = 0, \qquad \dot{\theta}_{b_d} = 0.$$

Therefore, Eq. (4.29) can be reformulated as

$$\sigma = \dot{\theta}_b + c\theta_b \tag{4.30}$$

From Eq. (4.30) we have

$$\dot{\sigma} = \ddot{\theta}_b + c\dot{\theta}_b \tag{4.31}$$

According to the structure of SOSMC, we have [213]

$$\dot{\sigma} = u + f \tag{4.32}$$

Comparing Eqs. (3.15), (4.31), and (4.32), we have

$$u = A_{c_3} + \hat{M}_{c_{31}}^{-1}\tau_r + \hat{M}_{c_{32}}^{-1}\tau_l, \qquad f = B_{c_3} \tag{4.33}$$

To develop the SOSMC, K_m and K_M which are two positive constants are chosen as

$$0 \le K_m \le 1 \le K_M \tag{4.34}$$

There exist two positive constants q and U_M which are selected as

$$\mid f \mid < qU_M, \qquad 0 < q < 1 \tag{4.35}$$

Also, the positive constant value C is chosen as

$$\mid \dot{f} \mid \le C \tag{4.36}$$

Considering the assumptions above, the equivalent control input u is defined as

$$u = -\lambda \mid \sigma \mid^{0.5} \text{sign}(\sigma) + \nu, \qquad \dot{\nu} = \begin{cases} -u, & \mid u \mid > U_M \\ -\alpha \text{sign}(\sigma), & \mid u \mid \le U_M \end{cases} \tag{4.37}$$

where, λ and α are two positive constants. Selecting

$$\lambda > \sqrt{\frac{2}{(K_m\alpha - C)}} \frac{(K_m\alpha + C)K_M(1+q)}{K_m^2(1-q)}, \qquad \alpha > C/K_m \tag{4.38}$$

all tracking errors converge to zero in finite time. The stability proof of SOSMC control is made by the theorem below.

Theorem:

If assumptions considered in Eqs. (4.34)-(4.36) are satisfied and the sliding surface is defined as Eq. (4.29), the *equivalent control input*(u) defined in Eq. (4.37) guarantees that the tracking error converges to zero in finite-time. To prove this theorem, three steps are defined as:

Step 1: The control input u enters the segment $[-U_M, U_M]$ in finite time.

Step 2: The sliding variable $\dot{\sigma}$ reaches the sliding surface σ in finite time.

Step 3: The tracking error e converges to zero in finite time.

Proof of step 1:

if $\mid u \mid > U_M$, a Lyapunov function of u is chosen as [214]

$$V_u = \frac{1}{2}u^2 \tag{4.39}$$

Considering Eqs. (4.32), (4.37), and (4.39), there is

$$\dot{V}_u = -u^2 - \frac{1}{2}\lambda \mid \sigma \mid^{-0.5} u^2(\frac{f}{u} + 1) \tag{4.40}$$

From Eqs. (4.34), (4.35), and (4.40) as well as considering $\mid u \mid > U_M$, it leads to

$$\dot{V}_u < -u^2 - \frac{1}{2}\lambda \mid \sigma \mid^{-0.5} u^2(1 - q) < -u^2 = -2V_u$$

Therefore,

$$\frac{dV_u}{dt} \leq -2V_u \Longrightarrow t - t_0 \leq \frac{1}{2}\ln\frac{V_u(t_0)}{V_u(t)}$$

The initial point of u which is denoted by u_0 reaches the segment $[-U_M, U_M]$ at time $t_1 = t_{U_M} - t_0$. From Eq. (4.39), we have

$$t_1 \leq \ln \mid u_0 \mid - \ln(U_M)$$

It can be concluded that control input u enters the segment $[-U_M, U_M]$ in finite time.

Proof of step 2:

When the control input u enters the segment $[-U_M, U_M]$ which means $| u | \leq U_M$, from Eq. (4.37) we have

$$\dot{u} = -\frac{\lambda}{2}\dot{\sigma} \mid \sigma \mid^{-0.5} - \alpha \text{sign}(\sigma) \tag{4.41}$$

Comparing Eqs. (4.32) and (4.41), it follows that

$$\ddot{\sigma} = -\frac{\lambda}{2}\dot{\sigma} \mid \sigma \mid^{-0.5} - \alpha \text{sign}(\sigma) + \dot{f} \tag{4.42}$$

Considering Eqs. (4.34)-(4.36), the Eq. (4.42) can be presented as

$$\ddot{\sigma} \in [-C, C] - [-K_m, K_M](\frac{\lambda}{2}\dot{\sigma} \mid \sigma \mid^{-0.5} + \alpha \text{sign}(\sigma)) \tag{4.43}$$

To analyze the motion of σ and $\dot{\sigma}$, the phase trajectory of point $(\sigma, \dot{\sigma})$ is defined in the phase plane. The gradient of the trajectory is obtained as

$$\frac{d\dot{\sigma}}{d\sigma} = \frac{d\dot{\sigma}/dt}{d\sigma/dt} = \frac{\ddot{\sigma}}{\dot{\sigma}} \tag{4.44}$$

Figure. 4.11 depicts the trajectory of $\sigma - \dot{\sigma}$ during the reaching phase.

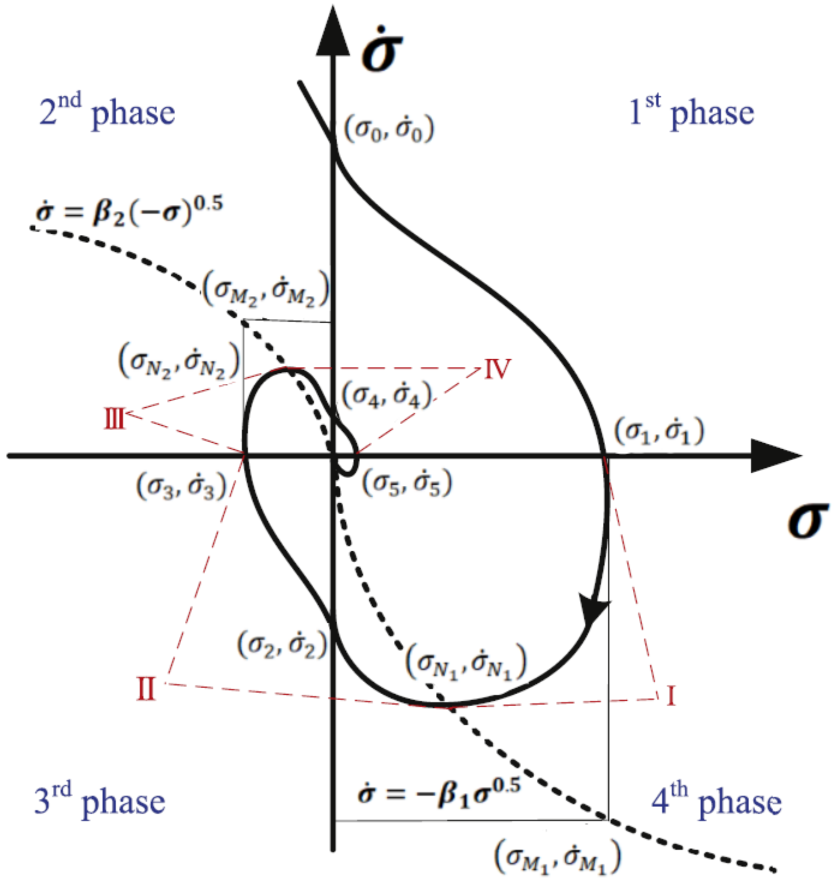

Figure 4.11: Phase trajectory of $\sigma - \dot{\sigma}$ during reaching phase.

The motion of $\sigma - \dot{\sigma}$ is divided into four phases and analyzed clockwise. The four phases are as below:

(a) Motion of the first phase:

In the first phase $\sigma > 0$, $\dot{\sigma} > 0$. Therefore, from Eq. (4.43) we have

$$\ddot{\sigma} \in [-C, C] - [-K_m, K_M](\frac{\lambda}{2}\dot{\sigma} \mid \sigma \mid^{-0.5} + \alpha) \Longrightarrow \ddot{\sigma} \leq C - K_m\alpha \tag{4.45}$$

Comparing Eqs. (4.44) and (4.45), it leads to

$$\dot{\sigma}d\dot{\sigma} = \ddot{\sigma}d\sigma \Longrightarrow \frac{1}{2}\dot{\sigma}^2\Big|_{\dot{\sigma}_0}^{\dot{\sigma}_1} = \int_{\sigma_0}^{\sigma_1} \ddot{\sigma}d\sigma \leq \int_{\sigma_0}^{\sigma_1} (C - K_m\alpha)d\sigma \Longrightarrow \sigma_1 \leq \frac{\dot{\sigma}_1^2 - \dot{\sigma}_0^2}{2(C - K_m\alpha)} + \sigma_0$$

As $\dot{\sigma}_1 = 0$ and $\sigma_0 = 0$, it leads to

$$\sigma_1 \le \frac{\dot{\sigma}_0^2}{2(K_m\alpha - C)} \tag{4.46}$$

(b) Motion of the fourth phase:

In the fourth phase, $\sigma > 0$ and $\dot{\sigma} < 0$. Therefore, Eq. (4.43) is rewritten as

$$\ddot{\sigma} \in [-C, C] - [K_m, K_M](-\frac{\lambda}{2}\dot{\sigma} \mid \sigma \mid^{-0.5} + \alpha) \tag{4.47}$$

When the point $(\sigma, \dot{\sigma})$ leaves the axis $\dot{\sigma} = 0$, from Eqs. (4.38) and (4.47) we have

$$\ddot{\sigma} \in [-C, C] - \alpha[K_m, K_M] \Longrightarrow \ddot{\sigma} \le C - K_m\alpha < 0 \tag{4.48}$$

Also, when the point $(\sigma, \dot{\sigma})$ is reaching axis $\sigma = 0$, there is

$$\ddot{\sigma} \in [-C, C] - [-K_m, K_M](-\infty) \Longrightarrow \ddot{\sigma} \to +\infty \tag{4.49}$$

Considering Eqs. (4.42) and (4.49), it can be concluded that $\ddot{\sigma}$ is continuous in the fourth phase. Also, the sign of $\ddot{\sigma}$ at the phase trajectory's boundary changes, which can be concluded that there is at least one point satisfying $\ddot{\sigma} = 0$. The point satisfying the $\ddot{\sigma} = 0$ is denoted by $(\sigma_{N_1}, \dot{\sigma}_{N_1})$. A curve $\dot{\sigma} = -\beta_1\sigma^{0.5}$ intersecting with phase trajectory at point $(\sigma_{N_1}, \dot{\sigma}_{N_1})$ is defined. The intersection of this curve with axis $\sigma = \sigma_1$ is denoted by $(\sigma_{M_1}, \dot{\sigma}_{M_1})$. Therefore, from Eq. (4.38) we have

$$\mid \dot{\sigma}_2 \mid \le \mid \dot{\sigma}_{N_1} \mid < n \mid \dot{\sigma}_0 \mid \tag{4.50}$$

where $n = \dfrac{(1-q)K_m}{(1+q)K_M}$. To prove Eq. (4.50), $\dot{\sigma}_{N_1} = 0$ on the curve $\dot{\sigma} = -\beta_1\sigma^{0.5}$ is considered, which follows that

$$0 < \frac{2}{\lambda}(\frac{K_m\alpha - C}{K_M}) \leq \beta_1 \leq \frac{2}{\lambda}(\frac{K_M\alpha + C}{K_m}) \tag{4.51}$$

According to the definition of $(\sigma_{M_1}, \dot{\sigma}_{M_1})$, it can be concluded that $|\ \dot{\sigma}_{N_1}\ | < |\ \dot{\sigma}_{M_1}\ |$. Since $|\ \dot{\sigma}_{N_1}\ |$ is the maximum value of $|\ \dot{\sigma}\ |$ in the fourth phase, therefore $|\ \dot{\sigma}_2\ | \leq |\ \dot{\sigma}_{N_1}\ |$. As the point $(\sigma_{M_1}, \dot{\sigma}_{M_1})$ is on the curve $\dot{\sigma} = -\beta_1\sigma^{0.5}$, we have

$$\dot{\sigma}_{M_1} = -\beta_1\sigma_{M_1}^{0.5} = -\beta_1\sigma_1^{0.5} \geq -\beta_1\sqrt{\frac{\dot{\sigma}_0^2}{2(K_m\alpha - C)}} \tag{4.52}$$

Combining Eqs. (4.51) and (4.52), it leads to

$$|\ \dot{\sigma}_{M_1}\ | \leq |\ \dot{\sigma}_0\ | \sqrt{\frac{1}{2(K_m\alpha - C)}}\frac{2(K_M\alpha + C)}{\lambda K_m}$$

λ is selected to satisfy Eq. (4.38). Then,

$$|\ \dot{\sigma}_{M_1}\ | < \frac{(1-q)K_m}{(1+q)K_M}\ |\ \dot{\sigma}_0\ |$$

It is obvious that $|\ \dot{\sigma}_2\ | \leq |\ \dot{\sigma}_{N_1}\ | < |\ \dot{\sigma}_{M_1}\ |$. Therefore,

$$|\ \dot{\sigma}_2\ | \leq |\ \dot{\sigma}_{N_1}\ | < n\ |\ \dot{\sigma}_0\ | \tag{4.53}$$

with $n = \dfrac{(1-q)K_m}{(1+q)K_M}$

(c) Motion of the third phase:

The third phase condition is similar to the first phase. For the third phase we have:

$$|\ \sigma_3\ | \leq \frac{\dot{\sigma}_2^2}{2(K_m\alpha - C)} < \frac{n^2\dot{\sigma}_0^2}{2(K_m\alpha - C)} \tag{4.54}$$

(d) Motion of the second phase:

The case of the second phase is similar to the fourth one. In this phase we have

$$| \dot{\sigma}_4 | \leq | \dot{\sigma}_{N_2} | < n^2 | \dot{\sigma}_0 | \tag{4.55}$$

Considering all four phases (Eqs. (4.46), (4.50), (4.54), and (4.55)), it follows that

$$| \sigma_{2i-1} | \leq n^{2i-2} \frac{\dot{\sigma}_0^2}{2(K_m \alpha - C)}, \qquad | \dot{\sigma}_{2i} | < n^i | \sigma_0 | \tag{4.56}$$

where $n = \dfrac{(1-q)K_m}{(1+q)K_M}$. It is obvious that $n < 1$. Therefore, σ and $\dot{\sigma}$ converge to zero.

Proof of step 3:

After sliding variable($\dot{\sigma}$) and sliding surface(σ) converge to zero, the tracking error($e = \theta_b - \theta_{b_d}$) enters the sliding surface, which leads to

$$\dot{e} + ce = 0 \tag{4.57}$$

The Lyapanov function is chosen as

$$V = \frac{1}{2} e^2 \tag{4.58}$$

Similar to the stability proof of SMC, the conditions below should be satisfied to achieve a finite-time stability.

$$\text{(a)} \;\; \dot{V} < 0 \;\; \text{for} \;\; e \neq 0, \qquad \text{(b)} \;\; \lim_{e \to \infty} V = \infty$$

It is obvious that condition (b) is satisfied by Eq. (4.58). From Eq. (4.57) and (4.58), we have

$$\dot{V} = e\dot{e} = -ce^2$$

Since c is a positive parameter, condition (a) is satisfied. Therefore, the tracking error converges to zero in finite-time.

From Eqs. (4.3), (4.33), and (4.37), the total torque of wheels can be obtained through the equation below

$$\tau_{\mathrm{w}} = \frac{2(-A_{c_3} - c\dot{\theta}_b - \lambda \mid \sigma \mid^{0.5} \operatorname{sign}(\sigma) + \nu)}{\hat{M}_{c31}^{-1} + \hat{M}_{c32}^{-1}} \tag{4.59}$$

4.5.2 Stability control of the proposed system

Considering Eqs. (3.23), (4.31), and (4.32), we have

$$u = A_{p3} + \hat{M}_{p31}^{-1}\tau_r + \hat{M}_{p32}^{-1}\tau_l + \hat{M}_{p34}^{-1}\tau_p, \qquad f = B_{p3} \tag{4.60}$$

From Eqs. (4.6), (4.37) and (4.60), τ_p is calculated as

$$\tau_p = \frac{-A_{p_3} - c\dot{\theta}_b - \lambda \mid \sigma \mid^{0.5} \operatorname{sign}(\sigma) + \nu}{\hat{M}_{p34}^{-1}} \tag{4.61}$$

4.5.3 Simulation results

The stability control of the TWRW through SOSMC control are simulated in 3 cases which are similar to those used for PID control. In Case 1 to Case 3, the controller gains for SOSMC are chosen as

Case 1:

For Case 1, the controller gains below are set.

$$c = 2, \qquad \lambda = 2, \qquad \alpha = 0.3, \qquad \epsilon = 0.05.$$

Case 2 and 3:

For Case 2 and Case 3, the controller gains are chosen as

$$c = 1.5, \qquad \lambda = 20, \qquad \alpha = 2, \qquad \epsilon = 0.05.$$

Figures. 4.12-4.14 depict the simulation results of TWRW stability control for the conventional and proposed systems through SOSMC control in Case 1 to Case 3, respectively. The performance analysis of both control systems for all three cases is similar to those investigated in CTC control simulation results (section 4.3.3). However, the maximum input power obtained for SOSMC is the smallest among other control schemes used in this chapter. For instance, the maximum input power of the conventional method in Case 2 for PID, CTC, SMC, and SOSMC are $410\,Watt$, $600\,Watt$, $500\,Watt$, and $300\,Watt$, respectively. Table. 4.5 shows the energy consumption of stability control through SOSMC control for both control methods in Case 1 to Case 3.

Table 4.5: Energy consumption of the conventional and the proposed systems through SOSMC control for TWRW stability control.

Case	1	2	3
Conventional system ($E_r + E_l$)	6.36 J	1822 J	764.64 J
Proposed system (E_p)	4.64 J	32.09 J	41.14 J

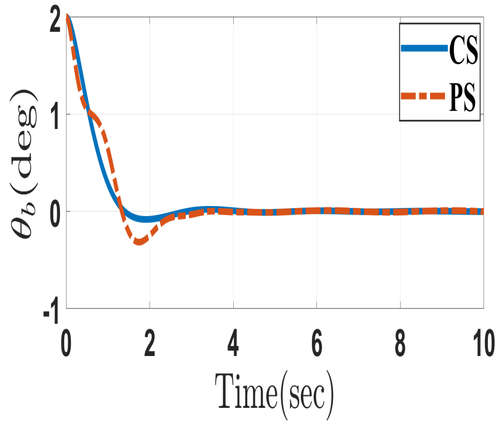

(a): Pitch angle

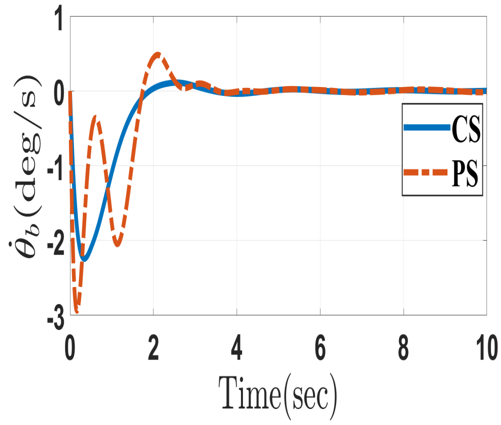

(b): Pitch angular velocity

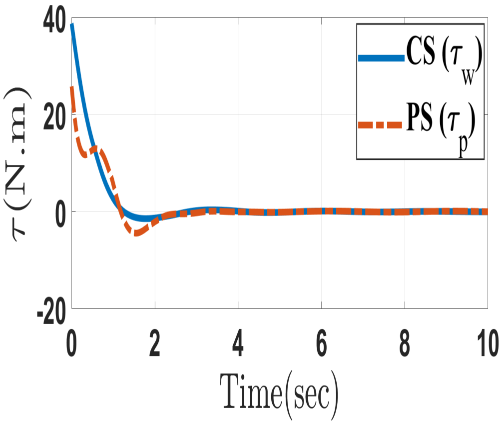

(c): Input torque

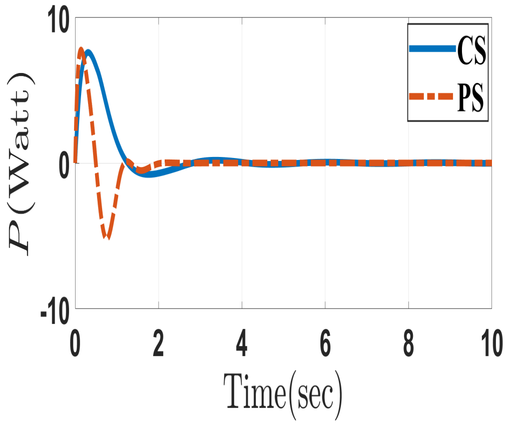

(d): Input power

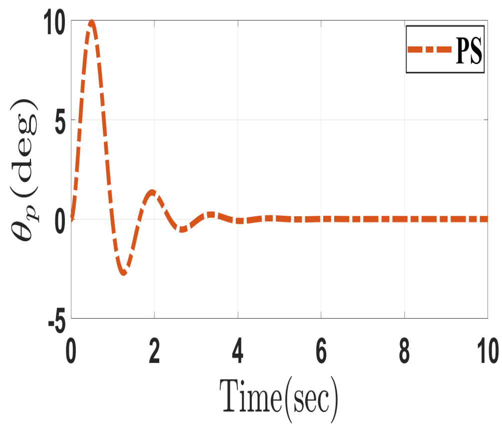

(e): Movable mechanism angle

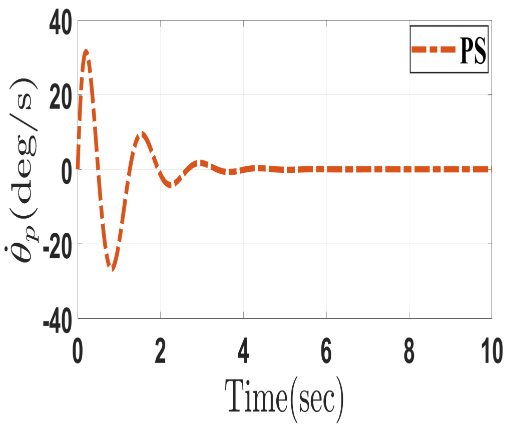

(f): Movable mechanism angular velocity

Figure 4.12: The TWRW stability control response for the conventional system (CS) and proposed system (PS) through SOSMC control in Case 1.

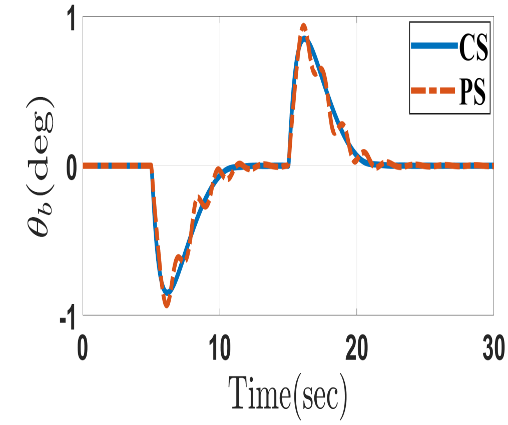

(a): Pitch angle

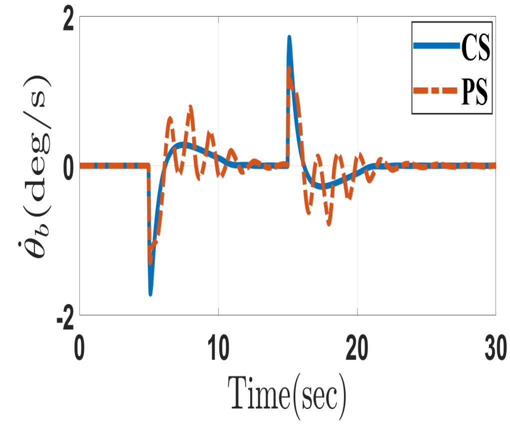

(b): Pitch angular velocity

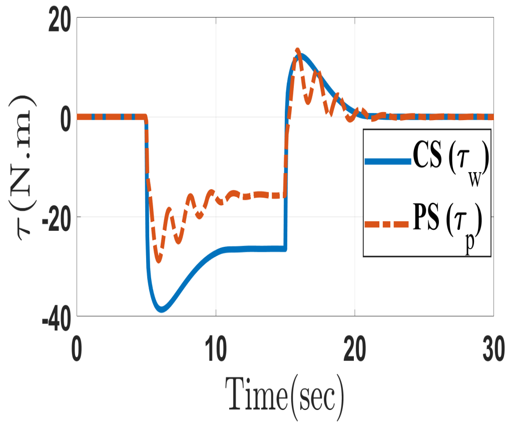

(c): Input torque

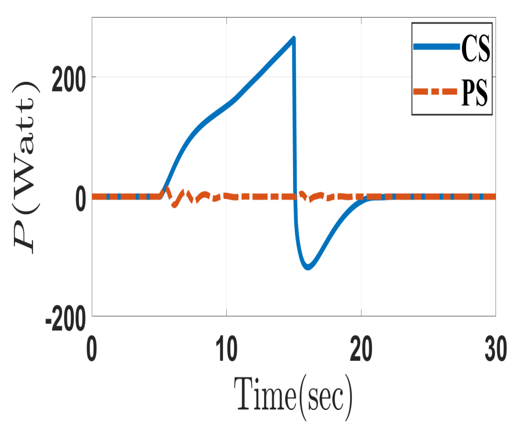

(d): Input power

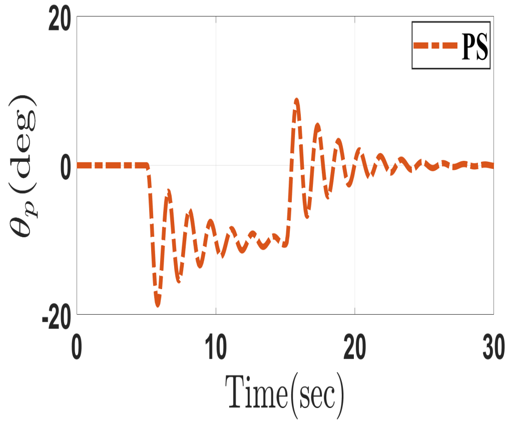

(e): Movable mechanism angle

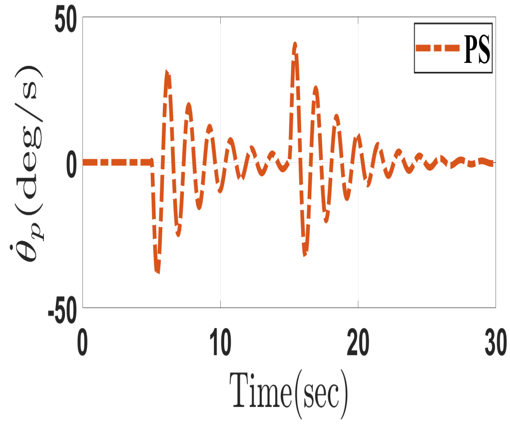

(f): Movable mechanism angular velocity

Figure 4.13: The TWRW stability control response for the conventional system (CS) and proposed system (PS) through SOSMC control in Case 2.

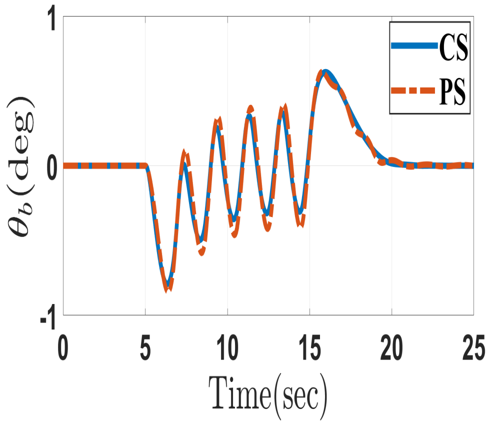

(a): Pitch angle

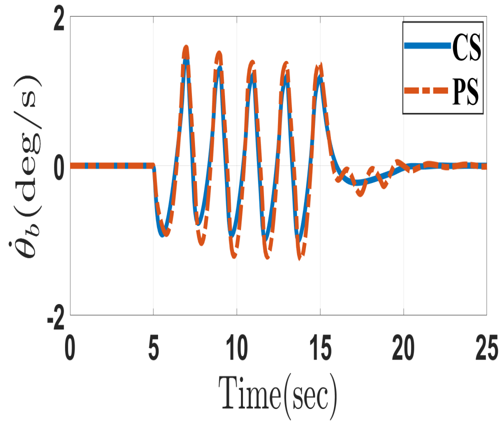

(b): Pitch angular velocity

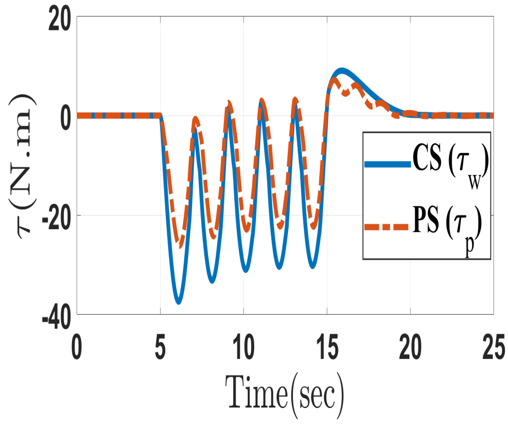

(c): Input torque

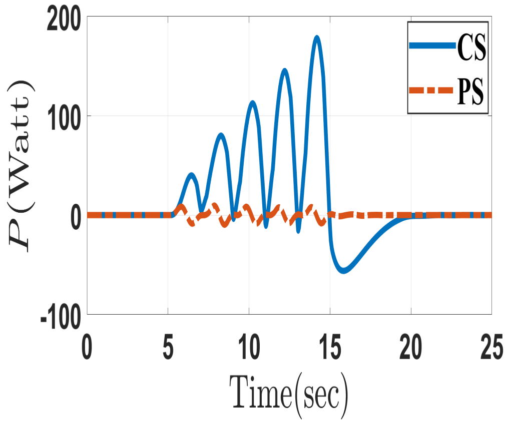

(d): Input power

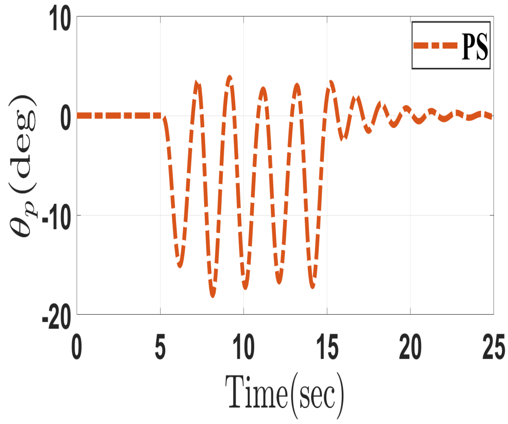

(e): Movable mechanism angle

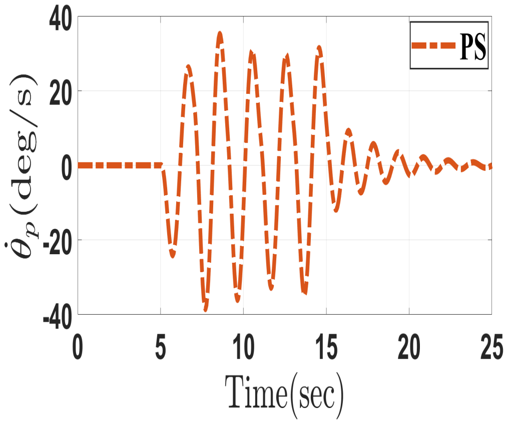

(f): Movable mechanism angular velocity

Figure 4.14: The TWRW stability control response for the conventional system (CS) and proposed system (PS) through SOSMC control in Case 3.

To evaluate the performance of the control schemes used in this chapter (PID, CTC, SMC, and SOSMC), the simulation results obtained for stability control of the proposed system in Case 2 are compared. In Case 2, the motion of the body's CoG disturbance is considered from $5\,sec$ to $15\,sec$. In this period, the input torque is applied to the movable mechanism (τ_p) to compensate the disturbance effects and keep pitch angle zero.

It is expected that when no disturbance is applied to the system (after time $15\,sec$), the input torque converges to zero. However, it can be seen in the simulation results, after $t = 15\,sec$ the high-frequency components remain in the input torque of the movable mechanism which affects the other control parameters. Figures. 4.15-4.20 depict the residual components in the control parameters of the proposed system in Case 2. It can be seen that the largest components are found in the PID control, while the model-based CTC control has lower residual components than PID control.

Though, through the SMC and SOSMC control which are classified as robust controllers, the lower components than PID and CTC remain in their responses. It can be seen that the lowest components are obtained through the SOSMC, which is known as one of the best robust controllers.

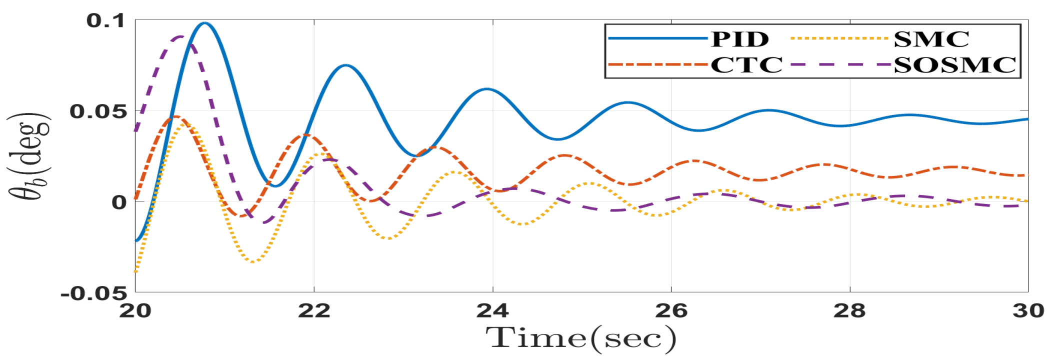

Figure 4.15: The residual components of pitch angle in stability control for the proposed system through PID, CTC, SMC, and SOSMC in Case 2.

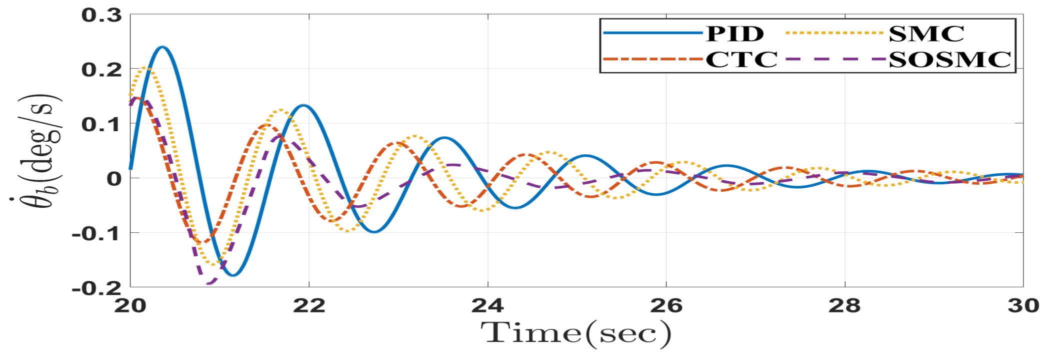

Figure 4.16: The residual components of pitch angular velocity in stability control for the proposed system through PID, CTC, SMC, and SOSMC in Case 2.

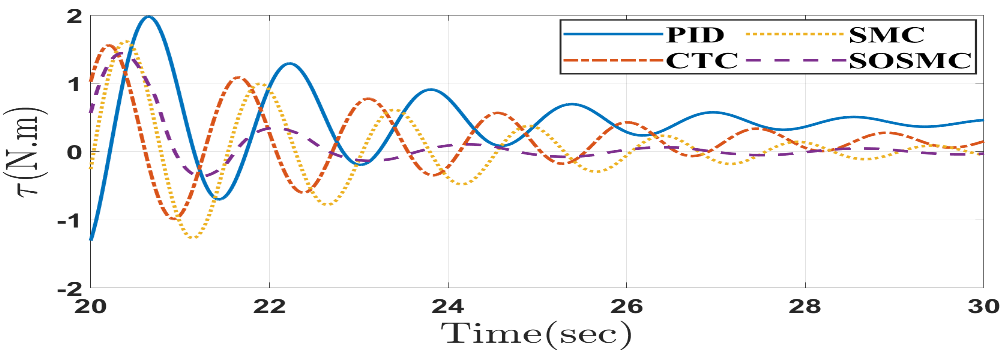

Figure 4.17: The residual components of input torque in stability control for the proposed system through PID, CTC, SMC, and SOSMC in Case 2.

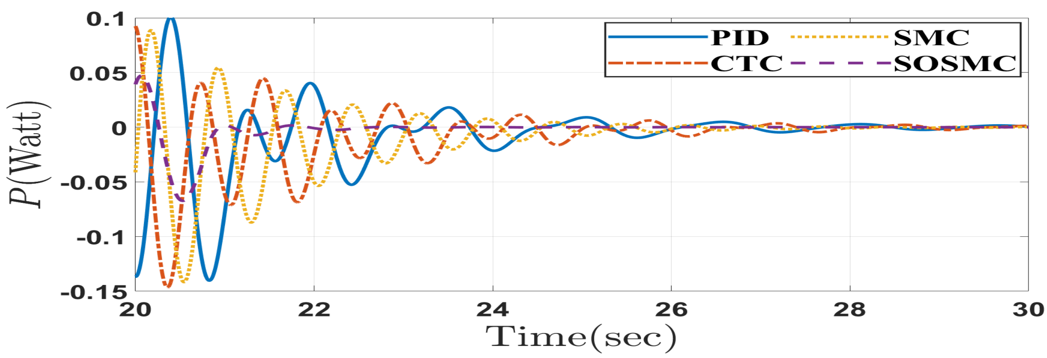

Figure 4.18: The residual components of input power in stability control for the proposed system through PID, CTC, SMC, and SOSMC in Case 2.

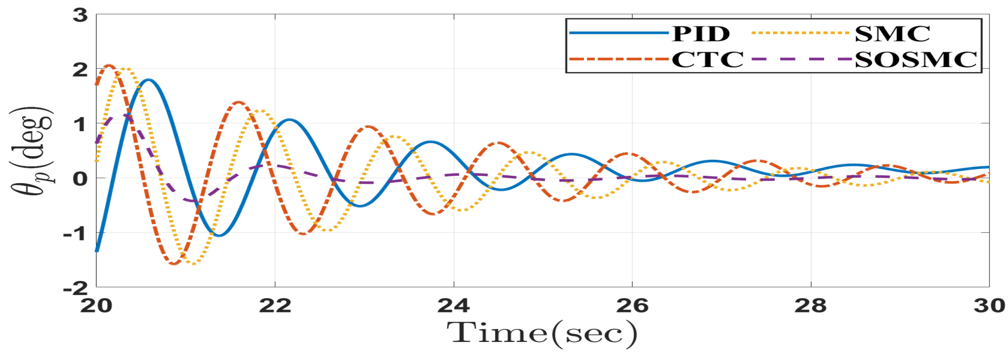

Figure 4.19: The residual components of movable mechanism angle in stability control for the proposed system through PID, CTC, SMC, and SOSMC in Case 2.

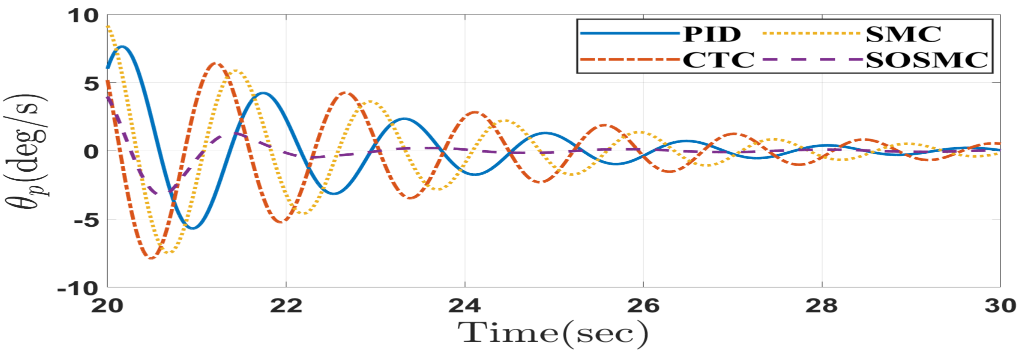

Figure 4.20: The residual components of movable mechanism angular velocity in stability control for the proposed system through PID, CTC, SMC, and SOSMC in Case 2.

4.6 Summary

In this chapter, the stability control of TWRW for the conventional and proposed systems through four control schemes (PID, CTC, SMC, and SOSMC) was developed. It is easy to develop the controller through PID control, as it doesn't require any information about the dynamic modelling. The only parameters needed to calculate the control inputs are the feedback of controller aim (pitch angle) and PID control gains. To achieve a more optimized stability control, the CTC control which is a model-based controller is used. In this controller, the nonlinear feedback of dynamic modelling is used to obtain the control input. However, the disturbance components are not considered in CTC control, which makes it non-robust against disturbances.

To design a robust controller, SMC and SOSMC are developed. The SMC control suffers from the chattering problem which appeared in the control input and makes it unusable for real-time systems. To resolve this problem, the non-smooth sign function used in SMC is replaced with the equivalent smooth function. In addition, the higher-order SMC controllers like SOSMC are used to resolve the chattering problem. The simulation results were provided to show the superiority of the proposed system over the conventional approach. The TWRW can reach its stability under both control systems, while the input torque, input power, and energy consumption in the proposed system are much lower than those obtained in the conventional one.

IIn the next chapter, the stability and direction control of TWRW for the conventional and the proposed approaches are developed. CTC, SMC, and SOSMC control schemes are used to develop the controllers. The simulation results are provided to demonstrate the superiority of the proposed system over the conventional one.

Chapter 5

Stability and Direction Control

5.1 Introduction

In addition to stability, the direction control is also important for a TWRW. When a TWRW is required to follow a path along a desired direction (defined by a yaw angle which is shown in Figure. 3.2b), achieving both stability and direction control is more challenging. In this chapter, the stability and direction control of the TWRW are developed. The control objectives are to track the desired yaw angle, while the pitch angle remains zero.

The control input in the conventional system is the right and left wheels' torques. It means that the wheels provide the stability and direction control inputs at the same time. However, in the proposed system, the input torque of the movable mechanism is added to the control inputs to assist the wheels for stability and direction control. In the conventional system, there are two control inputs including input torque of the right and left wheels, while there are three control inputs in the proposed system (input torque of the right and left wheels and the movable mechanism). However, in both control systems, there are two control outputs (pitch and yaw angle).

The stability and direction control for both control systems can be summarized as follows:

$$
\textbf{Conventional System}
\begin{cases}
\bullet\textbf{Controller input} \begin{cases} \text{Input torque of right wheel} \\ \text{Input torque of left wheel} \end{cases} \\[2ex]
\bullet\textbf{Controller aim} \begin{cases} \text{Stability (Pitch angle)} \\ \text{Direction (Yaw angle)} \end{cases}
\end{cases}
$$

$$
\textbf{Proposed System}
\begin{cases}
\bullet\textbf{Controller input} \begin{cases} \text{Input torque of right wheel} \\ \text{Input torque of left wheel} \\ \text{Input torque of added movable mechanism} \end{cases} \\[2ex]
\bullet\textbf{Controller aim} \begin{cases} \text{Stability (Pitch angle)} \\ \text{Direction (Yaw angle)} \end{cases}
\end{cases}
$$

According to the number of control input and output, both control systems are considered as a multiple input-multiple output (MIMO) system. In this chapter, the CTC, SMC, and SOSMC are used to develop stability and direction control.

5.2 CTC control

5.2.1 Stability and direction control of the conventional system

As there are two control objectives for stability (θ_b) and direction (θ_y) control (see Figure. 3.2), we need to define two control functions of CTC which can be expressed as

$$\ddot{e}_1 + K_{d_1}\dot{e}_1 + K_{p_1}e_1 + K_{i_1}\int e_1 dt = 0 \tag{5.1}$$

$$\ddot{e}_2 + K_{d_2}\dot{e}_2 + K_{p_2}e_2 + K_{i_2}\int e_2 dt = 0 \tag{5.2}$$

Tracking errors are defined through

$$e_1 = \theta_b - \theta_{b_d}, \qquad e_2 = \theta_y - \theta_{y_d}.$$

Where θ_{y_d} is the desired value of yaw angle. Therefore, Eqs. (5.1) and (5.2) can be rewritten as

$$\ddot{\theta}_b - \ddot{\theta}_{b_d} + K_{d_1}(\dot{\theta}_b - \dot{\theta}_{b_d}) + K_{p_1}(\theta_b - \theta_{b_d}) + K_{i_1}\int(\theta_b - \theta_{b_d})dt = 0 \tag{5.3}$$

$$\ddot{\theta}_y - \ddot{\theta}_{y_d} + K_{d_2}(\dot{\theta}_y - \dot{\theta}_{y_d}) + K_{p_2}(\theta_y - \theta_{y_d}) + K_{i_2}\int(\theta_y - \theta_{y_d})dt = 0 \tag{5.4}$$

where

$$\theta_{b_d} = 0 \qquad \dot{\theta}_{b_d} = 0 \qquad \ddot{\theta}_{b_d} = 0$$

Considering Eqs. (3.15), (3.17), (5.3), and (5.4), there is

$$A_{c_3} + B_{c_3} + \hat{M}_{c31}^{-1}\tau_r + \hat{M}_{c32}^{-1}\tau_l = -K_{d_1}\dot{\theta}_b - K_{p_1}\theta_b - K_{i_1}\int\theta_b dt \tag{5.5}$$

$$\frac{r}{d}[A_{c_1} + B_{c_1} - A_{c_2} - B_{c_2} + (\hat{M}_{c11}^{-1} - \hat{M}_{c21}^{-1})\tau_r + (\hat{M}_{c12}^{-1} - \hat{M}_{c22}^{-1})\tau_l] =$$
$$\ddot{\theta}_{y_d} + K_{d_2}(\dot{\theta}_{y_d} - \dot{\theta}_y) + K_{p_2}(\theta_{y_d} - \theta_y) + K_{i_2}\int(\theta_{y_d} - \theta_y)dt \quad (5.6)$$

B_{c_1}, B_{c_2}, and B_{c_3} contain the disturbance elements and should not be considered in the control input. From Eqs. (5.5) and (5.6), the input torques of the right and left wheels are calculated as

$$\begin{bmatrix} \tau_r \\ \tau_l \end{bmatrix} = \begin{bmatrix} \hat{M}_{c31}^{-1} & \hat{M}_{c32}^{-1} \\ \hat{M}_{c11}^{-1} - \hat{M}_{c21}^{-1} & \hat{M}_{c12}^{-1} - \hat{M}_{c22}^{-1} \end{bmatrix}^{-1} \begin{bmatrix} F_{c_1} \\ F_{c_2} \end{bmatrix} \quad (5.7)$$

where

$$F_{c_1} = -A_{c_3} - K_{d_1}\dot{\theta}_b - K_{p_1}\theta_b - K_{i_1}\int\theta_b dt$$

$$F_{c_2} = A_{c_2} - A_{c_1} + \frac{d}{r}[\ddot{\theta}_{y_d} + K_{d_2}(\dot{\theta}_{y_d} - \dot{\theta}_y) + K_{p_2}(\theta_{y_d} - \theta_y) + K_{i_2}\int(\theta_{y_d} - \theta_y)dt]$$

5.2.2 Stability and direction control of the proposed system

Considering Eqs. (3.23), (3.25), (5.3), and (5.4), we have

$$A_{p_3} + B_{p_3} + \hat{M}_{p31}^{-1}\tau_r + \hat{M}_{p32}^{-1}\tau_l + \hat{M}_{p34}^{-1}\tau_p = -K_{d_1}\dot{\theta}_b - K_{p_1}\theta_b - K_{i_1}\int\theta_b dt \quad (5.8)$$

$$\frac{r}{d}[A_{p_1} + B_{p_1} - A_{p_2} - B_{p_2} + (\hat{M}_{p11}^{-1} - \hat{M}_{p21}^{-1})\tau_r + (\hat{M}_{p12}^{-1} - \hat{M}_{p22}^{-1})\tau_l + (\hat{M}_{p14}^{-1} - \hat{M}_{p24}^{-1})\tau_p] =$$
$$\ddot{\theta}_{y_d} + K_{d_2}(\dot{\theta}_{y_d} - \dot{\theta}_y) + K_{p_2}(\theta_{y_d} - \theta_y) + K_{i_2}\int(\theta_{y_d} - \theta_y)dt \quad (5.9)$$

To assist the wheels for stability and direction control, the input torque of the movable mechanism is defined as

$$\tau_p = \beta(\tau_r + \tau_l) \tag{5.10}$$

where $\beta > 0$. B_{p_1}, B_{p_2}, and B_{p_3} which are the disturbance elements are removed from the control input. From Eqs. (5.8), (5.9), and (5.10), the control inputs are obtained as

$$\begin{bmatrix} \tau_r \\ \tau_l \\ \tau_p \end{bmatrix} = \begin{bmatrix} \hat{M}^{-1}_{p31} & \hat{M}^{-1}_{p32} & \hat{M}^{-1}_{p34} \\ \hat{M}^{-1}_{p11} - \hat{M}^{-1}_{p21} & \hat{M}^{-1}_{p12} - \hat{M}^{-1}_{p22} & \hat{M}^{-1}_{p14} - \hat{M}^{-1}_{p24} \\ \beta & \beta & -1 \end{bmatrix}^{-1} \begin{bmatrix} F_{p_1} \\ F_{p_2} \\ 0 \end{bmatrix} \tag{5.11}$$

where

$$F_{p_1} = -A_{p_3} - K_{d_1}\dot{\theta}_b - K_{p_1}\theta_b - K_{i_1}\int \theta_b dt$$

$$F_{p_2} = A_{p_2} - A_{p_1} + \frac{d}{r}[\ddot{\theta}_{y_d} + K_{d_2}(\dot{\theta}_{y_d} - \dot{\theta}_y) + K_{p_2}(\theta_{y_d} - \theta_y) + K_{i_2}\int(\theta_{y_d} - \theta_y)dt]$$

5.2.3 Simulation results

In this section, the performances of the TWRW stability and direction control for the conventional and proposed methods through CTC control are simulated and compared. The physical dimensions listed in Table. 4.1 are used for simulation. The control systems are simulated in two cases.

Case 1:

For Case 1, the initial values are set as

$$\theta_{b_0} = 0 \quad \dot{\theta}_{b_0} = 0 \quad \theta_{r_0} = 0 \quad \dot{\theta}_{r_0} = 0 \quad \theta_{l_0} = 0 \quad \dot{\theta}_{l_0} = 0 \quad \theta_{p_0} = 0 \quad \dot{\theta}_{p_0} = 0$$

For stability and direction control through the proposed system, the input torque of the wheels and the movable mechanism are combined to provide the control input, while the added mechanism's input torque is the only input for the stability control. Therefore, in this Chapter, the higher disturbances than those considered in Chapter. 4 are selected.

The motion of the body's CoG and the uncertainty of the body's mass are considered as

$$x_b = \begin{cases} 5 \mid \sin\frac{\pi}{2}(t-5) \mid cm & 5\,s \leq t < 15\,s \\ 0 & \text{elsewhere} \end{cases} \qquad \Delta m_b = 40kg$$

The desired yaw angle and yaw angular velocity are set as

$$\theta_{y_d} = \frac{\pi}{2} rad, \qquad \dot{\theta}_{y_d} = 0.$$

The following controller gains are set for the control system:

$$K_{p_1} = 200, \quad K_{d_1} = 30, \quad K_{i_1} = 0.5, \quad K_{p_2} = 2, \quad K_{d_2} = 3, \quad K_{i_2} = 0.01, \quad \beta = 0.8.$$

Case 2:

For Case 2, the same initial conditions, disturbances, and controller gains chosen in Case 1 are considered, while the desired yaw angle and its velocity are chosen as

$$\theta_{y_d} = \frac{\pi}{4} t\, rad, \qquad \dot{\theta}_{y_d} = \frac{\pi}{4} rad/s.$$

The motion of the body' CoG in Case 1 and Case 2 are depicted in Figure. 4.1.

Figures. 5.2 and 5.3 depict the simulation results of stability and direction control for the conventional and the proposed systems through CTC control in Case 1. The

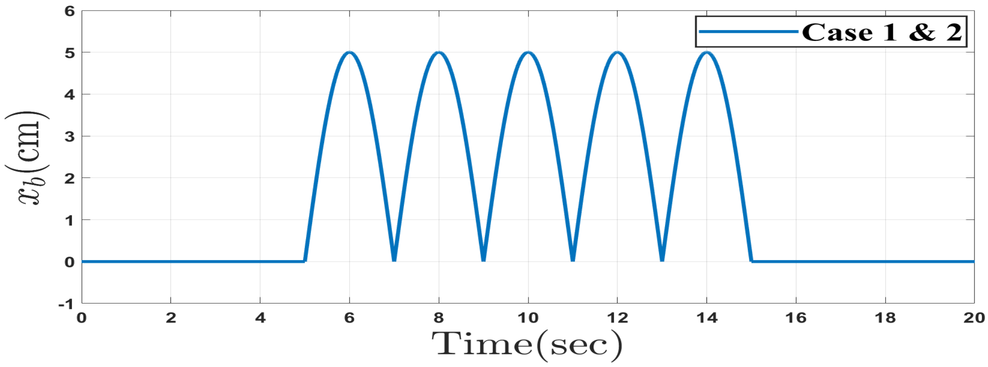

Figure 5.1: The motion of the body's CoG in Case1 and 2 for stability and direction control evaluation.

response of pitch angle and its velocity show that under both control systems, the TWRW can keep its stability as the range of pitch angle and its velocity are acceptable and after a period they converge to zero (see Figures. 5.2a and 5.2b). It can be seen in Figures. 5.2c and 5.2d, that the wheelchair can reach its desired yaw angle and yaw angular velocity. The variation of pitch and yaw angle and their velocities for both control systems are similar. The angular motion of the movable mechanism and its velocity are shown in Figures. 5.2e and 5.2f, respectively. It can be seen that the range of the movable mechanism displacement is small and acceptable.

The required input torque of the right and left wheels are depicted in Figures. 5.3a and 5.3b, respectively. The results show that the required torque through the proposed system is lower than the conventional approach. Similarly, the input power of the wheels in the proposed system is much lower than the conventional one (see Figures. 5.3c and 5.3d). Figures. 5.3e and 5.3f depict the input torque and power needed by the movable mechanism, respectively. It can be seen that they are lower than those needed by the right and left wheels.

Figures. 5.4 and 5.5 show the response of the system in Case 2. The TWRW under both control systems have the similar performance depicted in Case 1. The energy consumption of the motors in Case 1 and Case 2 can be found in Table. 5.1. It can be seen that the energy consumption of the right and left wheels in the proposed system are much lower than that of the conventional method. Furthermore, the energy consumption of the movable mechanism is very small and can be neglected. Therefore, the overall energy consumption in the proposed approach is much lower than the conventional one.

Table 5.1: Energy consumption of the conventional and the proposed system through CTC control for TWRW stability and direction control.

Energy consumption	Right wheel	Left wheel	movable mechanism	overall
Case 1				
Conventional system	1371 J	1370.90 J		2741.90 J
Proposed system	511.53 J	511.50 J	95.33 J	1118.36 J
Case 2				
Conventional system	1201.10 J	1368.40 J		2569.50 J
Proposed system	418.68 J	528.98 J	91.67 J	1039.33 J

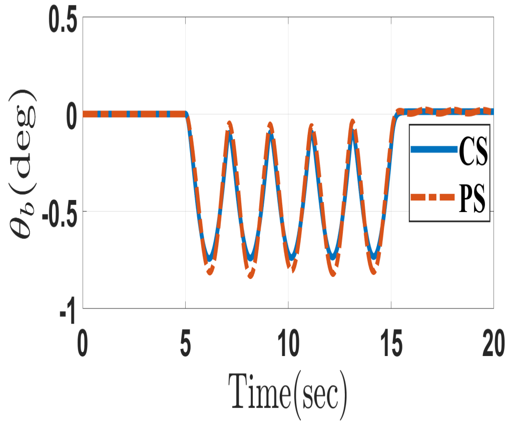

(a): Pitch angle

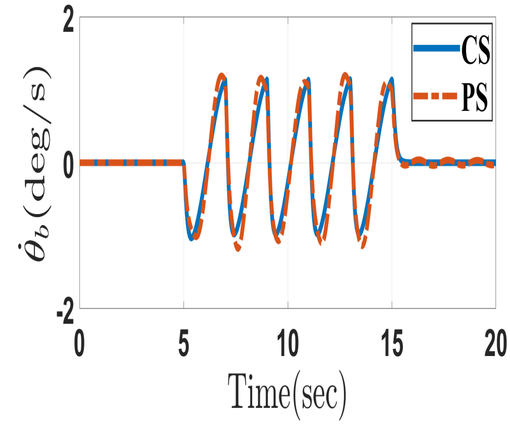

(b): Pitch angular velocity

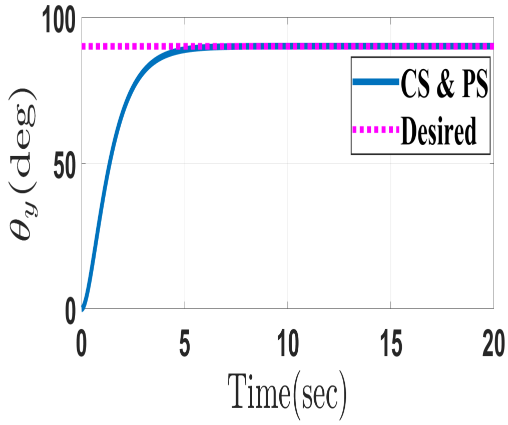

(c): Yaw angle

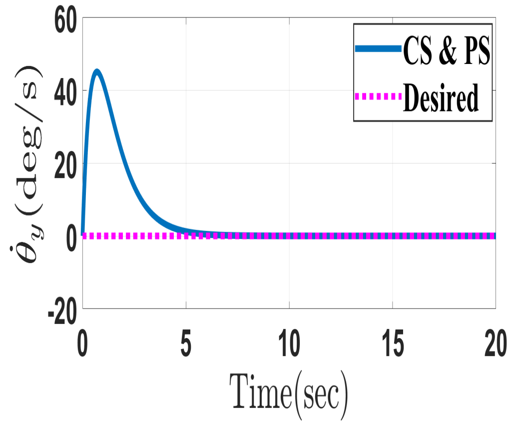

(d): Yaw angular velocity

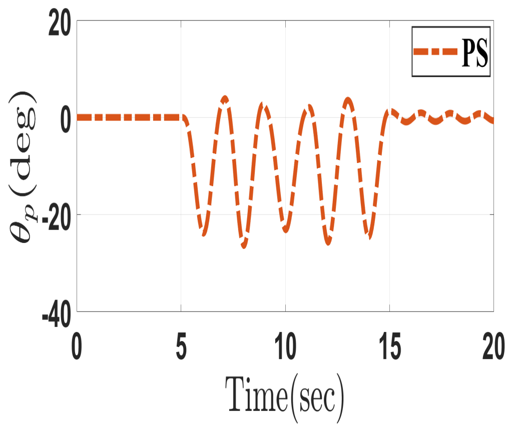

(e): Movable mechanism angle

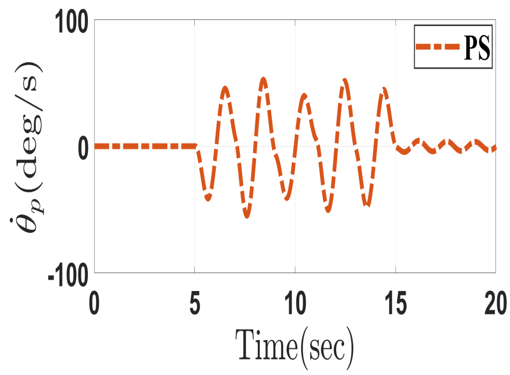

(f): Movable mechanism angular velocity

Figure 5.2: The TWRW stability and direction control response for the conventional system (CS) and proposed system (PS) through CTC control in Case 1.

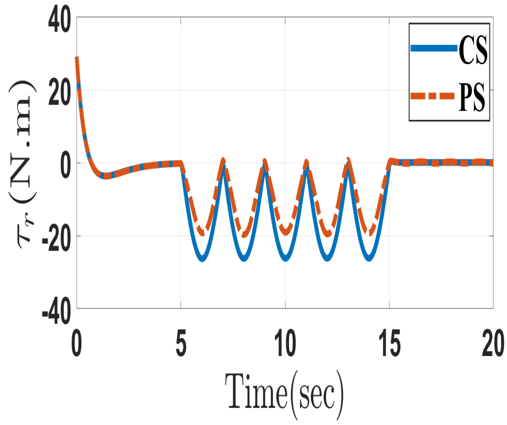

(a): Input torque of right wheel

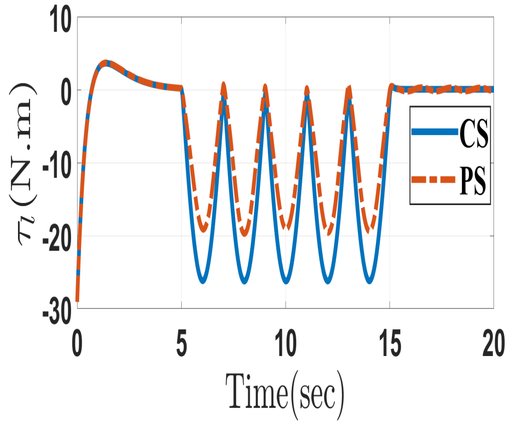

(b): Input torque of left wheel

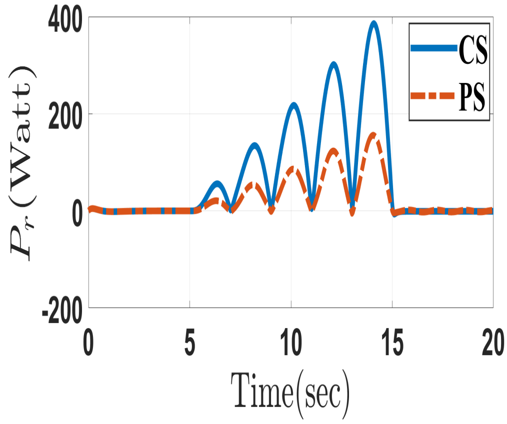

(c): Input power of right wheel

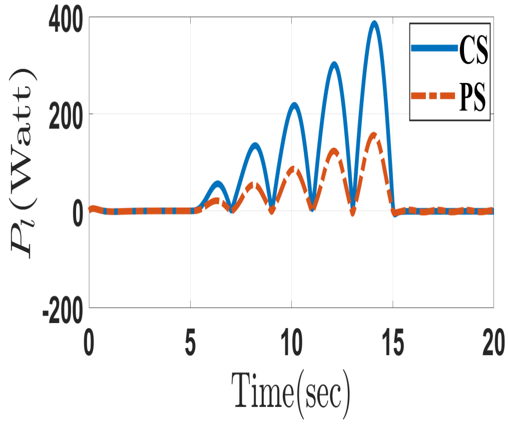

(d): Input power of left wheel

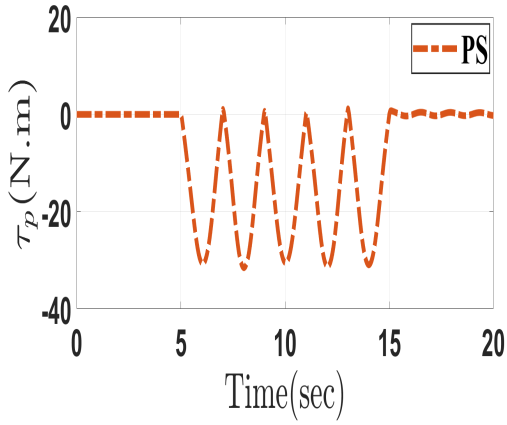

(e): Input torque of movable mechanism

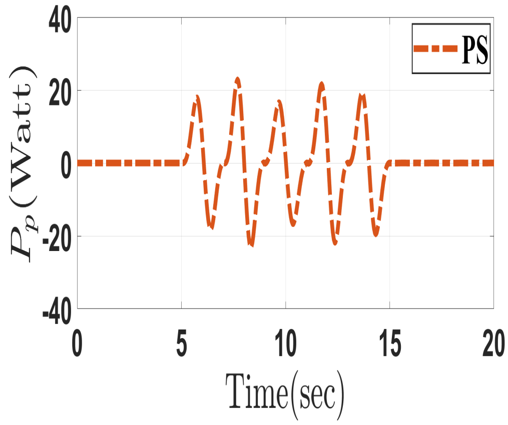

(f): Input power of movable mechanism

Figure 5.3: The control inputs of the TWRW stability and direction control for the conventional system (CS) and proposed system (PS) through CTC control in Case 1.

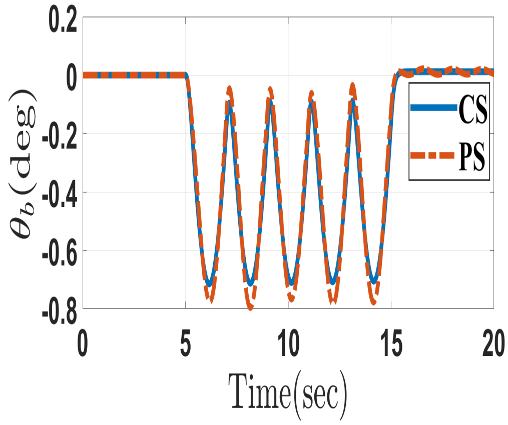

(a): Pitch angle

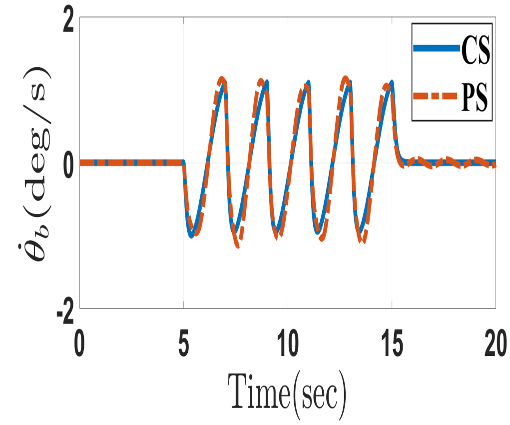

(b): Pitch angular velocity

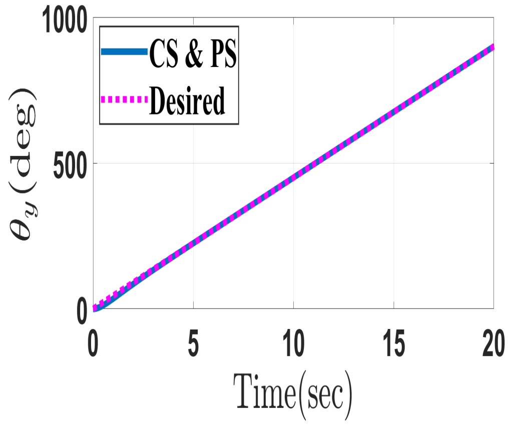

(c): Yaw angle

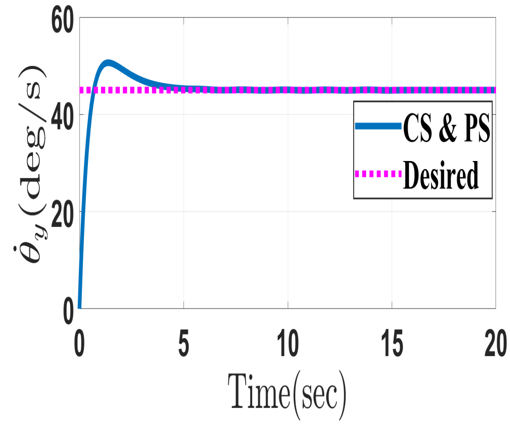

(d): Yaw angular velocity

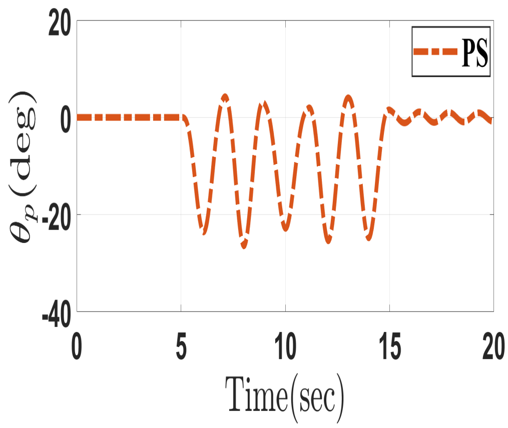

(e): Movable mechanism angle

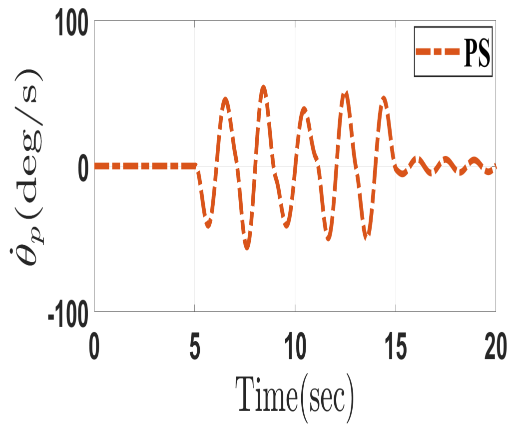

(f): Movable mechanism angular velocity

Figure 5.4: The TWRW stability and direction control response for the conventional system (CS) and proposed system (PS) through CTC control in Case 2.

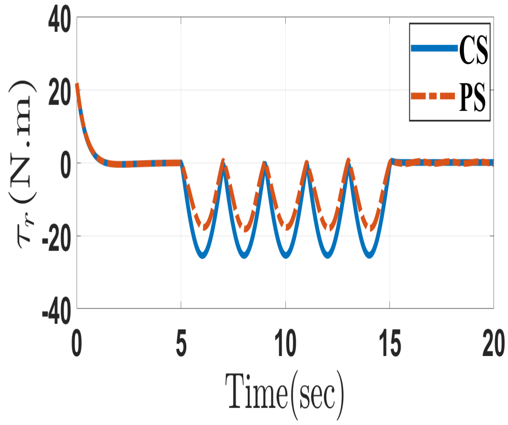

(a): Input torque of right wheel

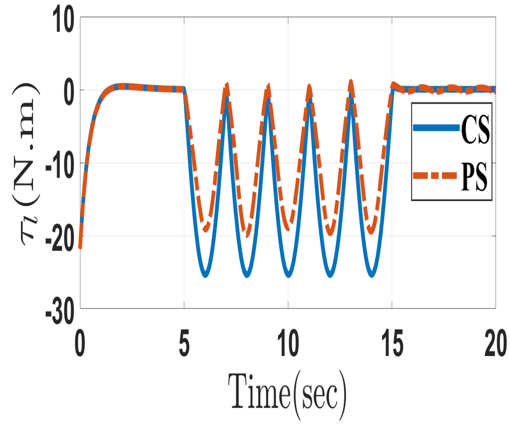

(b): Input torque of left wheel

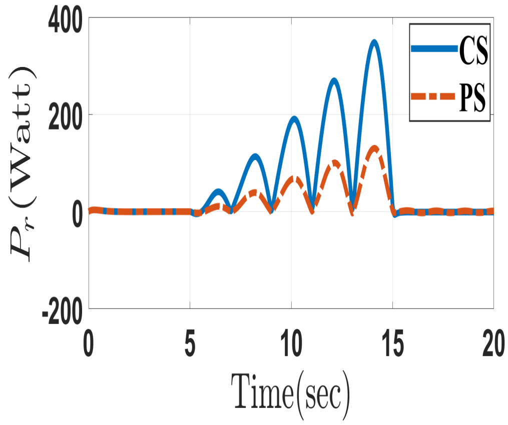

(c): Input power of right wheel

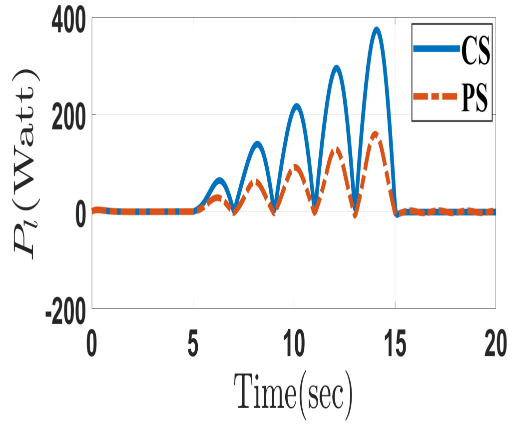

(d): Input power of left wheel

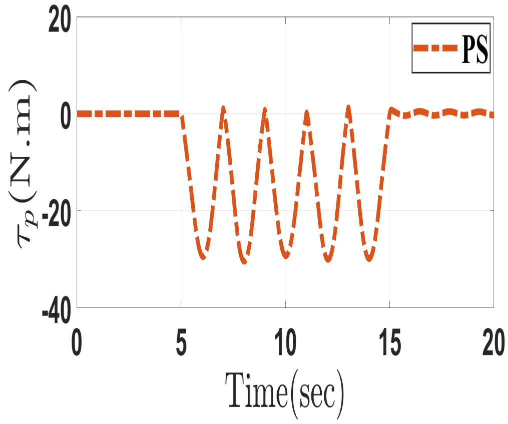

(e): Input torque of movable mechanism

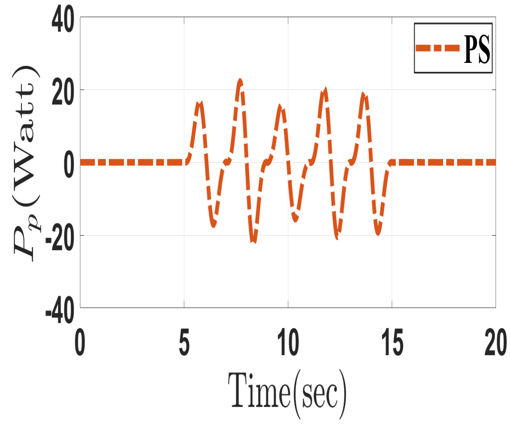

(f): Input power of movable mechanism

Figure 5.5: The control inputs of the TWRW stability and direction control for the conventional system (CS) and proposed system (PS) through CTC control in Case 2.

5.3 SMC control

5.3.1 Stability and direction control of the conventional system

In order to control pitch and yaw angle through the SMC control, a state vector is defined as

$$\mathbf{x} = \begin{bmatrix} x_1 & x_2 & x_3 & x_4 \end{bmatrix}^T$$

where

$$x_1 = \theta_b, \qquad x_2 = \dot{\theta}_b, \qquad x_3 = \theta_y, \qquad x_4 = \dot{\theta}_y.$$

Then,

$$\dot{x}_1 = x_2, \qquad \dot{x}_2 = \ddot{\theta}_b, \qquad \dot{x}_3 = x_4, \qquad \dot{x}_4 = \ddot{\theta}_y. \tag{5.12}$$

Considering Eqs. (3.15), (3.17), and (5.12), there is

$$\dot{x}_1 = x_2, \qquad \dot{x}_2 = A_{c_3} + B_{c_3} + \hat{M}_{c_{31}}^{-1}\tau_r + \hat{M}_{c_{32}}^{-1}\tau_l. \tag{5.13}$$

$$\dot{x}_3 = x_4, \quad \dot{x}_4 = \frac{r}{d}[A_{c_1} + B_{c_1} - A_{c_2} - B_{c_2} + (\hat{M}_{c_{11}}^{-1} - \hat{M}_{c_{21}}^{-1})\tau_r + (\hat{M}_{c_{12}}^{-1} - \hat{M}_{c_{22}}^{-1})\tau_l]. \tag{5.14}$$

The tracking errors are chosen as

$$e_1 = \theta_b - \theta_{b_d}, \qquad e_2 = \dot{\theta}_b - \dot{\theta}_{b_d}, \qquad e_3 = \theta_y - \theta_{y_d}, \qquad e_4 = \dot{\theta}_y - \dot{\theta}_{y_d}.$$

Similar to the Eq. (4.18), there is

$$\dot{e}_1 = e_2, \qquad \dot{e}_2 = u_1 + f_1, \qquad \dot{e}_3 = e_4, \qquad \dot{e}_4 = u_2 + f_2. \tag{5.15}$$

where

$$\mid f_1 \mid \leq L_1 > 0, \qquad \mid f_2 \mid \leq L_2 > 0.$$

Comparing Eqs. (5.13), (5.14), and (5.15), there is

$$u_1 = A_{c_3} + \hat{M}^{-1}_{c31}\tau_r + \hat{M}^{-1}_{c32}\tau_l, \qquad f_1 = B_{c_3}. \tag{5.16}$$

$$u_2 = \frac{r}{d}[A_{c_1} - A_{c_2} + (\hat{M}^{-1}_{c11} - \hat{M}^{-1}_{c21})\tau_r + (\hat{M}^{-1}_{c12} - \hat{M}^{-1}_{c22})\tau_l], \;\; f_2 = \frac{r}{d}(B_{c_1} - B_{c_2}). \tag{5.17}$$

where

$$\theta_{b_d} = 0, \qquad \dot{\theta}_{b_d} = 0, \qquad \ddot{\theta}_{b_d} = 0.$$

Two sliding surfaces are defined as

$$\sigma_1 = e_2 + c_1 e_1, \qquad \sigma_2 = e_4 + c_2 e_3. \tag{5.18}$$

The equivalent control inputs are assumed as

$$u_1 = -c_1 e_2 - \rho_1 \operatorname{sign}(\sigma_1), \qquad u_2 = -c_2 e_4 - \rho_2 \operatorname{sign}(\sigma_2). \tag{5.19}$$

The Lyapanov functions are defined as

$$V_1 = \frac{1}{2}\sigma_1^2, \qquad V_2 = \frac{1}{2}\sigma_2^2. \tag{5.20}$$

The conditions below should be satisfied to provide stability of SMC control.

$$\text{(a)}\;\; \dot{V}_1 < 0 \;\; \text{for} \;\; \sigma_1 \neq 0, \qquad \text{(b)}\;\; \lim_{\sigma_1 \to \infty} V_1 = \infty$$

$$\text{(c)}\;\; \dot{V}_2 < 0 \;\; \text{for} \;\; \sigma_2 \neq 0, \qquad \text{(d)}\;\; \lim_{\sigma_2 \to \infty} V_2 = \infty$$

Condition (b) and (d) are always satisfied by Eq. (5.20). For condition (a) and (c), we have

$$\dot{V}_1 \leq -\alpha_1 V_1^{1/2} = -\frac{\alpha_1}{\sqrt{2}} \mid \sigma_1 \mid, \qquad \dot{V}_2 \leq -\alpha_2 V_2^{1/2} = -\frac{\alpha_2}{\sqrt{2}} \mid \sigma_2 \mid .$$

Where $\alpha_1 \& \alpha_2 > 0$. By differentiating V_1 and V_2, we have

$$\dot{V}_1 = \sigma_1 \dot{\sigma}_1, \qquad \dot{V}_2 = \sigma_2 \dot{\sigma}_2.$$

Where

$$\dot{\sigma}_1 = \dot{e}_2 + c_1 \dot{e}_1 = u_1 + f_1 + c_1 e_2 = -\rho_1 \operatorname{sign}(\sigma_1) + f_1$$

$$\dot{\sigma}_2 = \dot{e}_4 + c_2 \dot{e}_3 = u_2 + f_2 + c_2 e_4 = -\rho_2 \operatorname{sign}(\sigma_2) + f_2$$

Therefore,

$$\dot{V}_1 = \sigma_1 f_1 - \sigma_1 \rho_1 \operatorname{sign}(\sigma_1) \leq - \mid \sigma_1 \mid (\rho_1 - L_1)$$

$$\dot{V}_2 = \sigma_2 f_2 - \sigma_2 \rho_2 \operatorname{sign}(\sigma_2) \leq - \mid \sigma_2 \mid (\rho_2 - L_2)$$

Condition (a) and (c) are satisfied, where

$$\rho_1 = L_1 + \frac{\alpha_1}{\sqrt{2}}, \qquad \rho_2 = L_2 + \frac{\alpha_2}{\sqrt{2}}.$$

Therefore, by selecting $u_1 = -c_1 e_2 - \rho_1 \operatorname{sign}(\sigma_1)$, $u_2 = -c_2 e_4 - \rho_2 \operatorname{sign}(\sigma_2)$, $\rho_1 = L_1 + \frac{\alpha_1}{\sqrt{2}}$, and $\rho_2 = L_2 + \frac{\alpha_2}{\sqrt{2}}$, the controller stability is guaranteed.

Comparing Eqs. (4.24), (5.16), (5.17), and (5.19), τ_r, τ_l are calculated as Eq. (5.7) where

$$F_{c_1} = -A_{c_3} - c_1 \dot{\theta}_b - \rho_1 \frac{\sigma_1}{\mid \sigma_1 \mid + \varepsilon_1}$$

$$F_{c_2} = A_{c_2} - A_{c_1} + \frac{d}{r}[\ddot{\theta}_{y_d} - c_2 e_4 - \rho_2 \frac{\sigma_2}{\mid \sigma_2 \mid + \varepsilon_2}]$$

5.3.2 Stability and direction control of the proposed system

Comparing Eqs. (3.23), (3.25), and (5.12), it leads to

$$\dot{x}_1 = x_2, \qquad \dot{x}_2 = A_{p_3} + B_{p_3} + \hat{M}^{-1}_{p_{31}}\tau_r + \hat{M}^{-1}_{p_{32}}\tau_l + \hat{M}^{-1}_{p_{34}}\tau_p. \tag{5.21}$$

$$\dot{x}_3 = x_4, \quad \dot{x}_4 = \frac{r}{d}[A_{p_1}+B_{p_1}-A_{p_2}-B_{p_2}+(\hat{M}^{-1}_{p_{11}}-\hat{M}^{-1}_{p_{21}})\tau_r+(\hat{M}^{-1}_{p_{12}}-\hat{M}^{-1}_{p_{22}})\tau_l+(\hat{M}^{-1}_{p_{14}}-\hat{M}^{-1}_{p_{24}})\tau_p]. \tag{5.22}$$

From Eqs. (5.15), (5.21), and (5.22), we have

$$u_1 = A_{p_3} + \hat{M}^{-1}_{p_{31}}\tau_r + \hat{M}^{-1}_{p_{32}}\tau_l + \hat{M}^{-1}_{p_{34}}\tau_p, \qquad f_1 = B_{p_3}. \tag{5.23}$$

$$u_2 = \frac{r}{d}[A_{p_1}-A_{p_2}+(\hat{M}^{-1}_{p_{11}}-\hat{M}^{-1}_{p_{21}})\tau_r+(\hat{M}^{-1}_{p_{12}}-\hat{M}^{-1}_{p_{22}})\tau_l+(\hat{M}^{-1}_{p_{14}}-\hat{M}^{-1}_{p_{24}})\tau_p], \;\; f_2 = \frac{r}{d}(B_{p_1}-B_{p_2}). \tag{5.24}$$

Comparing Eqs. (4.24), (5.10), (5.19), (5.23), and (5.24), the input torques are obtained as Eq. (5.11), where

$$F_{p_1} = -A_{p_3} - c_1\dot{\theta}_b - \rho_1\frac{\sigma_1}{\mid \sigma_1 \mid + \varepsilon_1}$$

$$F_{p_2} = A_{p_2} - A_{p_1} + \frac{d}{r}[\ddot{\theta}_{y_d} - c_2 e_4 - \rho_2\frac{\sigma_2}{\mid \sigma_2 \mid + \varepsilon_2}]$$

5.3.3 Simulation results

To simulate the stability and direction control through SMC control, the two cases which are similar to those used for CTC control are assumed. In Case 1 and Case 2, the controller gains are chosen as

$$c_1 = 10, \quad \rho_1 = 500, \quad \epsilon_1 = 0.1, \quad c_2 = 1, \quad \rho_2 = 2, \quad \epsilon_2 = 0.05, \quad \beta = 0.8.$$

Figures. 5.6-5.9 show the simulation results of the TWRW stability and direction control for the conventional and the proposed systems through SMC control in Case 1 and Case 2, respectively. The analysis of the control methods performances are similar to those mentioned in CTC control simulation results (section 5.2.3). Table. 5.2 shows the energy consumption of the motors in Case 1 and Case 2 through SMC control.

Table 5.2: Energy consumption of the conventional and the proposed systems through SMC control for TWRW stability and direction control.

Energy consumption	Right wheel	Left wheel	movable mechanism	overall
Case 1				
Conventional system	1289.80 J	1289.60 J		2579.40 J
Proposed system	476.93 J	476.90 J	89.21 J	1043.04 J
Case 2				
Conventional system	1127.20 J	1290.10 J		2417.30 J
Proposed system	384.76 J	488.01 J	85.57 J	958.34 J

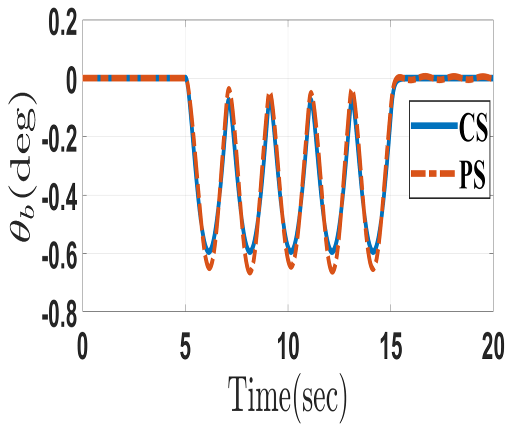

(a): Pitch angle

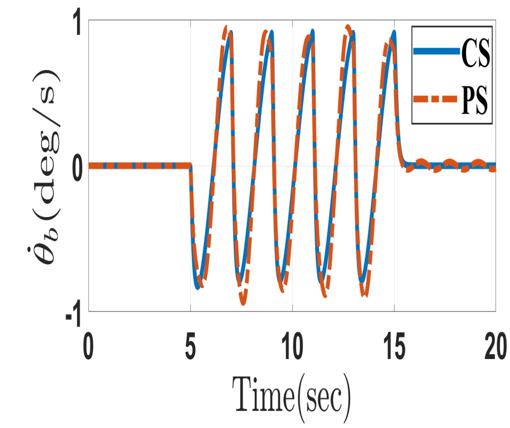

(b): Pitch angular velocity

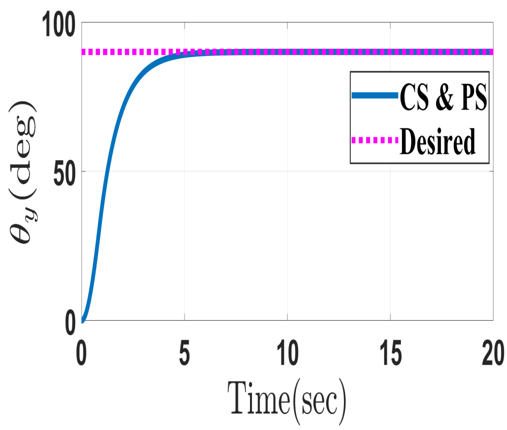

(c): Yaw angle

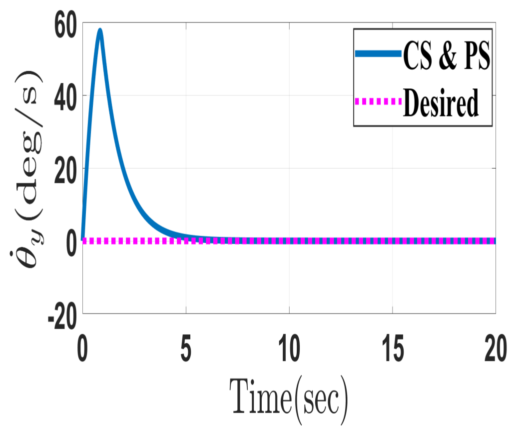

(d): Yaw angular velocity

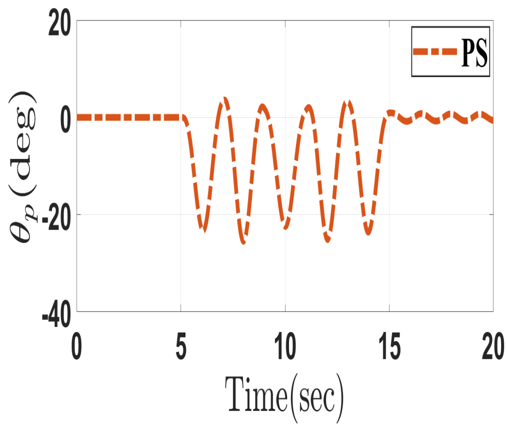

(e): Movable mechanism angle

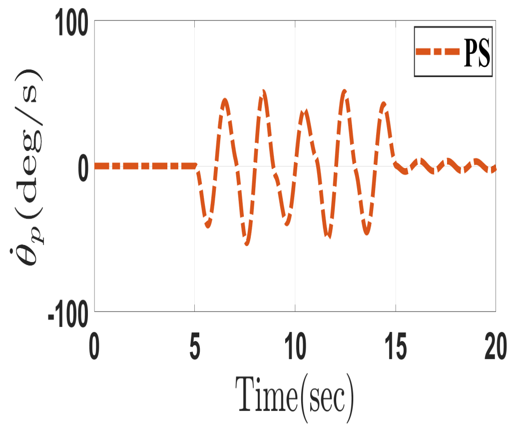

(f): Movable mechanism angular velocity

Figure 5.6: The TWRW stability and direction control response for the conventional system (CS) and proposed system (PS) through SMC control in Case 1.

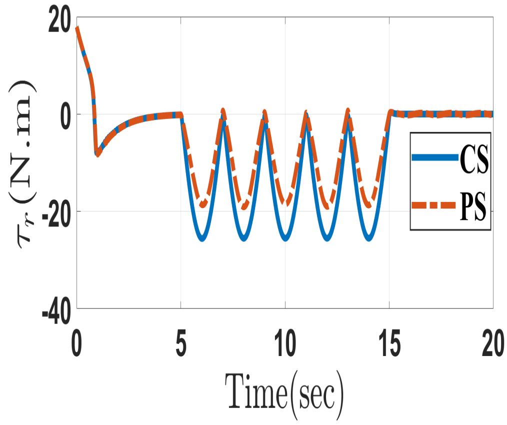

(a): Input torque of right wheel

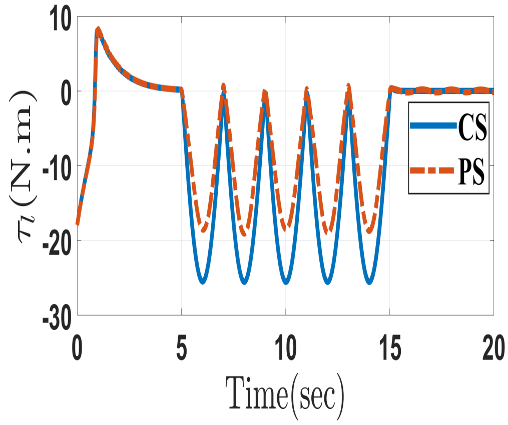

(b): Input torque of left wheel

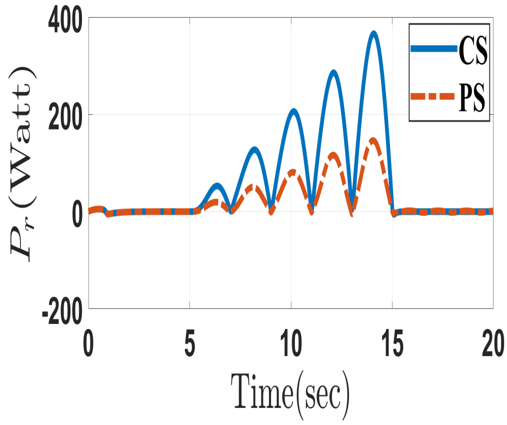

(c): Input power of right wheel

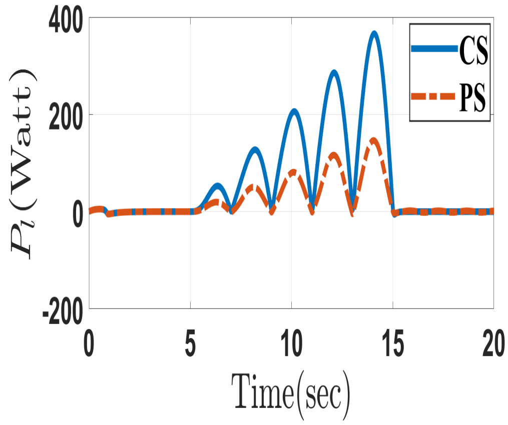

(d): Input power of left wheel

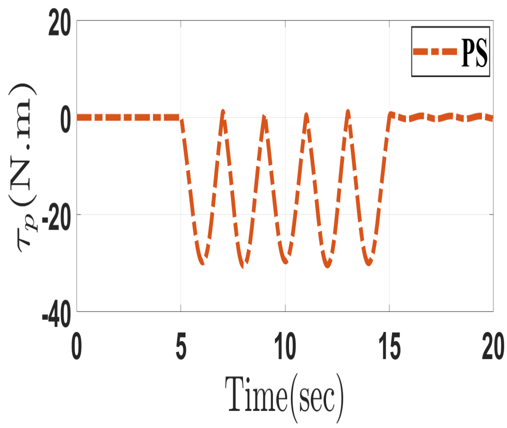

(e): Input torque of movable mechanism

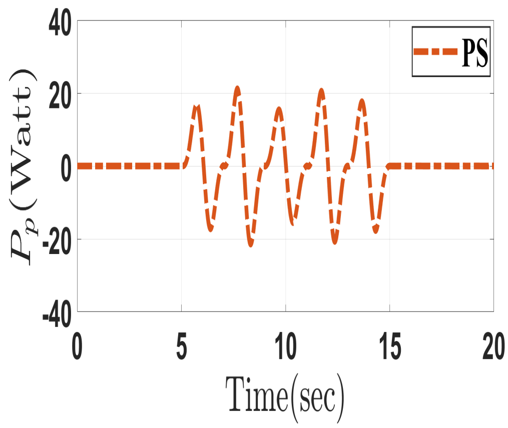

(f): Input power of movable mechanism

Figure 5.7: The control inputs of the TWRW stability and direction control for the conventional system (CS) and proposed system (PS) through SMC control in Case 1.

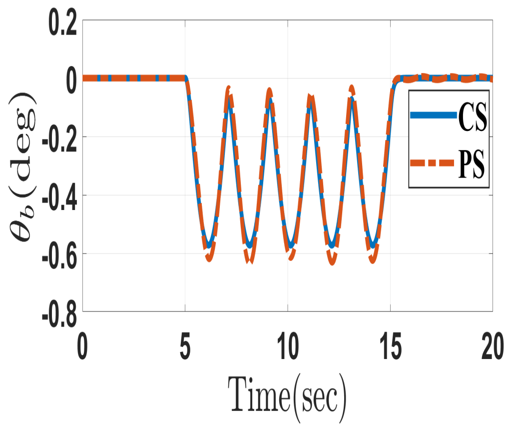

(a): Pitch angle

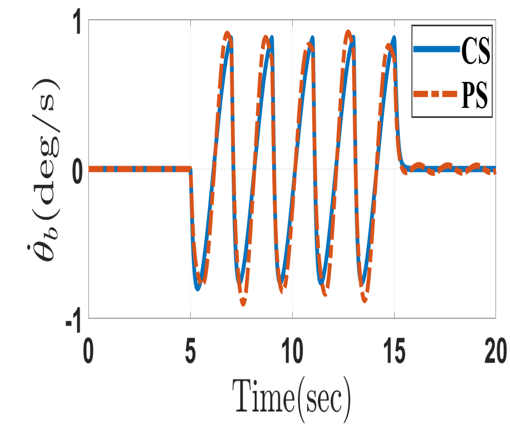

(b): Pitch angular velocity

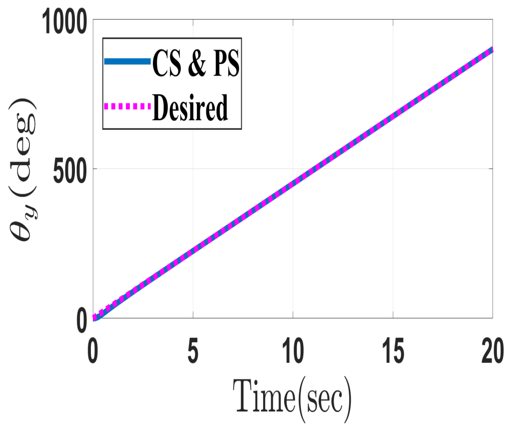

(c): Yaw angle

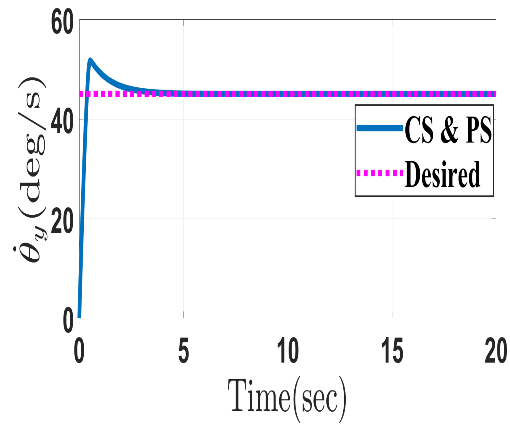

(d): Yaw angular velocity

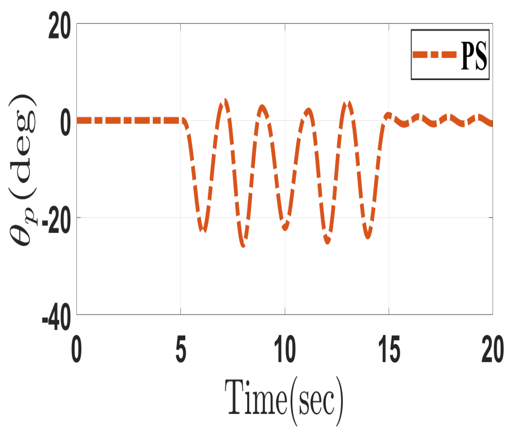

(e): Movable mechanism angle

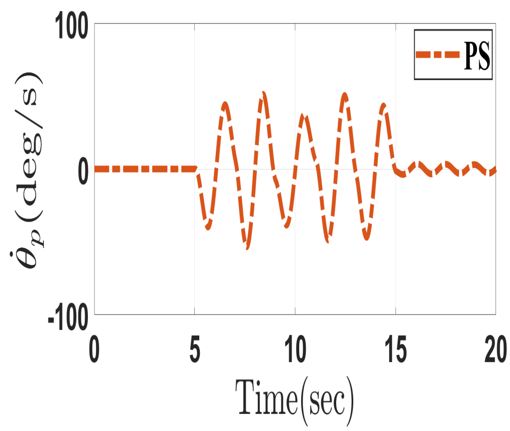

(f): Movable mechanism angular velocity

Figure 5.8: The TWRW stability and direction control response for the conventional system (CS) and proposed system (PS) through SMC control in Case 2.

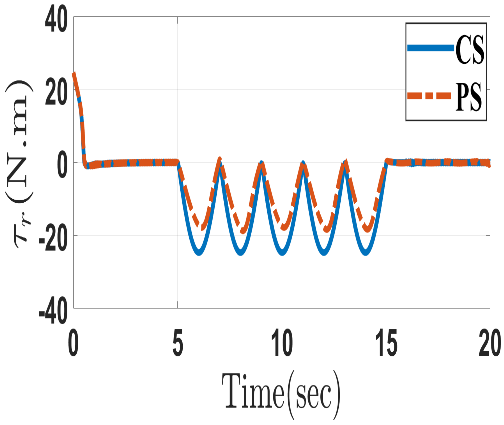

(a): Input torque of right wheel

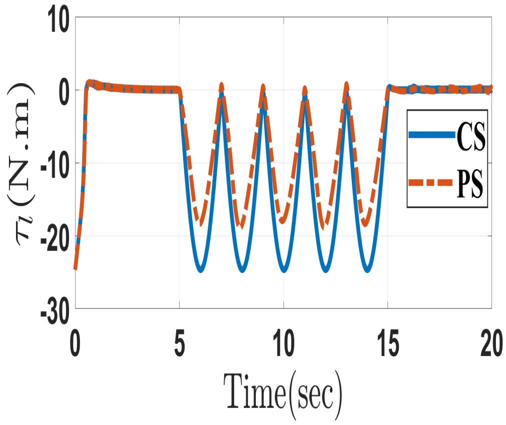

(b): Input torque of left wheel

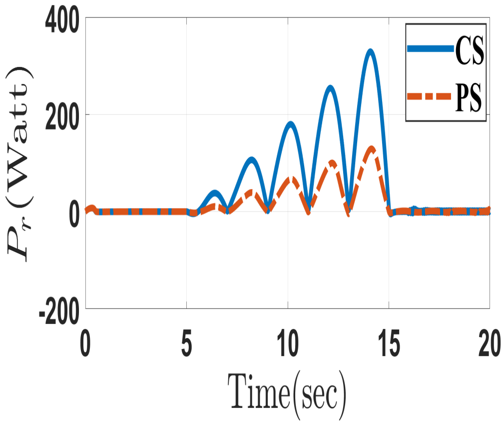

(c): Input power of right wheel

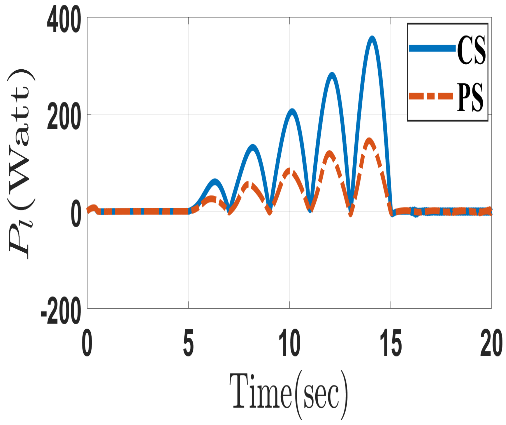

(d): Input power of left wheel

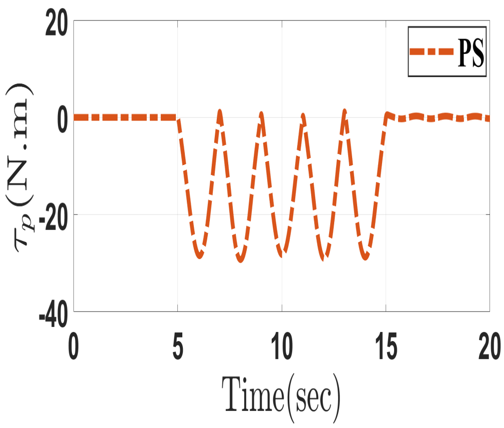

(e): Input torque of movable mechanism

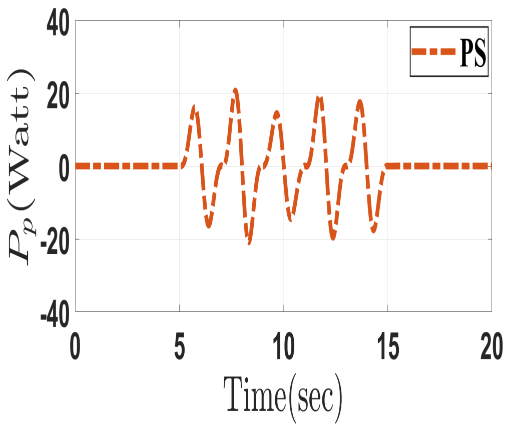

(f): Input power of movable mechanism

Figure 5.9: The control inputs of the TWRW stability and direction control for the conventional system (CS) and proposed system (PS) through SMC control in Case 2.

5.4 SOSMC control

5.4.1 Stability and direction control of the conventional system

To control two parameters including pitch and yaw angle through the SOSMC control, the sliding surface vector is defined as

$$\boldsymbol{\sigma} = \begin{bmatrix} \sigma_1 & \sigma_2 \end{bmatrix}^T, \;\; \sigma_1 = e_2 + c_1 e_1, \;\; \sigma_2 = e_4 + c_2 e_3. \tag{5.25}$$

where

$$e_1 = \theta_b - \theta_{b_d}, \qquad e_2 = \dot{\theta}_b - \dot{\theta}_{b_d}, \qquad e_3 = \theta_y - \theta_{y_d}, \qquad e_4 = \dot{\theta}_y - \dot{\theta}_{y_d}.$$

From Eq. (5.25), we have

$$\dot{\sigma}_1 = \dot{e}_2 + c_1\dot{e}_1 = (\ddot{\theta}_b - \ddot{\theta}_{b_d}) + c_1 e_2, \qquad \dot{\sigma}_2 = \dot{e}_4 + c_2\dot{e}_3 = (\ddot{\theta}_y - \ddot{\theta}_{y_d}) + c_2 e_4. \tag{5.26}$$

where

$$\theta_{b_d} = 0, \qquad \dot{\theta}_{b_d} = 0, \qquad \ddot{\theta}_{b_d} = 0.$$

According to the structure of SOSMC control, we have [213]

$$\dot{\sigma}_1 = u_1 + f_1, \qquad \dot{\sigma}_2 = u_2 + f_2. \tag{5.27}$$

Considering Eqs. (3.15), (3.17), (5.26) and (5.27), there is

$$u_1 = A_{c_3} + \hat{M}_{c_{31}}^{-1}\tau_r + \hat{M}_{c_{32}}^{-1}\tau_l, \qquad f_1 = B_{c_3}. \tag{5.28}$$

$$u_2 = \frac{r}{d}[A_{c_1} + B_{c_1} - A_{c_2} - B_{c_2} + (\hat{M}_{c11}^{-1} - \hat{M}_{c21}^{-1})\tau_r + (\hat{M}_{c12}^{-1} - \hat{M}_{c22}^{-1})\tau_l] - \ddot{\theta}_{y_d} + c_2 e_4,$$
$$f_2 = \frac{r}{d}(B_{c_1} - B_{c_2}). \tag{5.29}$$

The equivalent control inputs u_1 and u_2 are defined as

$$u_1 = -\lambda_1 \mid \sigma_1 \mid^{0.5} \text{sign}(\sigma_1) + \nu_1, \qquad u_2 = -\lambda_2 \mid \sigma_2 \mid^{0.5} \text{sign}(\sigma_2) + \nu_2. \tag{5.30}$$

where

$$\dot{\nu}_1 = \begin{cases} -u_1, & \mid u_1 \mid > U_{M_1} \\ -\alpha_1 \text{sign}(\sigma_1), & \mid u_1 \mid \leq U_{M_1} \end{cases}, \qquad \dot{\nu}_2 = \begin{cases} -u_2, & \mid u_2 \mid > U_{M_2} \\ -\alpha_2 \text{sign}(\sigma_2), & \mid u_2 \mid \leq U_{M_2} \end{cases}.$$

$$\lambda_1 > \sqrt{\frac{2}{(K_{m_1}\alpha_1 - C_1)} \frac{(K_{m_1}\alpha_1 + C_1)K_{M_1}(1+q_1)}{K_{m_1}^2(1-q_1)}}, \qquad \alpha_1 > C_1/K_{m_1}.$$
$$\lambda_2 > \sqrt{\frac{2}{(K_{m_2}\alpha_2 - C_2)} \frac{(K_{m_2}\alpha_2 + C_2)K_{M_2}(1+q_2)}{K_{m_2}^2(1-q_2)}}, \qquad \alpha_2 > C_2/K_{m_2}.$$
$$0 \leq K_{m_1} \leq 1 \leq K_{M_1}, \qquad 0 \leq K_{m_2} \leq 1 \leq K_{M_2}.$$

$$\mid f_1 \mid < q_1 U_{M_1}, \quad 0 < q_1 < 1, \quad \mid f_2 \mid < q_2 U_{M_2}, \quad 0 < q_2 < 1, \quad \mid \dot{f}_1 \mid \leq C_1, \quad \mid \dot{f}_2 \mid \leq C_2.$$

From Eqs. ,(5.28), (5.29), and (5.30), the right and left wheels' torques can be computed as Eq. (5.7), where

$$F_{c_1} = -A_{c_3} - c_1\dot{\theta}_b - \lambda_1 \mid \sigma_1 \mid^{0.5} \text{sign}(\sigma_1) + \nu_1$$

$$F_{c_2} = A_{c_2} - A_{c_1} + \frac{d}{r}[\ddot{\theta}_{y_d} - c_2 e_4 - \lambda_2 \mid \sigma_2 \mid^{0.5} \text{sign}(\sigma_2) + \nu_2]$$

The stability proof of this controller is similar to the method shown in Chapter. (4) for SOSMC control (section 4.5.1).

5.4.2 Stability and direction control of the proposed system

Considering Eqs. (3.23), (3.25), (5.26), and (5.27), it follows that

$$u_1 = A_{p_3} + \hat{M}^{-1}_{p_{31}}\tau_r + \hat{M}^{-1}_{p_{32}}\tau_l + \hat{M}^{-1}_{p_{34}}\tau_p, \qquad f_1 = B_{p_3}. \tag{5.31}$$

$$u_2 = \frac{r}{d}[A_{p_1} - A_{p_2} + (\hat{M}^{-1}_{p_{11}} - \hat{M}^{-1}_{p_{21}})\tau_r + (\hat{M}^{-1}_{p_{12}} - \hat{M}^{-1}_{p_{22}})\tau_l + (\hat{M}^{-1}_{p_{14}} - \hat{M}^{-1}_{p_{24}})\tau_p] - \ddot{\theta}_{y_d} + c_2 e_4,$$
$$f_2 = \frac{r}{d}(B_{p_1} - B_{p_2}). \tag{5.32}$$

From Eqs. (5.10), (5.30), (5.31), and (5.32), the input torques are calculated through Eq. (5.11), where

$$F_{p_1} = -A_{p_3} - c_1\dot{\theta}_b - \lambda_1 \mid \sigma_1 \mid^{0.5} \text{sign}(\sigma_1) + \nu_1$$

$$F_{p_2} = A_{p_2} - A_{p_1} + \frac{d}{r}[\ddot{\theta}_{y_d} - c_2 e_4 - \lambda_2 \mid \sigma_2 \mid^{0.5} \text{sign}(\sigma_2) + \nu_2]$$

5.4.3 Simulation results

The stability and direction control through SOSMC control are simulated in two cases which are similar to those used for CTC control. In Case 1 and Case 2, the controller gains below are set for both control systems:

$$c_1 = 1, \quad \lambda_1 = 3, \quad \alpha_1 = 9.9, \quad c_2 = 1, \quad \lambda_2 = 3, \quad \alpha_2 = 9.9, \quad \beta = 0.8.$$

The simulation results of the TWRW stability and direction control through SOSMC control in Case 1 and Case 2 are depicted in Figures. 5.10-5.13, respectively. The comparison between the conventional and the proposed approaches are similar to those discussed in CTC control simulation results (section 5.2.3). The energy consumption of the motors through SOSMC control are listed in Table. 5.3.

Table 5.3: Energy consumption of the conventional and the proposed systems through SOSMC control for TWRW stability and direction control.

Energy consumption	Right wheel	Left wheel	movable mechanism	overall
Case 1				
Conventional system	1053.40 J	1053.30 J		2106.70 J
Proposed system	388.63 J	388.61 J	72.33 J	849.57 J
Case 2				
Conventional system	896.88 J	1043.50 J		1940.38 J
Proposed system	298.23 J	391.06 J	68.87 J	758.16 J

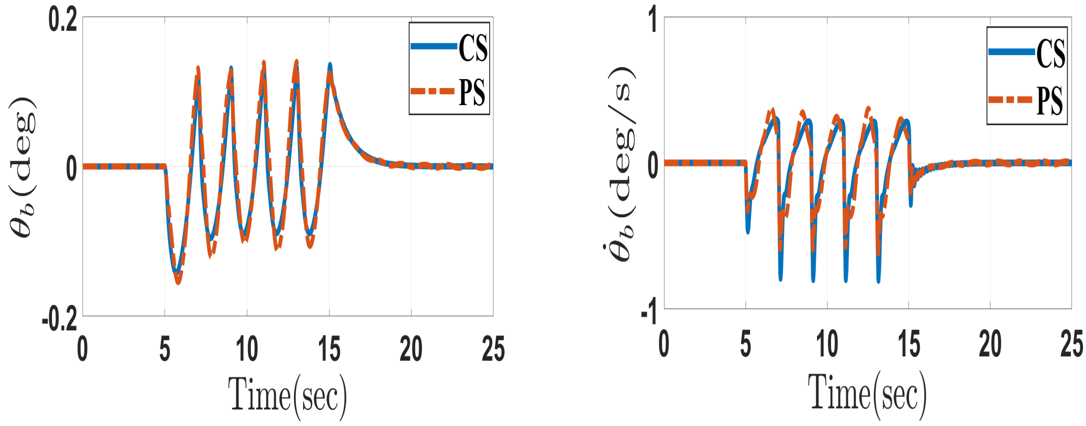

(a): Pitch angle (b): Pitch angular velocity

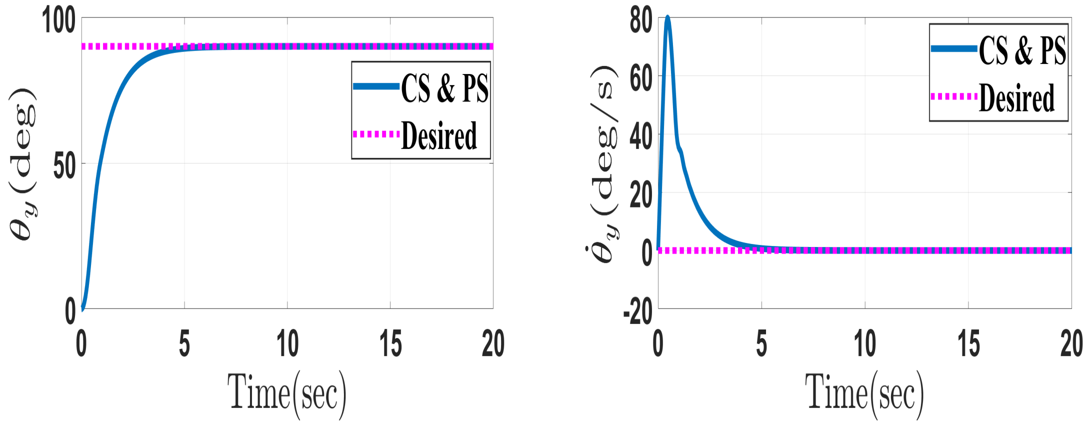

(c): Yaw angle (d): Yaw angular velocity

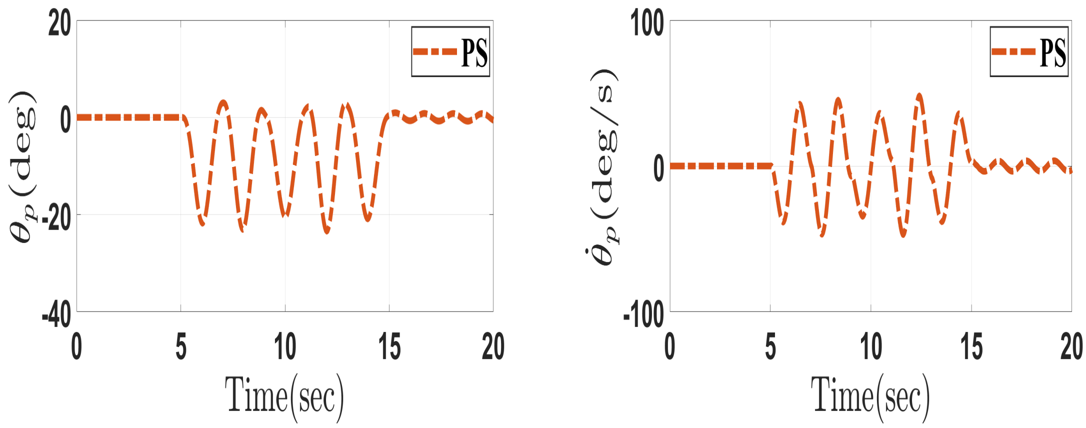

(e): Movable mechanism angle (f): Movable mechanism angular velocity

Figure 5.10: The TWRW stability and direction control response for the conventional system (CS) and proposed system (PS) through SOSMC control in Case 1.

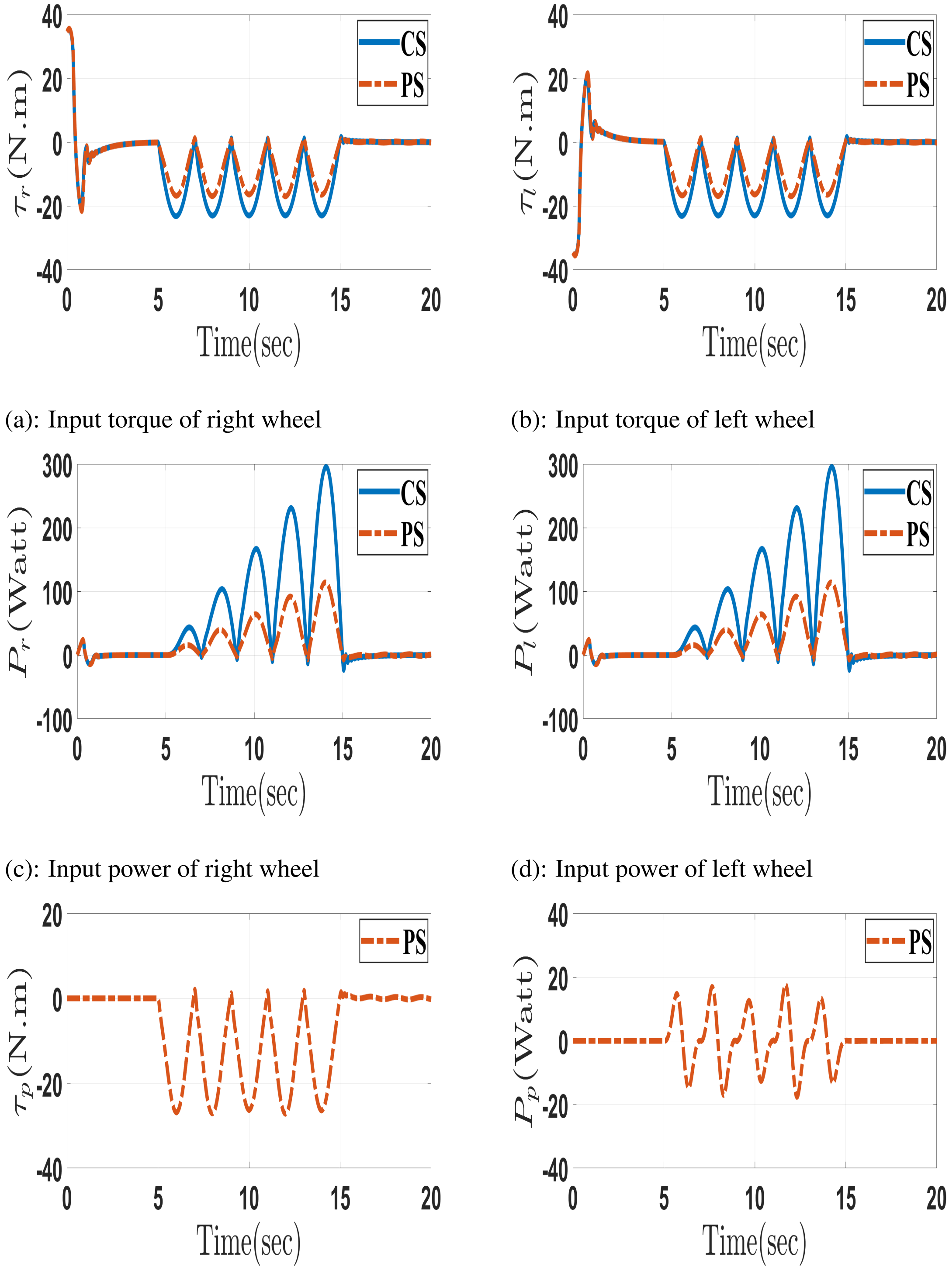

(a): Input torque of right wheel

(b): Input torque of left wheel

(c): Input power of right wheel

(d): Input power of left wheel

(e): Input torque of movable mechanism

(f): Input power of movable mechanism

Figure 5.11: The control inputs of the TWRW stability and direction control for the conventional system (CS) and proposed system (PS) through SOSMC control in Case 1.

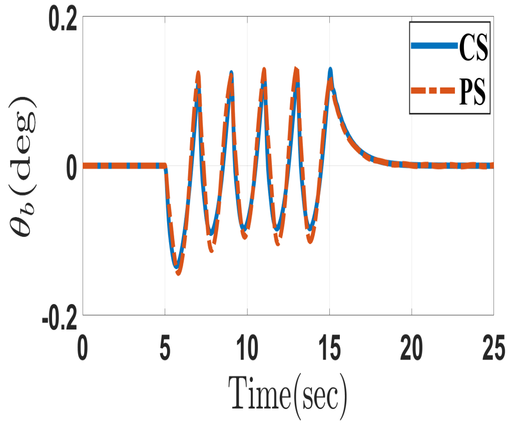

(a): Pitch angle

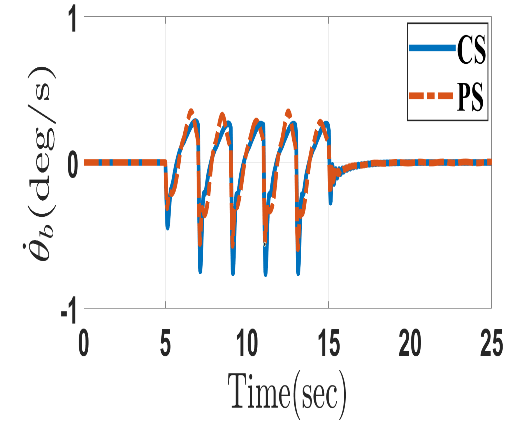

(b): Pitch angular velocity

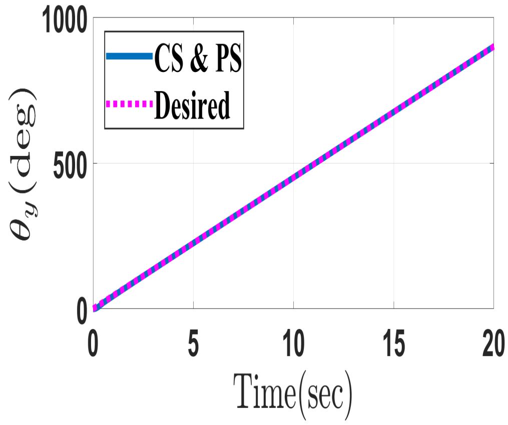

(c): Yaw angle

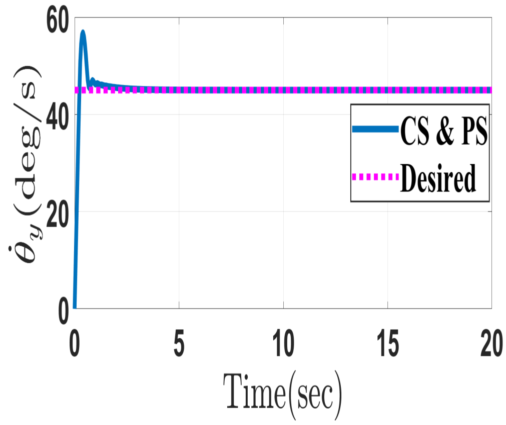

(d): Yaw angular velocity

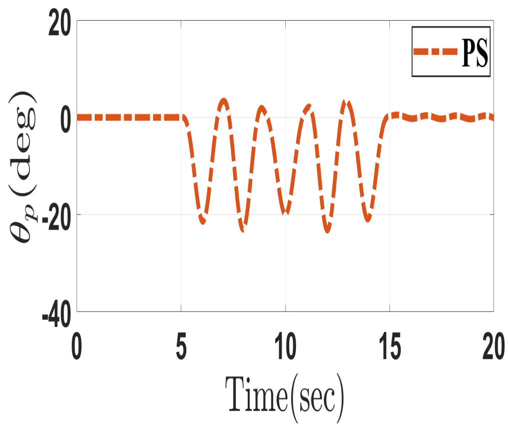

(e): Movable mechanism angle

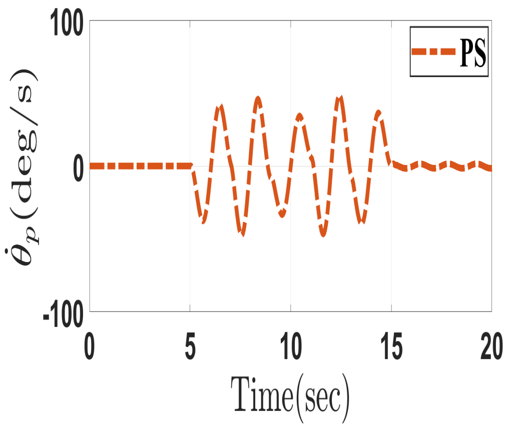

(f): Movable mechanism angular velocity

Figure 5.12: The TWRW stability and direction control response for the conventional system (CS) and proposed system (PS) through SOSMC control in Case 2.

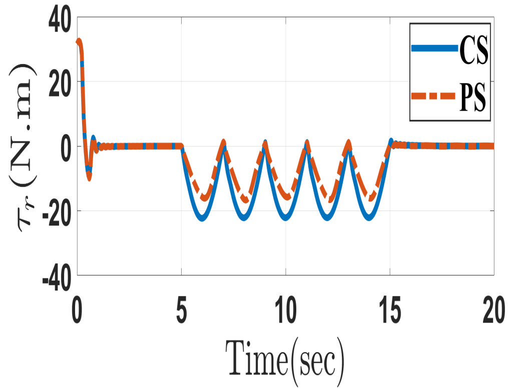

(a): Input torque of right wheel

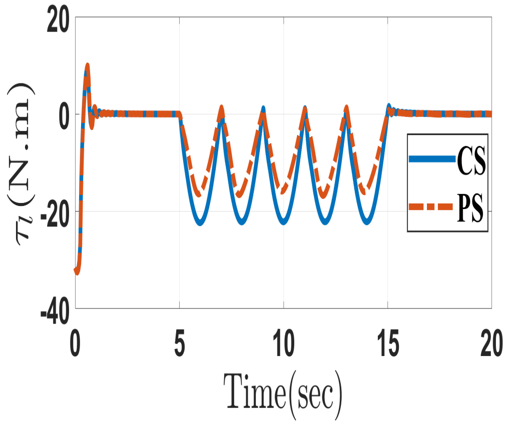

(b): Input torque of left wheel

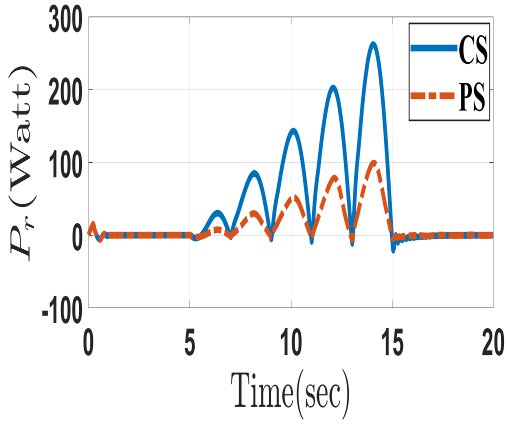

(c): Input power of right wheel

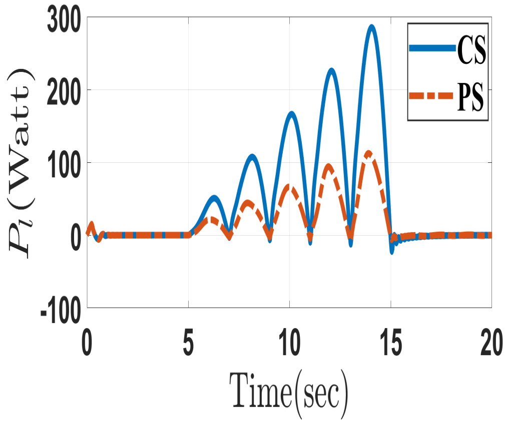

(d): Input power of left wheel

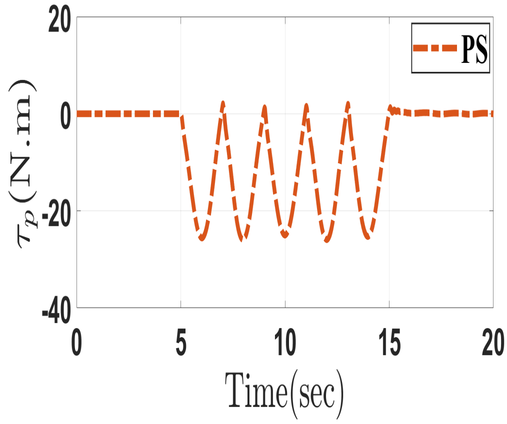

(e): Input torque of movable mechanism

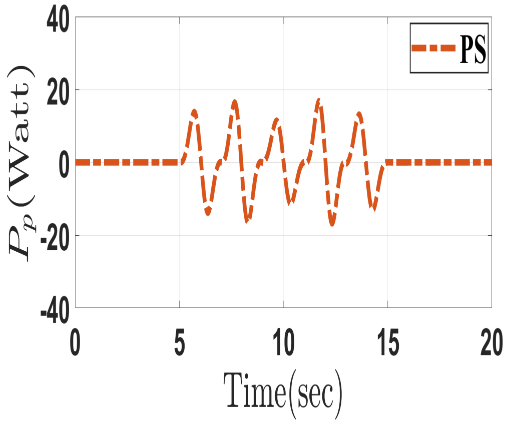

(f): Input power of movable mechanism

Figure 5.13: The control inputs of the TWRW stability and direction control for the conventional system (CS) and proposed system (PS) through SOSMC control in Case 2.

To compare the performance of the control schemes used for TWRW stability and direction control (CTC, SMC, and SOSMC), the simulation results of the proposed system through the above-mentioned control schemes in Case 2 are compared. Figures. 5.14-5.17 show the simulation results of the stability and direction control for the proposed system in Case 2. It can be seen that between $t = 5\,sec$ and $t = 15\,sec$ (when the motion of the body's CoG is considered), the pitch angle and pitch angular velocity obtained from SOSMC control has the smallest deviation from zero (see Figures. 5.14 and 5.15).

Furthermore, the yaw angle response obtained through the SOSMC converges to its desired value faster than the CTC and SMC (see Figure. 5.16). Additionally, when the motion of the body's CoG disturbance is applied, the response of yaw angular velocity in SOSMC has the smallest deviation from the desired value (see Figure. 5.17). It can be concluded that the most optimized and robust controller is achieved through the SOSMC control where the pitch and yaw angles and their velocities have the least deviation from their desired values, while the control inputs of all utilized control schemes are similar.

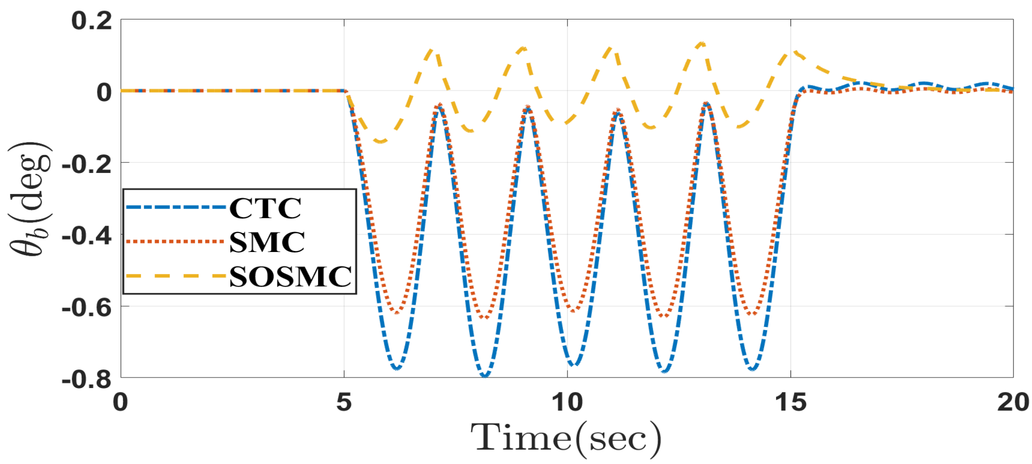

Figure 5.14: The pitch angle response of TWRW stability and direction control for the proposed system through CTC, SMC, and SOSMC in Case 2.

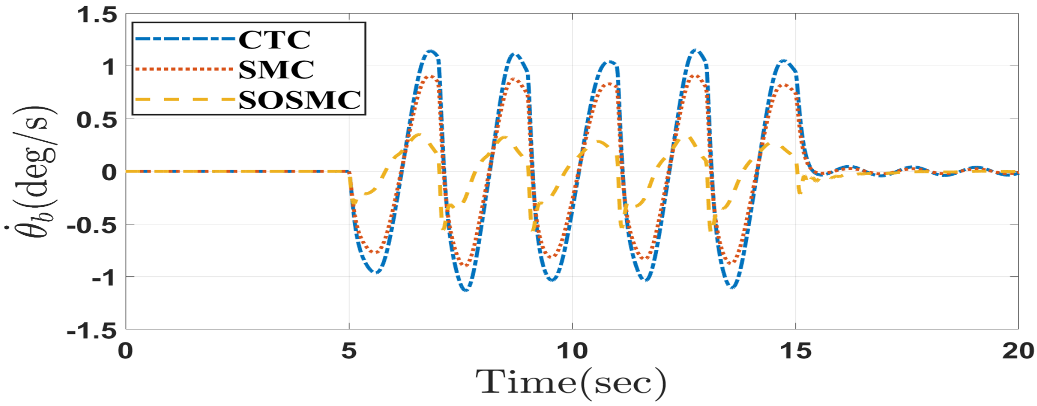

Figure 5.15: The pitch angular velocity response of TWRW stability and direction control for the proposed system through CTC, SMC, and SOSMC in Case 2.

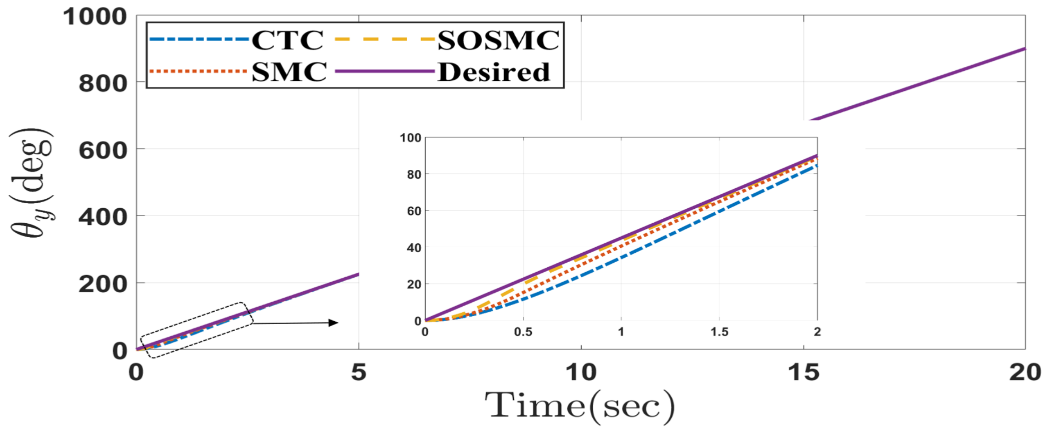

Figure 5.16: The yaw angle response of TWRW stability and direction control for the proposed system through CTC, SMC, and SOSMC in Case 2.

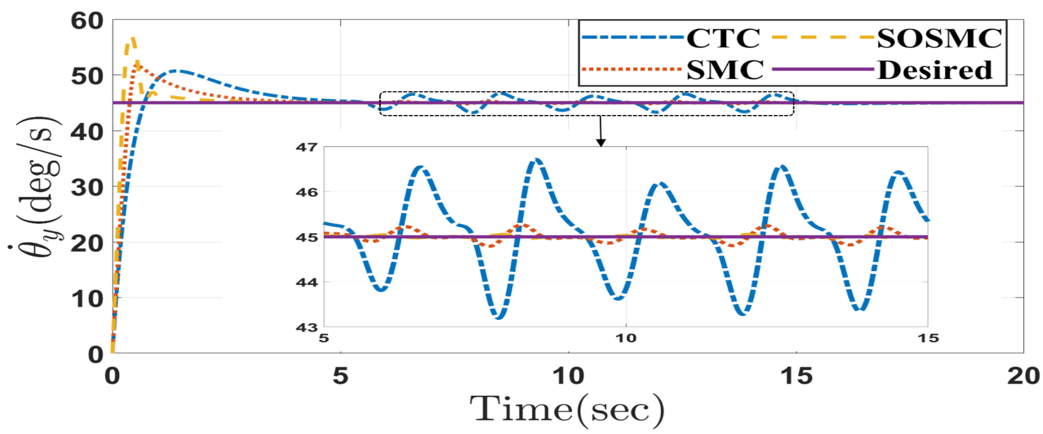

Figure 5.17: The yaw angular velocity response of TWRW stability and direction control for the proposed system through CTC, SMC, and SOSMC in Case 2.

5.5 Summary

In this chapter, the stability and direction control of the TWRW for the conventional and the proposed systems through CTC, SMC, and SOSMC were developed. The controller targets are stability (pitch angle) and direction (yaw angle). The TWRW should follow its desired yaw angle, while the pitch angle should remain zero. In the conventional system, the control inputs are the right and left wheels' torques. Whereas, in the proposed system, the movable mechanism is added to the system to aid the wheels for stability and direction control. Therefore, the number of control inputs for the conventional and proposed systems are two and three, respectively, although the number of control outputs for both control systems are two (pitch and yaw angle).

The development of control systems through CTC, SMC, and SOSMC are similar to the procedures explained in Chapter. 4. The simulation results were presented to assess the stability and direction control performances. Simulation results showed that the TWRW can follow its desired direction and keep its stability under both control systems. However, the required, input torque, input power, and energy consumption in the proposed system are much smaller than the conventional one.

In the next chapter, the experimental setup to model a scaled-down TWRW is explained. The mechanical components and controller devices of system are illustrated. The experimental results provided for the stability control prove the simulation results of Chapter. 4.

Chapter 6

Experimental Evaluation

6.1 Introduction

To confirm the simulation results, an experimental setup should be implemented to demonstrate the superiority of the proposed system over the conventional system. In this chapter, the design and modelling of a scaled-down TWRW is explained. The TWRW prototype comprises two driving wheels and a steel mass to be considered as the body (seat and rider). The movable mechanism is placed under the wheel's axle to assist with the stability control. Due to the time constraints, the experimental results were only obtained for stability control. The experimental results for stability and direction control are not analyzed in this thesis. The performance of the conventional and proposed systems are evaluated for stability control through PID, CTC, SMC, and SOSMC control. These control schemes are modelled in an embedded microcontroller system. The controller's feedback includes pitch angle, pitch velocity, the movable mechanism's angle and its angular velocity which are measured by the IMU sensors. The controller input is computed by the microcontrollers and is sent to the motor controller, so it can run the motors directly.

6.2 TWRW's mechanical components

The TWRW prototype designed in this chapter consists of two driving wheels equipped with brushless direct current (BLDC) motors. The wheels are connected to each other through a steel axle. The axle is lubricated well, which allows the wheels to freely rotate around the axle. Additionally, there is no clearance between the wheels' shafts and the axle. A light steel rod which its mass can be neglected is welded from one end to the middle of the wheels' axle. The $5kg$ steel mass is connected to the rod and placed at the top of the wheels' axle. This mass can be considered as the body (seat and rider) in a full-scaled TWRW. A pendulum-like movable mechanism which comprises a light rod and a $2kg$ steel mass placed at one end of the rod is placed under the wheels' axle and is able to freely rotate by a direct current (DC) motor around the motor's shaft. The input current and voltage of all motors are supplied by a 14 cell lithium battery. Figure. 6.1a and 6.1b show the TWRW prototype in the real and Solidwork models, respectively. The details of each components are explained below.

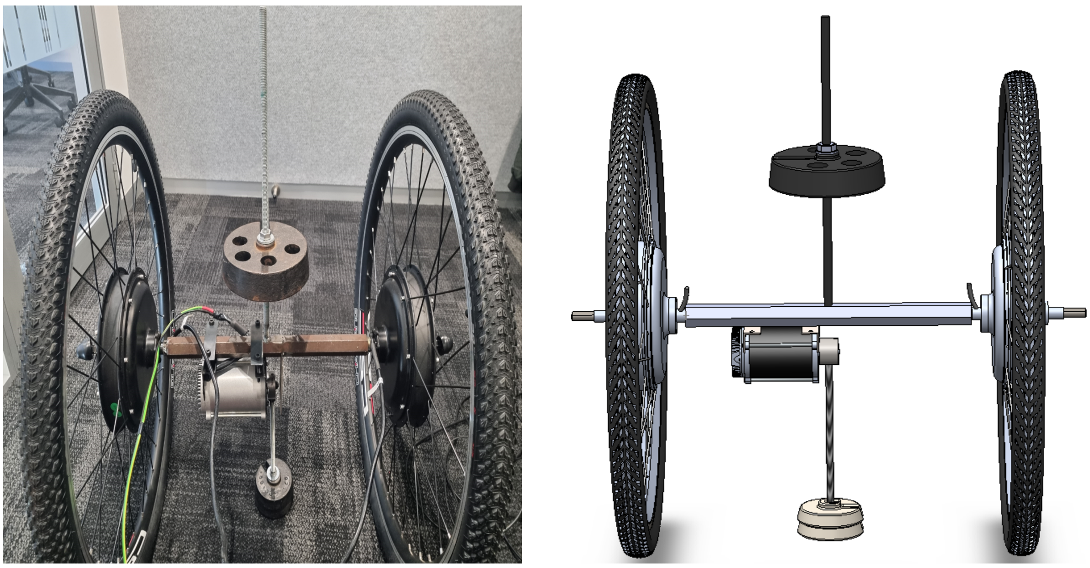

(a): Real model (b): Solidwork

Figure 6.1: The scaled-down model of the TWRW.

6.2.1 Driving wheels specifications

Each wheel is equipped with a BLDC motor. These motors are placed at the centre of each wheel to rotate the wheel's shaft. Figures. 6.2a and 6.2b depict the driving wheel in the real and Solidwork models, respectively. The physical dimensions of both wheels are same and can be found in Table. 6.1.

(a): Real model (b): Solidwork

Figure 6.2: The TWRW's driving wheel.

Table 6.1: Physical dimensions of the TWRW's wheel.

Property	**Symbol**	**Value**	**Unit**
Mass of each wheel	m_{w}	10	kg
Radius of each wheel	r	0.37	m
Length of wheels' axle	d	0.5	m
Moment of inertia of each wheel around its x axis	J_{w_x}	0.32	kg.m^2
Moment of inertia of each wheel around its y axis	J_{w_y}	0.32	kg.m^2
Moment of inertia of each wheel around its z axis	J_{w_z}	0.64	kg.m^2

Figure. 6.3 shows the BLDC motor mounted on the wheels, and its specifications are listed in Table. 6.2. The current and voltage of all TWRW's motors are supplied by a 14 cell lithium battery depicted in Figure. 6.4.

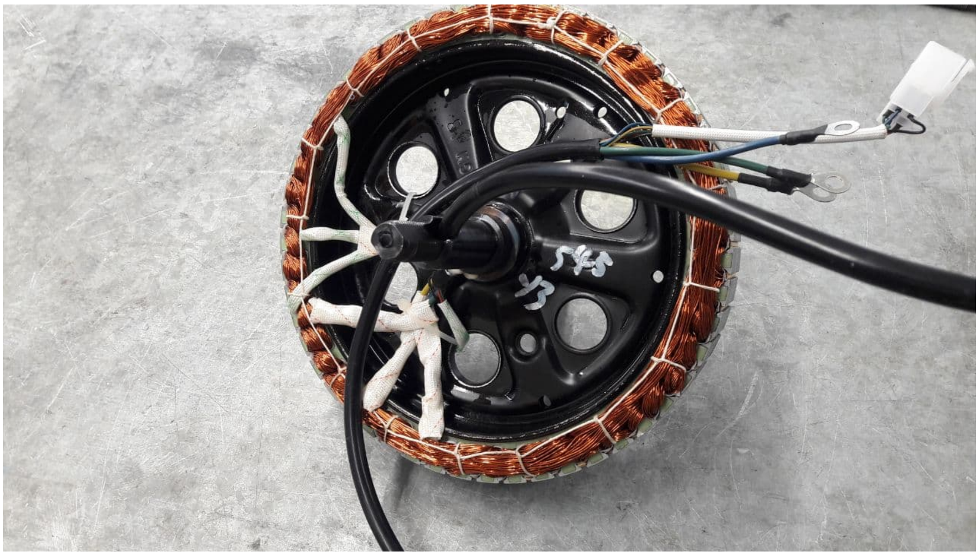

Figure 6.3: The BLDC motor of the TWRW's wheel.

Table 6.2: Motor specifications of the TWRW's driving wheels.

Motor Parameters	**Value**	**Unit**
Motor rating	1500	W
DC supply voltage	48	V
Motor rated current	55	A
Motor rated speed	60	km/h
Torque constant	0.9835	$N.m/A$

Explained in Chapter. 4, the controller input is the input torque of motors, while in the motor controllers there is no option to control the torque. To resolve this problem, the input current can be replaced by the input torque which is one of the control option

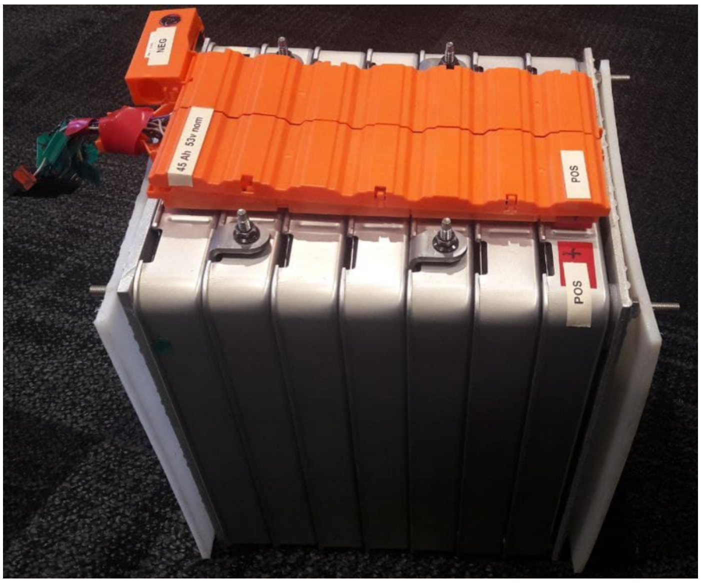

Figure 6.4: The TWRW's 14 cell lithium battery.

of the motor controllers. The input current can be obtained by the Equation below:

$$I = \tau / K_t \tag{6.1}$$

where I, τ, and K_t are the input torque, input current, and torque constant, respectively. As can be seen in Eq. 6.1, the input current can be obtained by dividing the input torque by the torque constant. To measure the torque constant of driving wheels, a torque with a specific value is applied to the wheel and the current which can keep system statically stable is recorded. To provide a torque with a specific value, a mass with a specific weight is hung from one side of the wheel, and the input current is manually set to keep the mass perpendicular to the wheel's axle. Figure. 6.5 depicts the setup to measure the torque constant of the driving wheels. This test should be done with different values of torque to obtain the torque constant more accurately.

Figure. 6.6 represents the torque-current graph, where the y axis is the input torque and x axis is the corresponding input current, where the torque constant is the graph's incline. As the graph is not accurately linear, the average of graph's incline is considered as the torque constant which its value can be found in Table. 6.2.

Figure 6.5: The torque constant measurement setup for the driving wheels.

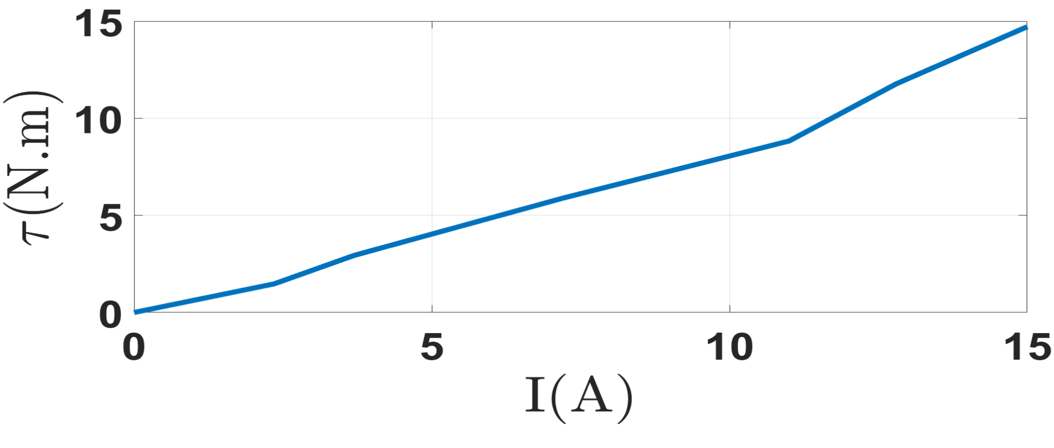

Figure 6.6: The input torque-input current graph of the driving wheel's motor for the torque constant measurement.

6.2.2 Body specifications

A light rod which its mass can be neglected is welded to the the middle of the wheels' axle. A $5kg$ steel mass is connected to the rod and placed at the top of the wheels' axle. This steel mass is assumed as the body which can freely rotate around the wheels' axle. The real and Solidwork models of the body can be seen in Figures. 6.7a and 6.7b, respectively. Table. 6.3 presents the physical dimensions of the body.

(a): Real model

(b): Solidwork

Figure 6.7: The TWRW's body.

Table 6.3: Physical dimensions of the TWRW's body.

Property	**Symbol**	**Value**	**Unit**
Mass of body	m_b	5	kg
Distance between the body's CoG and the middle of wheels axle	l	0.15	kg.m^2
Moment of inertia of body around its x axis	J_{b_x}	0.0182	kg.m^2
Moment of inertia of body around its y axis	J_{b_y}	0.0097	kg.m^2
Moment of inertia of body around its z axis	J_{b_z}	0.0099	kg.m^2

6.2.3 Movable mechanism specifications

The movable mechanism consists of a rod and a mass at one end of the rod. The mass of the rod is small and is neglected. This mechanism is placed under the wheel's axle to keep the body in the upright position. Figure. 6.8a and 6.8b depict the real and Solidwork models of the movable mechanism, respectively. The physical dimensions of the movable mechanism are listed in Table. 6.4.

The motion of the movable mechanism is supplied by a DC motor which its shaft is directly connected to the movable mechanism revolute joint. There is no clearance between the movable mechanism joint and the DC motor's shaft. Figure. 6.9 shows the DC motor used for the movable mechanism motion. The motor specifications are presented in Table. 6.4.

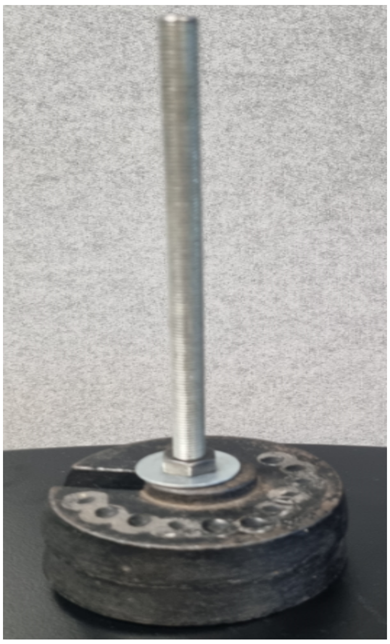

(a): Real model

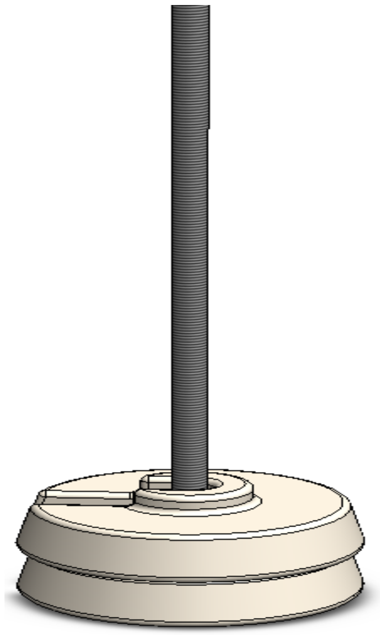

(b): Solidwork

Figure 6.8: The TWRW's movable mechanism.

Table 6.4: Physical dimensions of the TWRW's movable mechanism.

Property	**Symbol**	**Value**	**Unit**
Mass of movable mechanism	m_p	3	kg
Length of the movable mechanism's rod	l'	0.25	m
Distance between the movable mechanism joint and wheel's axle	b	0	m
Moment of inertia of movable mechanism around its x axis	J_{p_x}	0.0024	kg.m^2
Moment of inertia of movable mechanism around its y axis	J_{p_y}	0.0014	kg.m^2
Moment of inertia of movable mechanism around its z axis	J_{p_z}	0.0016	kg.m^2

Figure 6.9: The DC motor of TWRW's movable mechanism.

Table 6.5: Motor specifications of the TWRW's movable mechanism.

Motor Parameters	**Value**	**Unit**
Motor rating	800	W
DC supply voltage	36	V
Motor rated current	27.8	A
Motor rated speed	3000	rpm
Torque constant	0.085	$N.m/A$

A similar method used for the wheel's torque constant measurement is implemented to obtain the torque constant of the movable mechanism's motor. Figure. 6.10 depicts the torque-current graph of the movable mechanism's motor, where the torque constant is the graph's incline.

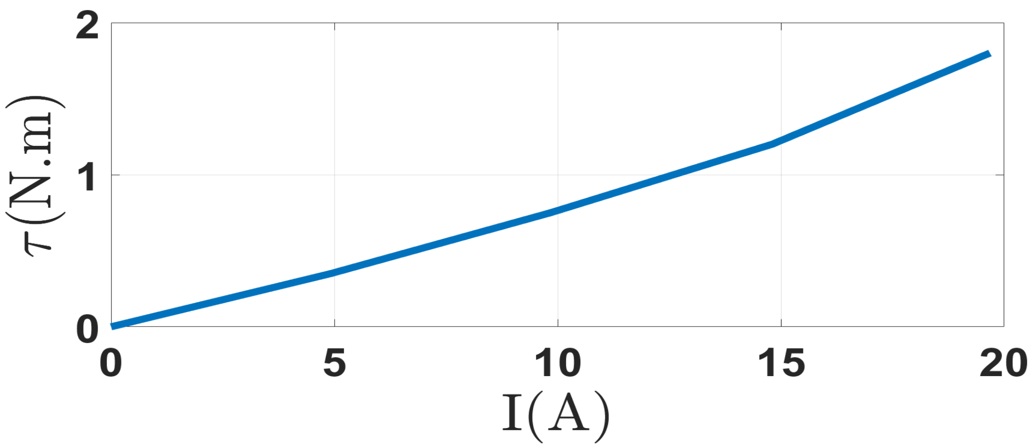

Figure 6.10: The input torque-input current graph of the movable mechanism's motor for the torque constant measurement.

6.3 TWRW's controller devices

To implement the stability control of the TWRW through the various control schemes developed in Chapter. 4, the TWRW's feedback including pitch angle, movable mechanism angle, and their velocities should be obtained. These parameters are obtained using two IMU sensors including VN-200 and MPU6050. According to the feedback values, the input torque of the right and left wheels for the conventional system and the input torque of the movable mechanism for the proposed system are computed. The MyRIO-1900 microcontroller is used to calculate the input torque and send the data to the Arduino mega 2560 by the universal asynchronous receiver/transmitter (UART) signals. The motor controller are not able to control the toque directly, while the current, speed, duty cycle, etc. can be controlled. Therefore, the input torque should transform into the parameters which can be controlled by the motor controller. The input current is chosen as the control parameter, where they are obtained through dividing the input torque by the torque constant. To run the wheels and movable mechanism motors, the input torque are transformed into the input current and they are sent to the motor controllers. The details of controller devices used for the TWRW stability control are illustrated below.

6.3.1 TWRW's IMU sensors

To measure the pitch angle and pitch angular velocity of the TWRW, a VN-200 which is a high accuracy IMU sensor is utilized. The VN-200 is a high performance inertial navigation system and consists of 3-axis gyroscope, accelerometer, and magnetometer. In addition, there is a global navigation satellite systems (GNSS) receivers, and advanced kalman filtering algorithms to measure accurate estimates of position, velocity, and orientation. Figure. 6.11 shows the VN-200 used in the experimental setup. The pitch angle and pitch angular velocity of the TWRW are defined as the body's angle and its angular velocity, respectively. Therefore, the sensor is attached to the body, where one of its axes should be always parallel to the wheels' axle. The angle and angular velocity obtained around this axis show the pitch angle and its velocity, respectively. Figure. 6.12 demonstrates that the position and orientation of the VN-200 attached to the body, which its y axis remains parallel with the wheels' axis when the body moves. This IMU sensor is connected to a personal computer (PC) through a universal serial bus (USB) port to read the sensor output. The LabVIEW block diagram developed by the VN-200 manufacturer (Vectornav) is able to read and plot the angle and angular velocity of the sensor's local coordinate frame with respect to time. The VN-200 specifications can be found in Table. 6.6.

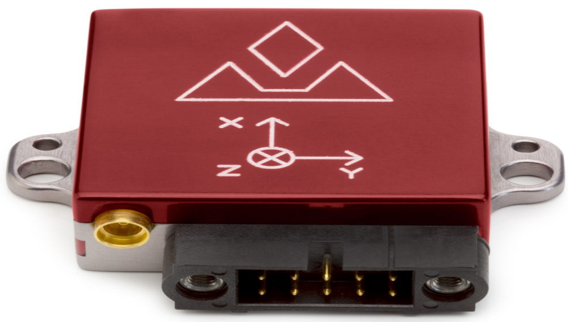

Figure 6.11: VN-200 IMU sensor.

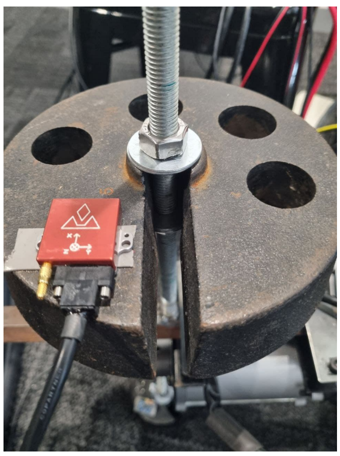

Figure 6.12: VN-200 attached to the body to measure the TWRW's pitch angle and its velocity.

Table 6.6: VN-200 specifications.

VN-200 specifications	Accelerometer	Gyroscope
Range	$\pm 16\,g$	$\pm 2000\,°/s$
In-Run Bias Stability	$< 0.04\,mg$	$< 10\,°/hr$
Non-linearity	$< 0.5\,\%FS$	$100\,ppm$
Cross-axis sensitivity	$\pm 0.05\,°$	$< 0.05\,°$

To measure the angle and angular velocity of the movable mechanism, a MPU6050 IMU sensor is utilized which contains 3-axis gyroscope, accelerometer and a digital motion processor. The accuracy of MPU6050 is not as high as the VN-200, while using a suitable filtering method we can reach the required feedback with an acceptable accuracy. This sensor supports inter-integrated circuit (I^2C) communications on its serial interface. The MPU6050 used in the experimental setup can be seen in Figure. 6.13. similar to the VN-200, the MPU6050 should be attached to the movable mechanism properly, where one of its axis remains parallel to the wheels'axle. Figure. 6.14 depicts the MPU6050 attached to the movable mechanism, where its y axis is always parallel to the wheels' axle. The MPU6050 specifications are listed in Table. 6.7.

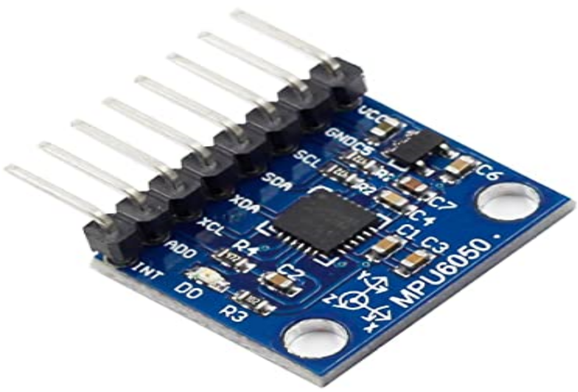

Figure 6.13: MPU6050 IMU sensor.

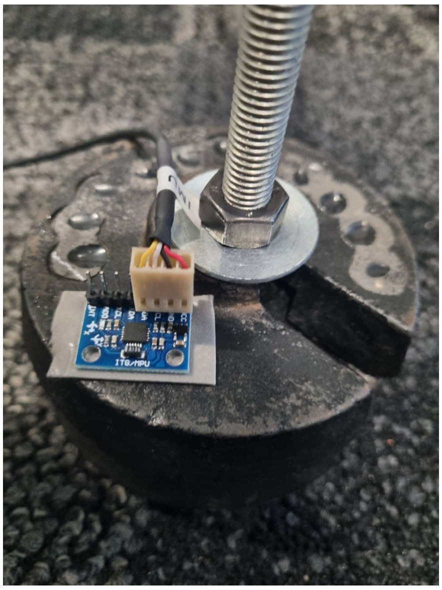

Figure 6.14: MPU6050 attached to the movable mechanism to measure its angle and angular velocity.

Table 6.7: MPU6050 specifications.

MPU6050 specifications	**Accelerometer**	**Gyroscope**
Range	$\pm 8\,g$	$\pm 1000\,°/s$
In-Run Bias Stability	$< 5\,mg$	$< 4°/s$
Non-linearity	$< 0.5\,\%$	$< 0.2\,\%$
Cross-axis sensitivity	$\pm 2\,°$	$\pm 2\,°$

6.3.2 TWRW's microcontrollers

To implement the control schemes developed in Chapter. 4, the MyRIO-1900 which is a real-time embedded microcontroller is used. This microcontroller is manufactured by the National Instruments company which includes 10 analog inputs, six analog outputs, and 40 digital input/output lines. It can connect to a host computer through a USB port or wireless fidelity (WiFi). The IMU sensors output can be read or sent to this microcontroller, which they are used as the control feedback of PID, CTC, SMC, and SOSMC controllers. All required computation to obtain the controllers input are modelled in the MyRIO-1900. The MyRIO-1900 which is shown in Figure. 6.15 can be programmed with LabVIEW.

Figure 6.15: The MyRIO-1900 microcontroller.

To provide the controller input by the MyRIO-1900 and send them to the motor controllers, two type of signals including pulse width modulation (PWM) and UART are commonly used. The maximum frequency of PWM which can be read by the motor controller is 50 Hz. This frequency is very low and not usable for the TWRW which requires a high frequency input to keep the body stable. Whereas, UART signal can be provided with higher frequency than PWM, and its frequency can reach up to 2 MHz. Therefore, the controller input computed by the MyRIO-1900 is provided by the UART signal.

We couldn't find the instruction to send the UART signal by the MyRIO-1900 to control input current through the motor controller (MTVESC50A). However, the instruction to control the current by MTVESC50A through the UART signal of the

Arduino mega 2560 was provided. To resolve this issue, The UART signal of MyRIO-1900 is sent to the Arduino mega 2560. Then, according to the Arduino code provided by the motor controller manufacturer, the input parameter is set as the input current for the motor controller. Arduino mega 2560 depicted in Figure. 6.16 is an open source hardware and software and is used to send the UART signals. This microcontroller comprises sets of digital and analog input/output and it can be programmed using C and C++ programming languages in the Arduino IDE.

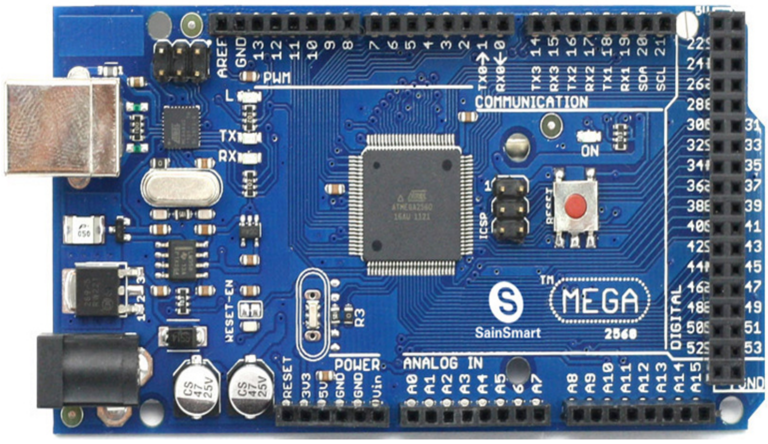

Figure 6.16: Arduino mega 2560 microcontroller.

6.3.3 TWRW's motor controller

The motor controller is a bridge between the microcontrollers and motors. In this project, we use a MTVESC50A which is a programmable motor controller. Through MTVESC50A, the current, speed, etc. of motors can be controlled, where it can be programmed by the VESC Tool open source software. The type of input signal (e.g. PWM, UART, etc.) are set and controlled through the VESC Tool. Figure. 6.17 depicts the MTVESC50A utilized for the TWRW prototype. Also, Figure. 6.18 represents the communication ports of the MTVESC50A.

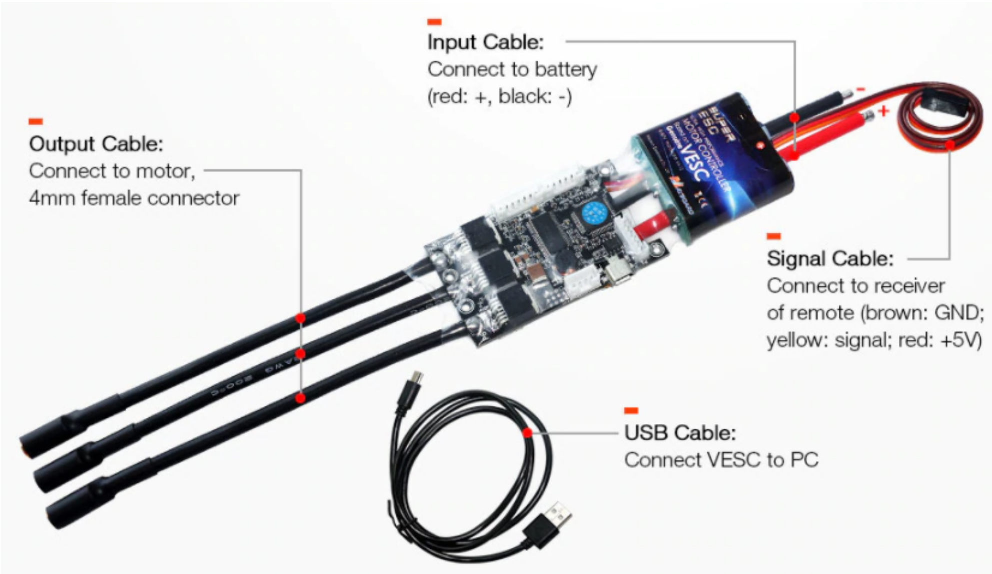

Figure 6.17: The MTVESC50A motor controller

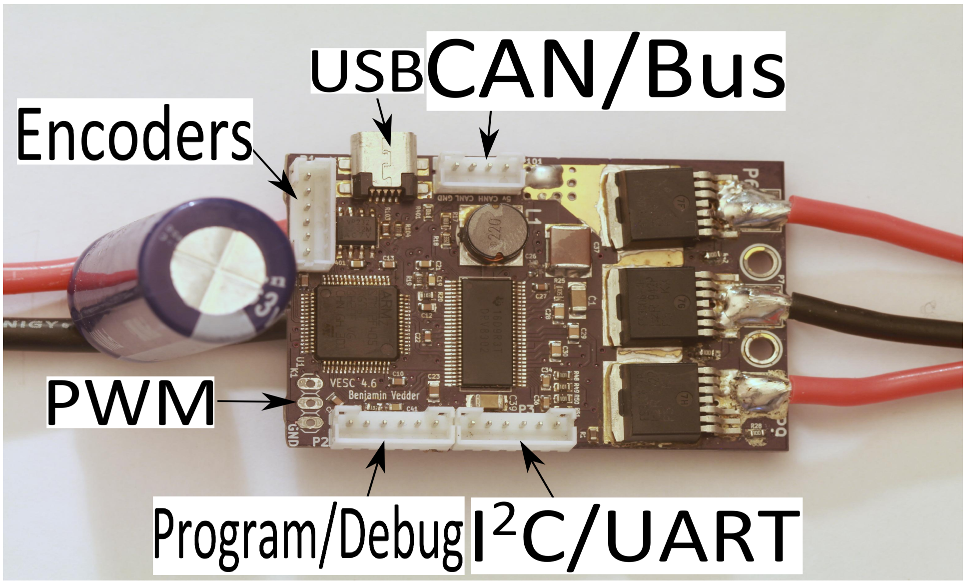

Figure 6.18: The MTVESC50A communication ports

6.4 Controller devices settings

To develop the stability control of the TWRW for the conventional and proposed systems, we need to set the proper setting for each controller devices. The IMU sensors are set to measure the required data and they are read by the MyRIO-1900 microcontroller. In addition, the TWRW's dynamic modelling and the control scheme structures are modelled in the MyRIO-1900. This microcontroller output is the input current which is sent to the Arduino mega 2560 by the UART signals. The proper code is provided by the Arduino IDE to receive the MyRIO-1900 data and set them as the input current. This data is sent to the MTVESC50A motor controller, where the motor controller input signal is set as UART. The details of each controller devices setting are explained below.

6.4.1 VN-200 setting

The pitch angle and pitch angular velocity of the TWRW are obtained though the VN-200. This sensor is connected to the host PC through a USB port. To read the VN-200 output, a LabVIEW block diagram developed by the sensor's manufacturer (VectorNav) are used. Through this block diagram, and attaching the sensor to the body in the proper position and orientation, the pitch and pitch angular velocity are achieved. The block diagram is modified to send the sensor output to the MyRIO-1900. The block diagram designed to read the VN-200 output can be found in Appendix C (see Figure. C.1).

6.4.2 MPU6050 setting

To obtain the angle and angular velocity of the movable mechanism, the MPU6050 is attached to the this mechanism, and send its output to the MyRIO though the I^2C port. To receive the MPU6050 output, a block diagram is developed in LabVIEW, where the accelerations and angular velocities measured from the MPU6050 are filtered through the Kalman Filter. This filter is one of the best known real-time filtering methods used for state estimation.

The angular velocity of the movable mechanism can be measured directly from the filtered output of gyroscope, while the movable mechanism angle is measured by the filtered accelerometer output. As the linear acceleration caused by the movable mechanism motion is small, it can be neglected and the overall acceleration will be solely due to gravity. The schematic view of the movable mechanism acceleration can be seen in Figure. 6.19.

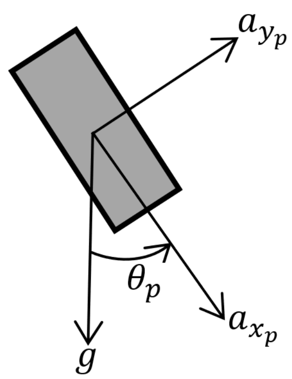

Figure 6.19: The scheme of the movable mechanism acceleration.

a_{x_p} and a_{y_p} are the filtered acceleration of the movable mechanism in x and y axes local frame, respectively. a_{x_p} and a_{y_p} can be obtained as:

$$a_{x_p} = \frac{g}{\cos\theta_p} \qquad a_{y_p} = -\frac{g}{\sin\theta_p} \tag{6.2}$$

From Eq. 6.2, we have

$$\cos\theta_p = \frac{a_{x_p}}{g} \qquad \sin\theta_p = -\frac{a_{y_p}}{g} \tag{6.3}$$

Therefore, θ_p can be obtained as

$$\theta_p = \text{atan2}(-a_{y_p}, a_{x_p})$$

The LabVIEW block diagram designed to obtain the angle and angular velocity of the movable mechanism using the MPU6050 can be found in Appendix C (see Figure. C.2).

To demonstrate the efficiency of the Kalman Filter in noise reduction, the movable mechanism is set on stationary position and its angle and angular velocity are measured by the MPU6050 sensor. The movable mechanism angle measured by the MPU6050 IMU sensor on stationary position without and with Kalman Filter are depicted in Figure. 6.20. Additionally, Figure. 6.21 shows the movable mechanism angular velocity measurement.

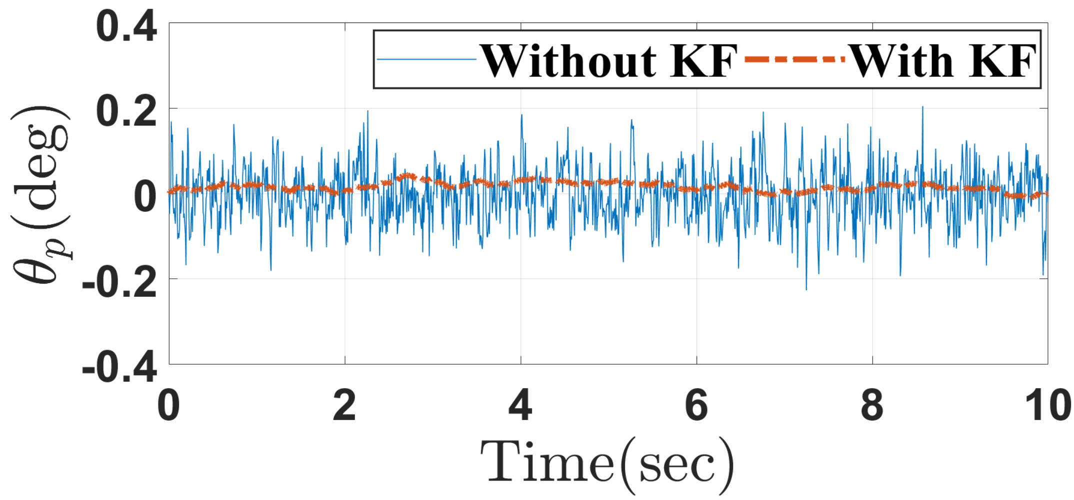

Figure 6.20: The movable mechanism angle measured by the MPU6050 IMU sensor on the stationary position without and with Kalman Filter (KF)

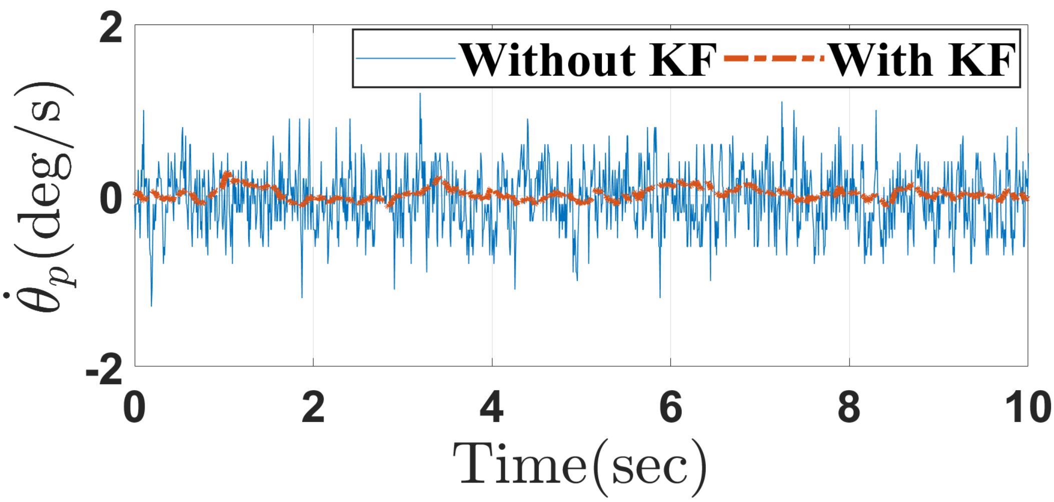

Figure 6.21: The movable mechanism angular velocity measured by the MPU6050 IMU sensor on the stationary position without and with Kalman Filter (KF)

It can be seen that Kalman Filter can significantly decrease the noise of the MPU6050 output and keep the angle and angular velocity of the movable mechanism around zero. Therefore, the MPU6050 output are reliable with the Kalman Filter and can be used to develop the stability control systems.

6.4.3 MyRIO-1900 setting

To implement the stability control schemes for the conventional and proposed systems through PID, CTC, SMC, and SOMSC control, the MyRIO-1900 is utilized. In PID control, the pitch angle and its velocity are multiplied by the controller gains to obtain the input torque. According to the input torque and torque constant of each motor, the input current of motors are computed. The input currents are sent to the Arduino through the UART signals.

For the conventional system developed by the model-based controllers (CTC, SMC, and SOSMC), the pitch angle and pitch velocity are used to obtain the dynamic modelling elements derived in Chapter. 3. In addition to the pitch angle and its velocity, the movable mechanism angle and its velocity are needed to establish the dynamic modelling elements of the proposed system. Considering the dynamic modelling components, controller gains, and the motors' torque constant, the input current of all motors are achieved. Similar to PID control, the input currents are sent to the Arduino through the UART signals.

Figures. C.3-C.6 provided in Appendix C depict the LabVIEW block diagram of the conventional system stability control developed by PID, CTC, SMC, and SOSMC control schemes, respectively. The TWRW's stability control LabVIEW block diagram for the proposed system through PID, CTC, SMC, and SOSMC control schemes are shown in Figures. C.7-C.10 (Appendix C), respectively.

6.4.4 Arduino mega 2560 setting

As there was no instruction to send the MyRIO-1900 output to the motor controller to control current by UART signals directly, we used the Arduino mega 2560 to form a communication between these two devices. The Arduino mega 2560 is one of the most commonly used microcontrollers and there was instructions to send the control input to the motor controller via UART channels. To receive the data from the MyRIO-1900 and set them as the control input and feed them to the MTVESC50A (motor controller), the code designed by the motor controller manufacturer for Arduino IDE is properly modified. The Arduino IDE code devolved to make communication between the MyRIO-1900 and MTVESC50A for the conventional and proposed approaches are shown in Appendix C (see Figures. C.11 and C.12).

6.4.5 MTVESC50A setting

The MTVESC50A motor controller is used to receive the UART signal sent by the Arduino mega 2560. This motor controller is configured by an open source software called VESC Tool, where the motor configurations such as maximum and minmum input current, voltage, speed, and duty cycle are set. In addition, the type of control input signal (e.g. UART, PWM, I^2C, and NRF) can be chosen in VESC tool. For safety measurement, the maximum and minimum input current of each BLDC motors (wheels' motors) are set $20A$ and $-20A$, respectively. Additionally, $1000\,rpm$ and $-1000\,rpm$ are chosen for the maximum and minimum speed, respectively. For the DC motor (movable mechanism's motor), the maximum and minimum current are set to $40A$ and $-40A$, respectively, and the speed ranges are similar to the BLDC motors. As the Arduino output are provided via the UART signals, the control input signal in VESC tool is chosen as UART. Figure. 6.22 depicts the VESC tool setting configured for the control input.

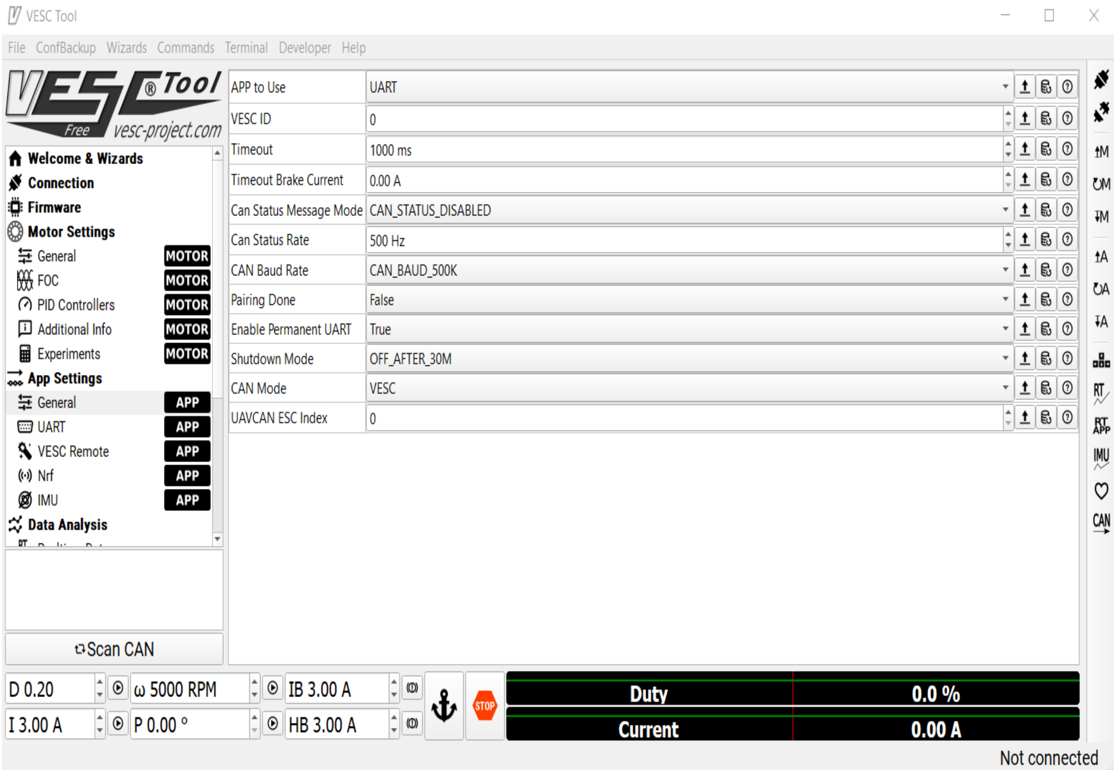

Figure 6.22: The VESC tool setting for the motor controller input configuration.

6.5 Experimental Results

To demonstrate the superiority of the proposed method over the conventional one and verify the simulation results obtained in Chapter. 4, the scaled-down TWRW prototype are experimentally tested. The physical dimensions of the experimental model are listed in Table. 6.8. To analyze the performance of the stability control for the conventional and proposed systems, the TWRW prototype is tested under two cases. As applying the disturbance with specific value to the model is a complicated procedure and requires advanced equipment, the model is only tested with non-zero initial condition. In these cases, the pitch angle is set to a desired initial angle when the control system is off. When the desired angle is reached, the control system switches on and stabilized the TWRW.

Table 6.8: Physical dimensions of the TWRW prototype for the experimental tests.

Property	**Value**	**Unit**
m_{w}	10	kg
m_b	5	kg
m_p	2	kg
J_{w_x}, J_{w_y}, J_{w_z}	0.32, 0.32, 0.64	kg.m^2
J_{b_x}, J_{b_y}, J_{b_z}	0.0182, 0.0097, 0.0099	kg.m^2
J_{p_x}, J_{p_y}, J_{p_z}	0.0024, 0.0014, 0.0016	kg.m^2
r	0.37	m
d	0.5	m
b	0	m
l	0.15	m
l'	0.25	m

As reaching the precise desired pitch angle considered for each case is not easy, the control system switches when the pitch angle is very close to the chosen initial condition values. To select the ideal controller gains, the motors capacity constraints including their maximum torque, current, speed, etc. are considered.

Case 1:

For Case 1, The initial values for pitch angle, the rotation angle of the right and left wheels, and the rotation angle of the movable mechanism angle are respectively chosen as

$$\theta_{b_0} = 5\,deg \quad \dot{\theta}_{b_0} = 0 \quad \theta_{r_0} = 0 \quad \dot{\theta}_{r_0} = 0 \quad \theta_{l_0} = 0 \quad \dot{\theta}_{l_0} = 0 \quad \theta_{p_0} = 0 \quad \dot{\theta}_{p_0} = 0$$

As the physical parameters considered for simulation and experimental are different (e.g. the mass of body for simulation and experimental tests are $80\,kg$, and $5\,kg$, respectively.), their initial conditions are not the same. Additionally, there are no external disturbances applied to the TWRW.

Case 2:

Similar to Case 1, in case 2 no external disturbances are applied to the system. The initial conditions are set as below:

$$\theta_{b_0} = 10\,deg \quad \dot{\theta}_{b_0} = 0 \quad \theta_{r_0} = 0 \quad \dot{\theta}_{r_0} = 0 \quad \theta_{l_0} = 0 \quad \dot{\theta}_{l_0} = 0 \quad \theta_{p_0} = 0 \quad \dot{\theta}_{p_0} = 0$$

For selecting the initial conditions and the controller gains, the constraint of the wheels and the movable mechanism's motors are considered.

6.5.1 PID control

To stabilize the TWRW for the conventional and proposed systems through PID control, the control gains below are selected for both control systems and both cases.

$$K_p = 12 \qquad K_d = 1 \qquad K_i = 0.1$$

Figure. 6.23 represents the experimental results of stability control for the conventional and proposed systems through PID control in Case 1. It can be seen that the pitch angle converges to zero in the proposed system, while it remains almost unchanged in the conventional system (see Figure. 6.23a). The convergence duration of pitch angle in the proposed system is almost $3\,sec$, while it is more (around $6\,sec$) for pitch angular velocity. Figure. 6.23b depicts the pitch angular velocity which converges to zero under both control systems. The required input torque for stability can be seen in Figure. 6.23c, where both control methods require almost same initial torque.

The input torque almost stays on its initial value in the conventional system, while it converges to zero in the proposed approach. It can be concluded that the initial torque in the conventional system depicted in Figure. 6.23c is not enough to move the left and right wheels. However it is enough for the movable mechanism to stabilize the wheelchair. The input power in both control methods are shown in Figure. 6.23d, where it doesn't change and remains zero in the conventional system as the driving wheels don't move. Whereas, the oscillation of input power can be seen in the proposed system which converges to zero when the TWRW reaches its stability.

The angle and angular velocity of movable mechanism in the proposed method are depicted in Figures. 6.23e and 6.23f, respectively. They show that the range of angular motion and velocity of the movable mechanism are small and in an acceptable range which doesn't affect the rider's comfort. The experimental result in Case 2 are shown in Figure. 6.24 which are similar to those obtained in Case 1.

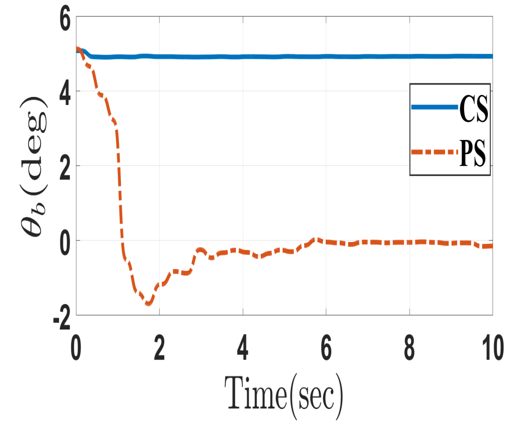

(a): Pitch angle

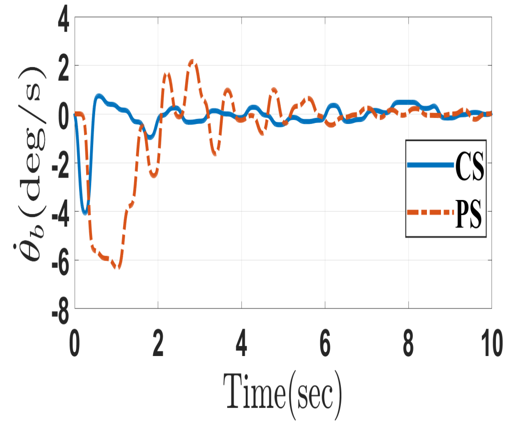

(b): Pitch angular velocity

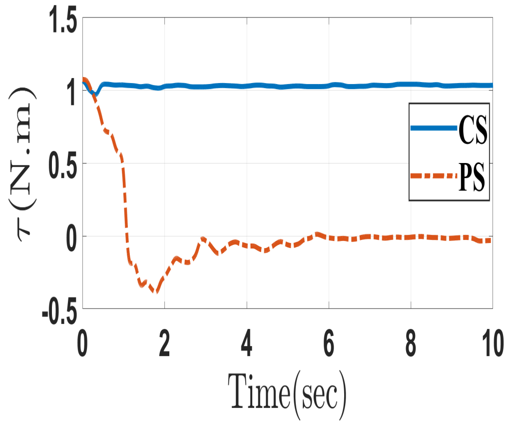

(c): Input torque

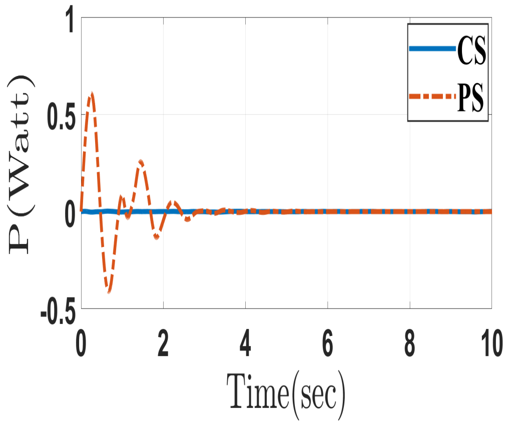

(d): Input power

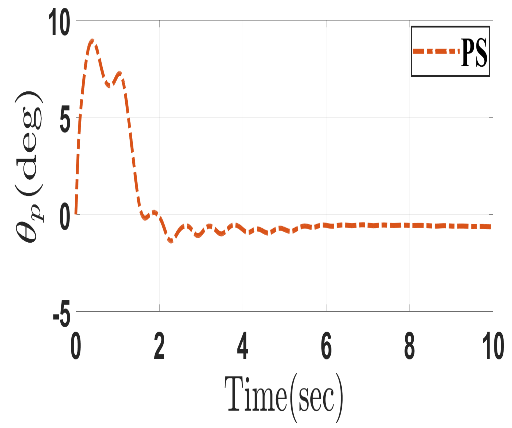

(e): Movable mechanism angle

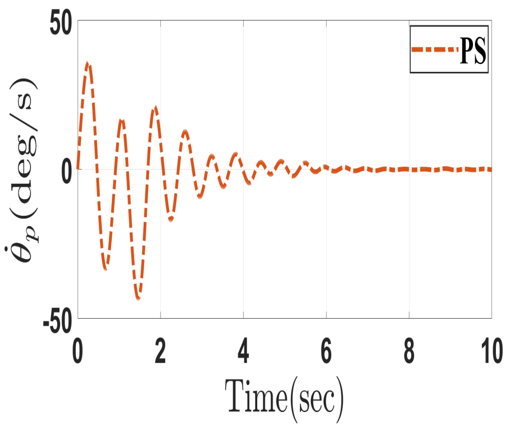

(f): Movable mechanism angular velocity

Figure 6.23: The TWRW experimental results for the stability control of the conventional system (CS) and the proposed system (PS) through PID control in Case 1.

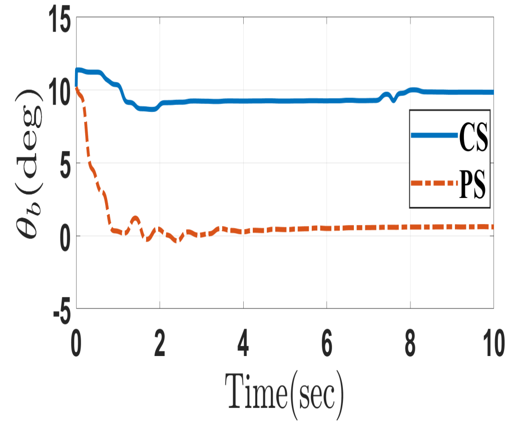

(a): Pitch angle

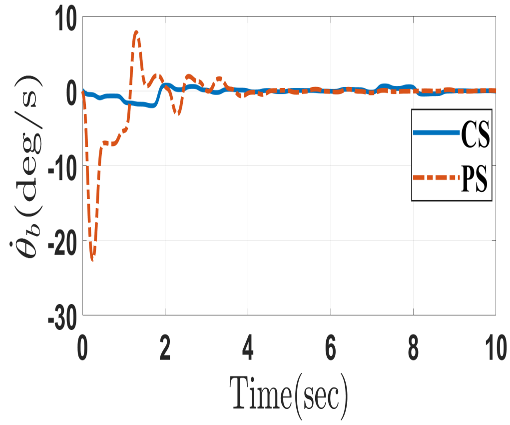

(b): Pitch angular velocity

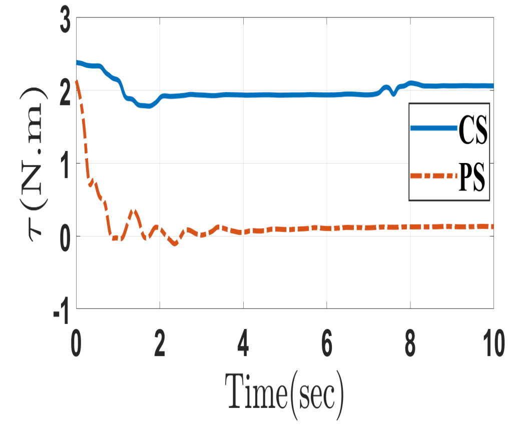

(c): Input torque

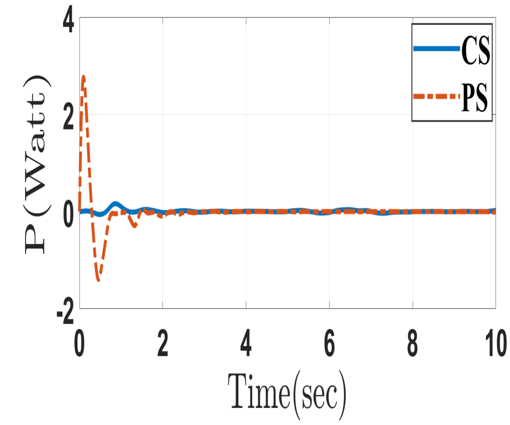

(d): Input power

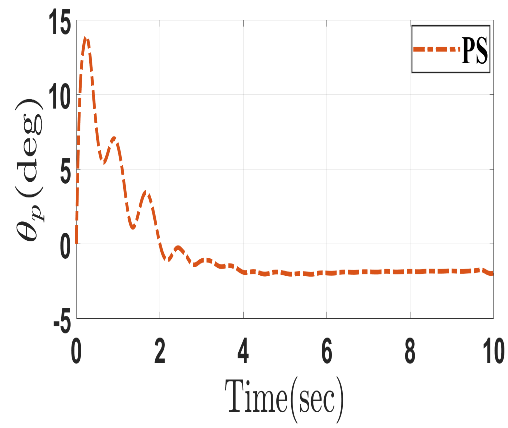

(e): Movable mechanism angle

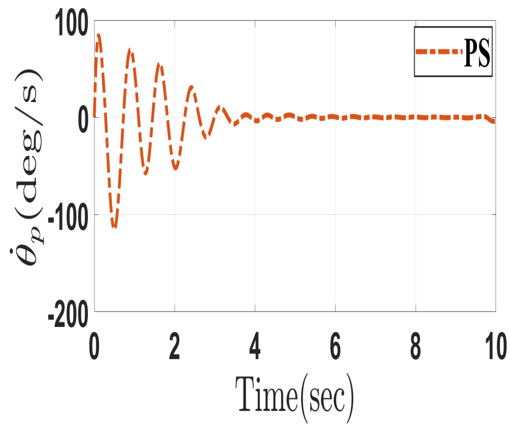

(f): Movable mechanism angular velocity

Figure 6.24: The TWRW experimental results for the stability control of the conventional system (CS) and the proposed system (PS) through PID control in Case 2.

The energy consumption under both control systems through PID control in Case 1 and Case 2 are listed in Table. 6.9. It can be seen that the energy consumption of the motors for the conventional system in both cases are almost zero as the input power of the driving wheels are near zero. The input torque and power are small and insufficient to drive the wheels, which causes failing control systems. To drive the wheels, larger control gains should be chosen which leads to increasing initial input torque. The same controller gains are chosen for both control systems to have reasonable comparison between their performances. Selecting the larger controller gains can result in exceeding the motor capacity of the movable mechanism. Therefore, the controller gains cannot exceed the values chosen for them.

Table 6.9: Energy consumption of the conventional and the proposed systems through PID control for the experimental tests of the TWRW stability control.

Case	1	2
Conventional system ($E_r + E_l$)	0.0175 J	0.2108 J
Proposed system (E_p)	0.4335 J	0.9610 J

6.5.2 CTC control

To implement the experimental test for the TWRW stability control through CTC control, the controller gains for the conventional and proposed control systems in both cases are set as

$$K_p = 9 \qquad K_d = 6 \qquad K_i = 0.05$$

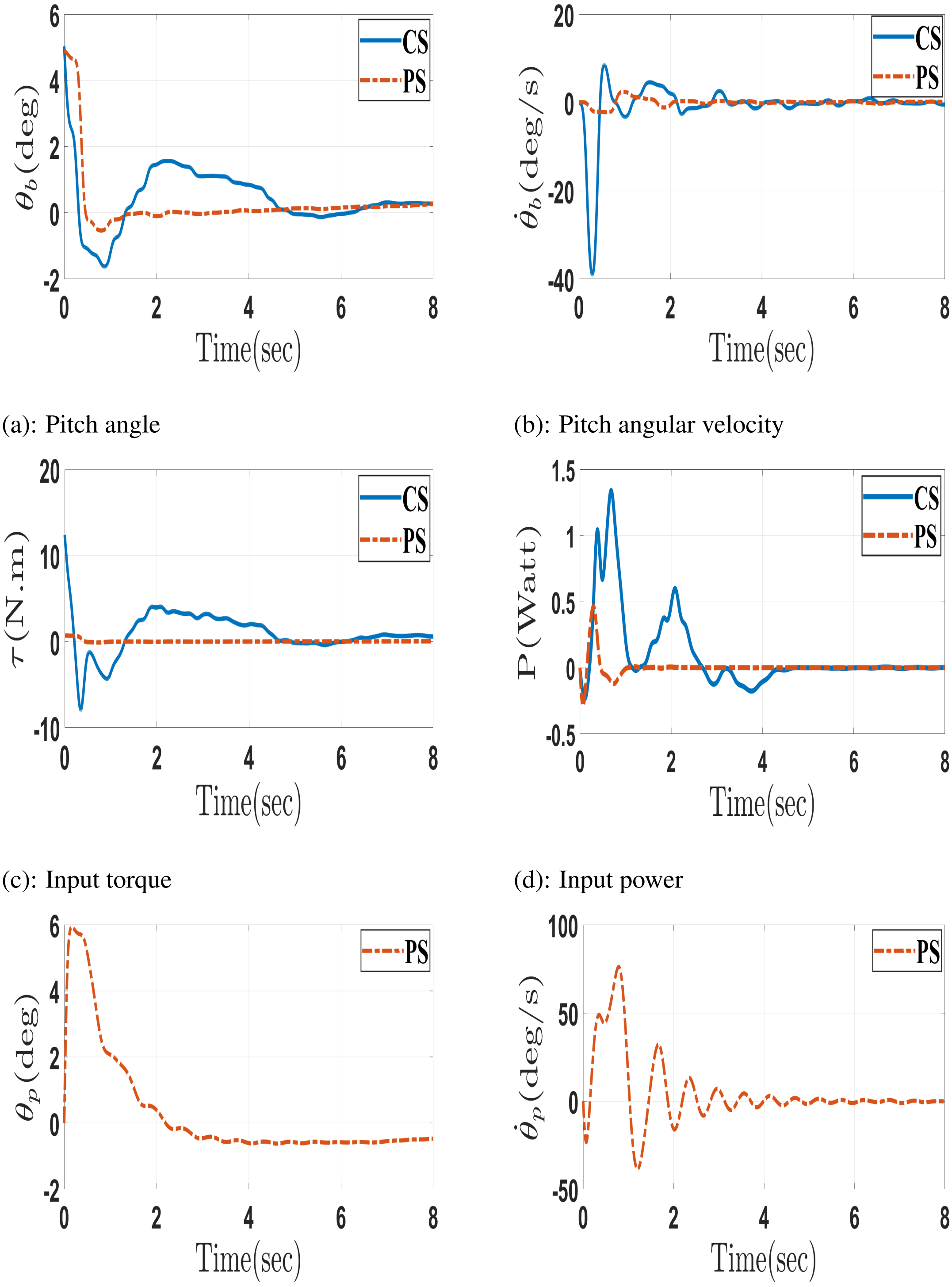

(a): Pitch angle

(b): Pitch angular velocity

(c): Input torque

(d): Input power

(e): Movable mechanism angle

(f): Movable mechanism angular velocity

Figure 6.25: The TWRW experimental results for the stability control of the conventional system (CS) and the proposed system (PS) through CTC control in Case 1.

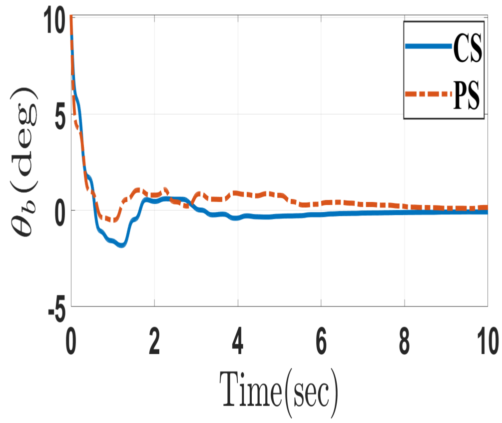

(a): Pitch angle

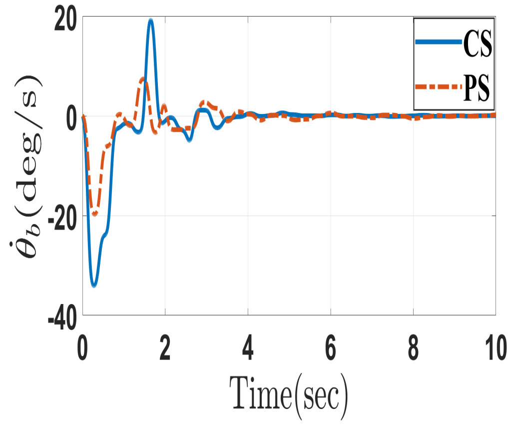

(b): Pitch angular velocity

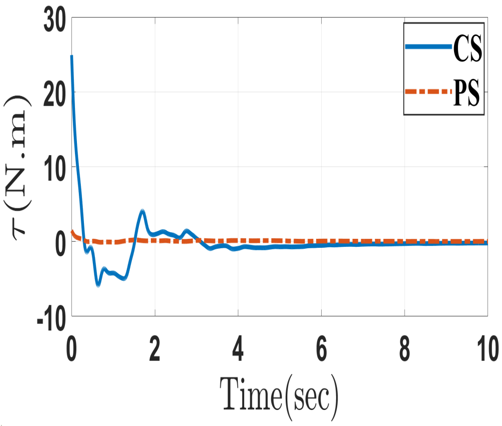

(c): Input torque

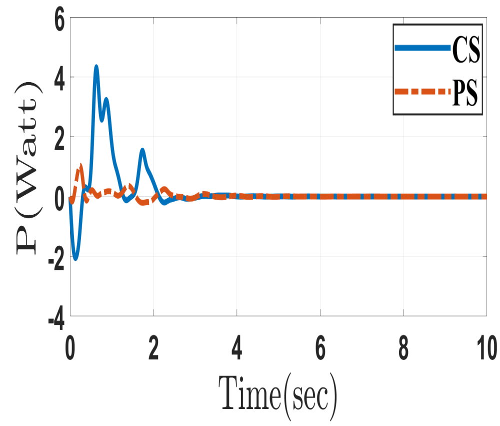

(d): Input power

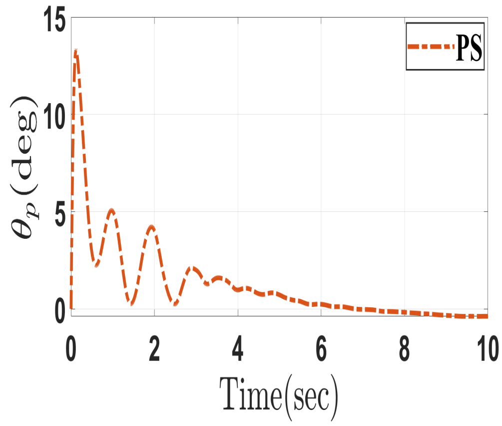

(e): Movable mechanism angle

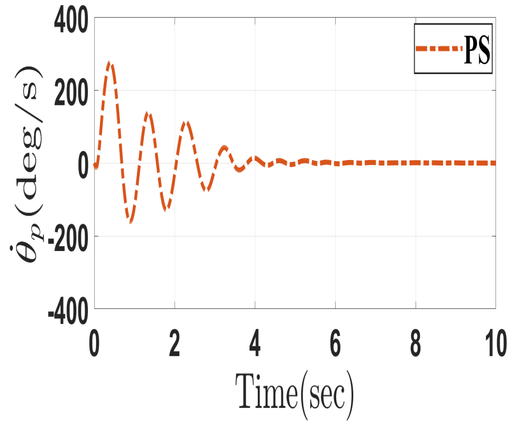

(f): Movable mechanism angular velocity

Figure 6.26: The TWRW experimental results for the stability control of the conventional system (CS) and the proposed system (PS) through CTC control in Case 2.

The experimental results of the TWRW stability control under both control systems through CTC control in Case 1 are represented in Figure. 6.25. It can be seen that the pitch angle and pitch angular velocity under both control approaches converge to zero, while they have less oscillation and faster convergence to zero in the proposed system than conventional one (see Figures. 6.25a, 6.25b).

In addition, the required input torque and power in the proposed system are much lower than the conventional approach (see Figures. 6.25c, 6.25d). The angle and angular velocity of the movable mechanism depicted in Figures. 6.25e, 6.25f, respectively show that they are very small and the movable mechanism can be operated with no effect on the comfort of rider.

Figure. 6.26 shows the experimental results through CTC control in Case 2 which are similar to the Case 1 results. Table. 6.10 depicts the energy consumption of the motors in experimental tests through CTC control. It can be seen that the energy consumption in Case 1 and Case 2 for the proposed method are significantly lower than those obtained in conventional approach, which hugely increase the battery's life.

Table 6.10: Energy consumption of the conventional and the proposed systems through CTC control for the experimental tests of the TWRW stability control.

Case	1	2
Conventional system ($E_r + E_l$)	1.1957 J	2.7169 J
Proposed system (E_p)	0.0754 J	0.1809 J

6.5.3 SMC control

To provide experimental results through SMC control, the controller gains below are chosen for both control systems.

$$c = 3 \qquad \rho = 2 \qquad \epsilon = 0.3$$

Figures. 6.27 and 6.28 represent the experimental results obtained for the TWRW stability control through SMC control in Case 1 and Case 2, respectively. Table. 6.11 depicts the energy consumption of motors in experimental tests through SMC control. The performance analysis of SMC control experimental results are similar to those provided in CTC control (section 6.5.2).

Table 6.11: Energy consumption of the conventional and the proposed systems through SMC control for the experimental tests of the TWRW stability control.

Case	1	2
Conventional system ($E_r + E_l$)	0.9136 J	3.0251 J
Proposed system (E_p)	0.0665 J	0.4393 J

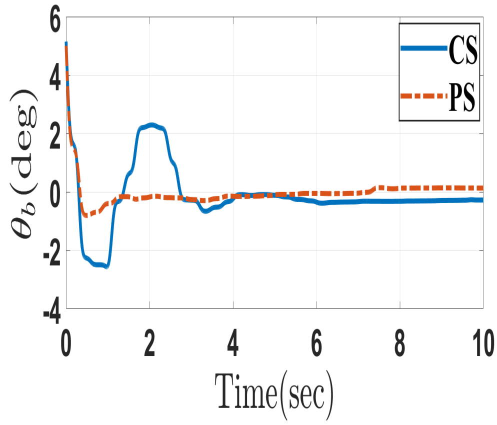

(a): Pitch angle

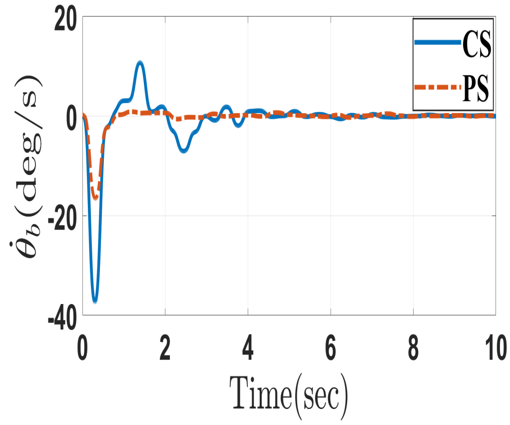

(b): Pitch angular velocity

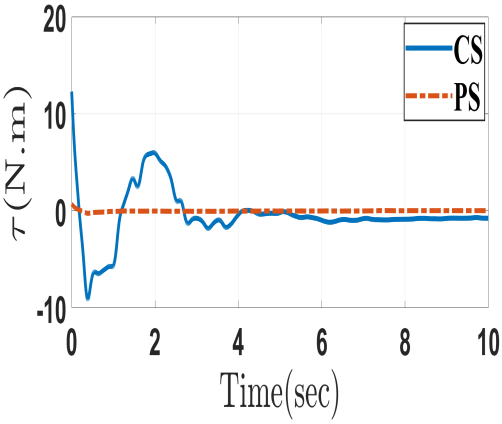

(c): Input torque

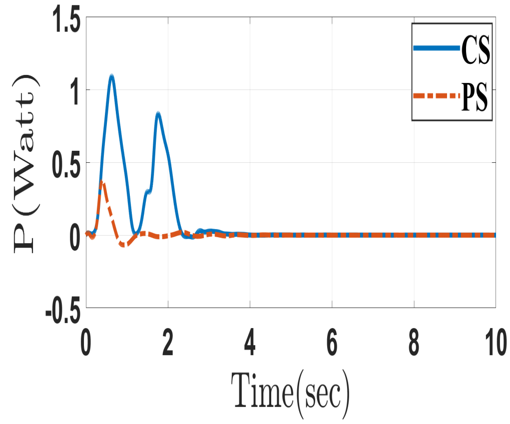

(d): Input power

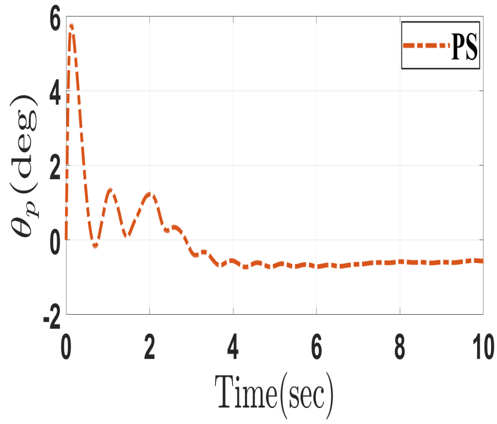

(e): Movable mechanism angle

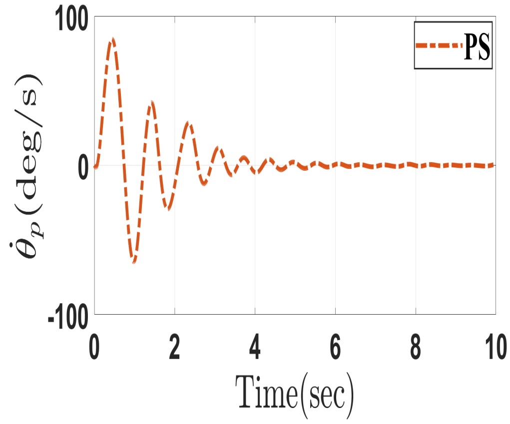

(f): Movable mechanism angular velocity

Figure 6.27: The TWRW experimental results for the stability control of the conventional system (CS) and the proposed system (PS) through SMC control in Case 1.

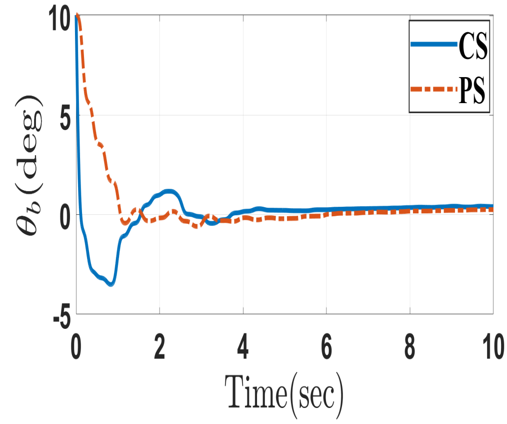

(a): Pitch angle

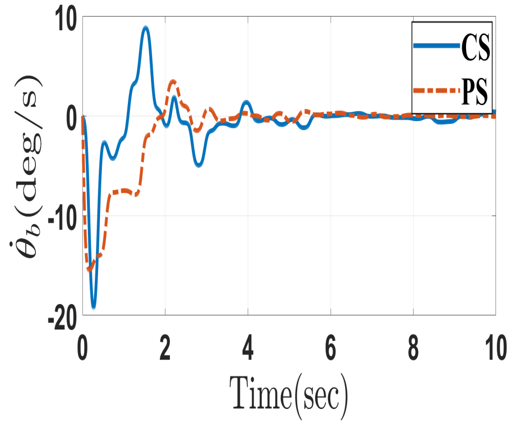

(b): Pitch angular velocity

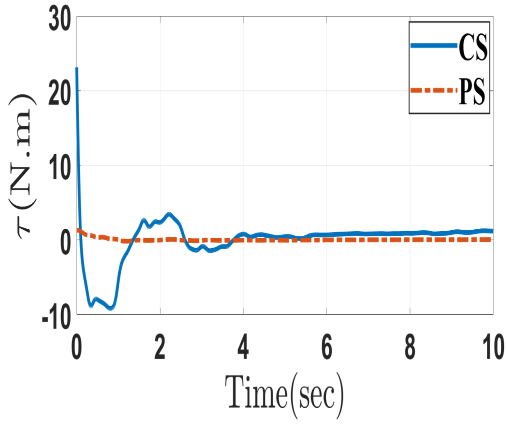

(c): Input torque

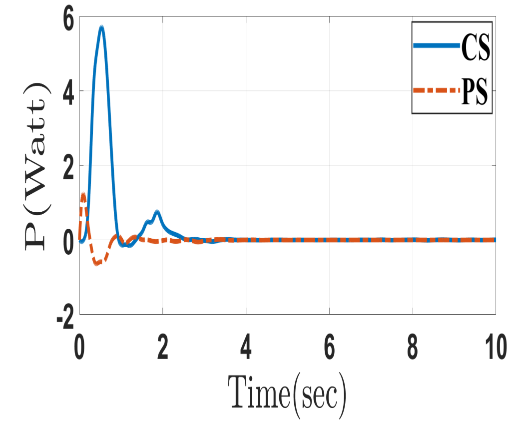

(d): Input power

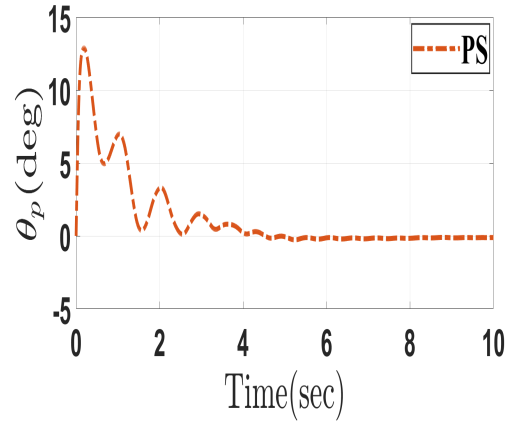

(e): Movable mechanism angle

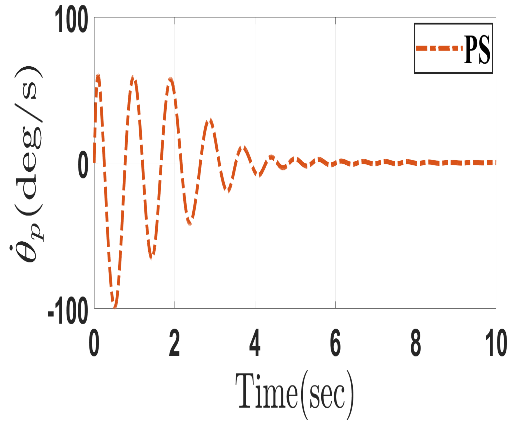

(f): Movable mechanism angular velocity

Figure 6.28: The TWRW experimental results for the stability control of the conventional system (CS) and the proposed system (PS) through SMC control in Case 2.

6.5.4 SOSMC control

The stability control of the TWRW are experimentally tested through SOSMC control where its controller gains are the same for the conventional and proposed approaches and chosen as below:

$$c = 3 \qquad \lambda = 2 \qquad \alpha = 0.3 \qquad \epsilon = 0.01$$

The experimental results of the TWRW stability control through SOSMC control in Case 1 and Case 2 are depicted in Figures. 6.29, 6.30, respectively. Table. 6.12 shows the energy consumption through SOSMC control under conventional and proposed systems. The comparison investigation between the conventional and the proposed systems for CTC, SMC, and SOSMC are similar. However, the maximum and minimum values of the control input through these control schemes are different.

For instance, the maximum input power for the proposed system in Case 1 through PID, CTC, SMC, and SOSMC are $0.6Watt$, $0.5Watt$, $0.4Watt$, and $0.25Watt$, respectively. Similarly, for Case 2 these values are $2.8Watt$, $1.5Watt$, $1.2Watt$, and $1.1Watt$, respectively. It can be seen that the maximum input power required in SOSMC control is the smallest value.

Table 6.12: Energy consumption of the conventional and the proposed systems through SOSMC control for the experimental tests of the TWRW stability control.

Case	1	2
Conventional system ($E_r + E_l$)	0.7462 J	2.8138 J
Proposed system (E_p)	0.1348 J	0.4750 J

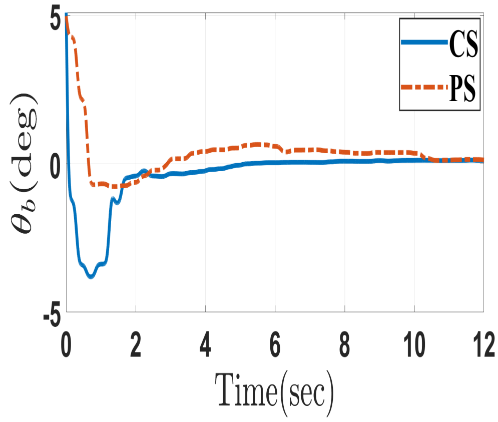

(a): Pitch angle

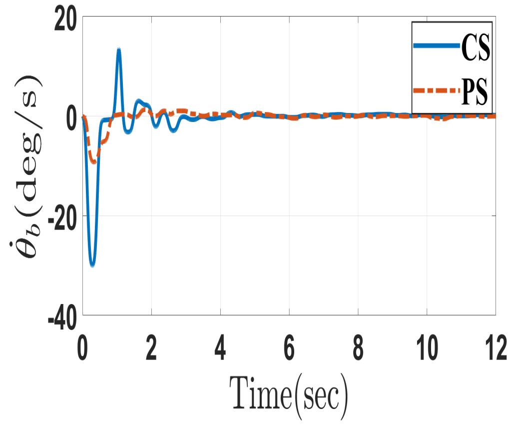

(b): Pitch angular velocity

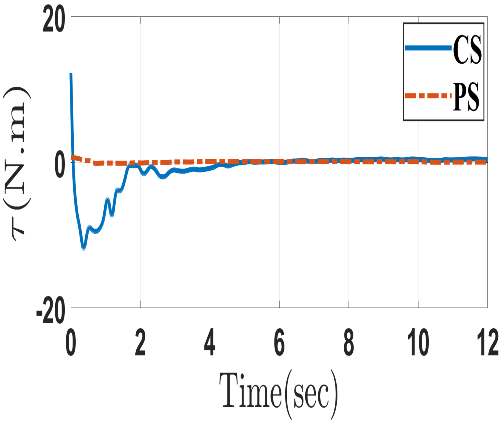

(c): Input torque

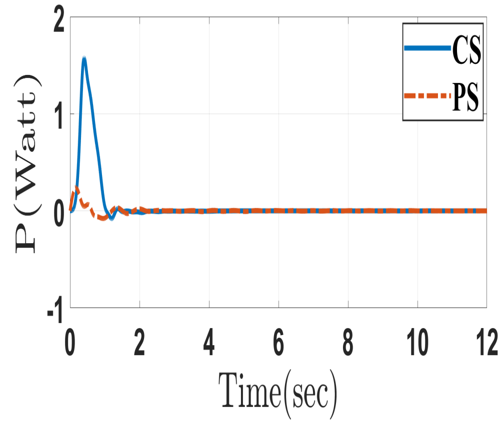

(d): Input power

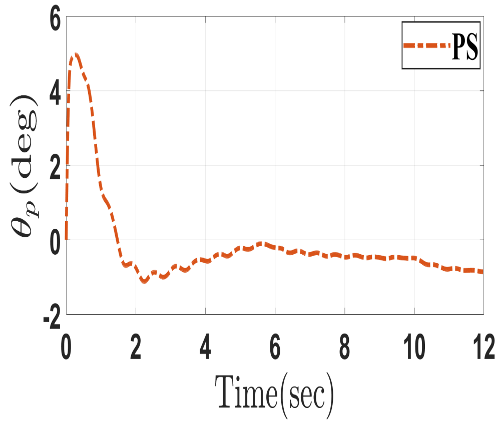

(e): Movable mechanism angle

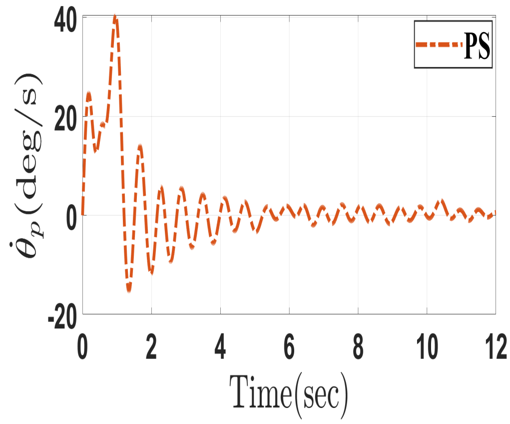

(f): Movable mechanism angular velocity

Figure 6.29: The TWRW experimental results for the stability control of the conventional system (CS) and the proposed system (PS) through SOSMC control in Case 1.

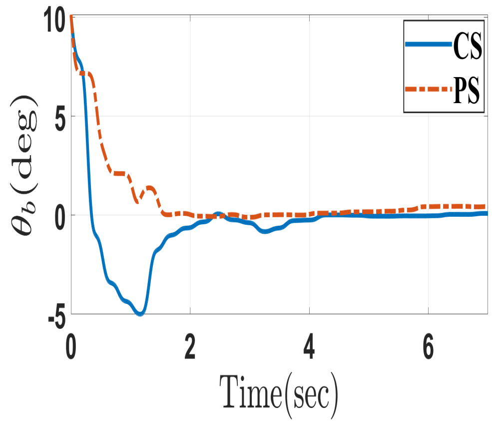

(a): Pitch angle

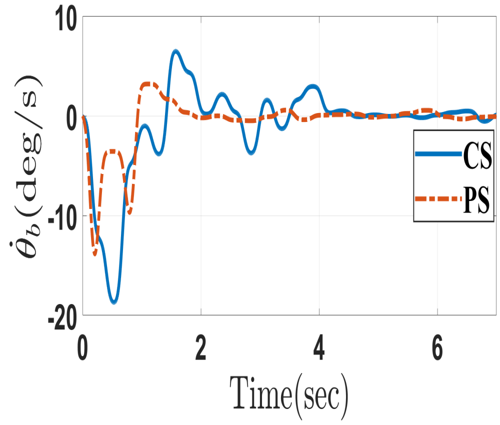

(b): Pitch angular velocity

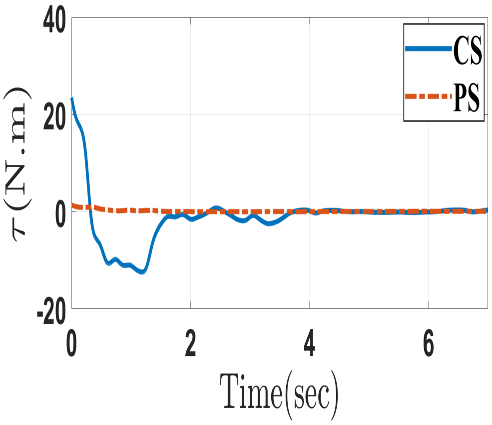

(c): Input torque

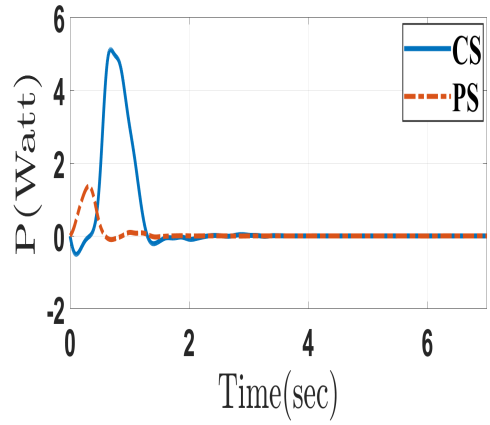

(d): Input power

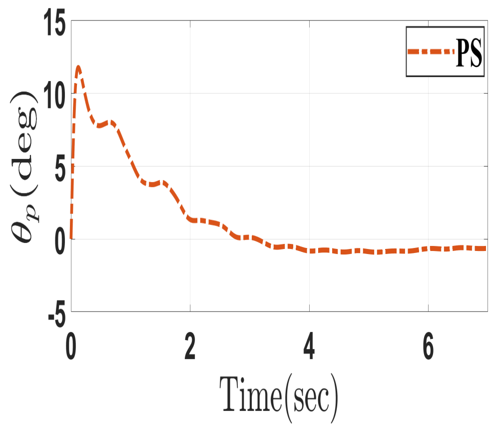

(e): Movable mechanism angle

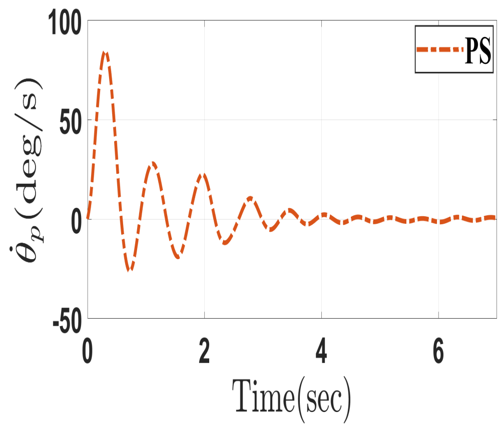

(f): Movable mechanism angular velocity

Figure 6.30: The TWRW experimental results for the stability control of the conventional system (CS) and the proposed system (PS) through SOSMC control in Case 2.

It can be seen that there are some differences on the trend of the system responses with those obtained for the simulation results. The reasons of these differences are the parameters that are not modeled in the simulation. They include sensor noise, internal and external friction forces, uncertainty of all physical parameters, etc.

6.6 Summary

In this chapter, the scaled-down TWRW prototype was designed and modeled. The model consists of two driving wheels equipped with BLDC motors, a $5kg$ steel mass considered as the body, and the movable mechanism. The movable mechanism comprises a light rod and a $2kg$ mass placed at one end of the rod, which its motion is powered by a DC motor. The input voltage and current of all TWRW's motors are provided by a 14 cell lithium battery. The high accuracy VN-200 and a MPU6050 IMU sensor are used to measure the state space of the body and the movable mechanism, respectively. The state space of these components including their angle and angular velocity are controller's feedback. To remove MPU6050 noise, a Kalman Filter is utilized to provide more reliable state space feedback.

To design stability control systems developed by PID, CTC, SMC, and SOSMC control (see Chapter. 4), the MyRIO-1900 microcontroller programmed by LabVIEW is utilized. The control input are provided by a UART signal as their input frequency can reach up to 2 MHz. However, there is no instruction to send the MyRIO-1900 UART signal and receive it by the motor controller (MTVESC50A). To resolve this problem, The Arduino mega 2560 is used to receive the MyRIO-1900 UART signal and send them as a control input to the motor controller. The MTVESC50A which is programmed by the VESC Tool is used as the motor controller to receive the microcontroller commands and transfer them appropriately to the motors.

To prove the simulation results of stability control provided in Chapter. 4, the experimental results are provided. The experimental results verify the simulation results, where the input torque, input power, and energy consumption in the proposed system are much lower than the conventional approach. In addition, in the proposed system the pitch angle and its velocity have less oscillation and faster convergence to zero than those obtained in the conventional method.

In the next chapter, the conclusion and future works of this research are provided.

Chapter 7

Conclusion and Future Studies

7.1 Conclusion

The TWRW has drawn people's attention and has become popular as they have better maneuverability than conventional robotics wheelchairs (four-wheeled robotic wheelchairs). However, they are statically unstable and an active controller is needed to keep the stability of the system. The stability control objective is to keep the rider in the upright position which is shown by pitch angle. Therefore, the controller should be designed in a way to keep the pitch angle near zero. The most conventional stability controller relies on the motion of driving wheels. This control system requires huge torque and power which can exceed the capacity of the wheels' motors.

In this research, a novel approach is proposed for the stability control of TWRW. A pendulum-like movable mechanism is added to the wheelchair to keep it stable. In this system, the torque is applied to the added mechanism, while in the conventional system the torque is applied to the right and left wheels. The Euler-Lagrange formulation is applied to establish the dynamic model. The PID, CTC, SMC, and SOSMC control schemes are developed for stability control. The effectiveness of the proposed system is simulated, while considering disturbances caused by uncertainties of the inertia parameter of the dynamic model and the rider's motion. The simulation results demonstrate that in the proposed approach, the stability of TWRW is achieved, while the input torque, input power, and energy consumption for the control system are much lower than the conventional method. The robustness of the control systems developed through the control schemes mentioned above is evaluated. As seen in the results, the TWRW can achieve the best robustness, and require the least input torque and power, when it is developed by SOSMC.

In addition to stability, direction control is also important. In the conventional system, the stability and direction control are achieved by the right and left wheels' motion. In the proposed system, the movable mechanism is added to the TWRW to aid the wheels for stability and direction control. This mechanism is mainly used for the stability of the system. The simulation results prove the superiority of the proposed system, where the controller objectives including pitch and yaw angle can follow their desired values. Whereas, the input torque, power, and energy consumption for the proposed system are smaller than the conventional one.

To verify the simulation results, the scaled-down prototype is built to achieve the experimental results. The experimental setup is provided to evaluate the stability control system, while the direction control is not considered. The prototype is equipped with two BLDC driving wheels and a DC motor to power the movable mechanism. The high-accuracy IMU sensor (VN-200) is used to measure the pitch angle and its velocity, and a MPU6050 sensor is attached to the added mechanism to measure its angle and angular velocity. The MPU6050 state feedback suffers from sensor noise. To reduce the noise, a Kalman Filter is used. This filtering method can provide the state feedback of the movable mechanism within an acceptable range. Two microcontrollers including MyRIO and Arduino, which are embedded real-time systems are utilized to develop the control system algorithm. The MTVESC50A motor controller is used to receive the commands from the microcontrollers and transfer them to the motors properly. The experimental results represent that under both control systems (conventional and proposed systems), TWRW can reach its stability. Whereas, the input torque, input power, and energy consumption in the proposed system are much lower than the conventional one, which significantly increases the battery' life.

7.2 Future studies

The work presented in this thesis, designed and developed the stability control of TWRW theoretically and implemented in practice. Due to time and budget constraints, the prototype has been modelled in a scaled-down size of a real TWRW. We aim to build a model in a larger size to be used as a wheelchair that a rider can sit on. In addition, the stability and direction control was developed theoretically and it was not provided for the experimental setup. We are interested in implementing this control system for the experimental model. For future works, the joystick can be mounted on the system to control the motion of the TWRW.

The performance of the proposed system should be evaluated under more cases. For example, it should be tested when the system passes from uneven surfaces, steps, etc. Additionally, the stability control can be analysed and tested for the different velocities of driving wheels. Furthermore, we are keen to design a proper braking system using the driving wheels and the movable mechanism.

References

[1] H. A. Yanco, “Wheelesley: A robotic wheelchair system: Indoor navigation and user interface,” in *Assistive technology and artificial intelligence*. Springer, 1998, pp. 256–268.

[2] L. Fehr, W. E. Langbein, and S. B. Skaar, “Adequacy of power wheelchair control interfaces for persons with severe disabilities: A clinical survey,” *Journal of rehabilitation research and development*, vol. 37, no. 3, pp. 353–360, 2000.

[3] C. Bühler, R. Hoelper, H. Hoyer, and W. Humann, “Autonomous robot technology for advanced wheelchair and robotic aids for people with disabilities,” *Robotics and autonomous systems*, vol. 14, no. 2-3, pp. 213–222, 1995.

[4] S. Ahmad, M. O. Tokhi, and N. Siddique, “Modular fuzzy control with input shaping technique for transformation of two-wheeled wheelchair to four-wheeled mode,” in *2010 IEEE Symposium on Industrial Electronics and Applications (ISIEA)*. IEEE, 2010, pp. 562–566.

[5] A. Dinale, K. Hirata, and T. Murakami, “Analytical design of a robust motion controller for a two-wheeled wheelchair system,” in *2013 16th International Conference on Advanced Robotics (ICAR)*. IEEE, 2013, pp. 1–6.

[6] N. Abdul Ghani and M. O. Tokhi, “Sit-to-stand and stand-to-sit control mechanisms of two-wheeled wheelchair,” *Journal of biomechanical engineering*, vol. 138, no. 4, 2016.

[7] N. Hirata and T. Murakami, “An approach to safety mechanism and control for improved operability in two-wheeled wheelchair,” in *2014 10th France-Japan/8th Europe-Asia Congress on Mecatronics (MECATRONICS2014-Tokyo)*. IEEE, 2014, pp. 121–126.

[8] K. Boniface, M. P. McKay, R. Lucas, A. Shaffer, and N. Sikka, “Serious injuries related to the segway® personal transporter: a case series,” *Annals of emergency medicine*, vol. 57, no. 4, pp. 370–374, 2011.

[9] R. Babazadeh, A. G. Khiabani, and H. Azmi, “Optimal control of segway personal transporter,” in *2016 4th International Conference on Control, Instrumentation, and Automation (ICCIA)*. IEEE, 2016, pp. 18–22.

[10] D. Xia, Y. Yao, and L. Cheng, "Indoor autonomous control of a two-wheeled inverted pendulum vehicle using ultra wide band technology," *Sensors*, vol. 17, no. 6, p. 1401, 2017.

[11] N. Minouchehr and S. K. Hosseini-Sani, "Design of model predictive control of two-wheeled inverted pendulum robot," in *2015 3rd RSI International Conference on Robotics and Mechatronics (ICROM)*. IEEE, 2015, pp. 456–462.

[12] S. Liang and Z. Wang, "Integral-type-observer-based control with measurement uncertainty and application to two-wheeled inverted pendulum," *International Journal of Robust and Nonlinear Control*, vol. 31, no. 7, pp. 2633–2651, 2021.

[13] M. Yue, C. An, and J.-Z. Sun, "An efficient model predictive control for trajectory tracking of wheeled inverted pendulum vehicles with various physical constraints," *International Journal of Control, Automation and Systems*, vol. 16, no. 1, pp. 265–274, 2018.

[14] T. MATSUNO, H. JIAN, T. FUKUDA, and K. DOI, "Stabilization of inverted pendulum cart with balancing mechanism by integrity trajectories in acceleration behavior," in *The Abstracts of the international conference on advanced mechatronics: toward evolutionary fusion of IT and mechatronics: ICAM 2010.5*. The Japan Society of Mechanical Engineers, 2010, pp. 337–344.

[15] Y. Sago, Y. Noda, K. Kakihara, and K. Terashima, "Parallel two-wheel vehicle with underslung vehicle body," *Mechanical Engineering Journal*, vol. 1, no. 4, pp. DR0036–DR0036, 2014.

[16] A. K. Singh, D. Chaturvedi, and N. K. Pal, "Design of a robust controller for inverted pendulum," *International Journal of Computer Applications*, vol. 112, no. 16, pp. 23–28, 2015.

[17] S. Nawawi, M. Ahmad, J. Osman, A. Husain, and M. Abdollah, "Controller design for two-wheels inverted pendulum mobile robot using pismc," in *2006 4th Student Conference on Research and Development*. IEEE, 2006, pp. 194–199.

[18] S. Nithya, N. Sivakumaran, T. Balasubramanian, and N. Anantharaman, "Model based controller design for a spherical tank process in real time," *IJSSST*, vol. 9, no. 4, pp. 25–31, 2008.

[19] E.-H. Zheng, J.-J. Xiong, and J.-L. Luo, "Second order sliding mode control for a quadrotor uav," *ISA transactions*, vol. 53, no. 4, pp. 1350–1356, 2014.

[20] A. A. Bature, S. Buyamin, M. N. Ahmad, M. Muhammad, and A. A. Muhammad, "Identification and model predictive position control of two wheeled inverted pendulum mobile robot," *Jurnal Teknologi*, vol. 73, no. 6, 2015.

[21] Y. Ganesan, S. Gobee, and V. Durairajah, “Development of an upper limb exoskeleton for rehabilitation with feedback from emg and imu sensor,” *Procedia Computer Science*, vol. 76, pp. 53–59, 2015.

[22] A. Erdogan and B. D. Argall, “The effect of robotic wheelchair control paradigm and interface on user performance, effort and preference: an experimental assessment,” *Robotics and Autonomous Systems*, vol. 94, pp. 282–297, 2017.

[23] Y. Onozuka, N. Tomokuni, G. Murata, and M. Shino, “Attitude control of an inverted-pendulum-type robotic wheelchair to climb stairs considering dynamic equilibrium,” *Robomech Journal*, vol. 7, no. 1, pp. 1–13, 2020.

[24] B. Woods and N. Watson, “A short history of powered wheelchairs,” *Assistive Technology*, vol. 15, no. 2, pp. 164–180, 2003.

[25] I. P. Ktistakis and N. G. Bourbakis, “A survey on robotic wheelchairs mounted with robotic arms,” in *2015 National Aerospace and Electronics Conference (NAECON)*. IEEE, 2015, pp. 258–262.

[26] L. Marchal-Crespo, J. Furumasu, and D. J. Reinkensmeyer, “A robotic wheelchair trainer: design overview and a feasibility study,” *Journal of neuroengineering and rehabilitation*, vol. 7, no. 1, pp. 1–12, 2010.

[27] T. F. Bastos-Filho, F. A. Cheein, S. M. T. Müller, W. C. Celeste, C. de la Cruz, D. C. Cavalieri, M. Sarcinelli-Filho, P. F. S. Amaral, E. Perez, C. M. Soria *et al.*, “Towards a new modality-independent interface for a robotic wheelchair,” *IEEE Transactions on Neural Systems and Rehabilitation Engineering*, vol. 22, no. 3, pp. 567–584, 2013.

[28] M. M. Store. Mede-move sln basic wheel chair foldable (red)lp. [Online]. Available: https://gibraltar.desertcart.com/products/104453564-med-e-move-sln-premium-basic-wheel-chair-foldable-red-lp

[29] L. H. van der Woude, A. J. Dallmeijer, T. W. Janssen, and D. Veeger, “Alternative modes of manual wheelchair ambulation: an overview,” *American journal of physical medicine & rehabilitation*, vol. 80, no. 10, pp. 765–777, 2001.

[30] Y. Vanlandewijck, D. Theisen, and D. Daly, “Wheelchair propulsion biomechanics,” *Sports medicine*, vol. 31, no. 5, pp. 339–367, 2001.

[31] C. L. Flemmer and R. C. Flemmer, “A review of manual wheelchairs,” *Disability and Rehabilitation: Assistive Technology*, vol. 11, no. 3, pp. 177–187, 2016.

[32] L. A. Zukowski, J. A. Roper, O. Shechtman, D. M. Otzel, J. Bouwkamp, and M. D. Tillman, “Comparison of metabolic cost, performance, and efficiency of propulsion using an ergonomic hand drive mechanism and a conventional manual wheelchair,” *Archives of physical medicine and rehabilitation*, vol. 95, no. 3, pp. 546–551, 2014.

[33] P. Requejo, S. Mulroy, L. L. Haubert, C. Newsam, J. Gronley, and J. Perry, "Evidence-based strategies to preserve shoulder function in manual wheelchair users with spinal cord injury," *Topics in Spinal Cord Injury Rehabilitation*, vol. 13, no. 4, pp. 86–119, 2008.

[34] J. W. Chow and C. E. Levy, "Wheelchair propulsion biomechanics and wheelers' quality of life: an exploratory review," *Disability and Rehabilitation: Assistive Technology*, vol. 6, no. 5, pp. 365–377, 2011.

[35] N. W. John, S. R. Pop, T. W. Day, P. D. Ritsos, and C. J. Headleand, "The implementation and validation of a virtual environment for training powered wheelchair manoeuvres," *IEEE transactions on visualization and computer graphics*, vol. 24, no. 5, pp. 1867–1878, 2017.

[36] F. Routhier, J. Lettre, W. C. Miller, J. F. Borisoff, K. Keetch, I. M. Mitchell, and C. R. Team, "Data logger technologies for powered wheelchairs: a scoping review," *Assistive technology*, vol. 31, no. 1, pp. 19–24, 2019.

[37] P. E. Hsu, Y. L. Hsu, K. W. Chang, and C. Geiser, "Mobility assistance design of the intelligent robotic wheelchair," *International Journal of Advanced Robotic Systems*, vol. 9, no. 6, p. 244, 2012.

[38] H. Seki, T. Sugimoto, and S. Tadakuma, "Novel straight road driving control of power assisted wheelchair based on disturbance estimation and minimum jerk control," in *Fourtieth IAS Annual Meeting. Conference Record of the 2005 Industry Applications Conference, 2005.*, vol. 3. IEEE, 2005, pp. 1711–1717.

[39] D. P. Miller and M. G. Slack, "Design and testing of a low-cost robotic wheelchair prototype," *Autonomous robots*, vol. 2, no. 1, pp. 77–88, 1995.

[40] S. Ahmad and M. Tokhi, "Forward and backward motion control of wheelchair on two wheels," in *2008 3rd IEEE Conference on Industrial Electronics and Applications*. IEEE, 2008, pp. 461–466.

[41] T. Altalmas, S. Ahmad, A. Aula, R. Akmeliawati, and S. Sidek, "Mechanical design and simulation of two-wheeled wheelchair using solidworks," in *IOP Conference Series: Materials Science and Engineering*, vol. 53, no. 1. IOP Publishing, 2013, p. 012042.

[42] A. M. Almeshal, K. M. Goher, A. Nasir, and M. O. Tokhi, "Steering and dynamic performance of a new configuration of a wheelchair on two wheels in various indoor and outdoor environments," in *2013 18th International Conference on Methods & Models in Automation & Robotics (MMAR)*. IEEE, 2013, pp. 223–228.

[43] N. F. Jamin and N. A. Ghani, "Two-wheeled wheelchair stabilization control using fuzzy logic controller based particle swarm optimization," in *2016 IEEE*

international conference on automatic control and intelligent systems (I2CACIS). IEEE, 2016, pp. 180–185.

[44] S. Arthanat, S. M. Nochajski, J. A. Lenker, S. M. Bauer, and Y. W. B. Wu, “Measuring usability of assistive technology from a multicontextual perspective: the case of power wheelchairs,” *American Journal of Occupational Therapy*, vol. 63, no. 6, pp. 751–764, 2009.

[45] K. Technologies. Motorized wheel chair / electric wheelchair keemed. [Online]. Available: https://shopee.ph/Motorized-Wheel-chair-Electric-Wheelchair-KeeMed-i.50969189.850909056

[46] S. Kim and S. Kwon, “Robust transition control of underactuated two-wheeled self-balancing vehicle with semi-online dynamic trajectory planning,” *Mechatronics*, vol. 68, p. 102366, 2020.

[47] S. Jeong, N. Maeda, and K. Kozai, “Driving assist control of wheeled inverted pendulum wheelchair using an active seat-slider,” in *2019 19th International Conference on Control, Automation and Systems (ICCAS)*. IEEE, 2019, pp. 162–167.

[48] Y. Takahashi and O. Tsubouchi, “Modern control approach for robotic wheelchair with inverse pendulum control,” in *5th International Conference on Intelligent Systems Design and Applications (ISDA'05)*. IEEE, 2005, pp. 364–369.

[49] R. Ando and A. Li, “An analysis on users' evaluation for self-balancing two-wheeled personal mobility vehicles,” in *2012 15th International IEEE Conference on Intelligent Transportation Systems*. IEEE, 2012, pp. 1525–1530.

[50] J. Mattie, J. Tavares, B. Matheson, E. Smith, I. Denison, W. C. Miller, and J. F. Borisoff, “Evaluation of the nino® two-wheeled power mobility device: a pilot study,” *IEEE transactions on neural systems and rehabilitation engineering*, vol. 28, no. 11, pp. 2497–2506, 2020.

[51] M. Moness, D. Mahmoud, and A. Hussein, “Real-time mamdani-like fuzzy and fusion-based fuzzy controllers for balancing two-wheeled inverted pendulum,” *Journal of Ambient Intelligence and Humanized Computing*, pp. 1–17, 2020.

[52] M. Nikpour, L. Huang, and A. M. Al-Jumaily, “Stability and direction control of a two-wheeled robotic wheelchair through a movable mechanism,” *IEEE Access*, vol. 8, pp. 45 221–45 230, 2020.

[53] N. Mostafa, H. Loulin, and M. Ahmed, “An approach on velocity and stability control of a two-wheeled robotic wheelchair,” *Appl Sci*, vol. 10, pp. 1–18, 2020.

[54] Y. Kim, S. H. Kim, and Y. K. Kwak, “Dynamic analysis of a nonholonomic two-wheeled inverted pendulum robot,” *Journal of Intelligent and Robotic Systems*, vol. 44, no. 1, pp. 25–46, 2005.

[55] A. Castro, “Modeling and dynamic analysis of a two-wheeled inverted-pendulum,” Ph.D. dissertation, Georgia Institute of Technology, 2012.

[56] C. Yang, Z. Li, R. Cui, and B. Xu, “Neural network-based motion control of an underactuated wheeled inverted pendulum model,” *IEEE Transactions on Neural Networks and Learning Systems*, vol. 25, no. 11, pp. 2004–2016, 2014.

[57] A. A. Bature, S. Buyamin, M. N. Ahmad, and M. Muhammad, “A comparison of controllers for balancing two wheeled inverted pendulum robot,” *International Journal of Mechanical & Mechatronics Engineering*, vol. 14, no. 3, pp. 62–68, 2014.

[58] Z. Li and C. Xu, “Adaptive fuzzy logic control of dynamic balance and motion for wheeled inverted pendulums,” *Fuzzy Sets and Systems*, vol. 160, no. 12, pp. 1787–1803, 2009.

[59] Z.-Q. Guo, J.-X. Xu, and T. H. Lee, “Design and implementation of a new sliding mode controller on an underactuated wheeled inverted pendulum,” *Journal of the Franklin Institute*, vol. 351, no. 4, pp. 2261–2282, 2014.

[60] R. Shalaby, M. El-Hossainy, and B. Abo-Zalam, “Fractional order modeling and control for under-actuated inverted pendulum,” *Communications in Nonlinear Science and Numerical Simulation*, vol. 74, pp. 97–121, 2019.

[61] R. Olfati-Saber, “Nonlinear control of underactuated mechanical systems with application to robotics and aerospace vehicles,” Ph.D. dissertation, Massachusetts Institute of Technology, 2001.

[62] A. A. Wardana, T. Takaki, M. Jiang, and I. Ishii, “Development of a single-wheeled inverted pendulum robot capable of climbing stairs,” *Advanced Robotics*, vol. 34, no. 10, pp. 674–688, 2020.

[63] A. Maddahi and A. H. Shamekhi, “Controller design for two-wheeled self-balancing vehicles using feedback linearisation technique,” *International Journal of Vehicle Systems Modelling and Testing*, vol. 8, no. 1, pp. 38–54, 2013.

[64] R. A. Cooper, M. L. Boninger, R. Cooper, and A. Kelleher, “Use of the independence 3000 ibot™ transporter at home and in the community: A case report,” *Disability and Rehabilitation: Assistive Technology*, vol. 1, no. 1-2, pp. 111–117, 2006.

[65] B. Panomruttanarug and P. Chotikunnan, “Self-balancing ibot-like wheelchair based on type-1 and interval type-2 fuzzy control,” in *2014 11th International Conference on Electrical Engineering/Electronics, Computer, Telecommunications and Information Technology (ECTI-CON)*. IEEE, 2014, pp. 1–6.

[66] S. Arthanat, J. M. Desmarais, and P. Eikelberg, "Consumer perspectives on the usability and value of the ibot® wheelchair: findings from a case series," *Disability and Rehabilitation: Assistive Technology*, vol. 7, no. 2, pp. 153–167, 2012.

[67] H. Uustal and J. L. Minkel, "Study of the independence ibot 3000 mobility system: an innovative power mobility device, during use in community environments," *Archives of physical medicine and rehabilitation*, vol. 85, no. 12, pp. 2002–2010, 2004.

[68] Y. Sugahara, N. Yonezawa, and K. Kosuge, "A novel stair-climbing wheelchair with transformable wheeled four-bar linkages," in *2010 IEEE/RSJ International Conference on Intelligent Robots and Systems*. IEEE, 2010, pp. 3333–3339.

[69] T. Kawamura and T. Murakami, "Vibration suppression for uprising control of two-wheel driven wheelchair," in *IECON 2011-37th Annual Conference of the IEEE Industrial Electronics Society*. IEEE, 2011, pp. 3323–3328.

[70] A. Nakamura and T. Murakami, "A stabilization control of two wheels driven wheelchair," in *2009 IEEE/RSJ International Conference on Intelligent Robots and Systems*. IEEE, 2009, pp. 4863–4868.

[71] K. Hirata and T. Murakami, "An assist control of step climbing motion in two-wheel electric powered wheelchair with controlled casters," in *2014 IEEE 13th International Workshop on Advanced Motion Control (AMC)*. IEEE, 2014, pp. 440–445.

[72] S. Hamatani, T. Nozaki, and T. Murakami, "Steering control in multi-degrees-of-freedom two-wheeled wheel chair on slope environment," in *IECON 2016-42nd Annual Conference of the IEEE Industrial Electronics Society*. IEEE, 2016, pp. 6181–6186.

[73] A. Dinale, K. Hirata, M. Zoppi, and T. Murakami, "Parameter design of disturbance observer for a robust control of two-wheeled wheelchair system," *Journal of Intelligent & Robotic Systems*, vol. 77, no. 1, pp. 135–148, 2015.

[74] L. Vermeiren, A. Dequidt, T. M. Guerra, H. Rago-Tirmant, and M. Parent, "Modeling, control and experimental verification on a two-wheeled vehicle with free inclination: An urban transportation system," *Control Engineering Practice*, vol. 19, no. 7, pp. 744–756, 2011.

[75] M. Baloh and M. Parent, "Modeling and model verification of an intelligent self-balancing two-wheeled vehicle for an autonomous urban transportation system," in *The conference on computational intelligence, robotics, and autonomous systems*, 2003, pp. 1–7.

[76] P. Petrov and M. Parent, "Dynamic modeling and adaptive motion control of a two-wheeled self-balancing vehicle for personal transport," in *13th International IEEE Conference on Intelligent Transportation Systems*. IEEE, 2010, pp. 1013–1018.

[77] H. Tirmant, M. Baloh, L. Vermeiren, T. Guerra, and M. Parent, "B2, an alternative two wheeled vehicle for an automated urban transportation system," in *Intelligent Vehicle Symposium, 2002. IEEE*, vol. 2. IEEE, 2002, pp. 594–603.

[78] F. Ding, J. Huang, Y. Wang, X. Gao, T. Matsuno, T. Fukuda, and K. Sekiyama, "Optimal braking control for uw-car using sliding mode," in *2009 IEEE International Conference on Robotics and Biomimetics (ROBIO)*. IEEE, 2009, pp. 117–122.

[79] L. Mao, J. Huang, F. Ding, T. Fukuda, and T. Matsuno, "Modeling and control for uw-car in rough terrain," in *Proceedings of the 10th World Congress on Intelligent Control and Automation*. IEEE, 2012, pp. 3747–3752.

[80] J. Huang, F. Ding, T. Fukuda, and T. Matsuno, "Modeling and velocity control for a novel narrow vehicle based on mobile wheeled inverted pendulum," *IEEE Transactions on Control Systems Technology*, vol. 21, no. 5, pp. 1607–1617, 2012.

[81] Segway. Gm and segway join forces to reinvent urban transportation. [Online]. Available: https://newatlas.com/segway-car-project-puma/11413/

[82] H. Kim and S. Jung, "Development and control of a personal robotic vehicle for amusement," in *International Conference on Hybrid Information Technology*. Springer, 2012, pp. 574–581.

[83] G. Motors. General motors en-v drives autonomously. [Online]. Available: http://youtu.be/zoKxx0GEEFE

[84] K. Goher, "Mathematical modelling and control of a two-wheeled puma-like vehicle," 2016.

[85] Y. Sago, K. Terashima, Y. Noda, and K. Kakihara, "Attitude control using active-mass-system in parallel two-wheel vehicle with underslung vehicle body," in *2014 IEEE International Conference on Systems, Man, and Cybernetics (SMC)*. IEEE, 2014, pp. 1532–1537.

[86] Y. Noda, Y. Sago, K. Terashima, K. Kakihara, and H. Kawamura, "Development of parallel two-wheel vehicle with lower gravity center of vehicle body." in *ICINCO (2)*, 2012, pp. 70–76.

[87] S. Ahmad and M. O. Tokhi, "Linear quadratic regulator (lqr) approach for lifting and stabilizing of two-wheeled wheelchair," in *2011 4th International Conference on Mechatronics (ICOM)*. IEEE, 2011, pp. 1–6.

[88] K. Goher, S. Ahmad, and O. M. Tokhi, "A new configuration of two wheeled vehicles: Towards a more workspace and motion flexibility," in *2010 IEEE International Systems Conference*. IEEE, 2010, pp. 524–528.

[89] K. M. Goher, "A two-wheeled machine with a handling mechanism in two different directions," *Robotics and biomimetics*, vol. 3, no. 1, pp. 1–22, 2016.

[90] A. M. Almeshal, K. M. Goher, and M. O. Tokhi, "Dynamic modelling and stabilization of a new configuration of two-wheeled machines," *Robotics and Autonomous Systems*, vol. 61, no. 5, pp. 443–472, 2013.

[91] A. M. Almeshal, K. M. Goher, A. Nasir, M. O. Tokhi, and S. A. Agouri, "Fuzzy logic optimized control of a novel structure two-wheeled robotic vehicle using hsdbc, sda and bfa: a comparative study," in *2013 18th International Conference on Methods & Models in Automation & Robotics (MMAR)*. IEEE, 2013, pp. 656–661.

[92] K. M. Goher and M. Tokhi, "Genetic algorithm based modeling and control of a two wheeled vehicle with an extended rod, a lagrangian based dynamic approach," in *2010 IEEE 9th International Conference on Cyberntic Intelligent Systems*. IEEE, 2010, pp. 1–6.

[93] K. M. Goher and S. O. Fadlallah, "Control of a two-wheeled machine with two-directions handling mechanism using pid and pd-flc algorithms," *International Journal of Automation and Computing*, vol. 16, no. 4, pp. 511–533, 2019.

[94] S. Ahmad, N. H. Siddique, and M. O. Tokhi, "A modular fuzzy control approach for two-wheeled wheelchair," *Journal of Intelligent & Robotic Systems*, vol. 64, no. 3, pp. 401–426, 2011.

[95] W. Ye, Z. Li, C. Yang, J. Sun, C.-Y. Su, and R. Lu, "Vision-based human tracking control of a wheeled inverted pendulum robot," *IEEE transactions on cybernetics*, vol. 46, no. 11, pp. 2423–2434, 2015.

[96] J. Huang, M. Zhang, S. Ri, C. Xiong, Z. Li, and Y. Kang, "High-order disturbance-observer-based sliding mode control for mobile wheeled inverted pendulum systems," *IEEE Transactions on Industrial Electronics*, vol. 67, no. 3, pp. 2030–2041, 2019.

[97] P. N. Dao and Y.-C. Liu, "Adaptive reinforcement learning strategy with sliding mode control for unknown and disturbed wheeled inverted pendulum," *International Journal of Control, Automation and Systems*, pp. 1–12, 2020.

[98] A. A. Wardana, T. Takaki, T. Aoyama, and I. Ishii, "Dynamic modeling and step-climbing analysis of a two-wheeled stair-climbing inverted pendulum robot," *Advanced Robotics*, vol. 34, no. 5, pp. 313–327, 2020.

[99] M. Muhammad, A. A. Bature, U. Zangina, S. Buyamin, A. Ahmad, and M. A. Shamsudin, "Velocity control of a two-wheeled inverted pendulum mobile robot: a fuzzy model-based approach," *Bulletin of Electrical Engineering and Informatics*, vol. 8, no. 3, pp. 808–817, 2019.

[100] M. Deng, A. Inoue, K. Sekiguchi, and L. Jiang, "Two-wheeled mobile robot motion control in dynamic environments," *Robotics and Computer-Integrated Manufacturing*, vol. 26, no. 3, pp. 268–272, 2010.

[101] D.-H. Kim and J.-H. Oh, "Tracking control of a two-wheeled mobile robot using input–output linearization," *Control Engineering Practice*, vol. 7, no. 3, pp. 369–373, 1999.

[102] M. Yue, S. Wang, and J.-Z. Sun, "Simultaneous balancing and trajectory tracking control for two-wheeled inverted pendulum vehicles: a composite control approach," *Neurocomputing*, vol. 191, pp. 44–54, 2016.

[103] K. D. Do and G. Seet, "Motion control of a two-wheeled mobile vehicle with an inverted pendulum," *Journal of Intelligent & Robotic Systems*, vol. 60, no. 3, pp. 577–605, 2010.

[104] L. Canete and T. Takahashi, "Modeling, analysis and compensation of disturbances during task execution of a wheeled inverted pendulum type assistant robot using a unified controller," *Advanced Robotics*, vol. 29, no. 22, pp. 1453–1462, 2015.

[105] M. T. Ravichandran and A. D. Mahindrakar, "Robust stabilization of a class of underactuated mechanical systems using time scaling and lyapunov redesign," *IEEE Transactions on Industrial Electronics*, vol. 58, no. 9, pp. 4299–4313, 2010.

[106] M. Yadav, A. K. Gupta, B. Pratap, and S. Saini, "Robust control design for inverted pendulum system with uncertain disturbances," in *2016 IEEE 1st International Conference on Power Electronics, Intelligent Control and Energy Systems (ICPEICES)*. IEEE, 2016, pp. 1–6.

[107] H. Fukushima, K. Muro, and F. Matsuno, "Sliding-mode control for transformation to an inverted pendulum mode of a mobile robot with wheel-arms," *IEEE Transactions on Industrial Electronics*, vol. 62, no. 7, pp. 4257–4266, 2014.

[108] R. Tang and R. Green, "Obstacle avoidance on a mobile inverted pendulum robot," in *2009 24th International Conference Image and Vision Computing New Zealand*. IEEE, 2009, pp. 254–259.

[109] Z. Kausar, K. Stol, and N. Patel, "The effect of terrain inclination on performance and the stability region of two-wheeled mobile robots," *International Journal of Advanced Robotic Systems*, vol. 9, no. 5, p. 218, 2012.

[110] M.-C. Tsai and J.-S. Hu, "Pilot control of an auto-balancing two-wheeled cart," *Advanced Robotics*, vol. 21, no. 7, pp. 817–827, 2007.

[111] F. Dai, X. Gao, S. Jiang, W. Guo, and Y. Liu, "A two-wheeled inverted pendulum robot with friction compensation," *Mechatronics*, vol. 30, pp. 116–125, 2015.

[112] J. H. Park and H. C. Cho, "An online trajectory modifier for the base link of biped robots to enhance locomotion stability," in *Proceedings 2000 ICRA. Millennium Conference. IEEE International Conference on Robotics and Automation. Symposia Proceedings (Cat. No. 00CH37065)*, vol. 4. IEEE, 2000, pp. 3353–3358.

[113] K. Yokoyama and M. Takahashi, "Dynamics-based nonlinear acceleration control with energy shaping for a mobile inverted pendulum with a slider mechanism," *IEEE Transactions on Control Systems Technology*, vol. 24, no. 1, pp. 40–55, 2015.

[114] S. Jeong and T. Takahashi, "Wheeled inverted pendulum type assistant robot: design concept and mobile control," *Intelligent Service Robotics*, vol. 1, no. 4, pp. 313–320, 2008.

[115] J. Li, X. Gao, Q. Huang, Q. Du, and X. Duan, "Mechanical design and dynamic modeling of a two-wheeled inverted pendulum mobile robot," in *2007 IEEE International Conference on Automation and Logistics*. IEEE, 2007, pp. 1614–1619.

[116] D. Choi and J.-H. Oh, "Human-friendly motion control of a wheeled inverted pendulum by reduced-order disturbance observer," in *2008 IEEE International Conference on Robotics and Automation*. IEEE, 2008, pp. 2521–2526.

[117] P. Oryschuk, A. Salerno, A. M. Al-Husseini, and J. Angeles, "Experimental validation of an underactuated two-wheeled mobile robot," *IEEE/ASME Transactions on Mechatronics*, vol. 14, no. 2, pp. 252–257, 2009.

[118] A. Blankespoor and R. Roemer, "Experimental verification of the dynamic model for a quarter size self-balancing wheelchair," in *Proceedings of the 2004 American Control Conference*, vol. 1. IEEE, 2004, pp. 488–492.

[119] S. Amagai, M. Kamatani, and T. Murakami, "A comparison study of velocity and torque based control of two-wheel mobile robot for human operation," in *2017 24th International Conference on Mechatronics and Machine Vision in Practice (M2VIP)*. IEEE, 2017, pp. 1–6.

[120] K. Hirata and T. Murakami, "A realization of step passage motion in two-wheel wheelchair systems utilizing variable repulsive compliance control," in *2013 IEEE International Symposium on Industrial Electronics*. IEEE, 2013, pp. 1–6.

[121] K. Hirata, M. Kamatani, and T. Murakami, “Advanced motion control of two-wheel wheelchair for slope environment,” in *IECON 2013-39th Annual Conference of the IEEE Industrial Electronics Society*. IEEE, 2013, pp. 6436–6441.

[122] S. Amagai and T. Murakami, “An approach to robust velocity control of two-wheel wheelchair,” in *IECON 2016-42nd Annual Conference of the IEEE Industrial Electronics Society*. IEEE, 2016, pp. 494–499.

[123] K. Hirata and T. Murakami, “Assisted control of step passage motion and its comfort evaluation in two-wheel wheelchair systems,” *IEEJ Transactions on Industry Applications*, vol. 133, no. 12, pp. 1120–1127, 2013.

[124] H.-J. Lee and S. Jung, “Control of a mobile inverted pendulum robot system,” in *2008 International Conference on Control, Automation and Systems*. IEEE, 2008, pp. 217–222.

[125] C. Yang, Z. Li, and J. Li, “Trajectory planning and optimized adaptive control for a class of wheeled inverted pendulum vehicle models,” *IEEE Transactions on Cybernetics*, vol. 43, no. 1, pp. 24–36, 2012.

[126] K. Sangfeel, S. Eunji, K. KyungSik, and S. Byung Seop, “Design of fuzzy logic controller for inverted pendulum-type mobile robot using smart in-wheel motor,” *Indian Journal of Science and Technology*, vol. 8, no. S5, pp. 187–96, 2015.

[127] W. Guo, X. Gao, S. Jiang, C. Zong, and F. Dai, “Lqr controller design for two-wheeled robot with a movable seat,” in *The 26th Chinese Control and Decision Conference (2014 CCDC)*. IEEE, 2014, pp. 5248–5253.

[128] F. Ding, J. Huang, Y. Wang, T. Matsuno, T. Fukuda, and K. Sekiyama, “Modeling and control of a novel narrow vehicle,” in *2010 IEEE International Conference on Robotics and Biomimetics*. IEEE, 2010, pp. 1130–1135.

[129] K. Pathak, J. Franch, and S. K. Agrawal, “Velocity and position control of a wheeled inverted pendulum by partial feedback linearization,” *IEEE Transactions on robotics*, vol. 21, no. 3, pp. 505–513, 2005.

[130] ——, “Velocity control of a wheeled inverted pendulum by partial feedback linearization,” in *2004 43rd IEEE Conference on Decision and Control (CDC)(IEEE Cat. No. 04CH37601)*, vol. 4. IEEE, 2004, pp. 3962–3967.

[131] W. Sun, S.-F. Su, J. Xia, and Y. Wu, “Adaptive tracking control of wheeled inverted pendulums with periodic disturbances,” *IEEE Transactions on Cybernetics*, vol. 50, no. 5, pp. 1867–1876, 2018.

[132] S. Kim and S. Kwon, “Dynamic modeling of a two-wheeled inverted pendulum balancing mobile robot,” *International Journal of Control, Automation and Systems*, vol. 13, no. 4, pp. 926–933, 2015.

[133] A. Sinha, P. Prasoon, P. K. Bharadwaj, and A. C. Ranasinghe, “Nonlinear autonomous control of a two-wheeled inverted pendulum mobile robot based on sliding mode,” in *2015 International Conference on Computational Intelligence and Networks*. IEEE, 2015, pp. 52–57.

[134] D. Choi, M. Kim, and J.-H. Oh, “Development of a rapid mobile robot with a multi-degree-of-freedom inverted pendulum using the model-based zero-moment point stabilization method,” *Advanced Robotics*, vol. 26, no. 5-6, pp. 515–535, 2012.

[135] N. Tomokuni and M. Shino, “Wheeled inverted-pendulum-type personal mobility robot with collaborative control of seat slider and leg wheels,” in *2012 IEEE/RSJ International Conference on Intelligent Robots and Systems*. IEEE, 2012, pp. 5367–5372.

[136] Z. Li, Y. Li, C. Yang, and N. Ding, “Motion control of an autonomous vehicle based on wheeled inverted pendulum using neural-adaptive implicit control,” in *2010 IEEE/RSJ International Conference on Intelligent Robots and Systems*. IEEE, 2010, pp. 133–138.

[137] Z. Li and C. Yang, “Neural-adaptive output feedback control of a class of transportation vehicles based on wheeled inverted pendulum models,” *IEEE Transactions on Control Systems Technology*, vol. 20, no. 6, pp. 1583–1591, 2011.

[138] A. OKUBANJO and O. OYETOLA, “Dynamic mathematical modeling and control algorithms design of an inverted pendulum system (ips),” *Turkish Journal of Engineering*, vol. 3, no. 1, pp. 14–24, 2019.

[139] M. Zafar, S. Hutchinson, and E. A. Theodorou, “Hierarchical optimization for whole-body control of wheeled inverted pendulum humanoids,” in *2019 International Conference on Robotics and Automation (ICRA)*. IEEE, 2019, pp. 7535–7542.

[140] H. Ahmadi Jeyed and A. Ghaffari, “A nonlinear optimal control based on the sdre technique for the two-wheeled self-balancing robot,” *Australian Journal of Mechanical Engineering*, pp. 1–9, 2020.

[141] S. Kim and S. Kwon, “Nonlinear control design for a two-wheeled balancing robot,” in *2013 10th International Conference on Ubiquitous Robots and Ambient Intelligence (URAI)*. IEEE, 2013, pp. 486–487.

[142] M. Muhammad, S. Buyamin, M. Ahmad, S. Nawawi, and A. Bature, “Multiple operating points model-based control of a two-wheeled inverted pendulum mobile robot,” *International Journal of Mechanical & Mechatronics Engineering*, vol. 13, no. 5, pp. 1–9, 2013.

[143] A. D. Hoang, H. Q. Nguyen, P. N. Dao, and T. H. Nguyen, "Output feedback adaptive reinforcement learning tracking control for wheel inverted pendulum systems," in *Research in Intelligent and Computing in Engineering*. Springer, 2021, pp. 535–547.

[144] I. Chawla and A. Singla, "Real-time stabilization control of a rotary inverted pendulum using lqr-based sliding mode controller," *Arabian Journal for Science and Engineering*, pp. 1–8.

[145] D. Chen, S. Li, and L. Liao, "A recurrent neural network applied to optimal motion control of mobile robots with physical constraints," *Applied Soft Computing*, vol. 85, p. 105880, 2019.

[146] C.-H. Chiu, Y.-F. Peng, and Y.-W. Lin, "Intelligent backstepping control for wheeled inverted pendulum," *Expert Systems with Applications*, vol. 38, no. 4, pp. 3364–3371, 2011.

[147] Z. Li, Y. Zhang, and Y. Yang, "Support vector machine optimal control for mobile wheeled inverted pendulums with unmodelled dynamics," *Neurocomputing*, vol. 73, no. 13-15, pp. 2773–2782, 2010.

[148] H. Chen, P. M. Wensing, and W. Zhang, "Optimal control of a differentially flat two-dimensional spring-loaded inverted pendulum model," *IEEE Robotics and Automation Letters*, vol. 5, no. 2, pp. 307–314, 2019.

[149] S. Jung and S. S. Kim, "Control experiment of a wheel-driven mobile inverted pendulum using neural network," *IEEE Transactions on Control Systems Technology*, vol. 16, no. 2, pp. 297–303, 2008.

[150] J.-J. Wang, "Simulation studies of inverted pendulum based on pid controllers," *Simulation Modelling Practice and Theory*, vol. 19, no. 1, pp. 440–449, 2011.

[151] M.-T. Ho and C.-Y. Lin, "Pid controller design for robust performance," *IEEE Transactions on Automatic Control*, vol. 48, no. 8, pp. 1404–1409, 2003.

[152] J. F. S. Trentin, S. Da Silva, J. M. D. S. Ribeiro, and H. Schaub, "Inverted pendulum nonlinear controllers using two reaction wheels: Design and implementation," *IEEE Access*, vol. 8, pp. 74 922–74 932, 2020.

[153] R. YUSOF and S. OMATU, "A multivariable self-tuning pid controller," *International Journal of Control*, vol. 57, no. 6, pp. 1387–1403, 1993.

[154] H. Azizan, M. Jafarinasab, S. Behbahani, and M. Danesh, "Fuzzy control based on lmi approach and fuzzy interpretation of the rider input for two wheeled balancing human transporter," in *IEEE ICCA 2010*. IEEE, 2010, pp. 192–197.

[155] S. Jung, H.-T. Cho, and T. C. Hsia, “Neural network control for position tracking of a two-axis inverted pendulum system: Experimental studies,” *IEEE Transactions on Neural Networks*, vol. 18, no. 4, pp. 1042–1048, 2007.

[156] K. Tanaka, “An introduction to fuzzy logic for practical applications,” 1997.

[157] H. A. Hagras, “A hierarchical type-2 fuzzy logic control architecture for autonomous mobile robots,” *IEEE Transactions on Fuzzy systems*, vol. 12, no. 4, pp. 524–539, 2004.

[158] M. E. Magana and F. Holzapfel, “Fuzzy-logic control of an inverted pendulum with vision feedback,” *IEEE transactions on education*, vol. 41, no. 2, pp. 165–170, 1998.

[159] C. Larbes, S. A. Cheikh, T. Obeidi, and A. Zerguerras, “Genetic algorithms optimized fuzzy logic control for the maximum power point tracking in photovoltaic system,” *Renewable energy*, vol. 34, no. 10, pp. 2093–2100, 2009.

[160] J. Nelson and L. G. Kraft, “Real-time control of an inverted pendulum system using complementary neural network and optimal techniques,” in *Proceedings of 1994 American Control Conference-ACC’94*, vol. 3. IEEE, 1994, pp. 2553–2554.

[161] N. D. Quyen, N. Van Thuyen, N. Q. Hoc, and N. D. Hien, “Rotary inverted pendulum and control of rotary inverted pendulum by artificial neural network,” in *Proc. Natl. Conf. Theor. Phys*, vol. 37, 2012, pp. 243–249.

[162] S. H. Zabihifar, H. Navvabi, and A. S. Yushchenko, “Dual adaptive neural network controller for underactuated systems,” *Robotica*, pp. 1–18.

[163] E. V. Kumar and J. Jerome, “Robust lqr controller design for stabilizing and trajectory tracking of inverted pendulum,” *Procedia Engineering*, vol. 64, pp. 169–178, 2013.

[164] M. K. Gupta, K. Bansal, and A. K. Singh, “Stabilization of triple link inverted pendulum system based on lqr control technique,” in *International Conference on Recent Advances and Innovations in Engineering (ICRAIE-2014)*. IEEE, 2014, pp. 1–5.

[165] A. Ghaffari, A. Shariati, and A. H. Shamekhi, “A modified dynamical formulation for two-wheeled self-balancing robots,” *Nonlinear Dynamics*, vol. 83, no. 1, pp. 217–230, 2016.

[166] D. Auckly, L. Kapitanski, and W. White, “Control of nonlinear underactuated systems,” *Communications on Pure and Applied Mathematics: A Journal Issued by the Courant Institute of Mathematical Sciences*, vol. 53, no. 3, pp. 354–369, 2000.

[167] X.-L. Zhang, H.-M. Fan, J.-Y. Zang, L. Zhao, and S. Hao, "Nonlinear control of triple inverted pendulum based on ga–pidnn," *Nonlinear Dynamics*, vol. 79, no. 2, pp. 1185–1194, 2015.

[168] P. Dang and F. L. Lewis, "Controller for swing-up and balance of single inverted pendulum using sdre-based solution," in *31st Annual Conference of IEEE Industrial Electronics Society, 2005. IECON 2005.* IEEE, 2005, pp. 6–pp.

[169] S. Kim and S. Kwon, "Nonlinear optimal control design for underactuated two-wheeled inverted pendulum mobile platform," *IEEE/ASME Transactions on Mechatronics*, vol. 22, no. 6, pp. 2803–2808, 2017.

[170] M. Nikpour, L. Huang, A. M. Al-Jumaily, and B. Lotfi, "Stability control of mobile inverted pendulum through an added movable mechanism," in *2018 25th International Conference on Mechatronics and Machine Vision in Practice (M2VIP).* IEEE, 2018, pp. 1–6.

[171] J. H. Park and K. D. Kim, "Biped robot walking using gravity-compensated inverted pendulum mode and computed torque control," in *Proceedings. 1998 IEEE International Conference on Robotics and Automation (Cat. No. 98CH36146)*, vol. 4. IEEE, 1998, pp. 3528–3533.

[172] W. Shang and S. Cong, "Nonlinear computed torque control for a high-speed planar parallel manipulator," *Mechatronics*, vol. 19, no. 6, pp. 987–992, 2009.

[173] G. V. Raffo, M. G. Ortega, V. Madero, and F. R. Rubio, "Two-wheeled self-balanced pendulum workspace improvement via underactuated robust nonlinear control," *Control Engineering Practice*, vol. 44, pp. 231–242, 2015.

[174] N. S. Ahmad, "Robust h_∞ fuzzy logic control for enhanced tracking performance of a wheeled mobile robot in the presence of uncertain nonlinear perturbations," *Sensors*, vol. 20, no. 13, p. 3673, 2020.

[175] G. V. Raffo, M. G. Ortega, and F. R. Rubio, "Nonlinear h_∞ control applied to the personal pendulum car," in *2007 European Control Conference (ECC).* IEEE, 2007, pp. 2065–2070.

[176] C. Acar and T. Murakami, "Underactuated two-wheeled mobile manipulator control using nonlinear backstepping method," in *2008 34th Annual Conference of IEEE Industrial Electronics*. IEEE, 2008, pp. 1680–1685.

[177] G. V. Raffo, V. Madero, and M. G. Ortega, "An application of the underactuated nonlinear h_∞ controller to two-wheeled self-balanced vehicles," in *2010 IEEE 15th Conference on Emerging Technologies & Factory Automation (ETFA 2010).* IEEE, 2010, pp. 1–6.

[178] P. K. Abeygunawardhana, M. Defoort, and T. Murakami, “Self-sustaining control of two-wheel mobile manipulator using sliding mode control,” in *2010 11th IEEE International Workshop on Advanced Motion Control (AMC)*. IEEE, 2010, pp. 792–797.

[179] J. Huang, Z.-H. Guan, T. Matsuno, T. Fukuda, and K. Sekiyama, “Sliding-mode velocity control of mobile-wheeled inverted-pendulum systems,” *IEEE Transactions on robotics*, vol. 26, no. 4, pp. 750–758, 2010.

[180] M. Chen and W.-H. Chen, “Sliding mode control for a class of uncertain nonlinear system based on disturbance observer,” *International journal of adaptive control and signal processing*, vol. 24, no. 1, pp. 51–64, 2010.

[181] M. Yue and X. Wei, “Dynamic balance and motion control for wheeled inverted pendulum vehicle via hierarchical sliding mode approach,” *Proceedings of the Institution of Mechanical Engineers, Part I: Journal of Systems and Control Engineering*, vol. 228, no. 6, pp. 351–358, 2014.

[182] T. Elmokadem, M. Zribi, and K. Youcef-Toumi, “Control for dynamic positioning and way-point tracking of underactuated autonomous underwater vehicles using sliding mode control,” *Journal of Intelligent & Robotic Systems*, vol. 95, no. 3, pp. 1113–1132, 2019.

[183] M.-C. Pai, “Discrete-time output feedback quasi-sliding mode control for robust tracking and model following of uncertain systems,” *Journal of the Franklin Institute*, vol. 351, no. 5, pp. 2623–2639, 2014.

[184] R. Guruganesh, B. Bandyopadhyay, H. Arya, and G. Singh, “Design and hardware implementation of autopilot control laws for mav using super twisting control,” *Journal of Intelligent & Robotic Systems*, vol. 90, no. 3, pp. 455–471, 2018.

[185] I. Eker, “Second-order sliding mode control with experimental application,” *ISA transactions*, vol. 49, no. 3, pp. 394–405, 2010.

[186] A. Ammar, “Second-order sliding mode-direct torque control and load torque estimation for sensorless model reference adaptive system–based induction machine,” *Proceedings of the Institution of Mechanical Engineers, Part I: Journal of Systems and Control Engineering*, vol. 235, no. 1, pp. 15–29, 2021.

[187] N. G. M. Thao, D. H. Nghia, and N. H. Phuc, “A pid backstepping controller for two-wheeled self-balancing robot,” in *International Forum on Strategic Technology 2010*. IEEE, 2010, pp. 76–81.

[188] Ö. Bebek, M. A. Suster, S. Rajgopal, M. J. Fu, X. Huang, M. C. Çavuşoğlu, D. J. Young, M. Mehregany, A. J. Van Den Bogert, and C. H. Mastrangelo, “Personal navigation via high-resolution gait-corrected inertial measurement

units," *IEEE transactions on Instrumentation and measurement*, vol. 59, no. 11, pp. 3018–3027, 2010.

[189] Z. Wang, W. Wang, C. Hu, X. Si, and J. Li, "A real-time prognostic method for the drift errors in the inertial navigation system by a nonlinear random-coefficient regression model," *Acta Astronautica*, vol. 103, pp. 45–54, 2014.

[190] A. R. Jiménez, F. Seco, J. C. Prieto, and J. Guevara, "Indoor pedestrian navigation using an ins/ekf framework for yaw drift reduction and a foot-mounted imu," in *2010 7th Workshop on Positioning, Navigation and Communication*. IEEE, 2010, pp. 135–143.

[191] M. Wu, Y. Wu, X. Hu, and D. Hu, "Optimization-based alignment for inertial navigation systems: Theory and algorithm," *Aerospace science and technology*, vol. 15, no. 1, pp. 1–17, 2011.

[192] H. Lee and S. Jung, "Balancing and navigation control of a mobile inverted pendulum robot using sensor fusion of low cost sensors," *Mechatronics*, vol. 22, no. 1, pp. 95–105, 2012.

[193] Y. S. Suh, "Attitude estimation by multiple-mode kalman filters," *IEEE Transactions on industrial electronics*, vol. 53, no. 4, pp. 1386–1389, 2006.

[194] J. Leavitt, A. Sideris, and J. E. Bobrow, "High bandwidth tilt measurement using low-cost sensors," *IEEE/ASME transactions on mechatronics*, vol. 11, no. 3, pp. 320–327, 2006.

[195] H. Ha, S. Ryu, and J. Lee, "A robust control of mobile inverted pendulum using single accelerometer," in *The Fifteenth International Symposium on Artificial Life and Robotics*, 2010.

[196] H.-W. Lee, S.-W. Ryu, and J.-M. Lee, "Optimal posture of mobile inverted pendulum using a single gyroscope and tilt sensor," in *2009 ICCAS-SICE*. IEEE, 2009, pp. 865–870.

[197] S. Nawawi, M. Ahmad, and J. Osman, "Real-time control of a two-wheeled inverted pendulum mobile robot," *World Academy of Science, Engineering and Technology*, vol. 39, pp. 214–220, 2008.

[198] Á. Odry, R. Fuller, I. J. Rudas, and P. Odry, "Kalman filter for mobile-robot attitude estimation: Novel optimized and adaptive solutions," *Mechanical systems and signal processing*, vol. 110, pp. 569–589, 2018.

[199] B. Strah and S. Rinderknecht, "High dynamics tilt estimation using simple observer," in *Eurocon 2013*. IEEE, 2013, pp. 1964–1971.

[200] N. Kaempchen and K. Dietmayer, “Data synchronization strategies for multi-sensor fusion,” in *Proceedings of the IEEE Conference on Intelligent Transportation Systems*, vol. 85, no. 1, 2003, pp. 1–9.

[201] M. S. Grewal and A. P. Andrews, *Kalman filtering: Theory and Practice with MATLAB*. John Wiley & Sons, 2014.

[202] F. Gustafsson, “Particle filter theory and practice with positioning applications,” *IEEE Aerospace and Electronic Systems Magazine*, vol. 25, no. 7, pp. 53–82, 2010.

[203] S.-h. P. Won, W. W. Melek, and F. Golnaraghi, “A kalman/particle filter-based position and orientation estimation method using a position sensor/inertial measurement unit hybrid system,” *IEEE Transactions on Industrial Electronics*, vol. 57, no. 5, pp. 1787–1798, 2009.

[204] G. Casiez, N. Roussel, and D. Vogel, “1€ filter: a simple speed-based low-pass filter for noisy input in interactive systems,” in *Proceedings of the SIGCHI Conference on Human Factors in Computing Systems*, 2012, pp. 2527–2530.

[205] S. R. Singiresu *et al.*, *Mechanical vibrations*. Addison Wesley Boston, MA, 1995.

[206] J. L. Meriam and L. G. Kraige, *Engineering mechanics: dynamics*. John Wiley & Sons, 2012, vol. 2.

[207] N. Esmaeili, A. Alfi, and H. Khosravi, “Balancing and trajectory tracking of two-wheeled mobile robot using backstepping sliding mode control: design and experiments,” *Journal of Intelligent & Robotic Systems*, vol. 87, no. 3-4, pp. 601–613, 2017.

[208] J. J. Craig, *Introduction to robotics: mechanics and control, 3/E*. Pearson Education India, 2009.

[209] P. J. From, J. T. Gravdahl, K. Y. Pettersen *et al.*, *Vehicle-manipulator systems*. Springer, 2016.

[210] R. M. Murray, Z. Li, S. S. Sastry, and S. S. Sastry, *A mathematical introduction to robotic manipulation*. CRC press, 1994.

[211] W. Bolton, *Mechatronics: electronic control systems in mechanical and electrical engineering*. Pearson Education, 2003.

[212] R. Vilanova and A. Visioli, *PID control in the third millennium*. Springer, 2012.

[213] Y. Shtessel, C. Edwards, L. Fridman, and A. Levant, *Sliding mode control and observation*. Springer, 2014.

[214] Z. Zhao, J. Yang, S. Li, Z. Zhang, and L. Guo, "Finite-time super-twisting sliding mode control for mars entry trajectory tracking," *Journal of the Franklin Institute*, vol. 352, no. 11, pp. 5226–5248, 2015.

Appendix A

Dynamic Model Details of the Conventional System

A.1 Dynamic model equations

If $q_i = \theta_r$

$$\frac{2r^2}{d^2}J_{y_{\mathrm{w}}}(\ddot{\theta}_r - \ddot{\theta}_l) + m_{\mathrm{w}}r^2\ddot{\theta}_r + J_{z_{\mathrm{w}}}\ddot{\theta}_r + \frac{1}{4}m_b r^2(\ddot{\theta}_r + \ddot{\theta}_l) + \frac{l^2r^2}{d^2}m_b[(\ddot{\theta}_r - \ddot{\theta}_l)\sin^2\theta_b$$
$$+ 2(\dot{\theta}_r - \dot{\theta}_l)\dot{\theta}_b\cos\theta_b\sin\theta_b] + \frac{1}{2}m_b rl[\ddot{\theta}_b\cos\theta_b - \dot{\theta}_b^{\,2}\sin\theta_b] + \frac{r^2}{d^2}J_{x_b}[(\ddot{\theta}_r - \ddot{\theta}_l)\cos^2\theta_b$$
$$- 2(\dot{\theta}_r - \dot{\theta}_l)\dot{\theta}_b\sin\theta_b\cos\theta_b] + \frac{r^2}{d^2}J_{y_b}[(\ddot{\theta}_r - \ddot{\theta}_l)\sin^2\theta_b + 2(\dot{\theta}_r - \dot{\theta}_l)\dot{\theta}_b\sin\theta_b\cos\theta_b] = \tau_r$$

If $q_i = \theta_l$

$$-\frac{2r^2}{d^2}J_{y_{\mathrm{w}}}(\ddot{\theta}_r - \ddot{\theta}_l) + m_{\mathrm{w}}r^2\ddot{\theta}_l + J_{z_{\mathrm{w}}}\ddot{\theta}_l + \frac{1}{4}m_b r^2(\ddot{\theta}_r + \ddot{\theta}_l) - \frac{l^2r^2}{d^2}m_b[(\ddot{\theta}_r - \ddot{\theta}_l)\sin^2\theta_b$$
$$+ 2(\dot{\theta}_r - \dot{\theta}_l)\dot{\theta}_b\cos\theta_b\sin\theta_b] + \frac{1}{2}m_b rl[\ddot{\theta}_b\cos\theta_b - \dot{\theta}_b^{\,2}\sin\theta_b] - \frac{r^2}{d^2}J_{x_b}[(\ddot{\theta}_r - \ddot{\theta}_l)\cos^2\theta_b$$
$$- 2(\dot{\theta}_r - \dot{\theta}_l)\dot{\theta}_b\sin\theta_b\cos\theta_b] - \frac{r^2}{d^2}J_{y_b}[(\ddot{\theta}_r - \ddot{\theta}_l)\sin^2\theta_b + 2(\dot{\theta}_r - \dot{\theta}_l)\dot{\theta}_b\sin\theta_b\cos\theta_b] = \tau_l$$

If $q_i = \theta_b$

$$
\begin{aligned}
& m_b l^2 \ddot{\theta}_b + \frac{1}{2} m_b r l (\ddot{\theta}_r + \ddot{\theta}_l) \cos\theta_b - \frac{1}{2} m_b r l (\dot{\theta}_r + \dot{\theta}_l) \dot{\theta}_b \sin\theta_b + J_{z_b} \ddot{\theta}_b \\
& - \frac{l^2 r^2}{d^2} m_b (\dot{\theta}_r - \dot{\theta}_l)^2 \cos\theta_b \sin\theta_b + \frac{1}{2} m_b r l (\dot{\theta}_r + \dot{\theta}_l) \dot{\theta}_b \sin\theta_b + \frac{r^2}{d^2} J_{x_b} (\dot{\theta}_r - \dot{\theta}_l)^2 \sin\theta_b \cos\theta_b \\
& - \frac{r^2}{d^2} J_{y_b} (\dot{\theta}_r - \dot{\theta}_l)^2 \sin\theta_b \cos\theta_b - m_b g l \sin\theta_b = 0
\end{aligned}
$$

A.2 Inertia and Coriolis force matrix elements

$$
\begin{aligned}
& M_{c_{11}} = M_{c_{22}} = (m_{\mathrm{w}} + \frac{1}{4} m_b) r^2 + J_{\mathrm{w}_z} + \frac{r^2}{d^2} [m_b l^2 \sin^2\theta_b + 2 J_{\mathrm{w}_y} + J_{b_x} \sin^2\theta_b + J_{b_y} \cos^2\theta_b], \\
& M_{c_{12}} = \frac{1}{4} m_b r^2 - \frac{r^2}{d^2} [m_b l^2 \sin^2\theta_b + 2 J_{\mathrm{w}_y} + J_{b_x} \sin^2\theta_b + J_{b_y} \cos^2\theta_b], \\
& M_{c_{13}} = M_{c_{23}} = \frac{1}{2} m_b r l \cos\theta_b, \quad M_{c_{33}} = m_b l^2 + J_{b_z}, \\
& C_{c_{11}} = C_{c_{22}} = W_{c_1} \dot{\theta}_b, \quad C_{c_{12}} = C_{c_{21}} = -W_{c_1} \dot{\theta}_b, \quad C_{c_{13}} = \frac{d}{r} W_{c_1} \dot{\theta}_y - W_{c_2}, \\
& C_{c_{23}} = -\frac{d}{r} W_{c_1} \dot{\theta}_y - W_{c_2}, \quad C_{c_{31}} = -\frac{d}{r} W_{c_1} \dot{\theta}_y, \quad C_{c_{32}} = \frac{d}{r} W_{c_1} \dot{\theta}_y
\end{aligned}
$$

where

$$
W_{c_1} = \frac{r^2}{2d^2} [(m_b l^2 + J_{b_x} - J_{b_y}) \sin 2\theta_b], \qquad W_{c_2} = \frac{1}{2} m_b r l \dot{\theta}_b \sin\theta_b.
$$

A.3 Disturbances elements

$$\Delta M_{11} = \Delta M_{22} = (\frac{1}{4} + \frac{l^2}{d^2}\sin^2\theta_b)\Delta m_b r^2, \quad \Delta M_{12} = (\frac{1}{4} - \frac{l^2}{d^2}\sin^2\theta_b)\Delta m_b r^2,$$
$$\Delta M_{13} = \Delta M_{23} = \frac{1}{2}\Delta m_b r l \cos\theta_b, \quad \Delta M_{33} = \Delta m_b l^2,$$
$$\Delta C_{11} = \Delta C_{22} = W_{c_3}\dot{\theta}_b, \quad \Delta C_{12} = \Delta C_{21} = -W_{c_3}\dot{\theta}_b, \quad \Delta C_{13} = \frac{d}{r}W_{c_3}\dot{\theta}_y - W_{c_4},$$
$$\Delta C_{23} = -\frac{d}{r}W_{c_3}\dot{\theta}_y - W_{c_4}, \quad \Delta C_{31} = -\frac{d}{r}W_{c_3}\dot{\theta}_y, \quad \Delta C_{32} = \frac{d}{r}W_{c_3}\dot{\theta}_y,$$

where

$$W_{c_3} = \frac{r^2}{2d^2}\Delta m_b l^2 \sin 2\theta_b, \qquad W_{c_4} = \frac{1}{2}\Delta m_b r l \dot{\theta}_b \sin\theta_b.$$

$$R_1 = \frac{r^2}{d^2}m_b x_b(x_b\cos^2\theta_b + l\sin 2\theta_b)(\ddot{\theta}_r - \ddot{\theta}_l) - \frac{1}{2}m_b x_b r(\sin\theta_b\ddot{\theta}_b + \cos\theta_b\dot{\theta}_b^2)$$
$$- \frac{r}{d}m_b x_b\dot{\theta}_b\dot{\theta}_y(x_b\sin 2\theta_b - 2l\cos 2\theta_b),$$
$$R_2 = \frac{r^2}{d^2}m_b x_b(x_b\cos^2\theta_b + l\sin 2\theta_b)(\ddot{\theta}_l - \ddot{\theta}_r) - \frac{1}{2}m_b x_b r(\sin\theta_b\ddot{\theta}_b + \cos\theta_b\dot{\theta}_b^2)$$
$$+ \frac{r}{d}m_b x_b\dot{\theta}_b\dot{\theta}_y(x_b\sin 2\theta_b - 2l\cos 2\theta_b),$$
$$R_3 = -\frac{1}{2}m_b x_b r\sin\theta_b(\ddot{\theta}_r + \ddot{\theta}_l) + m_b x_b^2\ddot{\theta}_b + \frac{1}{2}m_b x_b\dot{\theta}_y^2(x_b\sin 2\theta_b - 2l\cos 2\theta_b)$$
$$+ m_b g x_b\cos\theta_b.$$

A.4 EOM elements

$$
\begin{aligned}
&A_{c_1} = -\hat{M}_{c_{11}}^{-1}(C_{c_{11}}\dot{\theta}_r + C_{c_{12}}\dot{\theta}_l + C_{c_{13}}\dot{\theta}_b) - \hat{M}_{c_{12}}^{-1}(C_{c_{21}}\dot{\theta}_r + C_{c_{22}}\dot{\theta}_l + C_{c_{23}}\dot{\theta}_b) \\
&- \hat{M}_{c_{13}}^{-1}(C_{c_{31}}\dot{\theta}_r + C_{c_{32}}\dot{\theta}_l + G_{c_3}), \\
&B_{c_1} = -\hat{M}_{c_{11}}^{-1}(D_{c_1} + R_{c_1}) - \hat{M}_{c_{12}}^{-1}(D_{c_2} + R_{c_2}) - \hat{M}_{c_{13}}^{-1}(D_{c_3} + R_{c_3}), \\
&A_{c_2} = -\hat{M}_{c_{21}}^{-1}(C_{c_{11}}\dot{\theta}_r + C_{c_{12}}\dot{\theta}_l + C_{c_{13}}\dot{\theta}_b) - \hat{M}_{c_{22}}^{-1}(C_{c_{21}}\dot{\theta}_r + C_{c_{22}}\dot{\theta}_l + C_{c_{23}}\dot{\theta}_b) \\
&- \hat{M}_{c_{23}}^{-1}(C_{c_{31}}\dot{\theta}_r + C_{c_{32}}\dot{\theta}_l + G_{c_3}), \\
&B_{c_2} = -\hat{M}_{c_{21}}^{-1}(D_{c_1} + R_{c_1}) - \hat{M}_{c_{22}}^{-1}(D_{c_2} + R_{c_2}) - \hat{M}_{c_{23}}^{-1}(D_{c_3} + R_{c_3}), \\
&A_{c_3} = -\hat{M}_{c_{31}}^{-1}(C_{c_{11}}\dot{\theta}_r + C_{c_{12}}\dot{\theta}_l + C_{c_{13}}\dot{\theta}_b) - \hat{M}_{c_{32}}^{-1}(C_{c_{21}}\dot{\theta}_r + C_{c_{22}}\dot{\theta}_l + C_{c_{23}}\dot{\theta}_b) \\
&- \hat{M}_{c_{33}}^{-1}(C_{c_{31}}\dot{\theta}_r + C_{c_{32}}\dot{\theta}_l + G_{c_3}), \\
&B_{c_3} = -\hat{M}_{c_{31}}^{-1}(D_{c_1} + R_{c_1}) - \hat{M}_{c_{32}}^{-1}(D_{c_2} + R_{c_2}) - \hat{M}_{c_{33}}^{-1}(D_{c_3} + R_{c_3}).
\end{aligned}
$$

Appendix B

Dynamic Model Details of the Proposed System

B.1 Dynamic model equations

If $q_i = \theta_r$

$$
\begin{aligned}
&\frac{2r^2}{d^2} J_{w_y}(\ddot{\theta}_r - \ddot{\theta}_l) + m_w r^2 \ddot{\theta}_r + J_{w_z}\ddot{\theta}_r + \frac{1}{4} m_b r^2(\ddot{\theta}_r + \ddot{\theta}_l) + \frac{l^2 r^2}{d^2} m_b[(\ddot{\theta}_r - \ddot{\theta}_l)\sin^2\theta_b \\
&+ 2(\dot{\theta}_r - \dot{\theta}_l)\dot{\theta}_b \cos\theta_b \sin\theta_b] + \frac{1}{2} m_b r l[\ddot{\theta}_b \cos\theta_b - \dot{\theta}_b{}^2 \sin\theta_b] + \frac{r^2}{d^2} J_{b_x}[(\ddot{\theta}_r - \ddot{\theta}_l)\cos^2\theta_b \\
&- 2(\dot{\theta}_r - \dot{\theta}_l)\dot{\theta}_b \sin\theta_b \cos\theta_b] + \frac{r^2}{d^2} J_{b_y}[(\ddot{\theta}_r - \ddot{\theta}_l)\sin^2\theta_b + 2(\dot{\theta}_r - \dot{\theta}_l)\dot{\theta}_b \sin\theta_b \cos\theta_b] \\
&+ \frac{1}{2} m_p[\frac{r^2}{2}(\ddot{\theta}_r + \ddot{\theta}_l) + rb\ddot{\theta}_b \cos\theta_b - rb\dot{\theta}_b^2 \sin\theta_b - rl'(\ddot{\theta}_b + \ddot{\theta}_p)\cos(\theta_b + \theta_p) \\
&+ rl'(\dot{\theta}_b + \dot{\theta}_p)^2 \sin(\theta_b + \theta_p) + \frac{2r^2}{d^2}(\ddot{\theta}_r - \ddot{\theta}_l)(b^2 \sin^2\theta_b + l'^2 \sin^2(\theta_b + \theta_p) \\
&- 2l'b \sin\theta_b \sin(\theta_b + \theta_p)) + \frac{2r^2}{d^2}(\dot{\theta}_r - \dot{\theta}_l)(b^2 \dot{\theta}_b \sin 2\theta_b + l'^2(\dot{\theta}_b + \dot{\theta}_p)\sin(2\theta_b + 2\theta_p) \\
&- 2bl'\dot{\theta}_b \sin(2\theta_b + \theta_p) - 2l'b\dot{\theta}_p \sin\theta_b \cos(\theta_b + \theta_p))] + \frac{r^2}{d^2}(\ddot{\theta}_r - \ddot{\theta}_l)(J_{p_x}\cos^2(\theta_b + \theta_p) \\
&+ J_{p_y}\sin^2(\theta_b + \theta_p)) + \frac{r^2}{d^2}(\dot{\theta}_r - \dot{\theta}_l)(\dot{\theta}_b + \dot{\theta}_p)(J_{p_y} - J_{p_x})\sin(2\theta_b + 2\theta_p) = \tau_r
\end{aligned}
$$

If $q_i = \theta_l$

$$
\begin{aligned}
&-\frac{2r^2}{d^2}J_{\mathrm{w}_y}(\ddot{\theta}_r-\ddot{\theta}_l)+m_{\mathrm{w}}r^2\ddot{\theta}_l+J_{\mathrm{w}_z}\ddot{\theta}_l+\frac{1}{4}m_b r^2(\ddot{\theta}_r+\ddot{\theta}_l)-\frac{l^2r^2}{d^2}m_b[(\ddot{\theta}_r-\ddot{\theta}_l)\sin^2\theta_b\\
&+2(\dot{\theta}_r-\dot{\theta}_l)\dot{\theta}_b\cos\theta_b\sin\theta_b]+\frac{1}{2}m_b rl[\ddot{\theta}_b\cos\theta_b-\dot{\theta}_b{}^2\sin\theta_b]-\frac{r^2}{d^2}J_{b_x}[(\ddot{\theta}_r-\ddot{\theta}_l)\cos^2\theta_b\\
&-2(\dot{\theta}_r-\dot{\theta}_l)\dot{\theta}_b\sin\theta_b\cos\theta_b]-\frac{r^2}{d^2}J_{b_y}[(\ddot{\theta}_r-\ddot{\theta}_l)\sin^2\theta_b+2(\dot{\theta}_r-\dot{\theta}_l)\dot{\theta}_b\sin\theta_b\cos\theta_b]\\
&+\frac{1}{2}m_p[\frac{r^2}{2}(\ddot{\theta}_r+\ddot{\theta}_l)+rb\ddot{\theta}_b\cos\theta_b-rb\dot{\theta}_b^2\sin\theta_b-rl'(\ddot{\theta}_b+\ddot{\theta}_p)\cos(\theta_b+\theta_p)\\
&+rl'(\dot{\theta}_b+\dot{\theta}_p)^2\sin(\theta_b+\theta_p)-\frac{2r^2}{d^2}(\ddot{\theta}_r-\ddot{\theta}_l)(b^2\sin^2\theta_b+l'^2\sin^2(\theta_b+\theta_p)\\
&-2l'b\sin\theta_b\sin(\theta_b+\theta_p))-\frac{2r^2}{d^2}(\dot{\theta}_r-\dot{\theta}_l)(b^2\dot{\theta}_b\sin2\theta_b+l'^2(\dot{\theta}_b+\dot{\theta}_p)\sin(2\theta_b+2\theta_p)\\
&-2bl'\dot{\theta}_b\sin(2\theta_b+\theta_p)-2l'b\dot{\theta}_p\sin\theta_b\cos(\theta_b+\theta_p))]-\frac{r^2}{d^2}(\ddot{\theta}_r-\ddot{\theta}_l)(J_{p_x}\cos^2(\theta_b+\theta_p)\\
&+J_{p_y}\sin^2(\theta_b+\theta_p))-\frac{r^2}{d^2}(\dot{\theta}_r-\dot{\theta}_l)(\dot{\theta}_b+\dot{\theta}_p)(J_{p_y}-J_{p_x})\sin(2\theta_b+2\theta_p)=\tau_l
\end{aligned}
$$

If $q_i = \theta_b$

$$
\begin{aligned}
&m_b l^2\ddot{\theta}_b+\frac{1}{2}m_b rl(\ddot{\theta}_r+\ddot{\theta}_l)\cos\theta_b-\frac{1}{2}m_b rl(\dot{\theta}_r+\dot{\theta}_l)\dot{\theta}_b\sin\theta_b+J_{b_z}\ddot{\theta}_b\\
&-\frac{l^2r^2}{d^2}m_b(\dot{\theta}_r-\dot{\theta}_l)^2\cos\theta_b\sin\theta_b+\frac{1}{2}m_b rl(\dot{\theta}_r+\dot{\theta}_l)\dot{\theta}_b\sin\theta_b+\frac{r^2}{d^2}J_{b_x}(\dot{\theta}_r-\dot{\theta}_l)^2\sin\theta_b\cos\theta_b\\
&-\frac{r^2}{d^2}J_{b_y}(\dot{\theta}_r-\dot{\theta}_l)^2\sin\theta_b\cos\theta_b-m_b gl\sin\theta_b+\frac{1}{2}m_p[2b^2\ddot{\theta}_b+rb(\ddot{\theta}_r+\ddot{\theta}_l)\cos\theta_b\\
&+2l'^2(\ddot{\theta}_b+\ddot{\theta}_p)-rl'(\ddot{\theta}_r+\ddot{\theta}_l)\cos(\theta_b+\theta_p)+2bl'(\dot{\theta}_p^2+2\dot{\theta}_b\dot{\theta}_p)\sin\theta_p-2bl'(2\ddot{\theta}_b+\ddot{\theta}_p)\cos\theta_p\\
&-\frac{r^2}{d^2}(\dot{\theta}_r-\dot{\theta}_l)^2(b^2\sin2\theta_b+l'^2\sin(2\theta_b+2\theta_p)-2l'b\cos\theta_b\sin(\theta_b+\theta_p))]\\
&-\frac{r^2}{2d^2}(\dot{\theta}_r-\dot{\theta}_l)^2(J_{p_y}-J_{p_x})\sin(2\theta_b+2\theta_p)+J_{p_z}(\ddot{\theta}_b+\ddot{\theta}_p)-m_p gb\sin\theta_b\\
&+m_p gl'\sin(\theta_b+\theta_p)=0
\end{aligned}
$$

If $q_i = \theta_p$

$$\frac{1}{2}m_p[2l'^2(\ddot{\theta}_b + \ddot{\theta}_p) - rl'(\ddot{\theta}_r + \ddot{\theta}_l)\cos(\theta_b + \theta_p) - 2bl'\ddot{\theta}_b\cos\theta_p - 2bl'\dot{\theta}_b^2\sin\theta_p$$
$$- \frac{r^2}{d^2}(\dot{\theta}_r - \dot{\theta}_l)^2(l'^2\sin(2\theta_b + 2\theta_p) - 2l'b\sin\theta_b\cos(\theta_b + \theta_p))]$$
$$- \frac{r^2}{2d^2}(\dot{\theta}_r - \dot{\theta}_l)^2(J_{p_y} - J_{p_x})\sin(2\theta_b + 2\theta_p) + J_{p_z}(\ddot{\theta}_b + \ddot{\theta}_p) + m_p g l'\sin(\theta_b + \theta_p) = \tau_p$$

B.2 Inertia and Coriolis force matrix elements

$$M_{p_{11}} = M_{p_{22}} = (m_{\mathrm{w}} + \frac{1}{4}m_b + \frac{1}{4}m_p)r^2 + J_{\mathrm{w}_z} + \frac{r^2}{d^2}[m_b l^2 \sin^2\theta_b + 2J_{\mathrm{w}_y} + J_{b_x}\sin^2\theta_b$$
$$+ J_{b_y}\cos^2\theta_b + m_p b^2 \sin^2\theta_b + m_p l'^2 \sin^2(\theta_b + \theta_p) + J_{p_x}\sin^2(\theta_b + \theta_p) + J_{p_y}\cos^2(\theta_b + \theta_p)$$
$$- 2m_p b l' \sin\theta_b \sin(\theta_b + \theta_p)],$$
$$M_{p_{12}} = \frac{1}{4}(m_b + m_p)r^2 - \frac{r^2}{d^2}[m_b l^2 \sin^2\theta_b + 2J_{\mathrm{w}_y} + J_{b_x}\sin^2\theta_b + J_{b_y}\cos^2\theta_b + m_p b^2 \sin^2\theta_b$$
$$+ m_p l'^2 \sin^2(\theta_b + \theta_p) + J_{p_x}\sin^2(\theta_b + \theta_p) + J_{p_y}\cos^2(\theta_b + \theta_p) - 2m_p b l' \sin\theta_b \sin(\theta_b + \theta_p)],$$
$$M_{p_{13}} = M_{p_{23}} = \frac{1}{2}r\cos\theta_b(m_b l + m_p b) - \frac{1}{2}m_p r l' \cos(\theta_b + \theta_p),$$
$$M_{p_{14}} = M_{p_{24}} = -\frac{1}{2}m_p r l' \cos(\theta_b + \theta_p),$$
$$M_{p_{33}} = m_b l^2 + m_p(b^2 + l'^2) + J_{b_z} + J_{p_z} - 2m_p b l' \cos\theta_p,$$
$$M_{p_{34}} = m_p l'^2 - m_p b l' \cos\theta_p + J_{p_z}, \qquad M_{p_{44}} = m_p l'^2 + J_{p_z},$$
$$C_{p_{11}} = C_{p_{22}} = W_{p_1}\dot{\theta}_b + W_{p_2}\dot{\theta}_p, \qquad C_{p_{12}} = C_{p_{21}} = -W_{p_1}\dot{\theta}_b - W_{p_2}\dot{\theta}_p,$$
$$C_{p_{13}} = C_{p_{32}} = \frac{d}{r}W_{p_1}\dot{\theta}_y + \frac{1}{2}[m_p r l' \sin(\theta_b + \theta_p)](\dot{\theta}_b + \dot{\theta}_p) - \frac{1}{2}[(m_b l + m_p b)r\sin\theta_b]\dot{\theta}_b,$$
$$C_{p_{14}} = \frac{d}{r}W_{p_2}\dot{\theta}_y + \frac{1}{2}[m_p r l' \sin(\theta_b + \theta_p)](\dot{\theta}_b + \dot{\theta}_p),$$
$$C_{p_{23}} = C_{p_{31}} = -\frac{d}{r}W_{p_1}\dot{\theta}_y + \frac{1}{2}[m_p r l' \sin(\theta_b + \theta_p)](\dot{\theta}_b + \dot{\theta}_p) - \frac{1}{2}[(m_b l + m_p b)r\sin\theta_b]\dot{\theta}_b,$$
$$C_{p_{24}} = -\frac{d}{r}W_{p_2}\dot{\theta}_y + \frac{1}{2}[m_p r l' \sin(\theta_b + \theta_p)](\dot{\theta}_b + \dot{\theta}_p), \qquad C_{p_{33}} = m_p b l' \sin\theta_p \dot{\theta}_p,$$
$$C_{p_{34}} = m_p b l' \sin\theta_p(\dot{\theta}_b + \dot{\theta}_p), \quad C_{p_{41}} = -\frac{d}{r}W_{p_2}\dot{\theta}_y, \quad C_{p_{42}} = \frac{d}{r}W_{p_2}\dot{\theta}_y, \quad C_{p_{43}} = -m_p b l' \sin\theta_p \dot{\theta}_b.$$

where

$$W_{p_1} = \frac{r^2}{2d^2}[(m_b l^2 + m_p b^2 + J_{b_x} - J_{b_y})\sin 2\theta_b + (m_p l'^2 + J_{p_x} - J_{p_y})\sin 2(\theta_b + \theta_p)$$
$$- 2m_p b l' \sin(2\theta_b + \theta_p)],$$
$$W_{p_2} = \frac{r^2}{2d^2}[(m_p l'^2 + J_{p_x} - J_{p_y})\sin 2(\theta_b + \theta_p) - 2m_p b l' \sin\theta_b \cos(\theta_b + \theta_p)].$$

B.3 EOM elements

$$A_{p_1} = -\hat{M}_{p_{11}}^{-1}(C_{p_{11}}\dot{\theta}_r + C_{p_{12}}\dot{\theta}_l + C_{p_{13}}\dot{\theta}_b + C_{p_{14}}\dot{\theta}_p) - \hat{M}_{p_{12}}^{-1}(C_{p_{21}}\dot{\theta}_r + C_{p_{22}}\dot{\theta}_l + C_{p_{23}}\dot{\theta}_b + C_{p_{24}}\dot{\theta}_p)$$

$$- \hat{M}_{p_{13}}^{-1}(C_{p_{31}}\dot{\theta}_r + C_{p_{32}}\dot{\theta}_l + C_{p_{33}}\dot{\theta}_b + C_{p_{34}}\dot{\theta}_p + G_{p_3}) - \hat{M}_{p_{14}}^{-1}(C_{p_{41}}\dot{\theta}_r + C_{p_{42}}\dot{\theta}_l + C_{p_{43}}\dot{\theta}_b + G_{p_4}),$$

$$B_{p_1} = -\hat{M}_{p_{11}}^{-1}(D_{p_1} + R_{p_1}) - \hat{M}_{p_{12}}^{-1}(D_{p_2} + R_{p_2}) - \hat{M}_{p_{13}}^{-1}(D_{p_3} + R_{p_3}) - \hat{M}_{p_{14}}^{-1}(D_{p_4} + R_{p_4}),$$

$$A_{p_2} = -\hat{M}_{p_{21}}^{-1}(C_{p_{11}}\dot{\theta}_r + C_{p_{12}}\dot{\theta}_l + C_{p_{13}}\dot{\theta}_b + C_{p_{14}}\dot{\theta}_p) - \hat{M}_{p_{22}}^{-1}(C_{p_{21}}\dot{\theta}_r + C_{p_{22}}\dot{\theta}_l + C_{p_{23}}\dot{\theta}_b + C_{p_{24}}\dot{\theta}_p)$$

$$- \hat{M}_{p_{23}}^{-1}(C_{p_{31}}\dot{\theta}_r + C_{p_{32}}\dot{\theta}_l + C_{p_{33}}\dot{\theta}_b + C_{p_{34}}\dot{\theta}_p + G_{p_3}) - \hat{M}_{p_{24}}^{-1}(C_{p_{41}}\dot{\theta}_r + C_{p_{42}}\dot{\theta}_l + C_{p_{43}}\dot{\theta}_b + G_{p_4}),$$

$$B_{p_2} = -\hat{M}_{p_{21}}^{-1}(D_{p_1} + R_{p_1}) - \hat{M}_{p_{22}}^{-1}(D_{p_2} + R_{p_2}) - \hat{M}_{p_{23}}^{-1}(D_{p_3} + R_{p_3}) - \hat{M}_{p_{24}}^{-1}(D_{p_4} + R_{p_4}),$$

$$A_{p_3} = -\hat{M}_{p_{31}}^{-1}(C_{p_{11}}\dot{\theta}_r + C_{p_{12}}\dot{\theta}_l + C_{p_{13}}\dot{\theta}_b + C_{p_{14}}\dot{\theta}_p) - \hat{M}_{p_{32}}^{-1}(C_{p_{21}}\dot{\theta}_r + C_{p_{22}}\dot{\theta}_l + C_{p_{23}}\dot{\theta}_b + C_{p_{24}}\dot{\theta}_p)$$

$$- \hat{M}_{p_{33}}^{-1}(C_{p_{31}}\dot{\theta}_r + C_{p_{32}}\dot{\theta}_l + C_{p_{33}}\dot{\theta}_b + C_{p_{34}}\dot{\theta}_p + G_{p_3}) - \hat{M}_{p_{34}}^{-1}(C_{p_{41}}\dot{\theta}_r + C_{p_{42}}\dot{\theta}_l + C_{p_{43}}\dot{\theta}_b + G_{p_4}),$$

$$B_{p_3} = -\hat{M}_{p_{31}}^{-1}(D_{p_1} + R_{p_1}) - \hat{M}_{p_{32}}^{-1}(D_{p_2} + R_{p_2}) - \hat{M}_{p_{33}}^{-1}(D_{p_3} + R_{p_3}) - \hat{M}_{p_{34}}^{-1}(D_{p_4} + R_{p_4}),$$

$$A_{p_4} = -\hat{M}_{p_{41}}^{-1}(C_{p_{11}}\dot{\theta}_r + C_{p_{12}}\dot{\theta}_l + C_{p_{13}}\dot{\theta}_b + C_{p_{14}}\dot{\theta}_p) - \hat{M}_{p_{42}}^{-1}(C_{p_{21}}\dot{\theta}_r + C_{p_{22}}\dot{\theta}_l + C_{p_{23}}\dot{\theta}_b + C_{p_{24}}\dot{\theta}_p)$$

$$- \hat{M}_{p_{43}}^{-1}(C_{p_{31}}\dot{\theta}_r + C_{p_{32}}\dot{\theta}_l + C_{p_{33}}\dot{\theta}_b + C_{p_{34}}\dot{\theta}_p + G_{p_3}) - \hat{M}_{p_{44}}^{-1}(C_{p_{41}}\dot{\theta}_r + C_{p_{42}}\dot{\theta}_l + C_{p_{43}}\dot{\theta}_b + G_{p_4}),$$

$$B_{p_4} = -\hat{M}_{p_{41}}^{-1}(D_{p_1} + R_{p_1}) - \hat{M}_{p_{42}}^{-1}(D_{p_2} + R_{p_2}) - \hat{M}_{p_{43}}^{-1}(D_{p_3} + R_{p_3}) - \hat{M}_{p_{44}}^{-1}(D_{p_4} + R_{p_4}).$$

Appendix C

Experimental setup details

C.1 The LabVIEW block diagram for reading the IMU sensors

C.1.1 VN-200

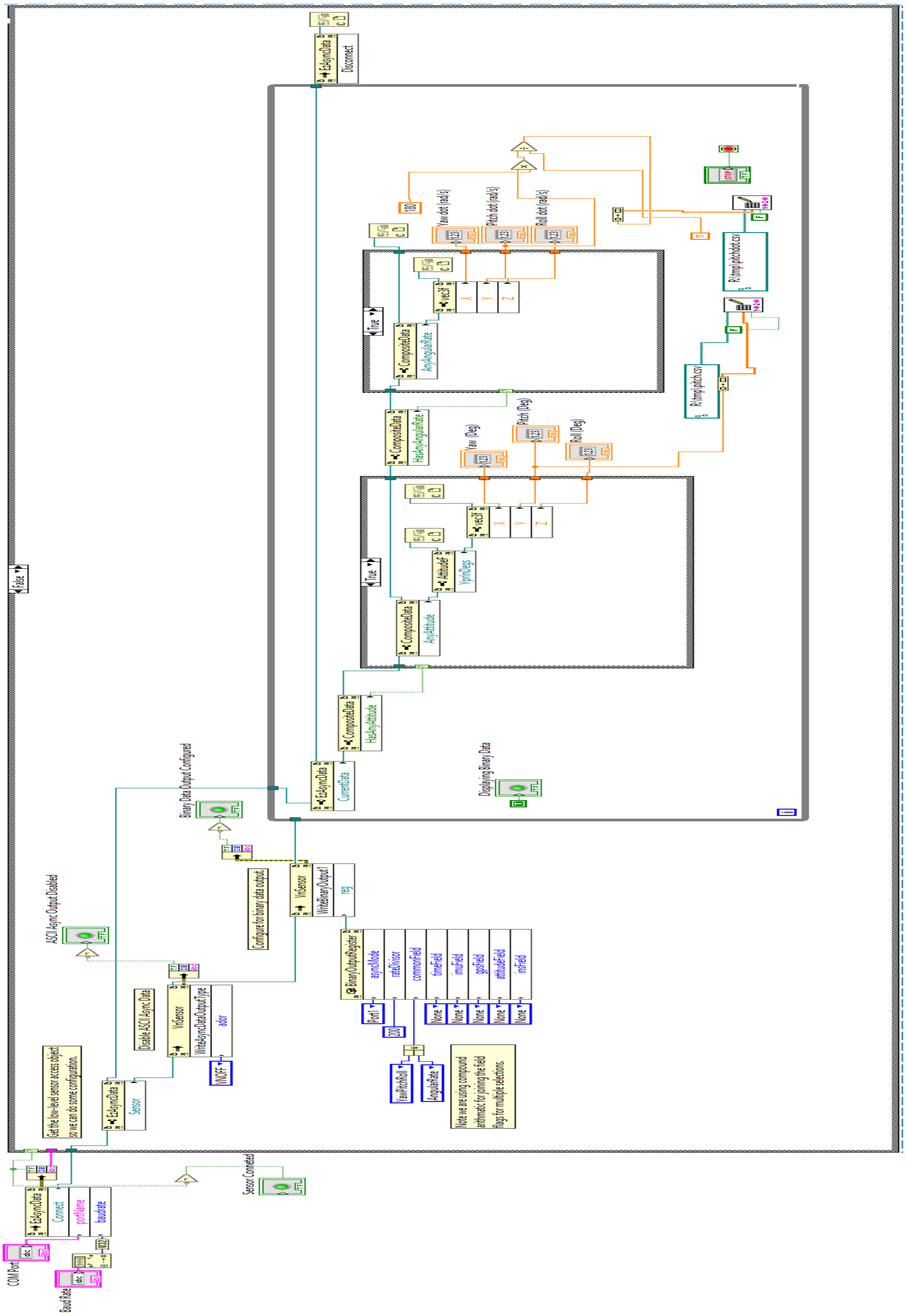

Figure C.1: The LabVIEW block diagram for reading pitch angle and pitch angular velocity by the VN-200 IMU sensor.

C.1.2 MPU6050

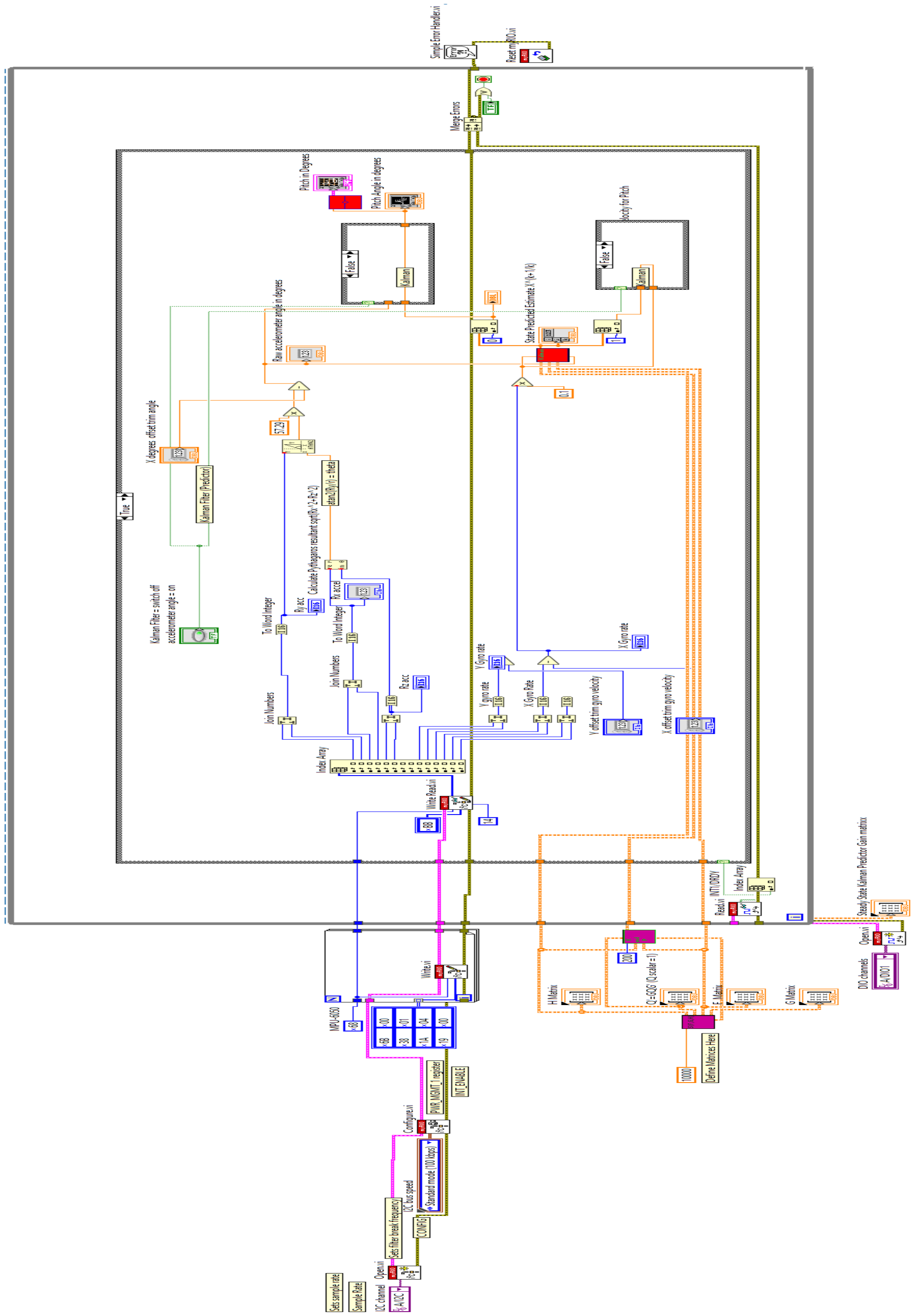

Figure C.2: The LabVIEW block diagram for reading the movable mechanism's angle and its velocity by the MPU6050 IMU sensor.

C.2 The LabVIEW block diagram for the TWRW stability control

C.2.1 Conventional system

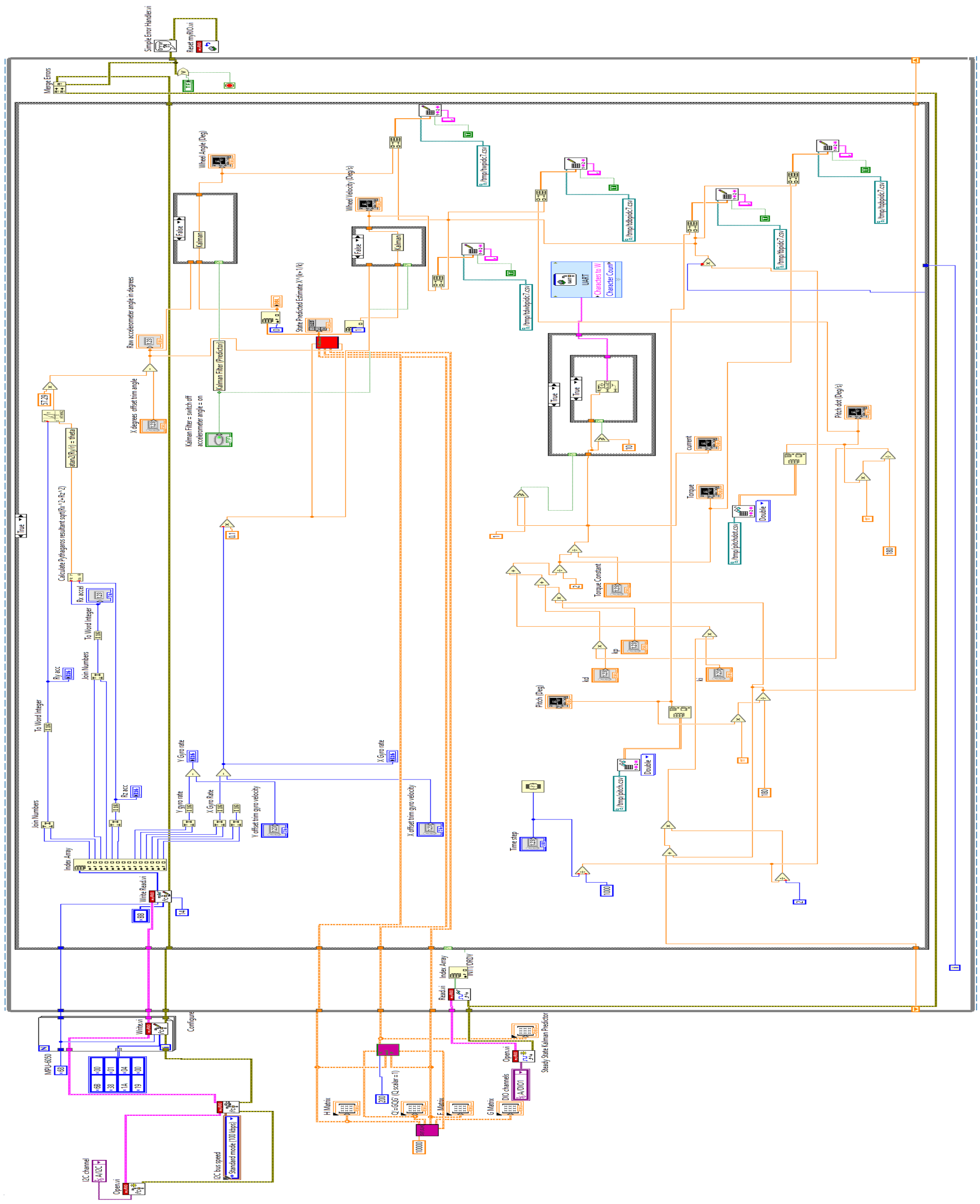

Figure C.3: The LabVIEW block diagram for stability control of the conventional system through PID control

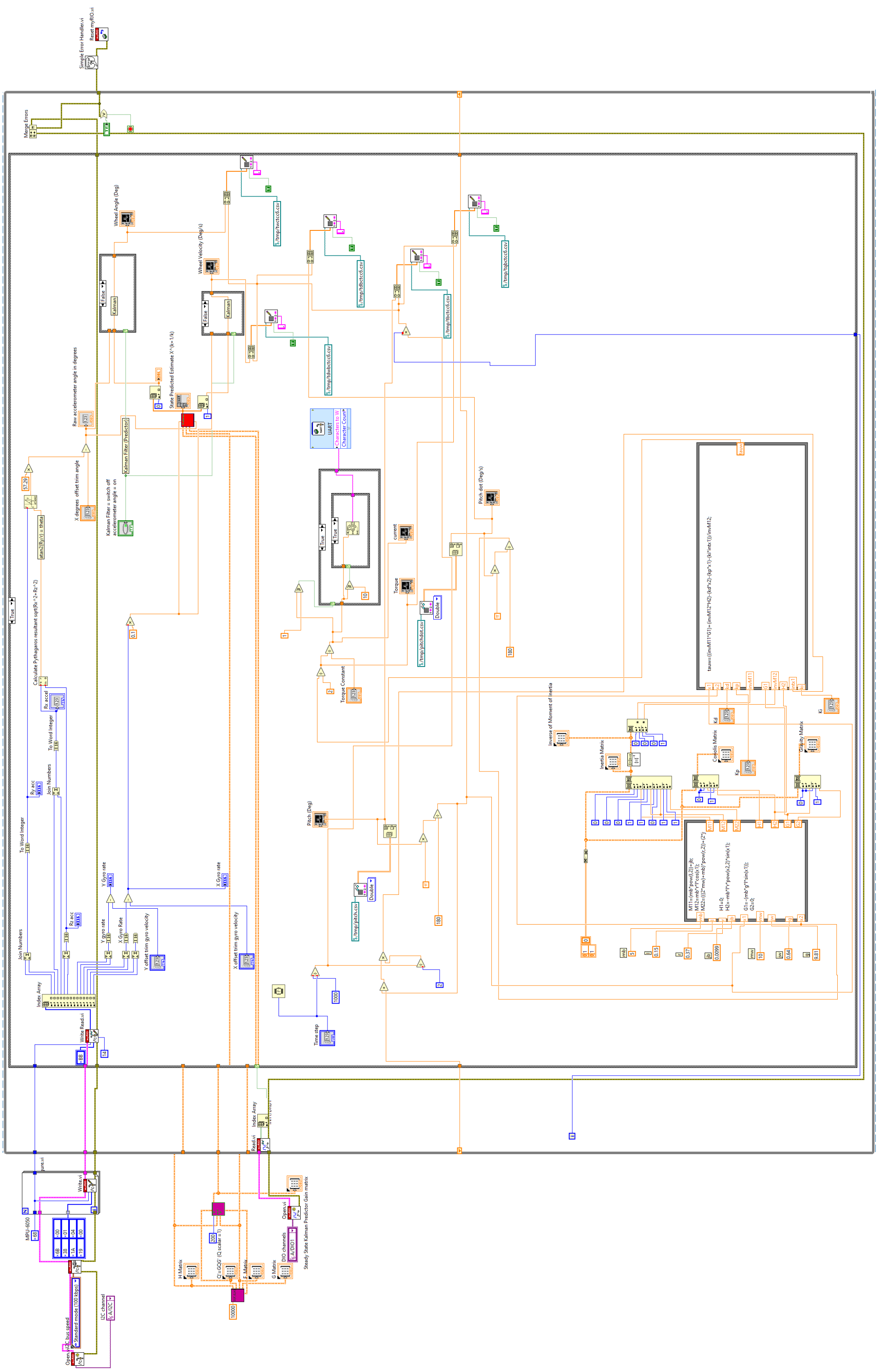

Figure C.4: The LabVIEW block diagram for stability control of the conventional system through CTC control

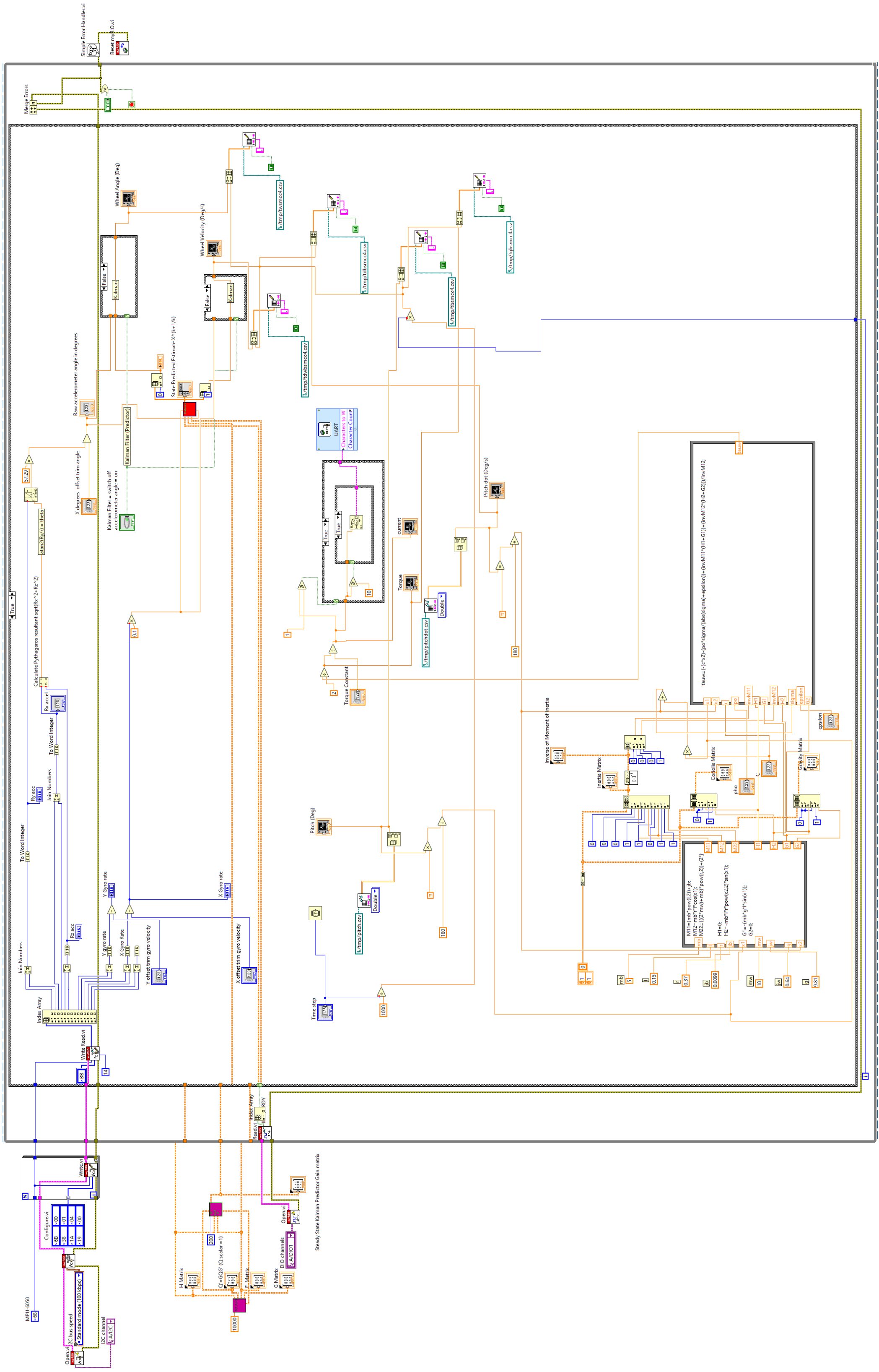

Figure C.5: The LabVIEW block diagram for stability control of the conventional system through SMC control

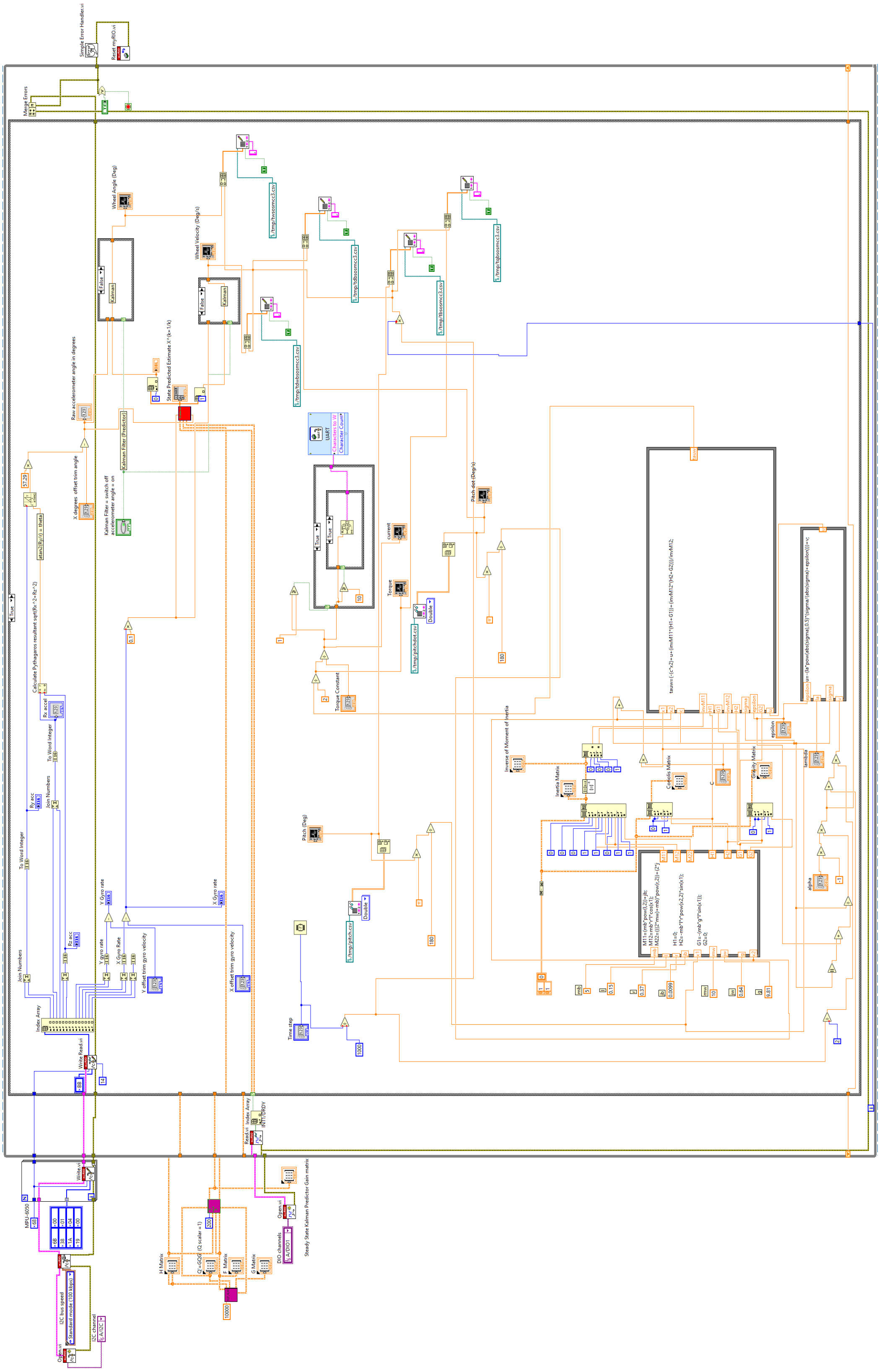

Figure C.6: The LabVIEW block diagram for stability control of the conventional system through SOSMC control

C.2.2 Proposed system

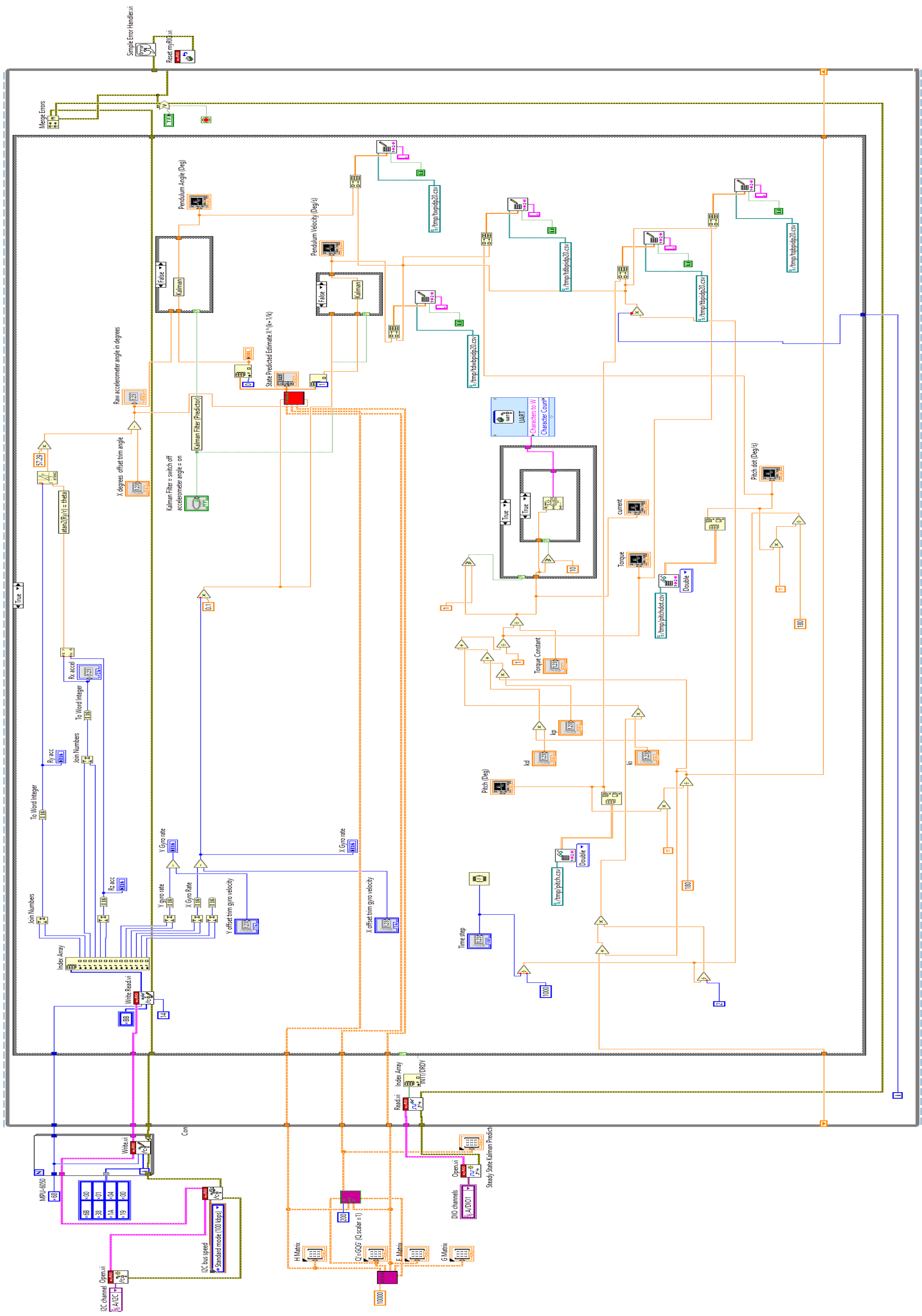

Figure C.7: The LabVIEW block diagram for stability control of the proposed system through PID control

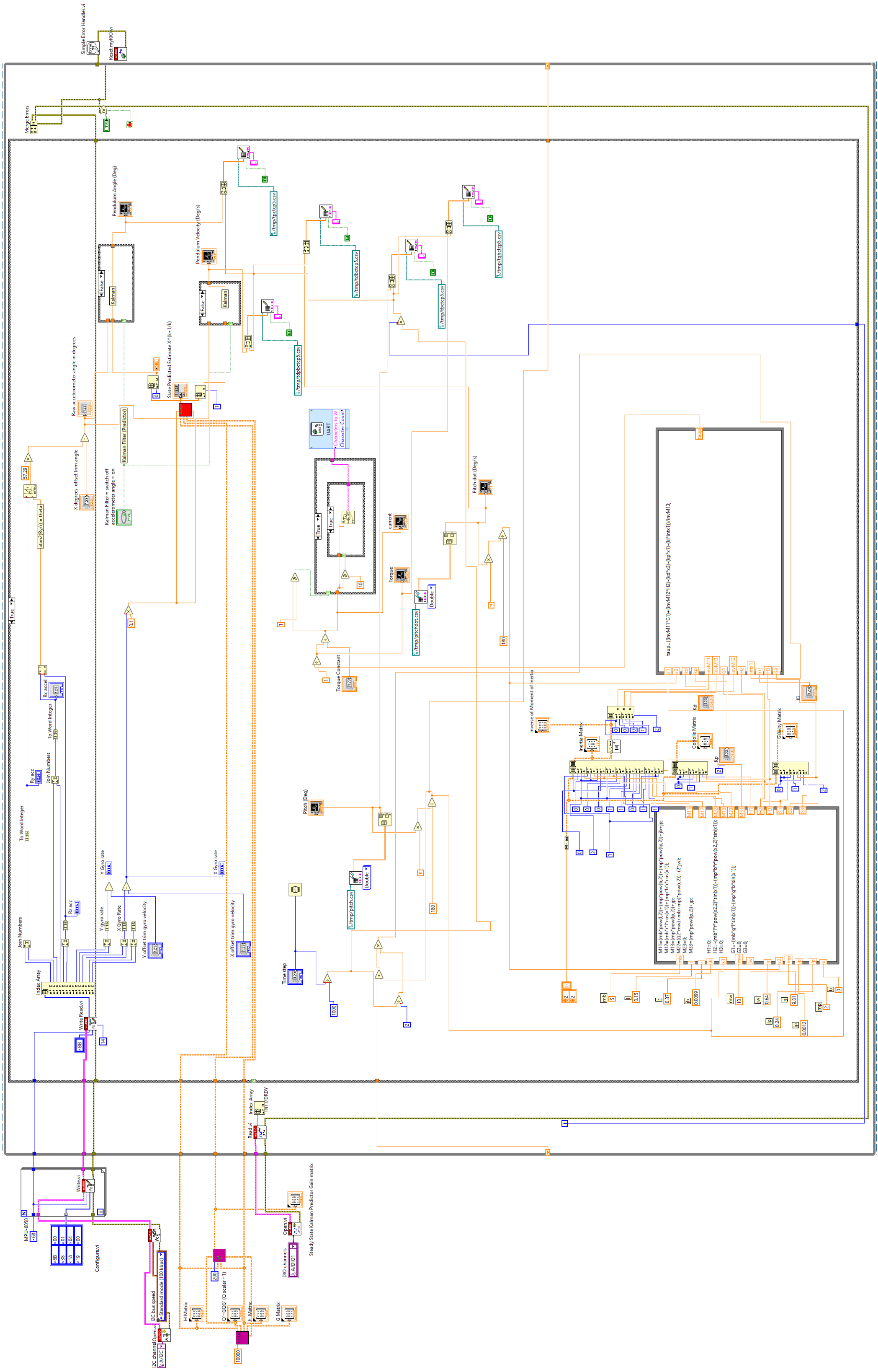

Figure C.8: The LabVIEW block diagram for stability control of the proposed system through CTC control

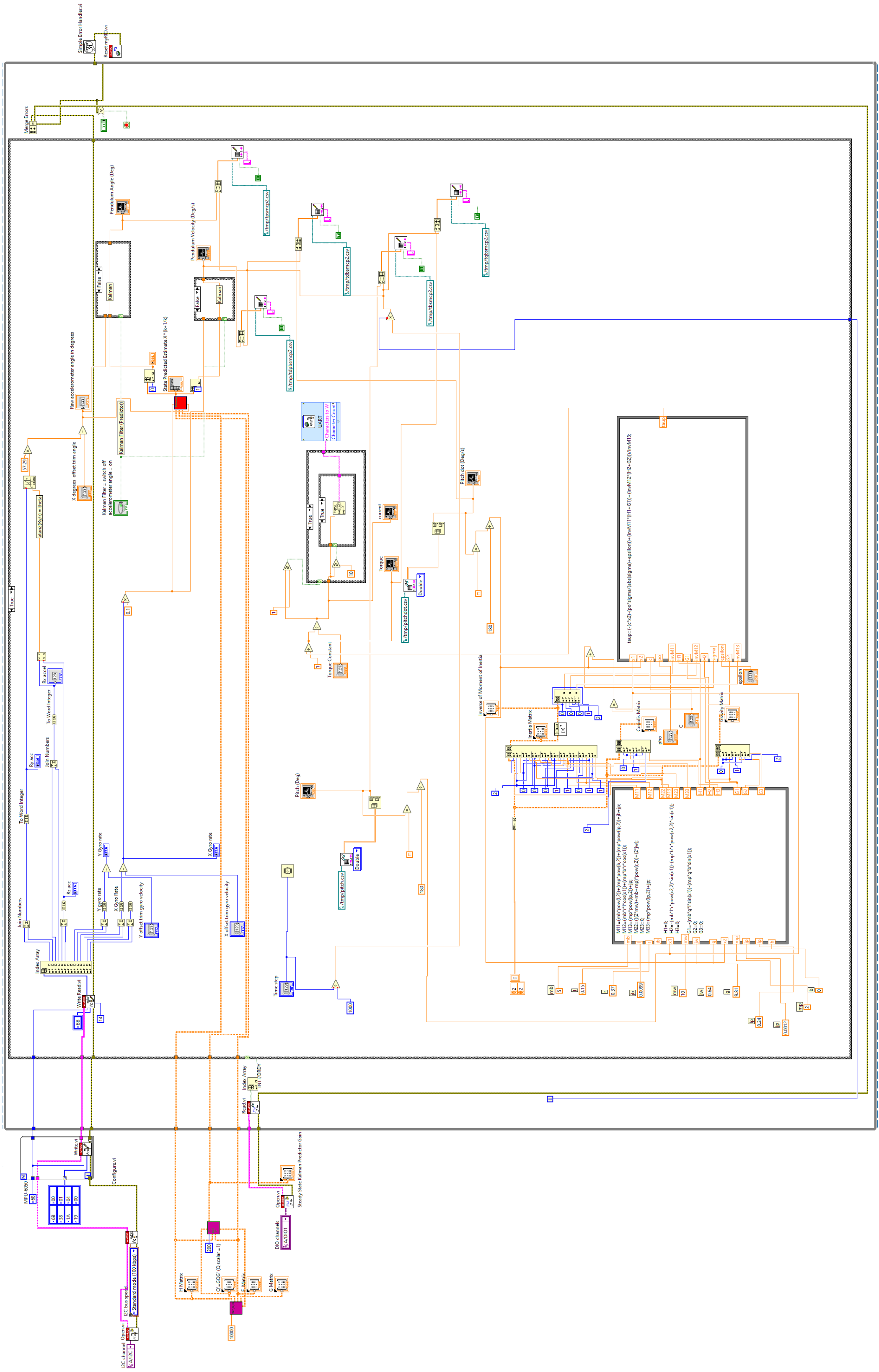

Figure C.9: The LabVIEW block diagram for stability control of the proposed system through SMC control

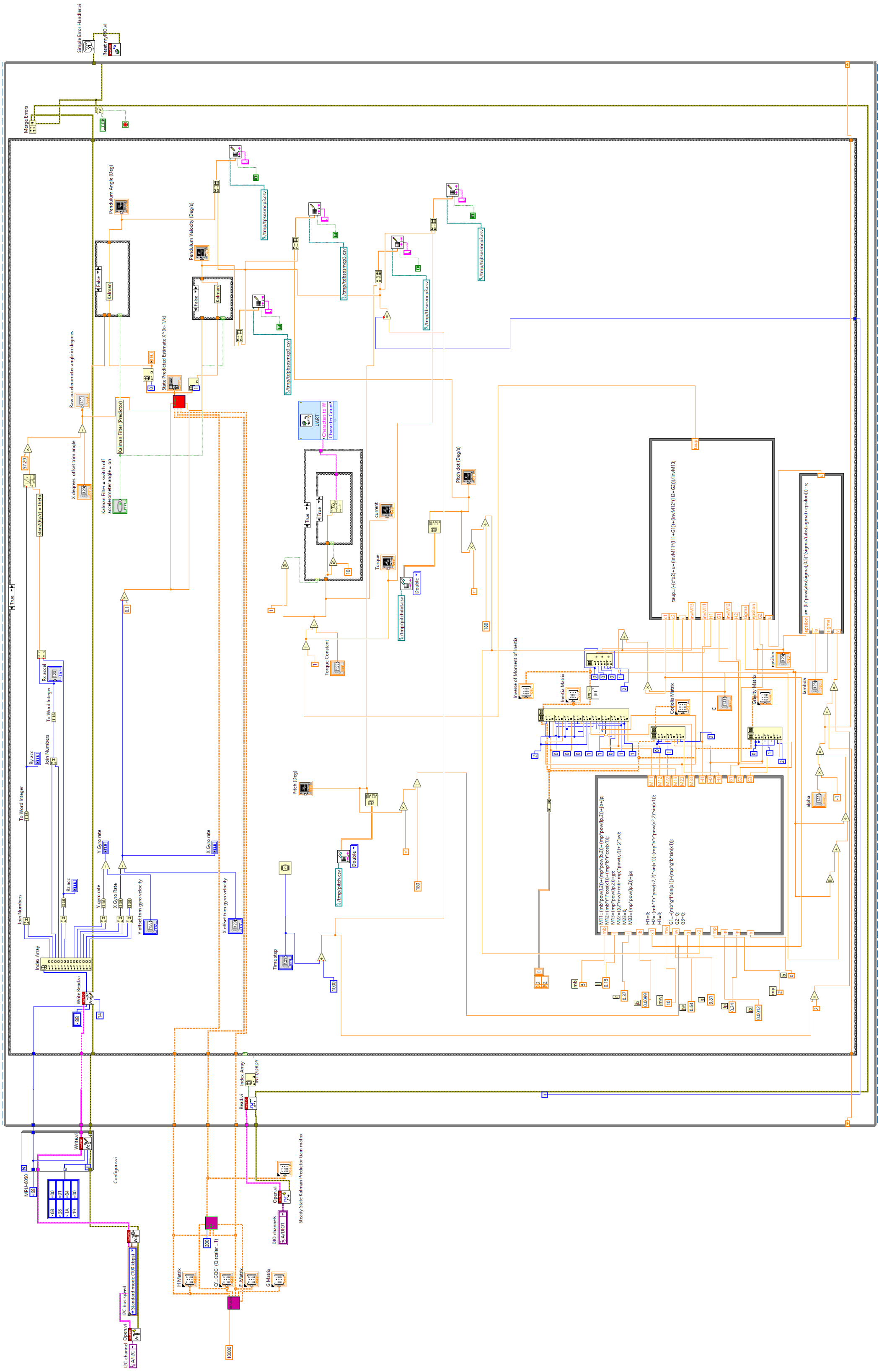

Figure C.10: The LabVIEW block diagram for stability control of the proposed system through SOSMC control

C.3 Arduino IDE code for the TWRW stability control

C.3.1 Conventional system

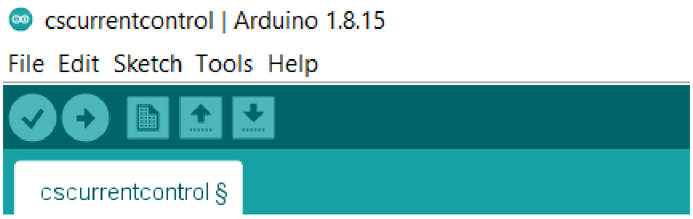


```
#include <VescUart.h>

VescUart UART1;
VescUart UART2;

float current ; /** The current in amps */

void setup() {
  Serial.begin(115200);
  Serial2.begin(115200);
  Serial1.begin(115200);
  // serial1=motor1
  Serial3.begin(115200);
  // serial3=motor2

  while (!Serial1) {;}
  UART1.setSerialPort(&Serial1);
  UART2.setSerialPort(&Serial3);
}

void loop() {
  if (Serial2.available() > 0) {
     current = Serial2.parseFloat();
     Serial.print("Current: ");
     Serial.println(current);
     UART1.setCurrent(current);
     UART2.setCurrent(current);
  }
}
```

Figure C.11: The Arduino IDE code for communication between the MyRIO-1900 and MTVESC50A for the conventional system

C.3.2 Proposed system

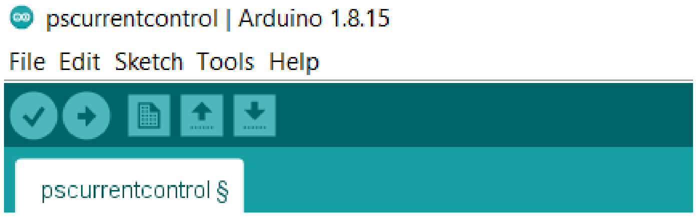


```
#include <VescUart.h>

VescUart UART1;

float current ; /** The current in amps */

void setup() {
  Serial.begin(115200);
  Serial2.begin(115200);
  Serial1.begin(115200);
  // serial1=motor1

  while (!Serial1) {;}

  UART1.setSerialPort(&Serial1);
}
void loop() {
  if (Serial2.available() > 0) {
     current = Serial2.parseFloat();
     Serial.print("Current: ");
     Serial.println(current);
     UART1.setCurrent(current);
  }
}
```

Figure C.12: The Arduino IDE code for communication between the MyRIO-1900 and MTVESC50A for the proposed system